

Imperial College London
Department of Chemical Engineering and Chemical Technology
Qatar Carbonates and Carbon Storage Research Centre

Interfacial Properties of Reservoir Fluids and Carbon Dioxide with Impurities

Yu Tsing Florence Chow

September 2016

A thesis submitted in part fulfilment of the requirements for the degree of
Doctor of Philosophy in Chemical Engineering and Chemical Technology
of Imperial College London
and the Diploma of Imperial College London

This is an original work by the author, and all else is appropriately referenced. The copyright of this thesis rests with the author and is made available under a Creative Commons Attribution Non-Commercial No Derivatives licence. Researchers are free to copy, distribute or transmit the thesis on the condition that they attribute it, that they do not use it for commercial purposes and that they do not alter, transform or build upon it. For any reuse or redistribution, researchers must make clear to others the licence terms of this work.

Publications

Y.T.F. Chow, D.K. Eriksen, A. Galindo, A.J. Haslam, G. Jackson, G.C. Maitland, J.P.M. Trusler, Interfacial tensions of systems comprising water, carbon dioxide and diluent gases at high pressures: Experimental measurements and modelling with SAFT-VR Mie and square-gradient theory, *Fluid Phase Equilibria*, 407 (2016) 159-176.

Y.T.F. Chow, G.C. Maitland, J.P.M. Trusler, Interfacial tensions of the (CO₂ + N₂ + H₂O) system at temperatures of (298 to 448) K and pressures up to 40 MPa, *The Journal of Chemical Thermodynamics*, 93 (2016) 392-403.

Table of Contents

1	Introduction.....	11
1.1	Paris Agreement.....	11
1.2	Carbon Capture and Storage (CCS).....	11
1.3	Storage Sites and Conditions	13
1.4	Impurities in the CO ₂ Stream	13
1.5	Design of CCS Processes	14
1.6	Interfacial Properties	15
2	Theoretical Background.....	17
2.1	Theory of Interfacial Forces.....	17
2.1.1	Interfacial Tension	17
2.1.2	Contact Angle	21
2.2	Measurement Techniques	24
2.2.1	Interfacial Tension	24
2.2.2	Contact Angle	30
2.3	Theoretical Modelling Methods for γ and θ	34
2.3.1	Interfacial Tension	34
3	Literature Review.....	45
3.1	Interfacial Tension	45
3.1.1	Experimental Measurement	45
3.1.2	Modelling.....	51
3.2	Contact Angle	53
3.2.1	Experimental Measurement	53
4	Experimental Methodology.....	58
4.1	Equipment Description	58
4.2	Equipment Design, Construction and Commissioning	62
4.2.1	Material of Construction	62
4.2.2	Pressure Vessel	62
4.2.3	Substrate Adjuster.....	65
4.2.4	Temperature regulation	66
4.2.5	Commissioning	66
4.3	Experimental Systems and Conditions	67
4.3.1	Interfacial Tension	67
4.3.2	Contact Angle	67
4.4	Materials.	67

4.5	Experimental Procedure	68
4.5.1	Interfacial Tension	68
4.5.2	Contact Angle	68
4.6	Validation.....	69
4.6.1	Interfacial Tension	69
4.6.2	Contact Angle	69
4.7	Data Analysis.....	70
4.7.1	Drop Image Analysis	70
4.7.2	Interfacial Tension	71
5	Results - Interfacial Tension	75
5.1	Binary Systems	75
5.1.1	(N ₂ + H ₂ O) System.....	76
5.1.2	(Ar + H ₂ O) System.....	79
5.1.3	(H ₂ + H ₂ O) System.....	82
5.2	Ternary Systems.....	86
5.2.1	(CO ₂ + N ₂ + H ₂ O) System.....	86
5.2.2	(CO ₂ + Ar + H ₂ O) System.....	87
5.2.3	(CO ₂ + H ₂ + H ₂ O) System.....	88
5.3	Modelling.....	90
5.3.1	Empirical Model	90
5.3.2	Square Gradient Theory + SAFT	94
6	Results - Contact Angle	103
6.1	Static Contact Angles.....	103
6.2	Dynamic Contact Angles	105
6.3	Vertical Scanning Interferometry (VSI) Analysis.....	105
7	Conclusion	107
7.1	Effect of Gas Impurities.....	107
7.2	Future Work.....	108
7.3	Summary	108
8	References.....	110
9	Appendix.....	124
9.1	Piping and Instrumentation Diagram (P&ID).....	124
9.2	List of IFP Apparatus Components.....	125
9.3	View Cell Design.....	129
9.4	Substrate Adjuster.....	130
9.5	Pressure Test Certificate	133

List of Figures

Figure 1.1 Components of the CCS chain: capture, transport, and storage.....	11
Figure 1.2 Operation dates and capacities of large-scale CCS projects in the Operate, Execute and Define stages across the world.....	12
Figure 1.3 The CCS process design cycle and the importance of CO ₂ -mixture thermophysical properties.....	14
Figure 1.4 <i>Left.</i> CO ₂ injection into a reservoir, sealed under an impermeable caprock. <i>Right.</i> CO ₂ capillary trapping by imbibing brine.....	15
Figure 2.1 Variation of density across an interface with the coordinate normal to its surface.....	17
Figure 2.2 Coordinates and reference points used in the derivation of the Young-Laplace equation.....	18
Figure 2.3 <i>Left.</i> Gibbs description of an ideal interface σ separating the two bulk phases α and β . <i>Centre.</i> Guggenheim description of an extended interface with a certain volume. <i>Right.</i> The position of the Gibbs-dividing plane based on the surface excess condition $\Gamma = 0$	19
Figure 2.4 A sessile drop on a planar solid surface, showing the contact angle θ : (<i>left</i>) magnified view of the rim of the drop and the three-phase contact line; (<i>right</i>) profile of the sessile drop and the associated interfacial tensions of the system.....	21
Figure 2.5 Circular liquid drop on a planar solid surface.....	21
Figure 2.6 Classification of wetting behaviour.....	23
Figure 2.7 Dependence of the experimentally measured apparent contact angle on velocity of forced wetting.....	23
Figure 2.8 Schematic of the (a) capillary rise method, (b) Wilhelmy plate method, (c) du Noüy ring method, and (d) maximum bubble pressure method (MBPM).....	24
Figure 2.9 Schematic of (a) a pendant drop with characteristic dimensions, d_e and d_s , and the coordinates used in the Young-Laplace equation, (b) a sessile drop with characteristic dimensions, R and h	25
Figure 2.10 <i>Left.</i> Image of a sessile drop for contact angle measurement. <i>Right.</i> Image of a captive bubble for contact angle measurement.....	31
Figure 2.11 Expansion and contraction method used to measure the advancing, θ_a , and receding angles, θ_r , corresponding to imbibition and drainage respectively.....	32
Figure 2.12 Tilting plate method used to measure the dynamic contact angle.....	33
Figure 3.1 Interfacial tension changes of a measured drop with time.....	46
Figure 4.1 Interfacial properties apparatus set-up.....	60
Figure 4.2 Interfacial properties apparatus.....	61

Figure 4.3 <i>Left.</i> Magnetic substrate adjuster assembly after installation into the view cell. <i>Top right.</i> Substrate holder inside the view cell, showing the inlet port positions. <i>Bottom right.</i> Substrate holder with a calcite substrate sample moulded to fit with PTFE tape.....	61
Figure 4.4 <i>Top left.</i> Dimensions of the end closure components. <i>Bottom left.</i> SolidWorks assembly of the end closure in the vessel. <i>Right.</i> Manufactured end closure components and installation tools.....	64
Figure 4.5 <i>Left.</i> Bird's-eye view of substrate holder positioning inside the view cell. <i>Centre.</i> Cross-section of the substrate adjuster, showing the magnetic coupling. <i>Right.</i> SolidWorks model of the substrate adjuster assembly.....	65
Figure 4.6 Substrate adjuster kit.....	66
Figure 4.7 <i>Left.</i> Heater shell enclosing the view cell. <i>Right.</i> Heater shell assembled on to the saddle supports.....	66
Figure 4.8 <i>Left.</i> PTFE-air dynamic contact angles from literature. <i>Right.</i> PTFE-air static contact angles from literature.....	70
Figure 4.9 Density difference calculation procedure.....	73
Figure 5.1 Interfacial tensions γ at various pressures p for the (N ₂ + H ₂ O) system.....	77
Figure 5.2 Difference in interfacial tension measurements of the (N ₂ + H ₂ O) system from model.....	78
Figure 5.3 Interfacial tensions γ at various pressures p for the (Ar + H ₂ O) system.....	80
Figure 5.4 Difference in interfacial tension measurements of the (Ar + H ₂ O) system from model.....	81
Figure 5.5 Interfacial tensions γ at various pressures p for the (H ₂ + H ₂ O) system.....	84
Figure 5.6 Difference in interfacial tension measurements of the (H ₂ + H ₂ O) system from model.....	85
Figure 5.7 Interfacial tensions at various pressures for the gas phase mixture composition of [x CO ₂ + (1 - x) N ₂], with $x = 0.5120$	91
Figure 5.8 Interfacial tensions at various pressures for the gas phase mixture composition of [x CO ₂ + (1 - x) Ar], with $x = 0.4973$	92
Figure 5.9 Interfacial tensions at various pressures for the gas phase mixture composition of [x CO ₂ + (1 - x) H ₂], with $x = 0.300$	93
Figure 5.10 Interfacial tensions γ at pressures p for (N ₂ + H ₂ O).....	97
Figure 5.11 Difference $\Delta\gamma = (\gamma_{\text{exp}} - \gamma_{\text{calc}})$ between experimental interfacial tensions γ_{exp} of the (N ₂ + H ₂ O) system and values γ_{calc} calculated using the SAFT + SGT approach.	98
Figure 5.12 Interfacial tensions γ at pressures p for (Ar + H ₂ O).....	99
Figure 5.13 Difference $\Delta\gamma = (\gamma_{\text{exp}} - \gamma_{\text{calc}})$ between experimental interfacial tensions γ_{exp} of the (Ar + H ₂ O) system and values γ_{calc} calculated using the SAFT + SGT approach.....	100
Figure 5.14 Interfacial tensions γ at pressures p for the (CO ₂ + N ₂ + H ₂ O) system.....	101
Figure 5.15 Interfacial tensions γ at pressures p for the (CO ₂ + Ar + H ₂ O) system.....	102
Figure 6.1 (CO ₂ + brine + calcite) captive bubble at start of the experiment, at 333 K.....	103
Figure 6.2 (CO ₂ + brine + calcite) drop at start of the experiment, at 333 K.....	103
Figure 6.3 (CO ₂ + N ₂ + brine + calcite) captive bubble at start of the experiment, at 333 K.....	103

Figure 6.4 Static contact angles for the (CO₂ + brine + calcite) system measured.....104

Figure 6.5 Vertical Scanning Interferometry (VSI) scans of two neighbouring sub-regions of the same reference substrate.....106

Figure 6.6 VSI scans of several neighbouring sub-regions on a substrate used for contact angle measurements of the (CO₂ + brine + calcite) system, at 333 K, from (2 to 50) MPa.....106

List of Tables

Table 1.1 Estimated pressure and temperature conditions of the CCS chain.....	13
Table 1.2 Estimated concentrations of potential impurities in the captured CO ₂ stream.....	14
Table 3.1 Studies of the interfacial tension of CO ₂ with H ₂ O or brine reported in literature.....	45
Table 3.2 Studies of the interfacial tension of water with various gases in binary and ternary systems reported in literature.....	49
Table 3.3 Previous modelling studies for the interfacial properties of (CO ₂ + H ₂ O), (N ₂ + H ₂ O), (Ar + H ₂ O) and (N ₂ + CO ₂ + H ₂ O); <i>T</i> and <i>p</i> refer to the temperature and pressure ranges examined, respectively.....	51
Table 3.4 Systems of substrate and fluids where contact angle measurements have been reported to the highest measured temperature and pressure.....	53
Table 3.5 Cleaning methods of the substrates prior to experiment as reported in literature.....	54
Table 4.1 Key design properties of Titanium Grade 4.....	62
Table 4.2 Pressure vessel design and corresponding high pressure duty assessment.....	63
Table 4.3 Interfacial tension systems studied at temperatures <i>T</i> and pressures <i>p</i> in this work.....	67
Table 4.4 Contact angle systems studied at temperatures <i>T</i> and pressures <i>p</i> in this work, for a 1 mol·kg ⁻¹ NaHCO ₃ brine solution, using the tilting plate (TP) method.....	67
Table 4.5 Description of chemical samples, where <i>x</i> denotes mole fraction of a single substance or a mixture of defined composition and ρ_e denotes electrical resistivity.....	68
Table 4.6 Water surface tension measurements as compared to IAPWS recommended correlation values, and the experimental systems for which the validation applies.....	69
Table 4.7 Thermodynamic properties of the pure components for the PR EoS. Equations of state (EoS) and partial molar volume models used in the calculation of the phase densities.....	73
Table 4.8 Binary interaction parameters k_{ij} and Henry's constants H_{ij} for use in the PR-NRTL model.....	74
Table 5.1 Fitting parameters of the empirical model (5.2) for the interfacial tension measurements.....	76
Table 5.2 Interfacial tension γ for (N ₂ + H ₂ O) at temperatures <i>T</i> and pressures <i>p</i> , with calculated density difference $\Delta\rho$	76
Table 5.3 Interfacial tension γ for (Ar + H ₂ O) at temperatures <i>T</i> and pressures <i>p</i> , with calculated density difference $\Delta\rho$	79
Table 5.4 Interfacial tension γ for (H ₂ + H ₂ O) at temperatures <i>T</i> and pressures <i>p</i> , with calculated density difference $\Delta\rho$	82
Table 5.5 Interfacial tensions γ at temperatures <i>T</i> and pressures <i>p</i> for the gas phase mixture composition of [<i>x</i> CO ₂ + (1 - <i>x</i>) N ₂], with <i>x</i> = 0.5120.....	86

Table 5.6 Interfacial tensions γ at temperatures T and pressures p for the gas phase mixture composition of $[x \text{ CO}_2 + (1 - x) \text{ Ar}]$, with $x = 0.4973$	87
Table 5.7 Interfacial tensions γ at temperatures T and pressures p for the gas phase mixture composition of $[x \text{ CO}_2 + (1 - x) \text{ H}_2]$, with $x = 0.300$	88
Table 5.8 Average absolute relative deviations Δ_{AAD} between experimental interfacial tensions and values calculated from Eq. (5.3) for isotherms at temperatures T , and overall average absolute relative deviations $\Delta_{\text{AAD,overall}}$ for each system investigated.....	90
Table 5.9 Pure-component parameters in SAFT-VR Mie.....	94
Table 5.10 Binary parameters used in SAFT-VR Mie between H_2O (component 1) and other components in the mixture.....	95
Table 5.11 SGT influence parameters a_1 and a_0 for the components studied in this work.....	95
Table 5.12 Average absolute relative deviations Δ_{AAD} between experimental interfacial tensions and values calculated from the SAFT + SGT approach.....	96

Acknowledgements

I would like to sincerely thank my two supervisors, Professor J P Martin Trusler and Professor Geoffrey C Maitland for their guidance and faith from the beginning to the completion of this research. Martin's incredible intellectual clarity, focus and professional rigour has guided the construction of an apparatus I feel proud of creating, and was used to conduct experimental research work of high quality to contribute to the scientific community. I am always inspired by Geoff's passion and commitment to making CCS a reality for future generations. He motivates by example, to bring about positive development in the world, setting ambitious goals and having the courage to work towards it. This work was supported by funding from the Qatar Carbonates and Carbon Storage Research Center (QCCSRC), provided jointly by Qatar Petroleum, Shell, and Qatar Science & Technology Park, and I gratefully acknowledge their support, providing me with the opportunity to embark on this intellectual challenge and contribute to this meaningful research to help tackle climate challenges.

I would like to acknowledge and thank the QCCSRC and Thermophysical Group Members, both past and present, who have contributed to this research work: Mr. Gavin Barnes' skilled craftsmanship in the construction of the interfacial properties rig; Dr. Mihaela Stevar for the collaboration work on the contact angle measurements, support and engaging technical discussions; Dr. Daniel Eriksen for creating the SAFT + SGT model to describe the interfacial tension data measured; Dr. Xuesong Li for her training and advice on making interfacial tension measurements; Mr. Benaiah Anabaraonye for the advice on reaction kinetics relating to calcite contact angle measurements, and intriguing discussions in the laboratory; Dr. Iain Macdonald, the QCCSRC project manager, for his organisation and assistance throughout this journey; and Dr. Yolanda Vincente-Sanchez, Dr. Saif Al Ghafri, Dr. Emmanuel Efika, Dr. Shane Cadogan, Dr. Jiafei Zhang, Mr. Weparn J Tay, Mr. Rayane Hoballah, Mr. Claudio Calabrese, and Mr. Hao Bian for their help in the Thermophysical Laboratories. A further thank you to mentors, Dr. Colin Hale and Professor Nina Thornhill.

I would like to dedicate this thesis to my parents, Catherine and Kwai Sum, who have always given me the freedom to do what I choose, supported my decision to study at Imperial College, and encouraged me to accomplish something I dreamt of doing 10 years ago in high school. Finally, I would like to show appreciation for my dearest family and friends, Freeman, Mandy, Victoria, Helen and George for putting up with my worst, and showing unwavering moral support.

Abstract

Interfacial tension measurements of the binary systems ($\text{N}_2 + \text{H}_2\text{O}$), ($\text{Ar} + \text{H}_2\text{O}$), and ($\text{H}_2 + \text{H}_2\text{O}$), and ternary systems ($\text{CO}_2 + \text{N}_2 + \text{H}_2\text{O}$), ($\text{CO}_2 + \text{Ar} + \text{H}_2\text{O}$) and ($\text{CO}_2 + \text{H}_2 + \text{H}_2\text{O}$), are reported at pressures of (0.5 to 50.0) MPa, and temperatures of (298.15 to 473.15) K. The design of a custom-built Interfacial Properties Rig was detailed. The pendant drop method was used. The expanded uncertainties at 95 % confidence are 0.05 K for temperature; 0.07 MPa for pressure; $0.019 \cdot \gamma$ for interfacial tension in the ($\text{N}_2 + \text{H}_2\text{O}$) system; $0.016 \cdot \gamma$ for interfacial tension in the ($\text{Ar} + \text{H}_2\text{O}$) system; $0.017 \cdot \gamma$ for interfacial tension in the ($\text{H}_2 + \text{H}_2\text{O}$) system; $0.032 \cdot \gamma$ for interfacial tension in the ($\text{CO}_2 + \text{N}_2 + \text{H}_2\text{O}$) system; $0.018 \cdot \gamma$ for interfacial tension in the ($\text{CO}_2 + \text{Ar} + \text{H}_2\text{O}$) system; and $0.017 \cdot \gamma$ for interfacial tension in the ($\text{CO}_2 + \text{H}_2 + \text{H}_2\text{O}$) system. The interfacial tensions of all systems were found to decrease with increasing pressure. The use of SGT + SAFT-VR Mie to model interfacial tensions of the binary and ternary systems was reported, for systems involving CO_2 , N_2 and Ar. The binary systems ($\text{N}_2 + \text{H}_2\text{O}$) and ($\text{Ar} + \text{H}_2\text{O}$), and ternary systems ($\text{CO}_2 + \text{N}_2 + \text{H}_2\text{O}$) and ($\text{CO}_2 + \text{Ar} + \text{H}_2\text{O}$), were modelled with average absolute relative deviations of 1.5 %, 1.8 %, 3.6 % and 7.9 % respectively. For the ($\text{CO}_2 + \text{Ar} + \text{H}_2\text{O}$) system, the agreement is satisfactory at the higher temperatures, but differs significantly at the lower temperatures. Contact angles of ($\text{CO}_2 + \text{brine}$) and ($\text{CO}_2 + \text{N}_2 + \text{brine}$) systems on calcite surfaces have also been measured, at 333 K and 7 pressures, from (2 to 50) MPa, for a $1 \text{ mol} \cdot \text{kg}^{-1}$ NaHCO_3 brine solution, using the static method on captive bubbles.

1 Introduction

The motivation for this research, in the interfacial properties of CO₂ streams with impurities at reservoir conditions, is outlined in this chapter; from the climate target of the Paris Agreement, the need for carbon capture and storage (CCS) to achieve the 2 °C Scenario (2DS), to the barriers of CCS deployment. We then focus on the storage part of the CCS chain, outlining suitable storage sites, storage conditions, the impurity specifications of the CO₂-rich storage stream and its implication on the design of storage processes. Lastly, the role that the interfacial properties studied in this work, interfacial tension and contact angle, play in storage process design is then highlighted.

1.1 Paris Agreement

In December 2015, the Paris Agreement was adopted by 195 countries, to limit global average temperature increase to well below 2 °C above pre-industrial levels by 2100 [1]. The partially-legally binding global climate deal will come into effect in 2020, and be updated every five years starting from 2023. The agreement allows each country to set their own action plan, in the form of intended nationally determined contributions, to achieve voluntary targets on reducing their anthropogenic greenhouse gas (GHG) emissions. The climate pledges currently submitted by 158 nations, representing 94 % of global emissions, is estimated to result in about 2.7 °C of warming by 2100 [2]. This suggests that further reductions will be required to achieve the climate mitigation goals. The pathway to decarbonisation will include a mix of technologies, such as nuclear, carbon capture and storage, renewables, fuel switching and energy efficiency. These solutions need to be safe, proven and cost-effective to encourage widespread deployment.

1.2 Carbon Capture and Storage (CCS)

Between 1970 and 2010, about 78 % of the total GHG emission increase resulted from fossil fuel combustion and industrial processes [3]. Economic development continues to be dependent on fossil fuel and carbon-intensive industries, but both the energy intensity of gross domestic product (GDP) and the carbon intensity of primary energy have to be reduced by about 50 % by 2050 [4]. CCS is a proven technology that can provide a near-term option to simultaneously continue fossil fuel use and reduce GHG emissions. It complements the longer-term energy system transformation required for nuclear and renewables. It is predicted by the UN's Intergovernmental Panel on Climate Change (IPCC) that the cost of halting global warming would double if CCS was not implemented [1].

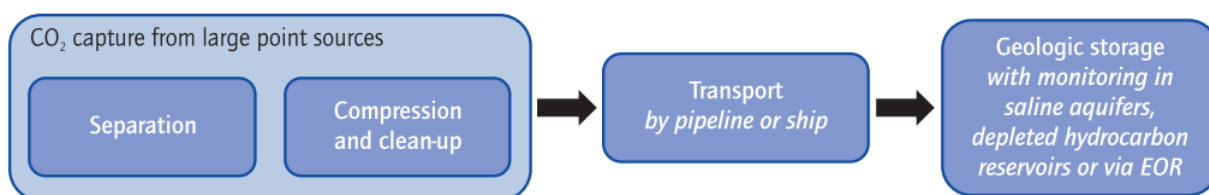


Figure 1.1 Components of the CCS chain: capture, transport, and storage; as reproduced from the IEA's 'Energy Technology Perspective 2012' [5].

Under the 2 °C Scenario, CCS is modelled to contribute a sixth of the emission reductions in 2050 [5], primarily from the power and industry sectors. Over 70 % of the CCS projects are projected to be in non-OECD countries. The IEA recommends that over 30 large-scale CCS projects should be in operation by 2020, to provide experience and demonstrate the possible cost reductions. There are currently 15 large-scale CCS projects in operation, with capture capacity of up to 28 million tonnes of CO₂ per year (Mtpa) [6], shown in Figure 1.2. Including projects in the early stages of planning, there

are 45 large-scale CCS projects, having a total capture capacity of 80 Mtpa. By 2050, over 3000 large-scale projects, with capture capacity of about 6000 Mtpa are required [5]. Therefore, CCS needs to be implemented at much faster rates globally.

Unlike other technologies, CCS itself does not offer commercial incentives. 'Sweet spots' where governmental policies and commercial interests coincide are required to overcome the capital cost barrier. Revenues from selling CO₂ for industrial use, hydrogen production, enhanced oil recovery (EOR) and CO₂ tax policies have been drivers that enabled some of the early CCS projects to be conducted. The Sleipner Project by Statoil was the world's first commercial CO₂ storage project, motivated by the Norwegian CO₂ tax [7]. CO₂ is captured from natural gas sweetening, and stored in the Utsira Formation, a deep saline sandstone reservoir. About 15.5 Mt of CO₂ have been injected since the start of the project in 1996 to June 2015, with no leakage detected using 3D seismic monitoring. In North America, CO₂ transport by pipeline is a mature technology, with over 6600 km of pipeline carrying CO₂ at flowrates of more than 60 Mtpa [8]. SaskPower's Boundary Dam Integrated Carbon Capture and Storage Project in Canada, was the world's first and largest commercial-scale CCS project to be installed in a coal-fired power plant, and started operation in 2014 [9]. Cost reductions of up to 30 % are estimated to be achievable on the next project. Through knowledge sharing, the findings of this project can benefit the wider industry across the world.

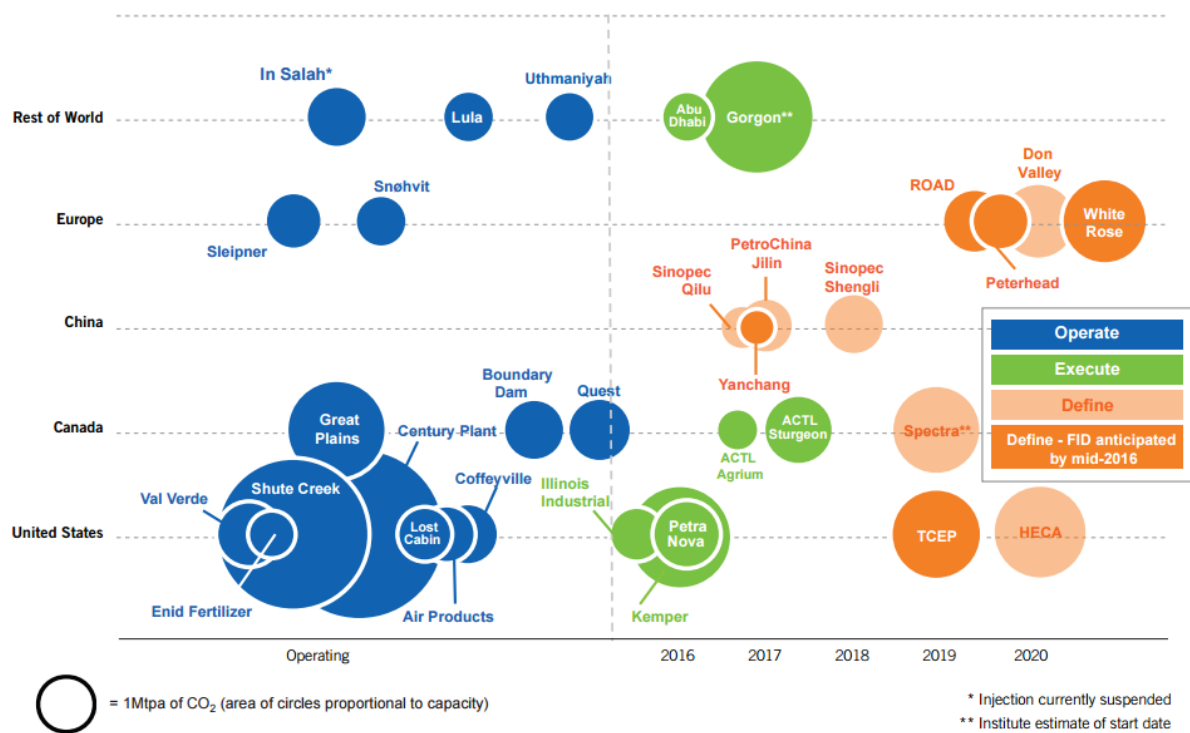


Figure 1.2 Operation dates and capacities of large-scale CCS projects in the Operate, Execute and Define stages across the world, as reproduced from the Global CCS Institute's 'Global Status CCS 2015' report [6]. The Peterhead and White Rose projects in the UK have been cancelled.

Amongst the successes, there are also projects that may never take off. For example, the UK government's recent decision to cancel a £1 billion CCS Competition, due to cuts in government spending, have resulted in the cancellation of the Peterhead and White Rose projects [10]. The UK government has instead chosen to invest in other low-carbon technologies with more public and private support, namely nuclear, renewable energy and smart grids. The high capital cost, lack of

public understanding and acceptance, safety concerns and intangible environmental benefits, have resulted in the short-sighted decision to overlook the potential of this crucial technology. From the outcomes of various CCS projects, it is clear that governmental commitment is vital to facilitate the deployment of CCS, at the pace that is required to meet the climate objectives.

The challenges ahead include commissioning demonstration projects that link the components of the CCS chain together, researching to lower cost, improve performance and safety of the technology, and devising suitable policies to create a market for CCS. The challenge that will be addressed in this research work is the storage component of the CCS chain.

1.3 Storage Sites and Conditions

The CO₂ captured from power stations and industry is compressed and transported by pipeline, and then injected into the underground storage site. Typical temperature and pressure conditions of the processes are listed in Table 1.1. Suitable storage locations include deep saline aquifers, with the greatest storage capacity, followed by depleted oil and gas reservoirs, and unmineable coal seams. Less information is available on the geological characteristics of deep saline aquifers as compared to depleted oil and gas fields. Geological uncertainties lead to significant risks in CO₂ storage, which can increase the long-term cost of the project [4].

Table 1.1 Estimated pressure and temperature conditions of the CCS chain [11].

CCS Component	p/MPa	T/K
Capture	0.05 to 8	298.15 to 1620.00
Transport	0.5 to 20	218.15 to 303.10
Storage	0.1 to 50	277.15 to 423.15

The CO₂ is injected to depths of greater than 800 m, in a supercritical state, with density greater than 300 kg·m⁻³ [12]. The CO₂ injection pressure needs to be higher than the surrounding reservoir fluid pressure [13]. In order of increasing time scales, the storage mechanisms include: structural trapping under an impermeable caprock, with the CO₂ buoyantly rising to the caprock, due to its lower density than the surrounding brine; capillary trapping, where CO₂ is immobilised in the pore space of the porous rock formation by brine; dissolution into the reservoir fluid to form a denser sinking fluid; and reaction to form carbonate minerals [14]. CO₂ storage projects focus on the structural and capillary trapping mechanisms, as they take effect in the first few hundreds of years [15]. The other two mechanisms, dissolution and mineral trapping, require much longer timescales to take effect, of thousands of years after injection.

1.4 Impurities in the CO₂ Stream

The CO₂ streams used for EOR tend to have purities of greater than 95 % [16], obtained from natural sources or from industry. The impact of higher levels of impurities on storage behaviour, arising from a wider spectrum of CO₂ sources with greater compositional variations, require further investigation. Along the different parts of the CCS chain, the composition of the CO₂ rich stream can fluctuate depending on the network of CO₂ sources, the capture technology used, the transport requirements of the pipeline, and any pre-treatment before storage. Potential impurities include N₂, Ar, H₂, O₂, H₂S, SO₂, NO_x, CO and CH₄ [11].

Table 1.2 Estimated concentrations of potential impurities in the captured CO₂ stream [11].

Component	Concentration/mol %	Component	Concentration/mol %
N ₂	0.02 to 10	SO ₂	< 0.0001 to 1.5
Ar	0.005 to 3.5	NO _x	0.0002 to 0.3
H ₂	0.06 to 4	CO	0.0001 to 0.2
O ₂	0.04 to 5	CH ₄	0.7 to 4
H ₂ S	0.01 to 1.5		

1.5 Design of CCS Processes

In order to design safe CCS processes, the fundamental science governing the behaviour of the chemical species present at the pressure and temperature conditions of interest, needs to be known. Thermodynamics and transport properties are the building blocks of the simulation models for CCS processes, as shown in Figure 1.3. As the process conditions cover a wide range of pressures, temperatures and complex multi-component fluid mixtures, it is not cost-effective to carry out experiments for every combination of parameters. Therefore, measuring the thermophysical data of relatively simpler binary to ternary component thermophysical data, for the pressure and temperature range, and using this to verify and improve predictive thermodynamic models is a way to simplify and tackle the problem. With the improved predictive thermodynamic models, multi-component data can then be used to test the model. The improved predictive thermodynamic models can be applied to enhance the process design, for safety and optimisation throughout the CCS chain.

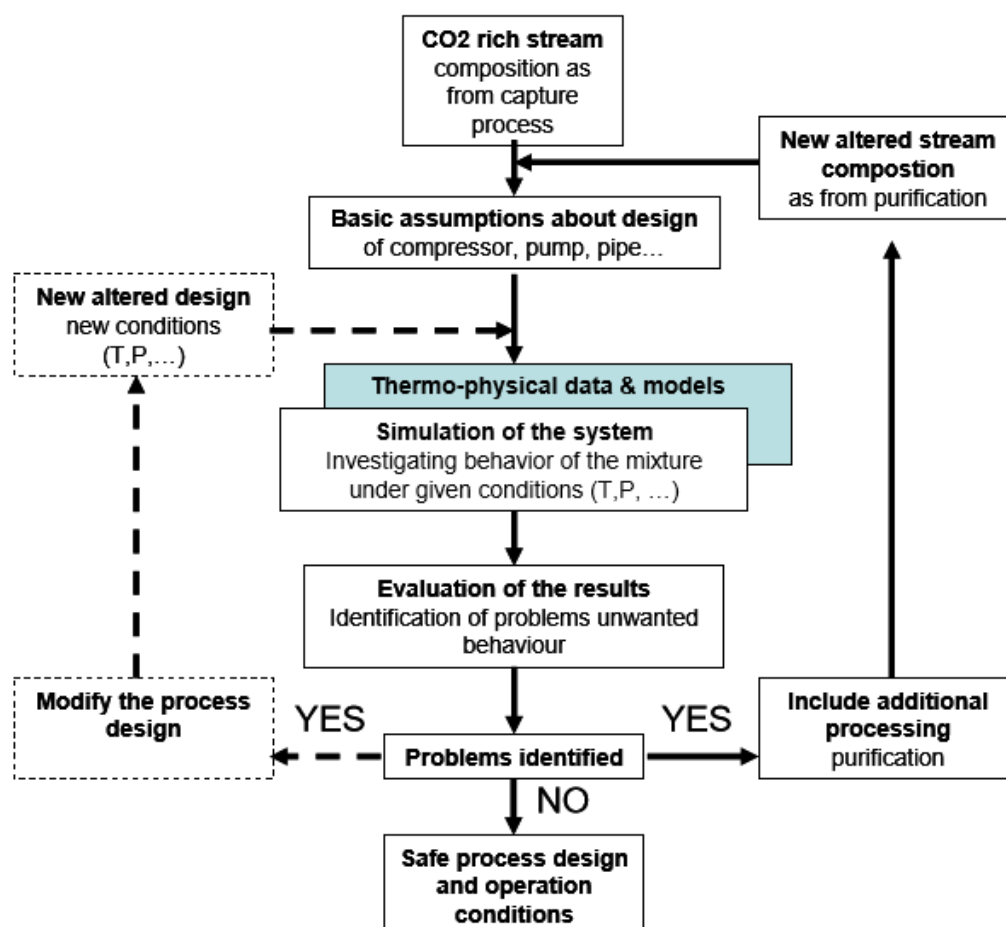


Figure 1.3 The CCS process design cycle and the importance of CO₂-mixture thermophysical properties, as reproduced from the review by Li *et al.*, 2011 [11].

1.6 Interfacial Properties

The ultimate storage capacity of a reservoir and seal system is determined from its structural, compositional, transport and hydrological characteristics. Reactive transport models and invasion percolation models are used to evaluate the long-term CO₂ storage performance at identified storage sites [6]. The transport properties of the reservoir and seals, primarily porosity and permeability, vary depending on the interaction between CO₂, impurities, reservoir fluids (oil and brine), injection make-up water, mineralogy, and fractures and matrices. These changes impact the long-term migration of CO₂. In carbonate reservoirs, fracture transport is expected to be of particular importance. In water-wet hydrocarbon reservoirs, the presence of an oil phase has less impact and is applicable in both CO₂-EOR and CO₂ storage. Invasion percolation models are dependent on threshold and capillary pressures, rather than permeability and viscosity of traditional Darcy flow simulations.

The capillary entry pressure can be estimated by [17]:

$$p_{c,e} = \frac{2\gamma \cos \theta}{r}, \quad (1.1)$$

where $p_{c,e}$ is the capillary entry pressure, γ is the gas-brine interfacial tension, r is the effective pore throat radius, g is gravitational acceleration, θ is the contact angle of the gas-brine-mineral surface. The capillary entry pressure is proportional to the interfacial tension, which can range from (20 to 70) mN·m⁻¹ under reservoir conditions; and the cosine of the contact angle, with limits of 1 to -1. The effective pore radius is in the order of 1 μm for reservoirs and 1 nm for caprock.

In the case of injection, the CO₂-rich stream needs to flow through the pores, so the CO₂ injection pressure is greater than the surrounding formation brine pressure. The amount of overpressure required is estimated from the capillary entry pressure, using the effective pore radius of the reservoir:

$$p_{\text{CO}_2} - p_{\text{brine}} > p_{c,e}, \quad (1.2)$$

This sets a lower limit for the injection pressure. For caprock and residual trapping, the effective pore radius is much smaller, and results in a higher capillary entry pressure. The amount of overpressure is:

$$p_{\text{CO}_2} - p_{\text{brine}} < p_{c,e}, \quad (1.3)$$

setting an upper limit for the injection pressure. If the injection pressure is above this limit the caprock can fail by hydraulic fracturing, or capillary failure, when CO₂ leaks through the caprock seal layer.

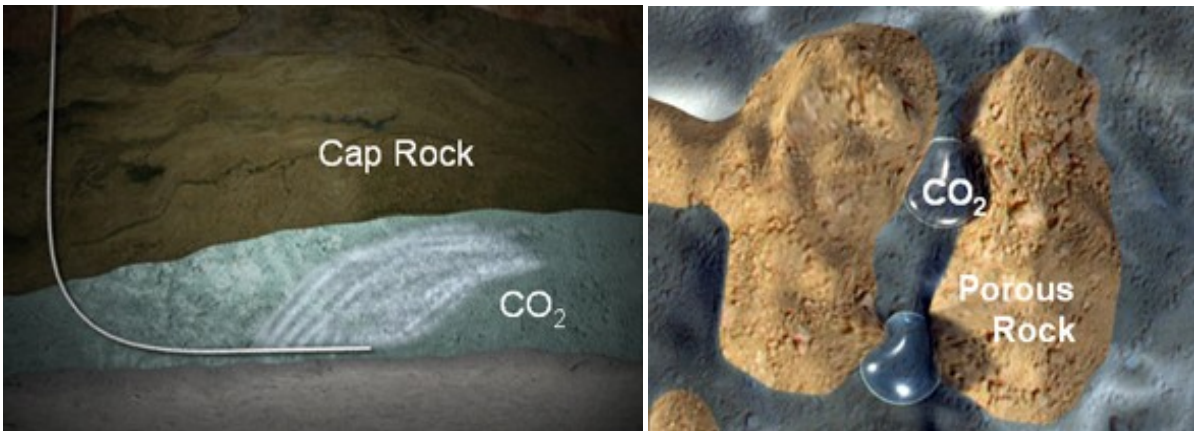


Figure 1.4 *Left.* CO₂ injection into a reservoir, sealed under an impermeable caprock [18]. *Right.* CO₂ capillary trapping by imbibing brine [19].

The contact angle is a measure of mineral wettability. Structural and capillary trapping are only effective if the rock formation is water-wet, when the cosine of the contact angle is non-negative. Drainage occurs when a non-wetting fluid displaces the wetting fluid, such as CO₂ gas injection into brine-filled reservoirs. Imbibition occurs when a wetting fluid displaces a non-wetting fluid, as when chase brine is injected after CO₂ injection. As CO₂ migrates through the formation, it is trapped in the pore space in immobilised non-wetting clusters, surrounded by the re-imbibing brine by snap-off and pore-body filling mechanisms [20]. The capillary trapping capacity depends on the maximum residual CO₂ saturation and the porosity of the formation, it is about 25 % of the pore space in sandstone [21].

This research work focuses on the interfacial tension and the contact angle variations of CO₂ streams with impurities at storage pressure and temperature conditions. The findings are used to advance understanding of these complex systems, improve thermodynamic modelling, and enhance the design of suitable CO₂ compositions for storage.

2 Theoretical Background

The theoretical basis for interfacial tensions and contact angles are introduced, along with derivations of important expressions, such as the Young-Laplace equation and Young's equation. The theories behind the various measurement methods are outlined. Automated measurement methods based on the underpinning Young-Laplace equation, are derived and documented. The selected pendant drop measurement method offers the greatest system flexibility and compatibility for this research at high pressures and temperatures. The theory behind modelling methods of interfacial tensions is introduced, with view of considering these various options when modelling the measured data.

2.1 Theory of Interfacial Forces

2.1.1 Interfacial Tension

An interface is the area separating two phases. For combinations of solid, liquid and gas, there can be solid-solid, solid-liquid, solid-gas and liquid-gas interfaces. For immiscible and partially-miscible fluids, fluid-fluid interfaces exist. However, as gases mix and do not phase separate, gas-gas interfaces do not exist. Interfaces have a particular thickness, over which the density changes from that of the bulk liquid to the bulk vapour, within a few molecules across the interface [22]. For salt solutions, the concentration of ions varies over a longer distance, and has a thicker interface characterised by the Debye length. The Debye length is a measure of how a charge carrier's electrostatic effect decays with distance, due to screening by other ions in solution. For a 0.1 M aqueous NaCl solution at 298 K, the Debye length is 0.96 nm [22]. Molecules simultaneously evaporate from the liquid phase and condense from the vapour phase. They also diffuse across the bulk phases.

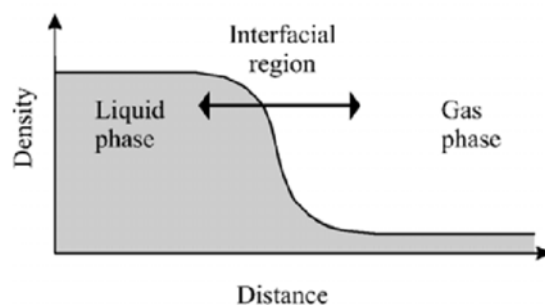


Figure 2.1 Variation of density across an interface with the coordinate normal to its surface [22].

Intermolecular attraction arises from van der Waals forces, and electrostatic forces in ionic and polar systems [23]. At the interfacial region, there is an imbalance of such forces, as the molecules are only partially surrounded by other molecules and the concentration is lower than in the bulk phase. This results in molecules in the interface having a higher potential energy than molecules in the bulk phase. Work needs to be done to bring a molecule from the bulk phase to the interface, to create new surface area. The surface tension is defined as the force per unit length that acts tangential to the surface everywhere on the perimeter, with units $\text{N}\cdot\text{m}^{-1}$. The excess free energy per unit area associated with a surface between two phases is called the surface energy, with units $\text{J}\cdot\text{m}^{-2}$. In the case of a liquid-fluid surface, the surface energy is numerically equivalent to the surface tension. The work done to increase the surface area corresponds to an increase in surface energy.

2.1.1.1 The Young-Laplace Equation

For a liquid surface to be curved there is a pressure difference across it; the pressure on one side must be larger than on the other side. For bubbles and drops, the pressure inside is higher than the pressure outside. The surface tension tends to minimise the surface area. For a free-floating liquid droplet, in the absence of gravity, a spherical shape will provide the least surface area for a given volume. For a drop hanging from a needle under gravity, the minimum free energy configuration is no longer spherical. There is a balance between minimising the surface energy and minimising the gravitational potential, causing the drop to become elongated. The Young-Laplace equation relates the pressure difference between two phases, Δp , and the curvature of the surface [24]:

$$\Delta p = \gamma \left(\frac{1}{R_1} + \frac{1}{R_2} \right), \quad (2.1)$$

where γ is the surface tension, R_1 and R_2 are the two principal radii of curvature. Δp is also known as the Laplace pressure.

Theoretically, if the shape of a liquid surface is known, the curvature and hence pressure difference can be determined. In the absence of external fields, the pressure is the same everywhere in the liquid, so Δp is constant, and the surface has the same curvature everywhere. Likewise, it is possible to calculate the equilibrium shape of a liquid surface, if the pressure difference, volume of the liquid and the contact line is known. In practice, the calculation of the shape of the liquid surface requires the solution of a second order partial differential equation, and is the basis of many optical interfacial tension measurement techniques.

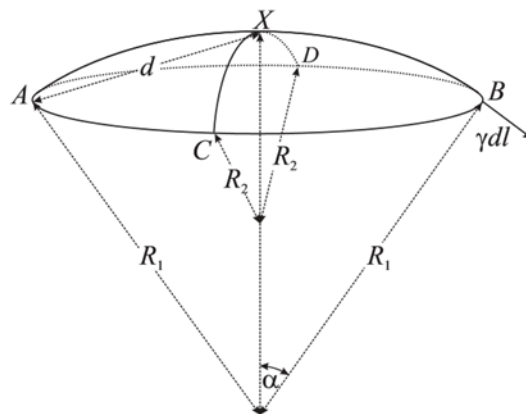


Figure 2.2 Coordinates and reference points used in the derivation of the Young-Laplace equation [22].

The Young-Laplace equation can be derived as follows (see Figure 2.2). An arbitrary point X is chosen from a small part of a liquid surface. A circle is drawn around point X , such that all points on the circle are the same distance d away from point X . On this circle, two arcs perpendicular to each other, AXB and CXD , are drawn. At B , consider a small segment on the circle with length dl . The surface tension pulls with a force γdl , and the vertical force on that segment is $\gamma dl \cdot \sin \alpha$. For small surface areas and a small α ,

$$\sin \alpha \approx \frac{d}{R_1}, \quad (2.2)$$

where R_1 is the radius of curvature along AXB .

The vertical force component at point B is

$$\gamma \cdot dl \cdot \frac{d}{R_1}. \quad (2.3)$$

The sum of the four vertical components at points A, B, C, and D is

$$\gamma \cdot dl \cdot \left(\frac{2d}{R_1} + \frac{2d}{R_2} \right) = \gamma \cdot dl \cdot 2d \cdot \left(\frac{1}{R_1} + \frac{1}{R_2} \right). \quad (2.4)$$

This equation is independent of the absolute orientation of AB and CD. Integrating over the borderline, with only 90 ° rotation of the four segments, results in the total vertical force caused by the surface tension:

$$\pi d^2 \cdot \gamma \cdot \left(\frac{1}{R_1} + \frac{1}{R_2} \right). \quad (2.5)$$

In equilibrium, this downward force is balanced by an upward force of the same magnitude, acting in the opposite direction. This upward force arises from an increase in pressure Δp on the concave side of $\pi d^2 \Delta p$. Equating these two forces gives the Young-Laplace equation [24]:

$$\Delta p \cdot \pi d^2 = \pi d^2 \cdot \gamma \cdot \left(\frac{1}{R_1} + \frac{1}{R_2} \right) \Rightarrow \Delta p = \gamma \left(\frac{1}{R_1} + \frac{1}{R_2} \right), \quad (2.6)$$

As point X was arbitrarily chosen, the Young-Laplace equation is valid everywhere on the liquid surface.

2.1.1.2 Thermodynamics of Interfaces

In the Gibbs convention, the two bulk phases α and β are considered to be separated by an infinitesimally-thin boundary layer, known as the Gibbs-dividing plane. Alternative models, such as the Guggenheim model [25, 26] takes the finite volume of the interfacial region into account.

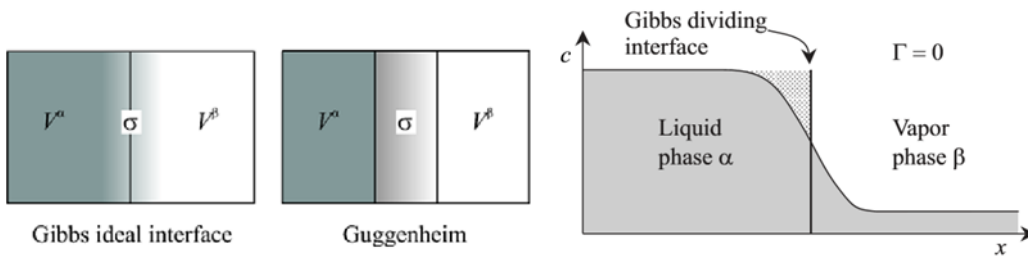


Figure 2.3 *Left.* Gibbs description of an ideal interface σ separating the two bulk phases α and β . *Centre.* Guggenheim description of an extended interface with a certain volume. *Right.* The position of the Gibbs-dividing plane based on the surface excess condition $\Gamma = 0$ [22].

The Gibbs model is more practical in most applications. The total volume of the system excludes the interface, as it is ideally thin i.e. $V^\sigma = 0$:

$$V = V^\alpha + V^\beta, \quad (2.7)$$

where V^α and V^β is the volume in the α and β bulk phases respectively.

The number of moles of the i^{th} species in the interface is given by

$$N_i^\sigma = N_i - c_i^\alpha V^\alpha - c_i^\beta V^\beta, \quad (2.8)$$

where N_i is the number of moles of the i^{th} species in the system, c_i^α and c_i^β are the concentrations of the i^{th} species in the α and β bulk phases respectively.

The enrichment or depletion of a species at the interface is defined by the interfacial excess, with units $\text{mol} \cdot \text{m}^{-2}$:

$$\Gamma_i = \frac{N_i^\sigma}{A_1}, \quad (2.9)$$

where A_1 is the interfacial area. The location of the ideal interface, the Gibbs-dividing plane, is positioned at where $\Gamma = 0$. For solutions, this surface excess condition is applied to the solvent.

At equilibrium, with constant volume, temperature, amount of material, the Helmholtz free energy, A , is minimal and the surface tension can be defined as:

$$\left. \frac{\partial A}{\partial A_1} \right|_{T, V, V^\beta, N_i} \equiv \gamma. \quad (2.10)$$

The surface area A_1 and V^β are related, if the volume changes, in general the surface area also changes. By a law of differential geometry, in general

$$\frac{\partial V}{\partial A_1} = \left(\frac{1}{R_1} + \frac{1}{R_2} \right)^{-1}. \quad (2.11)$$

In equilibrium, $dA/dA_1 = 0$,

$$\frac{dA}{dA_1} = \frac{\partial A}{\partial A_1} + \frac{\partial A}{\partial V^\beta} \cdot \frac{\partial V^\beta}{\partial A_1} = \gamma - (p^\beta - p^\alpha) \cdot \frac{\partial V^\beta}{\partial A_1} = 0. \quad (2.12)$$

By substituting eq. 2.11, defining $\Delta p = p^\beta - p^\alpha$, and rearranging eq. 2.12, we again arrive at the Young-Laplace equation (eq. 2.1).

The surface tension can also be defined as the increase in Gibbs free energy per increase in surface area at constant temperature, pressure and amount of material:

$$\left. \frac{\partial G}{\partial A_1} \right|_{T, p, N_i} \equiv \gamma. \quad (2.13)$$

From the Gibbs adsorption isotherm, it can be shown [22] that the amount of solute adsorbed at the interface, the interfacial excess of the solute, is related to the surface tension by:

$$\Gamma = -\frac{a}{RT} \cdot \left. \frac{\partial \gamma}{\partial a} \right|_T. \quad (2.14)$$

When a solute is enriched at the interface, the surface tension decreases with the addition of the solute. When a solute avoids the interface, the surface tension increases upon addition of the substance. The

surface excess is an experimentally measurable quantity, determined by measuring the surface tension variation with bulk concentration.

2.1.2 Contact Angle

The contact angle is an angle that is formed between a solid-gas, solid-liquid and liquid-gas interface, measured through the liquid, as shown in Figure 2.4. The region where solid, liquid, and gas coincide is the three-phase contact line, or wetting line. Each interface has a characteristic surface free energy per unit area. The contact angle achieves a value that minimises the free energy of the system and depends only on the material properties of the system.

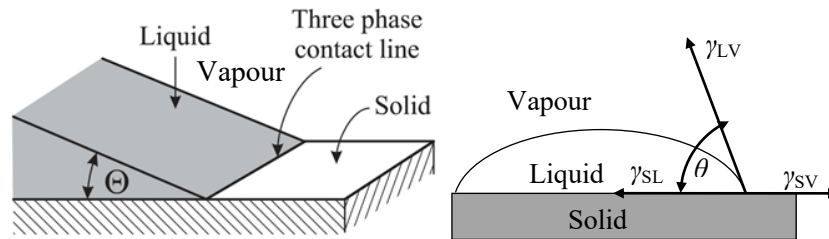


Figure 2.4 A sessile drop on a planar solid surface, showing the contact angle θ : (left) magnified view of the rim of the drop and the three-phase contact line [22]; (right) profile of the sessile drop and the associated interfacial tensions of the system.

2.1.2.1 Young's Equation

Young's equation [24] is a static equilibrium force balance of a drop on a homogenous, smooth and rigid ideal surface:

$$\gamma_{SV} = \gamma_{SL} + \gamma_{LV} \cdot \cos \theta_Y \quad (2.15)$$

where γ_{SV} , γ_{SL} , and γ_{LV} represent the solid-vapour, solid-liquid, and liquid-vapour interfacial tensions, respectively; and θ_Y is the Young's contact angle.

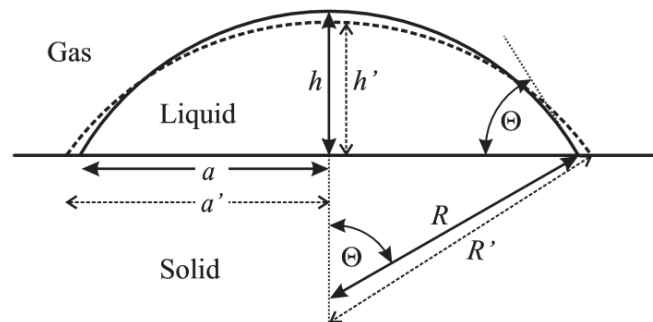


Figure 2.5 Circular liquid drop on a planar solid surface [22].

Young's equation can be derived for a circular drop on a planar solid surface, by considering the change in Gibbs free energy dG as the drop spreads an infinitesimal amount (see Figure 2.5). While spreading, the contact zone radius increases from a to a' , with radius of $a + da$. By assuming that the volume remains constant, the height decreases from h to h' , with height of $h + dh$. For a negative change in Gibbs free energy, the spreading process will occur spontaneously. Conversely, if the change in Gibbs free energy is positive, the drop will contract. The energetically most favourable situation is when $dG = 0$, in equilibrium.

Simplifying the proof, the drop is assumed to be sufficiently large so that the Laplace pressure does not lead to a significant change in Gibbs free energy, and also small enough for hydrostatic gravity effects to be negligible. The change in area due to drop spreading is $dA_{SL} = 2\pi a \cdot da$, and the resulting change in surface energy is $(\gamma_{SL} - \gamma_{SV})dA_{SL}$. The surface area of the liquid-gas interface also changes, based on the geometry of a spherical cap:

$$A_{LV} = \pi(a^2 + h^2). \quad (2.16)$$

A small change in the contact radius a , results in a change in liquid surface area by:

$$dA_{LV} = \frac{\partial A_{LV}}{\partial a} da + \frac{\partial A_{LV}}{\partial h} dh = 2\pi a \cdot da + 2\pi h \cdot dh. \quad (2.17)$$

The variables a and h are constrained by the constant volume condition. The volume of a spherical cap is:

$$V = \frac{\pi}{6}(3a^2h + h^3). \quad (2.18)$$

A small change in volume is expressed as:

$$dV = \frac{\partial V}{\partial a} da + \frac{\partial V}{\partial h} dh = \pi ah \cdot da + \frac{\pi}{2}(a^2 + h^2) \cdot dh. \quad (2.19)$$

As the volume is assumed to be constant, $dV = 0$. Using Pythagoras' law,

$$R^2 = a^2 + (R - h)^2 \Rightarrow a^2 = 2Rh - h^2. \quad (2.20)$$

Eq. 2.19 simplifies to:

$$\frac{dh}{da} = -\frac{2ah}{a^2 + h^2} = -\frac{a}{R}. \quad (2.21)$$

Substituting into eq. 2.18, with $\cos \theta = \frac{R-h}{R} = 1 - \frac{h}{R}$,

$$dA_{LV} = 2\pi a \cdot da - 2\pi h \frac{a}{R} \cdot da = 2\pi a \cdot \left(1 - \frac{h}{R}\right) da = 2\pi a \cdot \cos \theta \cdot da. \quad (2.22)$$

The total change in Gibbs free energy is:

$$dG = (\gamma_{SL} - \gamma_{SV})dA_{SL} + \gamma_{LV} \cdot dA_{LV} = 2\pi a(\gamma_{SL} - \gamma_{SV})da + 2\pi a\gamma_{LV} \cdot \cos \theta \cdot da. \quad (2.23)$$

In equilibrium, $dG/dA = 0$, simplifying to Young's equation in eq. (2.15).

2.1.2.2 Wettability

A fluid wets the surface better when a contact angle smaller than 90° is formed. When $\theta = 0^\circ$, the fluid is perfectly wetting, and the drop spreads to form a film on the surface [27]. The wettability of a surface can be classified by the spreading coefficient, S :

$$S \equiv \gamma_{SV} - (\gamma_{SL} + \gamma_{LV}). \quad (2.24)$$

The spreading coefficient is a measure of how strongly a liquid can spread on a surface. It represents the difference in free energy between a solid in contact with the vapour and a solid in contact with the liquid [28]. For spreading systems, $S > 0$; and for partially wetting systems, $S < 0$, and a finite contact angle is formed.

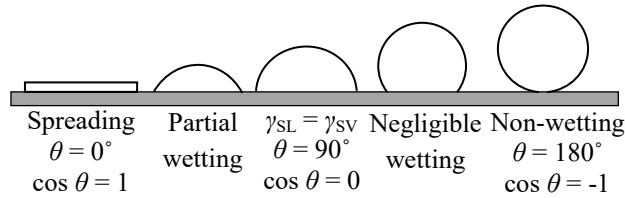


Figure 2.6 Classification of wetting behaviour.

2.1.2.3 Contact Angle Hysteresis

There are many meta-stable states of a fluid on a real solid, which means that the observed contact angle usually differs from the Young's contact angle [29]. The drop profile can change with time if the drop spreads, or if the liquid is soluble in either the vapour or solid. Wetting of a real surface is a dynamic process, and cannot be measured by a single static parameter. Instead, wetting is characterised by an approaching maximum contact angle, the advancing contact angle. The approaching minimum contact angle, receding contact angle, is a measure of adhesion. The difference between the two is the contact angle hysteresis [30], a measure of the difference in liquid-surface interfacial tension during advancing and receding. The contact angle hysteresis depends on the fluid states, adsorption, contamination, surface chemical and geometrical heterogeneities. Static contact angle measurements may yield any value between the advancing and receding contact angles.

The dynamic wetting of a fluid to displace another fluid can be classified into spontaneous and forced wetting. For spontaneous wetting, fluid spreading is thermodynamically favourable. In forced wetting, an external hydrodynamic or mechanical force encourages the solid-fluid interfacial area to increase beyond static equilibrium. Forced wetting is important in enhanced oil recovery, and the drainage and imbibition processes of CO_2 injection.

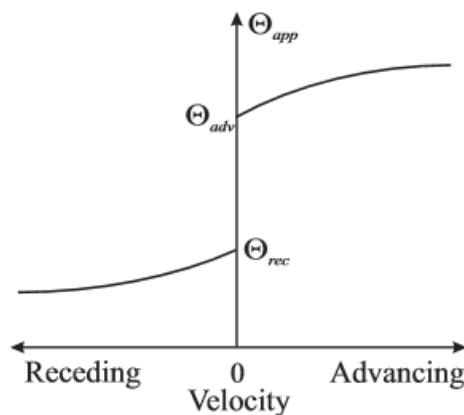


Figure 2.7 Dependence of the experimentally measured apparent contact angle on velocity of forced wetting [30].

When the three-phase contact line is forced to advance with a certain speed, the apparent contact angle becomes higher than the advancing contact angle, just before the wetting line advances.

Likewise, the apparent contact angle can become less than the receding contact angle when the wetting line is made to recede. The apparent contact angle depends on the speed v , viscosity η and surface tension of the liquid γ_{LV} . The contact angle dependence on these factors are correlated by the ratio of viscous to interfacial force, via the capillary number [30]:

$$C_a \equiv \frac{v\eta}{\gamma_{LV}}. \quad (2.25)$$

2.2 Measurement Techniques

2.2.1 Interfacial Tension

Surface tension can be measured by several techniques. The oldest approach is the capillary rise method, but the most common techniques are optical measurements of a sessile or pendant drop or bubble contour, which are then fitted with contours calculated using the Young-Laplace equation. The maximum bubble pressure method (MBPM), stalagmometric (drop weight) method, Wilhelmy plate method, du Noüy ring method, and spinning drop method are also used. The choice of method depends on the system to be measured, the accuracy needed, and if automation is required. Commercially available instruments of these measurement techniques are available for manual and automatic operation, manufactured by Fisher, CSC, Kahl, KSV, Lauda, NIMA, Cahn, Krüss, Sensa Dyne, ADSA, AST, FTA, Ramé-Hart, Temco, Kibron, and Kyowa [31]. At high pressures and temperatures, the modified MBPM and the pendant or sessile drop method have been used to measure the interfacial tensions of molten metal, alloys, and semiconductors [32]. For enhanced oil recovery, the pendant drop [33] and capillary wave [34] methods have been applied to measure the interfacial tensions between oil and another immiscible phase at reservoir conditions. Comparing the methods, the pendant drop method offers greatest system flexibility.

For dilute solutions, automated versions of the static methods such as the Wilhelmy plate or the pendant drop methods can be used to measure the relatively slow surface tension changes. For concentrated solutions with large changes in surface tension within a fraction of a second, dynamic methods based on capillary waves must be used. Thermal fluctuations lead to very low amplitude waves, with a broad range of frequencies, always being present on liquid surfaces. Purposely perturbing the liquid surface can create larger amplitude capillary waves. The frequency of the capillary wave surface oscillation is dependent on the surface tension and the wavelength [31].

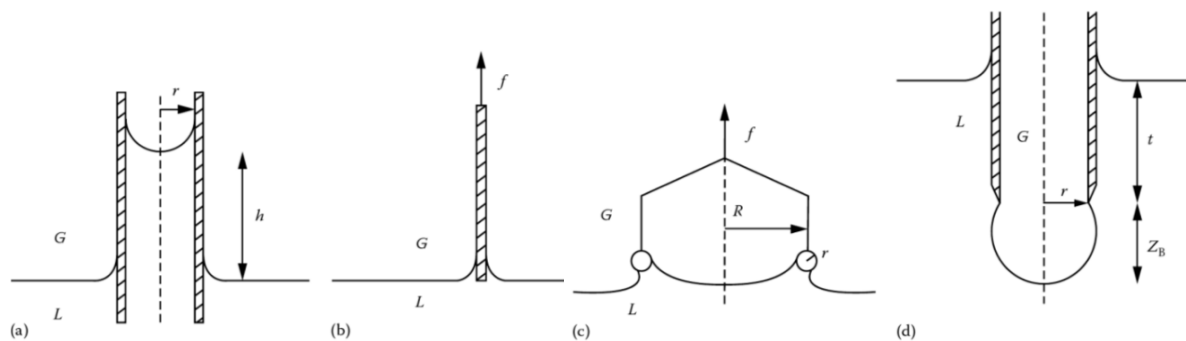


Figure 2.8 Schematic of the (a) capillary rise method, (b) Wilhelmy plate method, (c) du Noüy ring method, and (d) maximum bubble pressure method (MBPM) [31].

2.2.1.1 Axisymmetric Drop Shape Analysis

There are several optical methods based on the measurement of a drop or bubble contour to determine the surface or interfacial tension. As mentioned previously, a drop hanging from a needle under gravity assumes an elongated profile. Bashforth and Adams [35] were the earliest to use the Laplace equation in analysing sessile drop profile shapes, in 1883. They produced tables of sessile drop profiles for different surface tension and radius of curvature values. Fordham [36] and Mills [37] produced equivalent tables for pendant drop profiles. Rotenberg et al. [38] created the first generation of Axisymmetric Drop Shape Analysis (ADSA) algorithm, and the technique has been subsequently refined into the ADSA-P (profile) [39], ADSA-D (diameter) [40, 41], ADSA-HD (height and diameter) [42] methods. The ADSA-P method is the most frequently used algorithm.

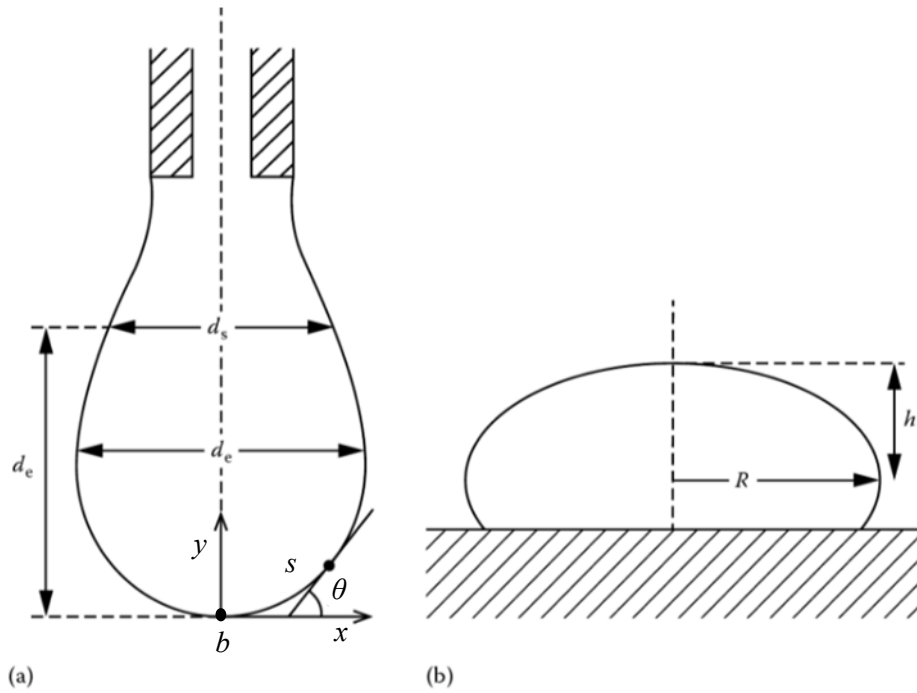


Figure 2.9 Schematic of (a) a pendant drop with characteristic dimensions, d_e and d_s , and the coordinates used in the Young-Laplace equation, (b) a sessile drop with characteristic dimensions, R and h [31].

The working equations for methods based on the formation and shape monitoring of axisymmetric drops can be established as follows. The Young-Laplace equation can be formulated as dimensionless first-order differential equations for an axisymmetric interface under gravity (see Figure 2.9):

$$\frac{dX}{dS} = \cos \theta, \quad (2.26)$$

$$\frac{dY}{dS} = \sin \theta, \quad (2.27)$$

$$\frac{d\theta}{dS} = 2 - \beta Y - \frac{\sin \theta}{X}, \quad (2.28)$$

$$X(0) = Y(0) = \theta(0) = 0, \quad (2.29)$$

where X , Y , and S are dimensionless parameters of the co-ordinates x , y , and s , respectively, through dividing by the radius of curvature at the drop apex, b . The parameter s is the arc length along the

drop surface measured from the drop apex, θ is the angle between the interface tangent and the horizontal, and β is a dimensionless shape parameter called the Bond number.

The shape of an axisymmetric drop, bubble or meniscus only depends on the Bond number, which is a measure of the ratio of the gravitational force/energy to the interfacial force/energy:

$$\beta = \Delta\rho g b^2 / \gamma = 2b^2 / a^2, \quad (2.30)$$

where $\Delta\rho$ is the density difference between the two fluid phases, g is the gravitational acceleration, γ is the interfacial tension, and a is the capillary constant with units of length:

$$a = \sqrt{2\gamma / \Delta\rho g}. \quad (2.31)$$

The shape of an axisymmetric surface can be calculated by solving the set of eq. 2.26 to 2.29, by numerical integration for both pendant and sessile drops.

2.2.1.2 Capillary Rise Method

The capillary rise method is the oldest method used to measure surface tension. A thin circular glass tube, the capillary, is used to observe the upward movement of a liquid due to surface tension. The thoroughly cleaned capillary is dipped into the test liquid, and if the adhesion forces are stronger than the cohesion forces between the liquid molecules, the liquid wets the walls and rises to a certain level, with a hemi-spherically concave meniscus. On the contrary, if the cohesion forces are stronger than the adhesion forces, the liquid level will decrease in the capillary and form a hemi-spherically convex meniscus. The surface tension is directly proportional to the change in height of the liquid, h .

By applying the Young-Laplace equation and equating to the hydrostatic pressure,

$$\Delta p = \frac{2\gamma}{r} = \Delta\rho g h, \quad (2.32)$$

where Δp is the pressure difference across the curved surface i.e. capillary pressure, r is the radius of curvature at the centre of the meniscus, $\Delta\rho$ is the density difference between the liquid and gas phase, g is the gravitational acceleration, and h is the change in height.

The surface tension can be calculated by rearranging eq. 2.32,

$$\gamma = \frac{r\Delta\rho g h}{2}. \quad (2.33)$$

For small capillary tubes with a very uniform diameter of less than 1 mm, r can be approximated by the capillary tube radius, assuming that the liquid completely wets the capillary wall. For larger tubes or increased accuracy, the value of r needs to be corrected for gravitational effects on the meniscus [43]. This method is mainly used for pure liquids and can produce high accuracy at relatively low cost, provided that the liquid wets the capillary wall with a contact angle of 0° .

2.2.1.3 Wilhelmy Plate Method

In the Wilhelmy plate method [44], a thin thoroughly cleaned plate of platinum or glass is used to measure the equilibrium surface or interfacial tension. The plate is suspended perpendicular to the interface and is attached to a scale or balance by a thin metal wire. The plate is pulled down by the wetting liquid, as the bottom of the plate comes into contact with the liquid meniscus. The force to maintain the plate edge at the same level with the flat liquid surface is measured with a tensiometer or microbalance. The Wilhelmy equation is applied to calculate the surface tension. This method can achieve 0.1 % accuracy for a completely wetting liquid, with zero contact angles.

The surface tension can be calculated by [44]:

$$\gamma = \frac{f}{2(l+t)\cos\theta}. \quad (2.34)$$

where l is the plate width, t is the plate thickness, θ is the contact angle and f is the force needed to detach the two plate surfaces from the liquid.

2.2.1.4 du Noüy Ring Method

In the du Noüy ring method [45], a very clean platinum ring is placed in contact with the liquid surface, and the surface is lowered until a maximum force on the ring is recorded. The maximum force is usually measured just prior to the raising the ring from the surface. This method requires knowledge of the liquid density, complete wetting of the ring by the liquid i.e. zero contact angle, and is not suitable for solutions that are slow in achieving surface equilibrium.

The surface tension is evaluated from:

$$\gamma = \left(\frac{f_{\max}}{4\pi R} \right) \left[F \left(\frac{R^3}{V}, \frac{R}{r} \right) \right], \quad (2.35)$$

where f_{\max} is the maximum force, R and r are the radii of the ring and wire, respectively, V is the liquid volume raised by the ring, and F is a tabulated correction factor [46].

2.2.1.5 Maximum Bubble Pressure Method

The maximum bubble pressure method measures surface tension by determining the pressure required to push a bubble out of a capillary tube, against the Laplace pressure [31]. A capillary tube is immersed in the liquid to a depth t , and gas is injected to a bubble of height Z_B at the tip of the tube. The increase in bubble pressure p_b , from ambient p_a , due to the interface is given by the sum of hydrostatic pressure and Laplace pressure [31]:

$$\delta p = p_b - p_a - \Delta\rho g t = \Delta\rho Z_B + \frac{2\gamma}{b}, \quad (2.36)$$

where b is the radius of curvature at the bubble apex, $\Delta\rho$ is the density difference between the liquid and gas phase, and g is the gravitational acceleration.

As the bubble pressure is increased, the bubble protrudes more out of the capillary, and the curvature increases according to the Young-Laplace equation. The maximum pressure is reached when the bubble forms a hemisphere, with the bubble radius coinciding with the wetted capillary radius. Further increases in volume will cause the bubble to become larger, thereby decreasing the pressure, and becoming unstable. The bubble will then detach from the capillary tube.

The maximum bubble overpressure is reached when $\delta p = \delta p_{\max}$, and rewriting eq. 2.30 in dimensionless form:

$$\frac{r}{\chi} = \frac{r}{b} + \frac{r}{a} \frac{Z_B}{b} \left(\frac{\beta}{2} \right)^{1/2}, \quad (2.37)$$

where r is the capillary tube radius, a is the capillary constant, β is the Bond number, and χ is a length defined by:

$$\chi = \frac{2\gamma}{\delta p_{\max}}. \quad (2.38)$$

The dimensionless quantity r/χ only depends on r/a , resolved by eq. 2.37 and numerical solutions to eq. 2.26 to 2.29 in the axisymmetric drop shape analysis. Tables of the standard solutions are used to evaluate the surface tension, via iterations [43]. The fluid densities, wetted capillary tube radius, and immersion depth of the tube are variables that need to be known for this method.

2.2.1.6 Pendant or Sessile Drop Method

In the pendant drop method, a drop of the fluid is formed, and hangs at the tip of the capillary tube, whilst surrounded by the second fluid. In the sessile drop method, the fluid rests on a flat surface, enclosed by the second fluid. These are optical methods based on analysis of the interface contour, using the axisymmetric drop shape analysis described in section 2.2.1.1. The imaged drop profile is compared to the shape and size of theoretical profiles obtained by numerical integration of eq. 2.26 to 2.29, for different values of β and b . After determining β and b , the interfacial tension can be calculated by (see 2.2.1.1):

$$\gamma = \Delta \rho g b^2 / \beta. \quad (2.39)$$

The shape of the drop only depends on the Bond number. For Bond numbers near zero, the interfacial tension effect is stronger than gravitational effects, and the drop assumes a nearly spherical shape. The drop is more deformed by gravity at larger Bond numbers.

Traditionally, drop shape analysis has been performed by photographing a drop, and then measuring the characteristic sizes of the drop from the photographic prints, which is time consuming. For pendant drops, characteristic sizes used to evaluate the size and shape parameters [47, 48] are the maximum diameter of the drop d_e and a ratio σ , given by:

$$\sigma = d_s / d_e, \quad (2.40)$$

where d_s is the diameter of the drop at a distance of d_e from the drop apex. In the case of sessile drops, a complete profile matching is often required.

This process is now automated with digital imaging and analysis [38, 39]. Several hundred coordinates on the edge of the drop are located with sub-pixel resolution. The size, shape, horizontal and vertical offsets of the theoretical profile depends on four parameters: β , b , and the pixel coordinates of the drop apex, x_0 and y_0 . The best fit of the theoretical profile to the measured edge coordinates is obtained by minimising an objective function. The height, width, surface area and volume of the drop or bubble can be calculated in an instant [49]. The accuracy and simplicity of the method makes it suitable for measurements involving high pressures and temperatures.

2.2.1.7 *Stalagmometric (Drop Weight) Method*

When a pendant drop grows too large and the gravitational force becomes greater than the surface tension, it becomes unstable and will detach from the capillary. In the drop weight method [31], the weight of a detached drop is measured. For a precise measure, several drops are weighed and averaged over the number of drops. The drops have to be formed slowly. The weight of the detached drop is related to the surface tension by:

$$\gamma = \left(\frac{mg}{r} \right) \left[F \left(\frac{r}{V^{1/3}} \right) \right], \quad (2.41)$$

where mg is the weight of the detached drop, r is the wetted radius of the capillary from which the drop hangs, V is the volume of the detached drop, F is an empirical correlation tabulated [47] as a function of $r/V^{1/3}$. The fluid density must be known to determine V and F .

2.2.1.8 *Spinning Drop Method*

The spinning drop method is similar to the pendant and sessile drop methods, where the shape is measured. However, the major perturbing force in this case is not gravity but a centrifugal force arising from rapid rotation. It is commonly used for interfacial tension measurements of immiscible liquids and is particularly useful for measuring very low values of interfacial tension, typically below $10^{-2} \text{ mN}\cdot\text{m}^{-1}$, for which the more traditional methods have low accuracy [31]. The deformation of the drop is brought about by radial pressure gradients in a rapidly spinning tube. A horizontal glass tube sealed at both ends is filled with the more dense liquid. The tube is spun about its axis, and a drop of the less dense liquid is injected into the tube. The drop moves to the centre of the tube and elongates due to the pressure difference. Surface tension acts against the elongation. The surface tension is related by [31]:

$$\gamma = \frac{1}{2} \left(\frac{r_{\max}}{r_{\max}^*} \right)^3 \Delta\rho \Omega^2, \quad (2.42)$$

where r_{\max} is the maximum drop radius, Ω is the angular velocity of rotation, r_{\max}^* is correlated to the aspect ratio r_{\max}/h_{\max} , and $2h_{\max}$ is the drop length.

2.2.2 Contact Angle

The study of static or dynamic contact angles of liquids on solids allow us to characterise the macroscopic chemical or physical properties of the solid-liquid interface. The interpretation of contact angle results is subject to constant debate in the literature [50]. The areas of concern include the method and conditions required to obtain consistent and reliable data, and the comprehension of basic wetting concepts. A key criterion for accurate contact angle determination requires that the liquid and solid surface to be nonreactive physically and chemically. The solid needs to be cleaned appropriately, and the liquid purified and free of surface contaminants. Measurements should not be carried out if distortion of the surface dimension, liquid adsorption, or dissolution of the surface material occurs. Surface characterisation techniques such as atomic force microscopy (AFM) or scanning electron microscopy (SEM), could be used to identify microscopic heterogeneities. The static contact angle methods involve measurement of a sessile drop or captive bubble. The dynamic methods for advancing or receding angles, and contact angle hysteresis, include the expansion and contraction method, tilting base method and Wilhelmy plate method.

2.2.2.1 Sessile Drop or Captive Bubble Method

Contact angles are commonly measured by optically imaging a sessile drop [50]. A goniometer [27] is comprised of a horizontal stage with a solid sample mount, positioned between a light source and a microscope or CCD camera. The solid surface has to be flat optically. A sessile drop is formed from a motorised liquid dispensing system. The liquid drop is suspended at the tip of the needle and either dropped onto the solid surface by gravity, or by moving the solid surface up slowly to catch the drop. The drop should be allowed to stabilise before taking a measurement, the time taken for water drops is about a second, and minutes to hours for more viscous fluids. The static state is achieved when all of the drop's kinetic energy has been dissipated. The contact angle can be determined with a protractor, or by analysing the imaged drop shape, in a similar way to surface tension measurements. The lens and CCD camera should be tilted 1° to 3° downwards to prevent blocking of the sessile drop contact line [51]. This also improves the identification of the baseline. The apparatus can be customised for high temperature and pressure measurements, with additional components such as an automated dispensing system, tilting base, and vibration-free table.

Surface heterogeneity should be small, less than the order of 100-200 μm , and cause no distortion on the sessile drop profile [50]. Liquid drop diameters used are usually in the millimetre range, around 1 to 5 mm. For measurement on rough or textured surfaces with large contact angles, the drop size is recommended to be at least 2 to 3 orders of magnitude larger than the roughness length scale to avoid considerable contact line distortion. The drops should also be small enough for negligible gravity effects. The caution for small drops include sensitivity to optical errors due to light scattering, diffraction, evaporation and uncertainty in locating the surface baseline as well as digitising the image for drop profile analysis. A high-quality clear image of the liquid-solid interface boundary will reduce errors in baseline identification and fitting of the drop profile.

The captive bubble method involves measuring the contact angle at the edge of a bubble (see Figure 2.10). The bubble is usually positioned at the top of a view cell which is filled with liquid. The optical measurement technique is similar to the sessile drop method. This method has the advantage of being unaffected by the needle and drop weight. The vapour phase is automatically saturated and less sensitive to contamination. Whether drops or bubbles are measured depends on the comparative density of the fluids, and the surface and capillary positions.



Figure 2.10 *Left.* Image of a sessile drop for contact angle measurement [52]. *Right.* Image of a captive bubble for contact angle measurement [53].

2.2.2.1.1 Profile Fitting Methods

In automated optical contact angle measurements, the drop or bubble profile is analysed by a numerical routine. The solid surface is aligned to a horizontal baseline, and the filter routine identifies the properly aligned profile. Numerical extrapolation of the profile at the contact point allows the contact angle to be calculated. Different numerical fits will produce different extrapolation results. Fitting methods include the tangential method, $\theta/2$ method, circle method [54-56], ellipse method [57, 58], Young-Laplace method [38, 40-42, 59], polynomial method [60, 61], and B-spline (basis spline) snakes method [62].

The tangent method takes the tangent at the pixel coordinates of the contact point. The curve-fitting nature of the method is prone to large errors due to disturbance in the drop shape by contaminants.

Extremely small drops, with negligible hydrostatic effects, are predicted by the Laplace equation to have a circular cross-section. In this special case, the contact angle can be calculated by the $\theta/2$ method [50]:

$$\tan\left(\frac{\theta}{2}\right) = \frac{H}{r}, \quad (2.43)$$

where θ is the contact angle, H is the height of the drop, and r is the contact radius of the drop.

The circle method fits the drop profile to a circle. The contact angle is calculated between the baseline and the tangent of the fitted circle at the contact point. This method is suitable for small drops or surfaces with small contact angles, as gravity effects are neglected here. In general, the circle fitting method will provide minimal fitting error for contact angles smaller than 20 °.

The ellipse method fits the drop profile to an elliptical shape, and calculates the contact angle at the contact point. The ellipse fitting method has no physical derivation basis and may lead to large deviation between the fitted curve and captured profile, especially for larger drops with larger contact angles.

The Young-Laplace or ADSA method [38], described in section 2.2.1.1, is suitable for drops with a high degree of symmetry. Gravity is assumed to be the only external force and the drop shape is axisymmetric under surface tension. ADSA-P is most commonly used in commercial software [42]. The Laplace equation is iteratively fitted to the drop shape, until fitting error is minimised. Out of the circle, ellipse, and ADSA-P method, the ADSA-P method provides the lowest fitting error as the drop volume and contact angle increases [50]. However, this fitting error is sensitive to drop profile noise levels and non-axisymmetric shapes.

Polynomial [60, 61] and B-spline fitting [62] is used for non-axisymmetric drops. The drop profile points near the local contact point, above the baseline, are fitted without any assumptions on the drop shape. The order of the polynomial and number of pixels in the curve-fitting procedure are the two primary parameters that can be optimised for different applications. Higher order polynomials are more affected by experimental noise. In B-spline fitting, a spline function is a piecewise polynomial function, and the places where the pieces meet are denoted as knots. The global fitting of the drop shape is also performed. The inter-knot distance is the main variable, establishing how many knots are required to properly map the drop profile. The accuracy of these two methods are sensitive to dust particles, contaminants, or surface irregularities.

2.2.2.2 Expansion and Contraction Method

In the expansion and contraction method, a capillary tube with diameter much smaller than the drop diameter is used to hold a drop or bubble in place on a surface (see Figure 2.11). The dynamic advancing and receding angles can be measured as the drop volume is increased slowly, at a rate of less than $0.2 \mu\text{L}\cdot\text{s}^{-1}$, to about $20 \mu\text{L}$, allowed to stabilise, and then withdraw liquid at the same rate, whilst keeping the position of the three-phase contact line constant [63].

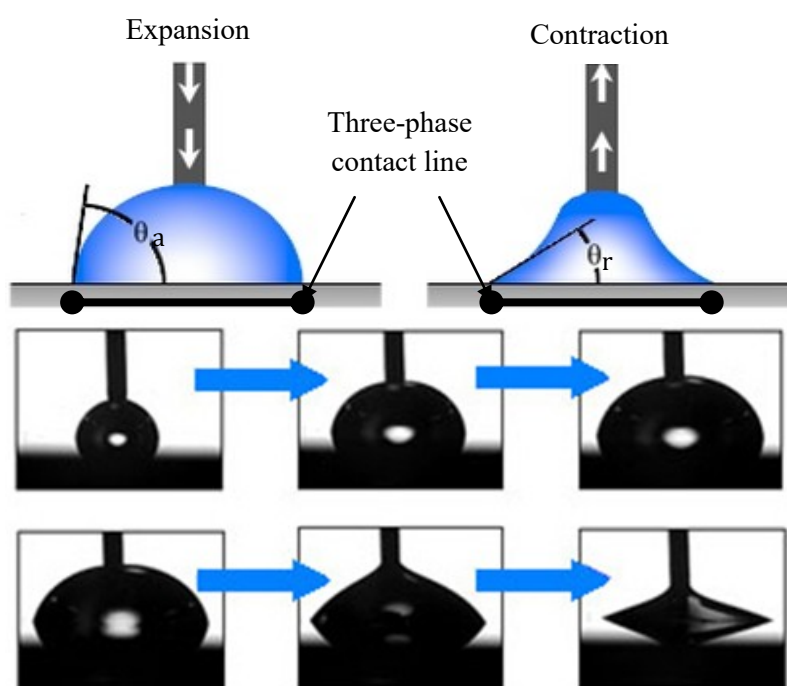


Figure 2.11 Expansion and contraction method used to measure the advancing, θ_a , and receding angles, θ_r , corresponding to imbibition and drainage respectively [63, 64].

The contact angle is measured by curve fitting methods. As the drop profile is disturbed by the capillary tube, the tangential method, ellipse fitting, polynomial fitting, and B-spline fitting are used. For low surface tension liquids, there may be preferential adhesion of the liquid to the needle. In this case a larger diameter needle with Teflon coating can provide a balance between adhesion and shape disturbance [50].

2.2.2.3 Tilting Plate Method

In the tilting plate method [65], the contact angle of a drop or bubble is measured at both sides as the substrate surface is tilted (see Figure 2.12). The advancing and receding angles are measured simultaneously. The tilt angle when the drop or bubble rolls off is referred to as the roll-off angle.

As the surface is tilted, gravity pulls the drop downwards, causing a distortion in the drop shape:

$$F = mg \cdot \sin \alpha , \quad (2.44)$$

where F is the pull force, m is the mass of the drop, g is gravitational acceleration, and α is the tilt angle. The frictional force, f , that prevents the drop from sliding is given by [50]:

$$f = \gamma_{LV} Rk \cdot (\cos \theta_{\min} - \cos \theta_{\max}) , \quad (2.45)$$

where γ_{LV} is the surface tension, R is the length scale for the contour of the drop, k is a fitted adjustable parameter, θ_{\max} is the contact angle at the lead edge, and θ_{\min} is the contact angle at the trail edge.

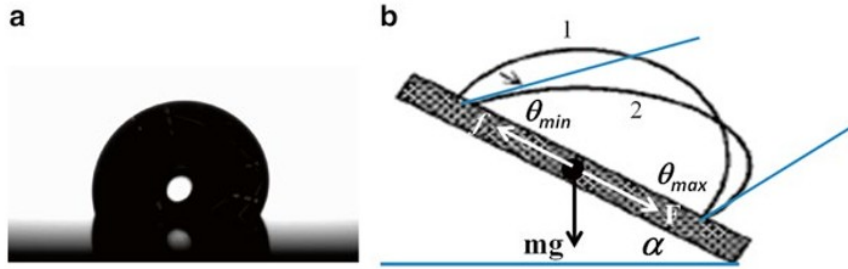


Figure 2.12 Tilting plate method used to measure the dynamic contact angle: a) image of a water drop on a tilted surface; b) forces acting on the drop as the plate is tilted, the lead edge angle, θ_{\max} , and trail edge angle, θ_{\min} , correspond to the advancing and receding angles, respectively [50].

When the two forces are balanced, the drop begins to move. There is a linear relationship [50] mathematically between $\sin \alpha$ and $\cos \theta_r - \cos \theta_a$, under the constraints of $\theta_a = \theta_{\max}$, and $\theta_r = \theta_{\min}$. Experimentally, this is not always the case. The receding contact line may never reach mechanical equilibrium. A comparison of the expansion-contraction method with the tilting base method reveals that the advancing angles measured agree [66], whereas the receding angles can be significantly different. There is an inequality between θ_a/θ_{\max} and θ_r/θ_{\min} for surfaces with large hysteresis [67].

2.2.2.4 Wilhelmy Plate Method

The Wilhelmy plate method [44] used to measure interfacial tension, described in section 2.1.1.3, can also be used to measure static and dynamic contact angles:

$$\cos \theta = \frac{f}{2(l+t)\gamma} . \quad (2.46)$$

where l is the plate width, t is the plate thickness, θ is the contact angle and f is the force needed to detach the two plate surfaces from the liquid. The advancing and receding angles are found by immersing or withdrawing the plate at a given velocity. The Wilhelmy plate method is a high-precision force measurement, without the subjective errors of optical methods, such as needle disturbances, baseline identification, and curve fitting errors [50]. The main drawback is in the specification of the test surface, which needs to be flat, rigid, homogeneous on both sides, and have well-defined dimensions.

2.3 Theoretical Modelling Methods for γ and θ

The objective of experimentally measuring interfacial phenomena of different systems is to observe the trends with variations in parameters such as temperature, pressure and composition; understand more about the behaviour and represent this by empirical relationships; to compare with theoretical models and to calibrate and validate their ability to predicatively model the dependency of interfacial tension on the various variables. Empirical models can be used directly if the pressure and temperature conditions, and component combinations match the ranges of the original experimental data. However, once the fluid mixture becomes more complex, such as having different compositions or multiple components, empirical models are no longer applicable. The need for predictive modelling of interfacial phenomena for complex mixtures is evident. This has been the subject of a large body of work in literature, with a myriad of theoretical approaches. The choice depends on the properties of the components modelled, and the ultimate purpose of the model. To close the loop between theory and reality, the models can be validated with experimental data. Likewise, limitations or errors in experimental measurements may be identified via comparison with models of well-established accuracy.

2.3.1 Interfacial Tension

There are various methods of modelling interfacial tensions, and these are considered in the following section. The empirical Parachor method of Macleod [68] and corresponding-state expressions of Guggenheim [25] are popular approaches to model interfacial tension. In the Parachor method, the IFT is correlated to the difference in bulk phase densities at equilibrium. The empirical methods can provide very accurate relations, but are not predictive. For models based on the corresponding-state principles, the IFT is related to a specific reference fluid. The density functional theory (DFT) [69, 70], though very accurate and predictive, requires significant computational power. The simplified square-gradient theory (SGT) [71] offers a predictive, but computationally less demanding approach to model the interfacial tensions of inhomogeneous fluid systems. The DFT can be written in terms of SAFT-VR free energy [72]. Similarly, the SGT can be coupled with the SAFT EoS [73]. These two methods with rigorous theoretical basis are described in detail in a review by Llovell et al. [72]. Various equations of state (EoS) have been used in combination with the DFT and SGT, commonly the Peng-Robinson EoS [74], or variations of the statistical associating fluid theory (SAFT) EoS [75].

2.3.1.1 Density Functional Theory

Density functional theory is one of the most successful, fully-predictive models for interfacial tension. The DFT methods are based on creating a free-energy functional, from which the thermodynamic properties of the inhomogeneous system are calculated. Reviews of the common approximations and approaches for constructing the free-energy functional can be found in the works of Davis [69] and Evans [76]. The numerical complexity of the DFT method has computational drawbacks when applied to complex multi-component mixtures in inhomogeneous systems [72].

For an open mixture at temperature T , chemical potential μ_i , for each component in a volume V . In the absence of external fields, the grand potential functional of an inhomogeneous system is given by [70]:

$$\Omega[\{\rho_m(\mathbf{r})\}] = A[\{\rho_m(\mathbf{r})\}] - \sum_{i=1}^n \mu_i \int d\mathbf{r} \rho_i(\mathbf{r}) \quad i = 1, \dots \quad (2.47)$$

$A[\{\rho_m(\mathbf{r})\}]$ is the "intrinsic" Helmholtz free-energy functional. The nomenclature of

$$A[\{\rho_m(\mathbf{r})\}] \equiv A[\rho_1(\mathbf{r}), \rho_2(\mathbf{r}), \dots] \quad , \quad (2.48)$$

is used to denote the functional dependence of A on all the densities $\rho_m(\mathbf{r})$ (at each point \mathbf{r}) for the set of components m of the mixture. In general, the notation $\{\rho_m(\mathbf{r})\}$ is used to denote all the density profiles of the mixture evaluated at position \mathbf{r} , i.e.

$$\{\rho_m(\mathbf{r})\} \equiv \rho_1(\mathbf{r}), \rho_2(\mathbf{r}), \dots \quad (2.49)$$

The minimum value of $\Omega[\{\rho_m(\mathbf{r})\}]$ is the equilibrium grand potential of the system and the corresponding equilibrium density profiles $\rho_i^{\text{eq}}(\mathbf{r})$ satisfy the following condition [70]:

$$\left. \frac{\delta \Omega[\{\rho_m(\mathbf{r})\}]}{\delta \rho_i(\mathbf{r})} \right|_{\text{eq}} = \left. \frac{\delta A[\{\rho_m(\mathbf{r})\}]}{\delta \rho_i(\mathbf{r})} \right|_{\text{eq}} - \mu_i = 0 \quad \forall \quad i = 1, \dots \quad (2.50)$$

The n Euler-Lagrange equations are equivalent to requiring that the Helmholtz free-energy functional to be a minimum, subject to constraint of constant number of particles. The undetermined multipliers correspond to the chemical potentials of each component in the bulk coexisting phases.

The free-energy functional can be defined with equations of states for the bulk fluid. In general, it is separated into two parts, a reference term that accounts for the ideal and short-range interactions, and a perturbative term for the long-range interactions [72]. The reference term can be represented by a local density approximation (LDA) or a weighted-density approximation (WDA). In the LDA, the free-energy contribution at a given point in the interface, is approximated to the homogeneous fluid evaluated at an appropriate local density. In the WDA, a weighted density over different points along the interface is used. It is a non-local functional of the original density, which depends on a number of weighting factors. The perturbative term accounts for long-range attractive interactions, and the correlations between molecules in the fluid are modelled with appropriate pair distribution functions. The distribution functions of inhomogeneous systems are usually unknown, so these molecular correlations are neglected in the calculation of the perturbative dispersion term in the mean-field approximation [72].

The equilibrium density profiles are first found by solving the Euler-Lagrange equations [77-81], via a modification of the Powell Hybrid method [82] included in the FORTRAN Minpack routine:

$$\begin{aligned} \mu_i = & \mu_i^{\text{ref}}(\{\rho_m(\mathbf{r})\}) + \sum_{j=1}^n \int d\mathbf{r}' m_i m_j \rho_j(\mathbf{r}') \\ & \times g_0^{\text{hs}} \left[\sigma_x; \overline{\xi}_x^{\text{eff}}(\lambda_{ij}; \{\rho_l(\mathbf{r}), \rho_m(\mathbf{r}')\}) \right] \phi_{ij}^{\text{attr}}(|\mathbf{r} - \mathbf{r}'|) \\ & + \sum_{j=1}^n \sum_{k=1}^n \int d\mathbf{r}' m_j \rho_j(\mathbf{r}') m_k \rho_k(\mathbf{r}') \\ & \times \frac{\partial g_0^{\text{hs}} \left[\sigma_x; \overline{\xi}_x^{\text{eff}}(\lambda_{ij}; \{\rho_l(\mathbf{r}), \rho_m(\mathbf{r}')\}) \right]}{\partial \rho_i(\mathbf{r})} \phi_{ij}^{\text{attr}}(|\mathbf{r} - \mathbf{r}'|) \end{aligned} \quad (2.51)$$

where μ_i^{ref} is the chemical potential of the hard-sphere reference system, g_0^{hs} is the pair radial distribution function of the homogeneous hard-sphere reference system, non-associating molecules are modelled as flexible chains formed from a m_i of identical attractive segments, at contact σ_x of

the pure-component system, potential range λ_{ii} , effective packing fraction $\overline{\xi_x^{\text{eff}}}(\lambda_{ij})$ using the mean-value theorem [83, 84].

Then the interfacial tension is evaluated from the following thermodynamic relation [72]:

$$\gamma = \frac{\Omega + pV}{A_{\text{I}}}, \quad (2.52)$$

by integrating the expression for the free-energy density across the interface, where A_{I} is the interfacial area, and p the bulk pressure.

2.3.1.2 Square Gradient Theory

The square gradient theory (SGT) is based on the van der Waals theory for inhomogeneous fluids [71], rediscovered by Cahn and Hilliard [85]. In the density profile calculation, the Helmholtz free-energy density is expanded as a Taylor series, and truncated after the second square-gradient term. The first term is calculated at each local density with an EoS for the bulk fluid. Consider a flat interface in thermodynamic equilibrium, at temperature T^{eq} , pressure p^{eq} , volume V^{eq} , with n components, and two equilibrium phases denoted as L and V. The equilibrium composition of the system is x^{eq} , and of the two phases are $x^{\text{eq,L}}$ and $x^{\text{eq,V}}$. The interfacial tension of the fluid can be expressed as [86]:

$$\gamma = \sqrt{2} \int_{\rho_w^{\text{V}}}^{\rho_w^{\text{L}}} \sqrt{(\Omega(\rho) + p^{\text{eq}}) \sum_{i,j=1}^n L_{ij} \frac{d\rho_i}{d\rho_w} \frac{d\rho_j}{d\rho_w}} d\rho_w, \quad (2.53)$$

$$\Omega(\rho) = \frac{A(\rho)}{V} - \sum_{i=1}^n \rho_i \mu_i^{\text{eq}} [T^{\text{eq}}, V^{\text{eq}}, n^{\text{eq}}]. \quad (2.54)$$

where the superscript 'eq' denotes properties at equilibrium, 'L' is the liquid phase, 'V' is the vapour phase; the subscript i, j refer to the component considered, w is a chosen reference component; Ω is the equilibrium grand potential of the system; μ_i is the chemical potential of component i ; ρ is the density, A is the Helmholtz free-energy, and L_{ij} is the cross-influence parameter between components i and j .

At equilibrium the grand potential of the system is at the minimum [87]:

$$\Omega(\rho) + p^{\text{eq}} = 0, \quad (2.55)$$

$$\left(\frac{\partial \Omega}{\partial \rho_i} \right)_{T^{\text{eq}}, V^{\text{eq}}, \rho_{j \neq i}^{\text{eq}}} = \mu_i - \mu_i^{\text{eq}} = 0, \quad i = 1, \dots, \quad (2.56)$$

$$\left(\frac{\partial^2 \Omega}{\partial \rho_i^2} \right)_{T^{\text{eq}}, V^{\text{eq}}, \rho_{j \neq i}^{\text{eq}}} = \left(\frac{\partial \mu_i}{\partial \rho_i} \right)_{T^{\text{eq}}, V^{\text{eq}}, \rho_{j \neq i}^{\text{eq}}} > 0, \quad i = 1, \dots. \quad (2.57)$$

Eq. (2.55) sets the constraint for mechanical equilibrium of the bulk phases ($p^{\text{L}} = p^{\text{V}}$). Eq. (2.56) requires each component in the equilibrium phases to have identical chemical potentials ($\mu_i^{\text{V}} = \mu_i^{\text{L}}$). Eq. (2.57) is the condition for curvature stability at interfaces, analogous to the Gibbs tangent-plane condition [88] for phase equilibria.

The limitation of the SGT is the introduction of the influence parameter, L , which appears in the square gradient term of the expansion. Determination of this parameter requires knowledge of the

usually unknown direct correlation function of the homogeneous fluid with temperature. In practice, it is commonly parameterized by fitting to experimental surface-tension data of pure fluids. The typical calculation approach as suggested by Carey [89-91] and Cornelisse [92-94], evaluates the influence parameter for pure fluids at the boiling temperature with experimental surface tension values, γ_{exp} , in eq. (2.53) with $n = 1$:

$$L_{ii}(T^0) = \gamma_{\text{exp}}^2(T^0) \left(\int_{\rho_w^{\text{V}}}^{\rho_w^{\text{L}}} \sqrt{2(\Omega(\rho) + p^{\text{eq}})} d\rho_i \right)^{-2}. \quad (2.58)$$

The pure-component influence parameters are applied to mixtures via geometric combining rules, which commonly include an adjustable unlike mixing parameter. This parameter is either adjusted to mixture surface tension data, or set to zero for a predictive surface tension calculation.

The principal working equations and subsequent numerical solution is simplified by the assumption of the geometric-mean rule for the unlike (cross) influence parameters [95]. The set of $(n - 1)$ equations to solve for densities between the equilibrium densities ρ_w^{V} and ρ_w^{L} is [96]:

$$\sqrt{L_{ww}} [\mu_i(\rho) - \mu_i^{\text{eq}}] = \sqrt{L_{ii}} [\mu_w(\rho) - \mu_w^{\text{eq}}], \quad i = 1, \dots \quad \dots \quad (2.59)$$

where $\mu_i(\rho)$ is the chemical potential of component i evaluated at T^{eq} , V , n between ρ^{V} and ρ^{L} . By solving eq. (2.59) for values of ρ_w varying between ρ_w^{V} and ρ_w^{L} , $\rho_{i \neq w}$ can be obtained, allowing for solution of eq. (2.53). Eq. (2.59) is a special case of the general solution, with well documented numerical solution methods [95, 96].

The choice of reference component w , is important. If only one reference component is used, then the density profile varies monotonically between ρ_w^{V} and ρ_w^{L} . If none of the component density profiles vary monotonically, then the solution domain can be divided into sub-domains. Each sub-domain has a reference component which exhibits monotonic behaviour in density. Eq. (2.59) is solved for each sub-domain, combining to give the full solution. Sahimi et al. [97] suggested a systematic selection scheme, where the component with the largest magnitude of dp_i/dp_w is chosen.

For a single-component fluid, eq. (2.53) can be simplified to a direct relation between the interfacial tension and the like influence parameter [92]:

$$\gamma = \sqrt{2} \int_{\rho_i^{\text{V}}}^{\rho_i^{\text{L}}} \sqrt{(\Omega(\rho) + p^{\text{eq}})} L_{ii} d\rho_i. \quad (2.60)$$

The like influence parameter for single components L_{ii} , can be obtained by comparing eq. (2.60) against experimental data for γ , as a function of temperature. A common approach is to correlate L_{ii} linearly with temperature [87]:

$$L_{ii} = a_{ii}^1 T + a_{ii}^0, \quad (2.61)$$

where a_{ii}^1 and a_{ii}^0 are constants obtained from interfacial tension data. For multi-components, a combining rule linking L_{ii} and L_{jj} with the unlike L_{ij} must be used. In the case of the geometric combining rule, and setting the adjustable binary parameter to zero:

$$L_{ij} = \sqrt{L_{ii} L_{jj}}. \quad (2.62)$$

Various EoS have been used with the SGT, such as combining with the SAFT EoS, as first carried out by Kahl and Enders [73]. The SGT provides a balance between computational complexity and rigour

for multi-component systems. The theory has been applied to liquid-liquid systems [98-101], associating systems [101-104], polymers [105], polar systems [104], (alkane + CO₂) systems [106] and (water + gas) systems [107-109].

2.3.1.3 Linear Gradient Theory

Linear gradient theory (LGT) of Zuo and Stenby [110] is an approximation to the SGT. The compositional variations between the equilibrium bulk phases are modelled to be linear. The calculations are numerically simpler.

$$\frac{d\rho_i(z)}{dz} = D_i, \quad (2.63)$$

where z is the position on the interface, with width h , and D_i is a constant for each component i .

$$D_i = \frac{\Delta\rho_i}{h} = \frac{\rho_i^\alpha - \rho_i^\beta}{h}, \quad (2.64)$$

where ρ_i^α and ρ_i^β are the densities of component i at the boundary conditions of the coexisting equilibrium phases. The interfacial tension is calculated by solving eq. (2.53), for the component with the maximum density difference between the two coexisting phases. It was originally applied to compute interfacial tensions in multi-component oil and gas systems. The application is inadequate for systems with interfacial adsorption, where the variation in composition throughout the interface is poorly represented by the linear assumption.

2.3.1.4 Equations of State

In the calculation and modelling of interfacial tension, it is imperative to have an accurate representation of the phase equilibria and Helmholtz free energy of the fluid system [111, 112]. This is resolved with engineering equations of state (EoS), which can be fitted to experimental data e.g. the Peng-Robinson cubic EoS [74, 113], or predictive e.g. molecularly-based approaches, such as SAFT [75].

2.3.1.4.1 The Peng-Robinson Equation

The Peng-Robinson equation of state (PR EoS) [74] is a cubic equation of state based on the van der Waals EoS for hard spheres, with empirical improvements in the attractive (perturbation) term. The PR EoS [74] provides better liquid density calculation than the Soave-Redlich-Kwong (SRK) [114], by constructing a smaller critical compressibility factor. The merit of this EoS is in its simple mathematical form, which can be solved readily, and therefore has widespread applications in industry. The limitations are the poor performance for non-spherical molecules, associating molecules, and representation of second derivative properties, such as heat capacities and speed of sound. In 1978, Peng and Robinson published an improved version of their 1976 EoS, known as the PR78 EoS [113]. For multi-component mixtures it is expressed as:

$$p = \frac{RT}{V-b} - \frac{a(T)}{V(V+b)+b(V-b)}, \quad (2.65)$$

$$a_i = 0.45724(RT_{c,i})^2 \alpha_i(T) / p_{c,i}, \quad (2.66)$$

$$\alpha_i(T) = \left[1 + m_i \left(1 - \left(\frac{T}{T_{c,i}} \right)^{1/2} \right) \right]^2, \quad (2.67)$$

$$\text{if } \omega_i \leq 0.491 \quad m_i = 0.37464 + 1.54226\omega_i - 0.26992\omega_i^2, \quad (2.68)$$

$$\text{if } \omega_i > 0.491 \quad m_i = 0.379642 + 1.48503\omega_i - 0.164423\omega_i^2 + 0.016666\omega_i^3, \quad (2.69)$$

$$b_i = 0.07780 RT_{c,i} / p_{c,i}. \quad (2.70)$$

With classical combining rules:

$$a = \sum_i^n \sum_j^n x_i x_j (1 - k_{ij}) \sqrt{a_i a_j}, \quad (2.71)$$

$$b = \sum_i^n \sum_j^n x_i x_j (b_i + b_j) (1 - l_{ij}) / 2, \quad (2.72)$$

where p is the pressure, R is the ideal gas constant, T is the temperature, V is the molar volume, n is the number of components in the mixture; a_i and b_i are EoS parameters for a pure component i ; $T_{c,i}$, $p_{c,i}$, ω_i are the critical temperature, critical pressure, and acentric factor of component i , respectively. The binary interaction parameters, k_{ij} and l_{ij} , in the combining rules are symmetrical, i.e. $k_{ij} = k_{ji}$. A non-null l_{ij} is only required for complex polar systems, and is generally set to zero for petroleum fluids. This equation of state [113] can be made predictive by using the group-contribution method to calculate the k_{ij} interaction parameters.

2.3.1.4.2 SAFT

The statistical associating fluid theory (SAFT) type EoS provides a better representation of molecular shape than the spherical assumption used in cubic equations [115-119]. The molecules are modelled as chains of m_i spherical segments of diameter σ_{ii} . The segments of each molecule interact with other molecules through a simple intermolecular potential, such as the square-well (SW) [83, 84], Yukawa [120], Lennard-Jones (LJ) [121], or Mie [122] potential. The generic SAFT equation is expressed as a sum of free-energy contributions:

$$A = A^{\text{ideal}} + A^{\text{mono}} + A^{\text{chain}} + A^{\text{assoc}}, \quad (2.73)$$

where A^{ideal} is the free-energy of an ideal gas mixture, A^{mono} is the contribution to the free-energy of intermolecular segment-segment repulsive and attractive interactions, A^{chain} is the change in free-energy from the formation of molecular chains from segments, and A^{assoc} is the change in free-energy from short range association interactions. The detailed derivation and analysis of each individual term can be found in the original publication [123].

The free-energy of an ideal gas mixture is given by [124]:

$$\frac{A^{\text{ideal}}}{Nk_B T} = \left(\sum_{i=1}^{n_c} x_i \ln(\rho_i \Lambda_i^3) \right) - 1, \quad (2.74)$$

where k_B is Boltzmann constant, N is the number of molecules, x_i is the mole fraction of component i , ρ_i is the number density of molecules of type i , and Λ_i is the thermal de Broglie wavelength, which includes rotational, vibrational, and translational contributions.

The free-energy due to the repulsion and attraction of monomeric spherical segments forming the chain molecules is described by the A^{mono} term. Applying the Barker-Henderson [125, 126] high-temperature perturbation expansion to third order:

$$A^{\text{mono}} = \left(\sum_{i=1}^n m_i x_i \right) A^{\text{HS}} + A_1 + A_2 + A_3, \quad (2.75)$$

where m_i is the chain length, and the reference system is a mixture of hard spheres with Helmholtz free energy A^{HS} . The reference hard-sphere term is evaluated using the approach of Boublik [127] and Mansoori et al. [128]:

$$\frac{A^{\text{HS}}}{Nk_{\text{B}}T} = \frac{6}{\pi\rho_s} \left[\left(\frac{\xi_2^3}{\xi_3^2} - \xi_0 \right) \ln(1 - \xi_3) + \frac{3\xi_1\xi_2}{1 - \xi_3} + \frac{\xi_2^3}{\xi_3(1 - \xi_3)^2} \right]. \quad (2.76)$$

where ρ_s is the number density of spherical segments, and ξ_k are the moment densities, defined by:

$$\xi_m = \frac{\pi\rho_s}{6} \sum_{k=1}^n x_{s,k} \sigma_{kk}^m, \quad (2.77)$$

where $x_{s,k}$ are the mole fraction of k -segments in the mixture, and σ_{kk}^m are the temperature dependent [126] diameter of the spherical segments of chain k .

In the SAFT-VR (variable range) approach for mixtures, the higher-order contributions to the perturbation expansion are constructed in a similar way, with summations of free-energy contributions per segment, and each contribution is the product of the corresponding inverse power of temperature, arriving at a series of mean-, fluctuation- and third-order terms:

$$\frac{A_q}{Nk_{\text{B}}T} = \left(\frac{1}{k_{\text{B}}T} \right)^q \left(\sum_{i=1}^n x_i m_i \right) a_q \quad q = 1, 2, 3. \quad (2.78)$$

The analytical expressions for the contributions a_q can be found in reference [123], The mean-attractive dispersive energy is accounted for in the first-order perturbation term a_1 . This is obtained by the mean-value theorem, to form an analytical expression from the radial distribution function of the reference hard-sphere fluid. The second-order fluctuation term a_2 , is evaluated by the improved macroscopic compressibility approximation (MCA) proposed by Zhang et al. [129]. The third-order term a_3 uses an empirical expression to incorporate higher-order terms fitted to critical- and phase-equilibrium data.

The packing fraction ξ_x of the mixtures is expressed as the segment size σ_x of a van der Waals one-fluid mixing rule:

$$\xi_x = (\pi/6) \rho_s \sum_{i=1}^n \sum_{j=1}^n x_{s,i} x_{s,j} \sigma_{ij}^3. \quad (2.79)$$

The chain formation of the molecules is accounted for in the Helmholtz free-energy by a sum of the contributions from the radial distribution function of the fluid intermolecular potential, evaluated at contact for the tangentially bonded segments:

$$\frac{A^{\text{chain}}}{Nk_{\text{B}}T} = - \sum_{i=1}^n x_i (m_i - 1) \ln g_{ii}(\sigma_{ii}), \quad (2.80)$$

where g_{ii} is the contact value of the pair correlation function for a system of monomers, described by the selected intermolecular potentials.

The association contribution to the free-energy, from short-range directional association between molecules, is described with the TPT1 formulation [35,38-41,56] of Wertheim:

$$\frac{A^{\text{assoc}}}{Nk_{\text{B}}T} = \sum_{i=1}^n x_i \sum_{a=1}^{n_{\text{sites},i}} n_{ai} \left[\ln X_{ai} - \frac{X_{ai}}{2} + \frac{1}{2} \right], \quad (2.81)$$

where $n_{\text{sites},i}$ is the number of site types on molecule i , n_{ai} is the number of sites of type a on molecule i and X_{ai} is the fraction of non-bonded sites of type a on molecule i . The fraction of non-bonded sites of type a on molecule i is given by the mass-action equation:

$$X_{ai} = \frac{1}{1 + \rho \sum_{j=1}^n x_j \sum_{b=1}^{n_{\text{sites},j}} n_{b,j} X_{bj} \Delta_{abij}}, \quad (2.82)$$

where b is the set of sites capable of bonding with site a , and Δ_{abij} is the association interaction parameter. The integrated association parameter is given as a product of the Mayer function of the bonding interaction between sites a and b , F_{ab} , the association kernel I , and the bonding-volume of association K_{ab} [130]:

$$\Delta_{ab} = F_{ab} K_{ab} I. \quad (2.83)$$

The Mayer function of the bonding interaction is expressed as:

$$F_{ab} = \exp\left(\frac{\mathcal{E}_{ab}^{\text{assoc}}}{k_{\text{B}}T}\right) - 1, \quad (2.84)$$

where $\mathcal{E}_{ab}^{\text{assoc}}$ is the energy of association. The results of the reference hypernetted chain (RHNC) integral equation theory for the radial distribution function is mapped to the association kernel I , by using [130]:

$$I(T^*, \rho^*, \lambda_{\text{R}}) = \sum_{i=0}^{i+j \leq 10} \sum_{j=0} a_{ij}(\lambda_{\text{r}}) (\rho^*)^i (T^*)^j, \quad (2.85)$$

where T^* is the reduced temperature ($T^* = k_{\text{B}}T/\epsilon$), ρ^* is the reduced density ($\rho^* = \rho\sigma^3$) and a_{ij} are the mapping constants as a function of the repulsive exponent:

$$a_{ij}(\lambda_{\text{R}}) = \sum_{k=0}^6 b_{i,j,k} \lambda_{\text{r}}^k, \quad (2.86)$$

where $b_{i,j,k}$ are mapping constants given in reference [130].

The segment-segment interactions can be represented with potential energy functions of increasing complexity and sophistication, starting from the very simple three parameter square well [83, 84] potential, to the Yukawa [120], Lennard-Jones [121], and Mie [122] potentials.

2.3.1.4.2.1 Square-Well Potential

The repulsive and attractive interactions of the spherical segments can be described by a square-well potential:

$$u_{kl}(r_{kl}) = \begin{cases} \infty & r_{kl} \leq \sigma_{kl} \\ -\varepsilon_{kl} & \sigma_{kl} < r_{kl} \leq \lambda_{kl}\sigma_{kl} \\ 0 & r_{kl} > \lambda_{kl}\sigma_{kl} \end{cases}, \quad (2.87)$$

where r_{kl} is the distance between the centres of the two segments k and l , σ_{kl} is the segment diameter, $\lambda_{kl}\sigma_{kl}$ is the range of the dispersive interaction of depth $-\varepsilon_{kl}$.

The directional short-range association interactions between sites a and b on segments k and l is modelled by:

$$u_{kl,ab}^{\text{assoc}}(r_{kl,ab}) = \begin{cases} -\varepsilon_{kl,ab}^{\text{assoc}} & \text{if } r_{kl,ab} \leq r_{kl,ab}^c \\ 0 & \text{if } r_{kl,ab} > r_{kl,ab}^c \end{cases}, \quad (2.88)$$

where $r_{kl,ab}$ is the distance between centres of two associating sites a and b , $r_{kl,ab}^c$ is the cut-off range of the a - b interaction between segments k and l , and $-\varepsilon_{kl,ab}^{\text{assoc}}$ is the short-range interaction energy between sites a and b on segments k and l .

The contact value of the pair radial distribution function for the square-well potential is evaluated from a first-order high-temperature expansion about a hard-sphere reference system [123]:

$$g_{ij}^{\text{sw}} = g_{d,ij}^{\text{HS}}(\sigma_{ij}) + \beta \varepsilon_{ij} g_{1,ij}(\sigma_{ij}), \quad (2.89)$$

where $g_{d,ij}^{\text{HS}}$ is the contact value of the radial distribution function for the reference system of a mixture of hard spheres at the packing fraction of the mixture.

2.3.1.4.2.2 Mie Potential

The intermolecular interactions described by the Mie potential includes the effects of solvation, hydrogen-bonding or association-like interactions, by assigning appropriate attractive sites via additional off-centre short-range square-well potentials between particular molecules [131]. The Helmholtz free-energy of this model fluid is constructed by applying the TPT1 of Wertheim [132-135]. The free-energy of the system can be calculated from the free-energy and fluid structure of the reference system of monomeric segments. In the Mie potential, the interaction between segments k and l , with distance between the centres of the two segments r_{kl} , is given by [136]:

$$u_{kl}(r_{kl}) = \frac{\lambda_{r,kl}}{\lambda_{r,kl} - \lambda_{a,kl}} \left(\frac{\lambda_{r,kl}}{\lambda_{a,kl}} \right)^{\lambda_{a,kl}/(\lambda_{r,kl} - \lambda_{a,kl})} \varepsilon_{kl} \left[\left(\frac{\sigma_{kl}}{r_{kl}} \right)^{\lambda_{r,kl}} - \left(\frac{\sigma_{kl}}{r_{kl}} \right)^{\lambda_{a,kl}} \right], \quad (2.90)$$

where σ_{kl} is the segment diameter, ε_{kl} is the depth of the potential, $\lambda_{r,kl}$ and $\lambda_{a,kl}$ are the repulsive and attractive exponents of the segment-segment interactions, respectively.

The directional short-range association interactions between sites a and b on segments k and l is modelled by the square well potential in Eq. (2.88). The short-range sites are offset from the segment centre by a distance of $r_{kk,aa}^d$, such that the short range interactions can be expressed by a bonding

volume parameter $K_{kl,ab}$ in the TPT1 framework [137], and does not discriminate between the relative site positions.

The contact value of the pair radial distribution function for the Mie potential is calculated from a second-order [123] expansion about a hard-sphere reference system [131]:

$$g_{ij}^{\text{Mie}} = g_{d,ij}^{\text{HS}}(\sigma_{ij}) \exp \left[(\varepsilon / k_{\text{B}} T) g_{1,ij}(\sigma_{ij}) / g_{d,ij}^{\text{HS}}(\sigma_{ij}) + (\varepsilon / k_{\text{B}} T)^2 g_{2,ij}(\sigma_{ij}) / g_{d,ij}^{\text{HS}}(\sigma_{ij}) \right] \quad (2.91)$$

where g_1 and g_2 are the perturbation contributions, $g_{d,ij}^{\text{HS}}$ is obtained from the hard-sphere expression of Boublík [138]. Perturbation terms of first and second order are approximated by the corresponding values at contact distances equal to the diameter d_{ij} of the hard sphere reference system:

$$g_q(\sigma_{ij}) \approx g_q(d_{ij}), \quad q = 1, 2 \quad (2.92)$$

The first order perturbation expansion is obtained using the pressure from the Clausius virial and the free energy routes [75, 123, 139]. The second-order term is an expression based on the MCA.

2.3.1.4.2.3 Combining Rules for Mixtures

The mixture properties calculation requires values for parameters of the cross (unlike) interactions between components i and j . The unlike segment size is calculated using the Lorentz combining rule:

$$\sigma_{ij} = \frac{\sigma_{ii} + \sigma_{jj}}{2}. \quad (2.93)$$

The unlike dispersive interaction energy is given by a modified Berthelot rule, a geometric mean with corrections for size effects, through a procedure given by Hudson and McCoubrey [140] as detailed in reference [141]:

$$\varepsilon_{ij} = (1 - k_{ij}) \frac{\sqrt{\sigma_{ii}^3 \sigma_{jj}^3}}{\sigma_{ij}^3} \sqrt{\varepsilon_{ii} \varepsilon_{jj}}, \quad (2.94)$$

where k_{ij} is a binary interaction parameter, which can be adjusted using binary experimental data.

The combining rule for unlike exponents in the square-well potential is expressed as:

$$\lambda_{ij} = \frac{\lambda_{ii} \sigma_{ii} + \lambda_{jj} \sigma_{jj}}{\sigma_{ii} + \sigma_{jj}}, \quad (2.95)$$

The combining rule for unlike exponents in the Mie potential is expressed as [123]:

$$\lambda_{ij} = (1 - \Gamma_{ij}) \left(3 + \sqrt{(\lambda_{ii} - 3)(\lambda_{jj} - 3)} \right), \quad (2.96)$$

where Γ_{ij} is an adjustable binary interaction parameter.

2.3.1.4.2.4 *Thermodynamic Properties*

The homogeneous fluid expressions of the Helmholtz free energy for associating chain molecules can be used to determine all the thermodynamic properties of the system [88]. In phase equilibria and interfacial tension calculations, the pressure and chemical potential are the most important factors. The pressure is given by:

$$p = - \left(\frac{\partial A}{\partial V} \right)_{T,N}, \quad (2.97)$$

and the chemical potential of component i is given by:

$$\mu_i = \left(\frac{\partial A}{\partial N_i} \right)_{T,V,N_j \neq N_i}. \quad (2.98)$$

3 Literature Review

3.1 Interfacial Tension

3.1.1 Experimental Measurement

3.1.1.1 CO_2 with Water or Brine

Carbon sequestration in sedimentary aquifers has been a key motivator for interfacial tension measurements involving the CO_2 -water or CO_2 -brine systems. In the case of enhanced oil recovery using CO_2 injection, the measurement systems revolve around combinations of CO_2 and hydrocarbons, such as crude oil. Earlier experimental work employed the capillary rise technique; with the introduction of digitised profile fitting and analysis, the pendant drop method, and its variations, with ADSA has become the prevalent measurement technique. The optical method typically consists of a high pressure high temperature view cell, diffuse light source, CCD camera to capture the shape of the drop formed from a capillary tube, and image edge detection with automated solution of the Laplace equation. A list of the conditions and systems studied in literature is summarised in the Table 3.1. As discussed by Georgiadis *et al.* [142], the inconsistency in the literature data was possibly due to the selected measurement timeframe, contamination by surface-active impurities particularly in long-duration experiments, location of temperature measurement, and inaccuracy in the density difference term used in the IFT calculation.

Table 3.1 Studies of the interfacial tension of CO_2 with H_2O or brine reported in literature; here, T and p refer to the temperature and pressure ranges examined, respectively.

Method	Aqueous Phase	T/K	p/MPa	Year	Reference
Capillary rise	H_2O	298	2 to 5	1957	Slowinski <i>et al.</i> [143]
Pendant drop	H_2O	311, 344	7.0 to 24.1	1957	Heuer [144]
Pendant drop	H_2O	310 to 411	0.1 to 103	1959	Hough <i>et al.</i> [145]
Capillary rise	H_2O	298	0.6 to 6.1	1974	Massoudi and King [146]
Capillary rise	Brine	298	0.6 to 6.1	1975	Massoudi and King [147]
Capillary rise	H_2O	285 to 318	0.4 to 6.0	1978	Jho <i>et al.</i> [148]
Capillary rise	H_2O	278 to 344	0.1 to 15.7	1995	Chun and Wilkinson [149]
Pendant drop	H_2O	313, 333	0.1 to 20	1997	Wesch <i>et al.</i> [150]
Pendant drop	H_2O	314, 343	0.4 to 27.9	1998	Jaeger [151]
Pendant drop	H_2O	308, 318	6.6 to 28	1999	da Rocha <i>et al.</i> [152]
Pendant drop	H_2O	278 to 335	0.1 to 20	2002	Hebach <i>et al.</i> [153]
Pendant drop	H_2O	293 to 313	2 to 9	2004	Tewes and Boury [154]
Capillary rise	H_2O , surfactant	293 to 344	0.1 to 20	2005	Park <i>et al.</i> [155]
Pendant drop	H_2O + crude oil	339.2	13.1 to 33.8	2005	Sun and Chen [156]
Pendant drop	Brine, crude oil	300, 331	0.1 to 31.4	2005	Yang <i>et al.</i> [157]
Sessile drop	H_2O	296	0.1 to 13.6	2006	Dickson <i>et al.</i> [158]
Pendant drop	H_2O , surfactant	318	1.16 to 16.56	2007	Akutsu <i>et al.</i> [159]
Pendant drop	H_2O	308 to 383	5 to 45	2007	Chiquet <i>et al.</i> [160]
Pendant drop	H_2O , ethanol, corn germ oil	313	0.1 to 27	2008	Sutjiadi-Sia <i>et al.</i> [161]
Rising drop	Brine	300 to 373	4.5 to 25.5	2009	Chalbaud <i>et al.</i> [162, 163]
Pendant drop	H_2O , brine	293 to 398	2 to 27	2009	Bachu and Bennion [164]

Pendant drop	H ₂ O, brine	309 to 398	2 to 27	2009	Bachu and Bennion [165]
Pendant drop	H ₂ O	298 to 374	1 to 60	2010	Georgiadis <i>et al.</i> [142]
Rising drop	Brine	300 to 373	5 to 25	2010	Aggelopoulos <i>et al.</i> [166]
Sessile drop	H ₂ O, brine	297	0.1 to 20	2010	Espinoza and Santamarina [167]
Pendant drop	H ₂ O	298 to 333	1.48 to 20.76	2011	Bikkina <i>et al.</i> [168]
Pendant drop	Brine	323 to 448	2 to 50	2012	Li <i>et al.</i> [169, 170]
Pendant drop	H ₂ O, brine	298 to 448	1 to 60	2015	Chow <i>et al.</i> [171] ^a
Pendant drop	H ₂ O	298 to 469	0.5 to 70	2016	Pereira <i>et al.</i> [172]

^a reanalysis of the raw data from references [142, 169, 170].

Time Variation

Once a drop was introduced into the view cell, the timeframe selected for analysis was important. Hebach *et al.* [153] separated the drop's IFT variation with time into three regimes, A, B and C, shown in Figure 3.1. The rapid decrease in IFT with time at interval A was caused by the initial diffusion and convection process, with mixing and temperature gradients, combined with the dissolution effects of CO₂ into the aqueous phase. This period can be shortened by pre-saturating the two co-existing phases. The interfacial tension measurements should be measured at phase equilibrium, such that the CO₂-rich phase is saturated with water or brine, and the aqueous phase saturated with CO₂. Otherwise, a stable drop profile cannot be obtained due to mass transfer effects. In regime B, the IFT reaches a steady-state value, which was used for collecting data for analysis. The long-term ageing effects of the drop were described by interval C, and were possibly attributed to surfactant migration to the drop interface.

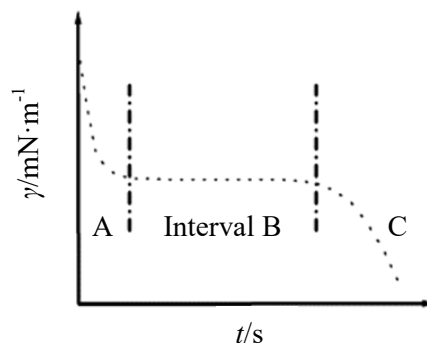


Figure 3.1 Interfacial tension changes of a measured drop with time: A is the initial CO₂ dissolution period, B is the steady interval used for data collection, and C is drop ageing [153].

The time allowed for interval A varied among the various studies. Bikkina *et al.* [168] suggested that some of the inaccuracies observed in literature arose due to short pre-saturation times. Bachu and Bennion [164, 165], Bikkina *et al.* [168], and Aggelopoulos *et al.* [166] used a 24 hour pre-saturation time to allow the phases to reach equilibrium. Chiquet *et al.* [160] allowed several minutes for the mixing and saturation of water and CO₂, prior to injection into the view cell. In da Rocha *et al.*'s [152] experiments, the drop profile was measured one hour after drop formation. Hebach *et al.* [153] provided an equilibration time of 10 minutes. Chalbaud *et al.* [162, 163] allowed 8 to 15 minutes after drop formation for the drop to reach equilibrium, depending on the pressure and temperature.

Georgiadis *et al.* [142] presented the steady experimental values reached 300 seconds after drop formation, for the lowest measured temperature of 297.9 K, at (10.0, 15.0, and 20.0) MPa. The same

authors also provided the rationale for selecting this time duration by considering the mass transfer diffusion of CO₂ into a theoretical spherical liquid water drop interface. Sutjiadi-Sia *et al.* [161] allowed about 220 seconds for the interfacial tension values to reach a constant value. Aggelopoulos *et al.* [166] measured several minutes after drop formation. Li *et al.* [169, 170] used an equilibration time of 150 seconds, chosen by observing plots of experimental data with time. Similarly, Akutsu *et al.* [159] selected an equilibration time of about 2 minutes. Tewes and Boury [154], and Yang *et al.* [157] did not pre-equilibrate the fluid phases prior to measurement, with the aim of observing the dynamic variation of IFT as CO₂ dissolves into a fresh brine phase.

The measurement period once regime B has been reached was generally described less clearly by the authors. Heuer [144] took measurement 10 seconds after drop formation. Hebach *et al.* [153] measured the drop in regime B for 20 seconds. Georgiadis *et al.* [142] measured the IFT in this regime for 300 seconds. Li *et al.* [169, 170] measured the IFT for 450 seconds. Bikkina *et al.* [168] carried out measurements for 24 hours. The long duration was probably a reason for the consistently 5-7 mN·m⁻¹ lower IFT values than those reported in literature. Tewes and Boury [154] observed the IFT variation for as long as 100,000 seconds. Chun and Wilkinson [149] carried out capillary rise measurements for several days, with local equilibrium being reached.

In summary, the equilibration time required for different systems depends on the chemical species present, the rate of diffusion at the measured temperature, and is generally no less than 120 s. A suitable measurement period is when the IFT is steady and does not decrease with time.

Density Difference

The interfacial tension measurement by the pendant drop method requires knowledge of the phase density difference. At the temperature and pressure conditions of interest, the aqueous phase density can be approximated by pure water or brine density, and the non-aqueous phase density by pure CO₂ density. As found by King *et al.* [173] and Hebach *et al.* [174], the non-aqueous phase density had no measurable change from that of pure CO₂ density, over a temperature range of (284 to 332) K, for pressures below 30 MPa. For the aqueous phase density, the pure water approximation was used by several authors [142, 146-149, 153, 155, 157].

However, at conditions close to density inversion, where CO₂ density is comparable to water density, this approximation can lead to considerable error in the calculated IFT. When CO₂ dissolves into water or brine, the density of the aqueous phase increases. This is of particular importance at low temperatures and high pressures. Sutjiadi-Sia *et al.* [161] reported higher IFT values by about 3 mN·m⁻¹ when pure water densities were used, instead of the CO₂-saturated aqueous densities. Chow *et al.* [171] calculated an increase in IFT by 4 mN·m⁻¹ in their reanalysis of Georgiadis *et al.*'s [142] lowest temperature and highest pressure data point, when the CO₂ saturated aqueous-phase densities were used. The phase density difference can be determined by direct measurement with a vibrating tube densimeter, as carried out by Bachu and Bennion [164, 165], Chiquet *et al.* [160], Hebach *et al.* [174], and Pereira *et al.* [172]; or with a PVT instrument used by Sun and Chen [156]. Alternatively, the phase density differences were obtained by calculation from correlations published in literature [162, 163, 166-170, 175].

The chosen method of analysis depends on the resources available. Computation is relatively faster and more flexible, but dependent on the accuracy of the original model. Direct measurement will provide the exact values for the temperature and pressure combinations required, but are subject to

experimental errors. In both cases, the consideration of CO₂ dissolution in water is highly recommended for low temperature and high pressure data analysis.

Effect of Pressure

In general for the CO₂ with water or brine systems, the IFT was found to decrease with increasing pressure, and to level off to a pseudo-plateau above a certain pressure. Chiquet *et al.* [160] quoted this pressure to be at 20 MPa. At low pressures, the IFT steeply decreases with pressure, with almost linear behaviour. Chiquet *et al.* hypothesised at low pressures, the IFT linearly extrapolate to the water surface tension at $p \approx 0$. They carried out this extrapolation for their lowest pressure measurement at 5 MPa. This is supported by the measurements of Chun and Wilkinson [149], and Hebach *et al.* [174] at 0.1 MPa, and Tewes and Boury [154] at 2 MPa. This observation is useful for carrying out sensibility checks on the measured data.

Chalbaud *et al.* [162, 163] noticed a similar plateau effect to 26 mN·m⁻¹, for the lowest salinity brine, used for comparing with CO₂-water results. The authors modified the Parachor method to include the plateau value, in order to empirically fit the IFT to the density difference variable. Hebach *et al.* [153] provided a regression curve for ease of interpolation of their results, as a function of density difference. Georgiadis *et al.* [142] also observed two distinct linear regions at low temperatures, linked to the phase transition of CO₂ from gas to liquid or supercritical state. Empirical relations were used to describe the IFT variation with pressure. At low temperatures, a dual-linear correlation was used, with two sets of parameters above and below an apparent point of intersection. The second correlation was a rational function which fitted the smooth variation of IFT with pressure at higher temperatures. Li *et al.* provided empirical relations for interfacial tension as a function of temperature, pressure and brine molality. However, this correlation has interpolation problems between fitted data points at low pressures due to the negative power terms. In a later work by Li *et al.* [169, 170], the difference in IFT from water surface tension at the same temperature is found to be nearly linear with CO₂ solubility, and a correlation is provided for the range of conditions studied. This latter relation does not have the interpolation problem, but has a greater fitting uncertainty.

Effect of Temperature

The IFT variation with temperature is more complex than the dependence on pressure. Generally, the IFT decreases with increasing temperature. A crossover of the isotherms is observed at temperatures below the critical temperature, when the CO₂ changes from a gas to liquid or supercritical state.

Effect of Salt

Chiquet *et al.* [160] observed negligible effect with addition of salt. However, the brine used was of very low salinity, which was not representative of most deep saline aquifer conditions. Cai *et al.* [176] observed an increase in IFT with addition of salt in the aqueous phase, for hydrocarbon with water or brine systems. The IFT increase depends on the salt concentration, but not the salt species. Duchateau and Broseta [177] showed that the IFT of (gas + brine) systems was simply related to the surface tension of the brine and the (gas + H₂O) interfacial tensions at the same pressure and temperature. Along an isotherm, they found that increasing the salinity shifted the (gas + brine) IFT to higher values. This is similarly observed by Li *et al.* [170], who measured the (CO₂ + brine) IFT for various salts over wide ranges of pressure, temperature and molality. The same authors provided a simple empirical correlation that can be used to predict IFTs of other brine systems at high pressures.

3.1.1.2 Gases with Water or Brine

Various authors have carried out interfacial tension measurements on gas-water or gas-brine systems, using the capillary rise technique or the pendant drop method, to high pressures and temperatures. A list of the conditions and systems studied in literature is summarised in the Table 3.2. Methane, nitrogen, argon and hydrogen are light gases that have low solubility in water, and the aqueous phase density change, due to dissolution of these gases, were generally neglected.

Table 3.2 Studies of the interfacial tension of water with various gases in binary and ternary systems reported in literature; here, T and p refer to the temperature and pressure ranges examined, respectively.

Method	System	T/K	p/MPa	Year	Reference
Pendant drop	$N_2 + H_2O$	300 to 411	0.1 to 103	1952	Hough <i>et al.</i> [145]
Capillary rise	$N_2 + H_2O$	298	2 to 10	1957	Slowinski <i>et al.</i> [143]
Capillary rise	$N_2 + H_2O$	303	0.1 to 12	1962	Masterton <i>et al.</i> [178]
Capillary rise	$N_2 + H_2O$	298	*	1974	Massoudi and King [146]
Pendant drop	$N_2 + H_2O$	298 to 573	20 to 280	1994	Wiegand and Franck [179]
Pendant drop	$N_2 + H_2O$	298 to 473	10 to 100	1997	Tian <i>et al.</i> [180]
Pendant drop	$N_2 + H_2O$	298 to 373	1 to 30	2001	Yan <i>et al.</i> [181]
Pendant drop	$N_2 + CO_2 + H_2O$	298 to 373	1 to 30	2001	Yan <i>et al.</i> [181]
Capillary rise	$Ar + H_2O$	303	0.1 to 12	1962	Masterton <i>et al.</i> [178]
Capillary rise	$Ar + H_2O$	298	0.1 to 8.0	1974	Massoudi and King [146]
Pendant drop	$Ar + H_2O$	298 to 473	10 to 100	1994	Wiegand and Franck [179]
Capillary rise	$H_2 + H_2O$	298	2 to 10	1957	Slowinski <i>et al.</i> [143]
Capillary rise	$H_2 + H_2O$	298	0.1 to 7.5	1974	Massoudi and King [146]
Capillary rise	$O_2 + H_2O$	298	*	1974	Massoudi and King [146]
Capillary rise	$CO + H_2O$	298	*	1974	Massoudi and King [146]
Pendant drop	$He + H_2O$	300 to 411	0.1 to 103	1952	Hough <i>et al.</i> [145]
Capillary rise	$He + H_2O$	298	2 to 10	1957	Slowinski <i>et al.</i> [143]
Capillary rise	$He + H_2O$	298	0.1 to 8.0	1974	Massoudi and King [146]
Pendant drop	$H_2S + H_2O$	313 to 393	0.5 to 14.6	2008	Shah <i>et al.</i> [182]
Pendant drop	$H_2S + CO_2 + H_2O$	350	0.5 to 15.6	2008	Shah <i>et al.</i> [182]
Capillary rise	$N_2O + H_2O$	298	*	1974	Massoudi and King [146]
Pendant drop	$CH_4 + H_2O$	296 to 411	0.1 to 103	1951	Hough <i>et al.</i> [183]
Pendant drop	$CH_4 + H_2O$	300 to 411	0.1 to 103	1952	Hough <i>et al.</i> [145]
Capillary rise	$CH_4 + H_2O$	298	2 to 7	1957	Slowinski <i>et al.</i> [143]
Capillary rise	$CH_4 + H_2O$	298	0.1 to 7.5	1974	Massoudi and King [146]
Pendant drop	$CH_4 + H_2O$	296 to 450	0.1 to 83	1971	Jennings and Newman [184]
Capillary rise	$CH_4 + H_2O$	293 to 323	0.1 to 6.9	1978	Jho <i>et al.</i> [148]
Rising bubble	$CH_4 + H_2O$	298 to 398	0.3 to 66	1995	Sachs and Meyn [185]
Rising bubble	$CH_4 + H_2O$	298 to 373	1 to 30	2000	Ren <i>et al.</i> [186]
Rising bubble	$CH_4 + H_2O + H_2O$	298 to 373	1 to 30	2000	Ren <i>et al.</i> [186]
Rising bubble	$CH_4 + H_2O + \text{surfactant}$	273, 279	0.4 to 9.5	2004	Sun <i>et al.</i> [187]

*The raw data was not reported, but a polynomial fit with pressure was provided.

Slowinski *et al.* [143] studied the surface tension of various gases with water at room temperature, and presented their results in graphical form. Massoudi and King [146] provided a polynomial

expansion with pressure for the numerous gases studied, but graphically only presented the data for a few gases. Masterton *et al.* [178] provided their (N₂ + H₂O) system results in graphical form, whereas the (Ar + H₂O) system was only reported in terms of a fitted quadratic equation. The (CH₄ + H₂O) system has been studied by more extensively [143, 145, 146, 148, 183-186].

The interfacial tension of the (N₂ + H₂O) system has been measured by Wiegand and Franck [179], Tian *et al.* [180], Yan *et al.* [181]. Interfacial tensions of the (N₂ + H₂O) system measured at or above 373 K, was found to initially decrease with pressure until about 75 MPa, after which the IFT reaches a pseudo-plateau, before increasing gradually with pressure. Tian *et al.* [180] measured the IFT of water and nitrogen, from pressures of (10 to 100) MPa, at temperatures of (298 to 473) K. Measurements at $p = 0.1$ MPa were made at $T = 298$ K only. Yan *et al.* [181] also measured this system, from pressures of (1 to 30) MPa, at temperatures of (298 to 373) K. These three data sets are in general agreement with each other, but with noticeable deviations at the lowest pressures reported by Tian *et al.* [180].

The interfacial tension of the (Ar + H₂O) system has been measured by Massoudi and King [146], and Wiegand and Franck [179], for a sparse set of pressure and temperature conditions. In Wiegand and Franck's work, only two data points were reported at $T = 373$ K. The density difference of 433.34 kg·m⁻³ used at $p = 30$ MPa differs greatly from that calculated for the pure fluids (366.40 kg·m⁻³), from the equations of state of pure water [188] and pure argon [189] as implemented in the REFPROP 9.1 software [190].

The IFT of the (H₂ + H₂O) system at 298 K has been reported in literature by Slowinski *et al.* [143], and Massoudi and King [146], up to 10 MPa. In the latter work, hydrogen interfacial tension is expressed as a linear function of pressure at 298 K.

For the (H₂S + H₂O) system at the two lower temperatures investigated by Shah *et al.* [191], the interfacial tensions are observed to decrease with increasing pressure, when the pressures are below the saturation pressure of H₂S. This decrease persists for the high temperature measurement at 393.15 K, until a pseudo-plateau is reached at 10 mN·m⁻¹, at about 12 MPa. At pressures above saturation pressure of H₂S for 313.15 K and 343.15 K, the interfacial tensions level off and become fairly invariant with pressure increases.

The interfacial tension for various compositions of the ternary mixture (CO₂ + N₂ + H₂O) have been measured by Yan *et al.* [181] at pressures of (1 to 30) MPa and temperatures of (298 to 373) K. The interfacial tension of the ternary mixture (CO₂ + H₂S + H₂O), with 70 mol% CO₂ and 30 mol% H₂S in the initial gas mixture, have been studied by Shah *et al.* [182] at $T = 350$ K and at pressures up to 15.6 MPa. They found that the IFT is approximately equal to the molar average IFT of the binary systems of (H₂S + H₂O) and (CO₂ + H₂O) at the same temperature and pressure. Ren *et al.* [186] measured the IFT of the (CH₄ + H₂O + H₂O) system at various compositions, using a rising bubble method. The phase density differences, due to CO₂ dissolution, were obtained by calculation from correlations published in literature. Interfacial tensions of the ternary system (CO₂ + Ar + H₂O) have not been reported in the published literature.

To summarise the literature, measurements of CO₂-water, gas-water IFT under reservoir conditions have been carried out by several authors, by the capillary rise method, the pendant drop method and the rising bubble method. (Gas + brine) IFT can be obtained from empirical correlations if the (gas + H₂O) IFT and the brine surface tension are both known. Only one source of literature data is available for the IFT of the (CO₂ + N₂ + H₂O) system up to 30 MPa and 373 K. No literature sources are found to report the ternary systems of CO₂, water or brine, and Ar, H₂, O₂, SO₂, NO_x, or CO. The gaps in the

literature provide motivation to investigate the interfacial tensions of binary and ternary component systems involving CO₂, gas and water or brine, at elevated pressures and temperatures. The potential applications of using a simple molar average of the binary system IFTs to predict ternary system IFTs is appealing, but require further research.

3.1.2 Modelling

The modelling of interfacial tension of inhomogeneous fluid systems requires a correct representation of the phase equilibria and the Helmholtz free energy of the fluid system. The choice of equation of state dictates this representation, as analysed in [111, 112].

Table 3.3 Previous modelling studies for the interfacial properties of (CO₂ + H₂O), (N₂ + H₂O), (Ar + H₂O) and (N₂ + CO₂ + H₂O); T and p refer to the temperature and pressure ranges examined, respectively.

System	T/K	p/MPa	Approach	Equation of State	Year	Ref
CO ₂ + H ₂ O	-	-	SGT	PR [74]	1993	[192]
CO ₂ + H ₂ O	313	0 to 25	LGT	SRK [114]	2001	[193]
CO ₂ + H ₂ O	298.15 to 318.15	0 to 5.9	Cahn-Type	PR	2007	[194]
CO ₂ + H ₂ O	297.9 to 373.3	1 to 60	DFT	SAFT-VR [75]	2010	[195]
CO ₂ + H ₂ O	287 to 313	0.1 to 25	SGT	SAFT-VR Mie 2006 [196]	2010	[197]
CO ₂ + H ₂ O	300 to 383	0 to 30	Simulation	-	2012	[198]
CO ₂ + H ₂ O	298.2 to 333.2	0 to 25	SGT	PCP-SAFT [199]	2012	[108]
CO ₂ + H ₂ O	297.8 to 374.3	1.01 to 60	LGT	CPA [200]	2013	[201]
CO ₂ + H ₂ O	298.15 to 398.15	0.1 to 60	SGT	sPC-SAFT [202]	2014	[109]
CO ₂ + H ₂ O	298.15 to 303.15	0 to 25	Simulation	SAFT- γ Mie [203]	2014	[204]
CO ₂ + H ₂ O	284.15 to 312.15	1 to 6	SGT	CK-SAFT [205]	2014	[206]
N ₂ + H ₂ O	298.15 to 373.15	1 to 30	LGT	SRK [207]	2001	[181]
N ₂ + H ₂ O	298.15 to 373.15	1 to 30	LGT	CPA	2013	[201]
N ₂ + H ₂ O	298.15 to 373.15	1 to 30	LGT	CPA	2015	[208]
Ar + H ₂ O	298.15 to 318.15	0 to 8	Cahn-Type	PR [209]	2007	[194]
N ₂ + CO ₂ + H ₂ O	298.15 to 373.15	1 to 30	LGT	CPA	2013	[201]

Several theoretical approaches have been reported in the literature that allow for either predictive or correlative descriptions of the interfacial properties of binary and multi-component systems. The applications of density functional theory (DFT) with a molecular equation of state have been reported by both Llovell *et al.* [210] for (CO₂ + hydrocarbon) systems and by Georgiadis *et al.* [78] for (CO₂ + H₂O) and (CO₂ + hydrocarbon) systems. This method has the merit of being fully predictive and was shown to provide a generally good estimate of the experimental data. However, DFT is computationally demanding and unsuitable for routine application. The simpler gradient-theory (GT) approaches, such as square-gradient theory (SGT) and linear-gradient theory (LGT), have been successful when combined with either cubic or molecular equations of state. As described in Section 2.3, these methods involve binary influence parameters, the like-like influence parameters to be fitted to surface tension data of the pure components; and unlike influence parameters to be either estimated from a combining rule or fitted to experimental data.

Miqueu *et al.* [211, 212] combined GT with the Peng-Robinson equation of state to describe the IFT of binary and multicomponent (CH₄ + hydrocarbon) and (CO₂ + hydrocarbon) systems without fitting the unlike influence parameters. Muller *et al.* [213] and Mejía *et al.* [86] also applied GT predicatively for mixtures, using SAFT equations of state, and obtained good estimates for (alcohol + water) and

(CO₂ + hydrocarbon) systems. However, to fit the IFT of more challenging systems like the (CO₂ + H₂O) system with a GT model, Lafitte *et al.* [214] had to resort to fitting the unlike influence parameters. Yan *et al.* [181] concluded that the GT model was unsuitable for the (CO₂ + N₂ + H₂O) system. Khosharay and Varaminian [215] combined the cubic-plus-association equation of state (CPA EOS) with GT and this was applied successfully to systems involving high concentrations of carbon dioxide in the vapour phase, using data from Georgiadis *et al.* [142] and Yan *et al.* [181]. The model predicted (N₂ + H₂O) interfacial tensions with average absolute deviations (AAD) of 0.5 %; (CO₂ + H₂O) interfacial tensions with AAD of 2.0 %; and (CO₂ + N₂ + H₂O) interfacial tensions with AAD of 1.8 %. Chow *et al.* [216] used the SAFT-VR Mie + SGT approach to model the interfacial tensions of (CO₂ + H₂O) with AAD of 4.2 %.

3.2 Contact Angle

3.2.1 Experimental Measurement

Contact angle measurements for systems of CO₂ with gases, water or brine, on various substrates reported in literature are summarised in Table 3.4. The substrate cleaning methods adopted by the various authors are summarised in Table 3.5.

Table 3.4 Systems of substrate and fluids where contact angle measurements have been reported to the highest measured temperature and pressure.

Substrate	Fluids	<i>T</i> /K	<i>p</i> /MPa	Year	Reference
Quartz, sapphire, stainless steel, Teflon, PVC	CO ₂ Water	313	30.0	1997	Wesch <i>et al.</i> [150]
Glass	CO ₂ Water	296	20.4	2006	Dickson <i>et al.</i> [158]
Mica, quartz	CO ₂ Brine (NaCl)	298	11.0	2007	Chiquet <i>et al.</i> [160]
Glass micromodels	CO ₂ Water	333	10.0	2009	Chalbaud <i>et al.</i> [162]*
Dolomite	Alkane Water	303	32.0	2009	Jaeger and Pietsch [217]
Quartz, oil-wet quartz, calcite, PTFE	CO ₂ Brine, water	298	20.0	2010	Espinoza and Santamarina [167]
Quartz, calcite	CO ₂ Water	323	20.0	2011	Bikkina <i>et al.</i> [168]
Mica, quartz, calcite, carbonate	CO ₂ , H ₂ S Brine (NaCl)	413	15.0	2012	Broseta <i>et al.</i> [218]
Silica micromodels	CO ₂ Brine (NaCl)	318	8.5	2012	Kim <i>et al.</i> [219]
Quartz, Teflon	CO ₂ Brine	473	103.4	2012	Saraji <i>et al.</i> [220]
Coal	CO ₂ + N ₂ Water	318	16.0	2006 2011 2012	Siemons <i>et al.</i> [221] Sakurovs <i>et al.</i> [222] Kaveh <i>et al.</i> [223]
Mica, quartz, calcite, feldspar	CO ₂ Brine, water	309 339	40	2013	Farokhpoor <i>et al.</i> [224, 225]
Mica, quartz, calcite, amorphous silica, dolomite, kaolinite, and illite	CO ₂ , N ₂ Brine	323	20	2013	Wang <i>et al.</i> [226]
Quartz	CO ₂ Brine, water	323	25	2014	Iglauer <i>et al.</i> [227]

*Qualitative study.

Table 3.5 Cleaning methods of the substrates prior to experiment as reported in literature.

Substrate	Cleaning Method	Reference
Quartz	Washed with acetone and dried	[150]
Quartz	Cleaned with a tensioactive solution under ultrasonic agitation for 30 min, then rinsed with a 10% nitric-acid solution and finally washed with DI water.	[160]
Calcite Quartz	Unspecified	[167]
Calcite	Cleaned with Millipore water in a bath sonicator for 15 min and dried in the oven at 378 K, for 2 h	[168]
Quartz	Used as received for 1 st cycle and for following cycles sequentially cleaned with acetone and Millipore water for 30 min in a bath sonicator and dried in the oven at 378 K, for 2 h	[168]
Calcite Quartz	Unspecified	[218]
Calcite	Washed with Deconex solution under ultrasonic bath and rinsed with distilled water in the end	[224, 225]
Quartz	Washed with a Deconex cleaning detergent solution under ultrasonic bath for 20 min, then washed with distilled water, then rinsed with a 6 % nitric-acid solution while heated to 30°C and finally washed with distilled water	[224, 225]
Quartz	First rinsed with isopropyl alcohol then immersed in sulfuric acid solution containing 10% Nocromix and sonicated for 30 min, soaked inside this solution overnight, washed thoroughly with water and boiled in distilled water for about 2 h, and rinsed and stored inside fresh distilled water. A few minutes before each test, the substrates were dried by absorbing their bulk water with a filter paper and then blown-dried with ultrahigh-purity (UHP) nitrogen.	[220]
Calcite Quartz	Soaked in an acetone bath for 3 h then heated to 393 K for 2 h, sonicated in DI water, and flushed with nitrogen to dry.	[226]
Quartz	Cleaned with acetone and DI water; Cleaned with piranha solution (H ₂ SO ₄ :H ₂ O ₂) Cleaned with oxygen (air) plasma	[227]

Broseta *et al.* [218] measured the advancing and receding contact angles, and wetting behaviour of acid gases (CO₂ and H₂S) in brines (salinity up to NaCl saturation) on mica, quartz, calcite and carbonate-rich rock samples, up to 413.15 K and 15 MPa, using a captive bubble method. Structural and local capillary trapping which depends on the water-receding (gas-advancing) drainage angle, was found to be unaffected by the presence of dense acid gases. Residual trapping which depends on the water-advancing (gas-receding) imbibition angle, was found to change more significantly at high CO₂ density or brine salinity, where adhesion was observed on mica. Wettability reversal was observed for liquid H₂S on mica. The substrate-gas systems were studied at sparse combinations of temperature and brine salinity, over varying pressure ranges. The drainage and imbibition angles were reported over a range corresponding to the highest and lowest pressures along an isotherm, the 2 to 3 intermediate pressure measurements were omitted. The contact angles were provided as a range so the

changes over the isotherm with pressure were precluded. H₂S studies were carried out at temperatures different from the CO₂ studies, impeding direct comparisons.

For (mica + CO₂), the drainage contact angles were similar over the 0.5 to 14 MPa pressure range, between 28 ° and 45 °. High salinity brine increased the contact angles to 40-50 °. Mica wettability was unaltered when brine was drained by dense CO₂, whereas imbibition angles increased significantly (more than 30 °) at high brine salinity and/or when the CO₂ phase was dense. In the (mica + H₂S) measurements, the similar refractive indices of liquid H₂S and water posed challenges for the image processing software to identify the bubble contours. Gaseous H₂S was found to increase drainage angle from 63 ° at 1.5 MPa to 77 ° at 3.5 MPa, rendering mica to be less water-wet than in CO₂. Mica was intermediate-wet for imbibition, as angles were in the range of 90 °. Mica was observed to be H₂S-wet at pressures above 3.5 MPa (10 and 13 MPa), where drainage angles increased to about 110 ° and imbibition angles increased to about 150 °.

The (quartz + CO₂) measurements were in agreement with Chiquet *et al.* [160] and Wesch *et al.* [150], where drainage angles increased only slightly over the pressure range of 1 to 10 MPa. The opposite trend was reported by Bikkina *et al.* [168], where contact angles increased slightly with pressure when the CO₂ was gaseous, and a sudden decrease was observed when the CO₂ is liquid or supercritical. Broseta *et al.* [218] found that the drainage angles (*c.a.* 30-40 °) did not vary much with pressure, with some increases in imbibition contact angles when CO₂ is a liquid or supercritical, and for high salinity brine. This was compared to the quartz contact angle of about 47 ° at 298 K, from Bikkina *et al.* [168]. (Quartz + H₂S) contact angles remained fairly constant over the pressure range investigated (42-45 °). On the carbonate-rich rock sample, both CO₂ and H₂S were observed to have low drainage and imbibition angles of about 30 °, negligible hysteresis, and were insensitive to pressure variations from 1 to 15 MPa.

Bikkina *et al.* [168] reported sessile drop contact angle measurements for the CO₂-water system over quartz and calcite surfaces at representative storage conditions. Calcite contact angles were measured to be 40-48 °, compared with 35 ° at 0.5 MPa to 43 ° at 14 MPa, at 308 K for low salinity brine, from Broseta *et al.* [218]. The contact angles did not change with drop volume, when varied from 3 to 38 mm³. Seal failure and drop evaporation was reported for one of the high pressure measurements. Contrary to the findings of Broseta *et al.* [218], pressurisation water receding contact angles and depressurisation water advancing contact angles were observed to have no significant differences. Contact angles were observed to be fairly invariant with temperature. Repeated exposure to dense water saturated CO₂ were observed to result in increased contact angles to intermediate-wet behaviour. This contact angle shift observation was not reported elsewhere, and was under debate of surface contamination [228].

Espinoza and Santamarina [167] observed in their room temperature sessile drop measurements that contact angle varied with CO₂ pressure, increasing on non-wetting surfaces such as PTFE and oil-wet quartz, and decreasing slightly in water-wet quartz and calcite surfaces. The latter observation was in agreement with Bikkina *et al.*'s [168] findings. The droplet size ranged from 10 to 30 mm³. Images were captured 8 minutes after each pressure step. However, the bulk fluid phase and droplet was not pre-equilibrated prior to commencement of the measurements. This could result in unreliable contact angles, as the interfacial behaviour was interrupted by dissolution effects. The water droplet advanced or receded during pressurisation. The contact angle of non-wetting PTFE experienced a distinctive increase from 100 ° to 140 ° when the bulk fluid transitions from a gas to liquid, and then remained constant with pressure increases. Oil-wet quartz contact angle was observed to increase with pressure up to the CO₂ vapour-liquid boundary, and contact angle was similar for brine and deionised water at

all pressures. Contact angles on amorphous silica SiO_2 and calcite CaCO_3 remained nearly constant with pressure, but increased by 20° and 4° respectively in brine.

Chiquet *et al.* [160] observed greater drainage angle variations with pressure on mica than quartz. At low pressure both substrates had drainage angles of about $10\text{--}30^\circ$, at 11 MPa the drainage angle increased to 60° for mica and 35° for quartz. Quartz wettability was invariant with brine salinity, whereas the drainage contact angle of mica increased by about 25° from 0.1 to 1 M NaCl for a constant pressure. Contact angle variations were postulated to be caused by the decrease in pH, from 7 to 3, when pressure was increased from zero CO_2 partial pressure to pressures above 8 MPa respectively. The pH decrease was sufficient to bring the negative surface charge density down close to zero. The charge density of quartz and mica surfaces in water vanished when the pH was between 2 and 3. The repulsive electrostatic interactions between the brine interfaces tended to stabilise the brine film and favour water-wettability. However, this stability was reduced at high CO_2 pressure or low pH.

Wesch *et al.* [150] reported contact angle increases of about 40° over a pressure range of 0.1 to 30 MPa, at 313 K, for non-wetting substrates, Teflon and PVC, and wetting substrate unpolished stainless steel. A steep increase at pressures close to the CO_2 vapour-liquid boundary was observed, and beyond this boundary, contact angle remained fairly constant with further increases in pressure. A similar trend was observed for the originally water-wet polished sapphire and quartz, but the contact angle increase was less pronounced, about 10° . The different wetting behaviour was attributed to the ability of CO_2 to penetrate into the grooves of the surface below the water droplet. Dickson *et al.* [158] found that contact angles increased significantly with CO_2 pressure at room temperature, on two glass substrates with different hydrophilicities.

Farokhpoor *et al.* [224, 225] measured the CO_2 contact angle on reservoir rock representative minerals, including muscovite mica, quartz, calcite, and feldspar, in brine at reservoir conditions. The captive-needle drop method was used for a CO_2 droplet formed underneath the substrate, and the drop profile fitted with polynomial fitting. The advancing contact angle was measured. Quartz, calcite and feldspar were found to be strongly water wet with little variation in contact angles to pressure increases. The muscovite mica changed from being strongly water-wet to intermediate water-wet with increasing pressure. To study the effects of calcite surface reaction in the acidic conditions, the contact angle variation with time was measured. The water wettability of the calcite did not change significantly. A maximum contact angle was observed for the quartz, calcite and feldspar samples near the critical pressure of CO_2 at 309 K. For muscovite mica, the contact angle was observed to increase with pressure.

Wang *et al.* [226] conducted static pendant contact angle measurements and captive advancing or receding tests for CO_2 -brine systems at 323 K, and 20 MPa, for seven representative minerals including quartz, calcite, amorphous silica, dolomite, kaolinite, illite, and phlogopite mica. Adhesion was observed for CO_2 droplets on phlogopite mica, amorphous silica, and calcite surfaces. The adhered droplets wetted the surface and became attached to the mineral, making them difficult to remove. CO_2 droplets on quartz, dolomite, kaolinite, and illite surfaces did not wet the surface, with contact angles between 16° and 22° . The droplets that did not adhere to the surface typically formed a small contact with the mineral surface. Adhered droplets were more wetting with larger contact angles, and often had differences between the left and right side contact angles of the droplet. This could be because the three-phase contact line was not circular and was distorted. This axisymmetric character of adhered droplets has been ascribed to pinning and heterogeneities on the surface. This contact line distortion was uncommon for droplets that were non-wetting.

Iglauer *et al.* [227] measured the sessile and advancing contact angle of water or brine drops in CO₂ on quartz, representative of sandstone, at 323 K, up to 25 MPa. They addressed the large uncertainty in reported data, and showed that it was caused by surface contamination. Inappropriate cleaning methods would result in artificially high contact angle measurements. They used a strongly oxidising piranha solution, or oxygen plasma to clean the substrates. The water contact angle on a clean quartz substrate is found to be low, 0-30 °, and increases with pressure; demonstrating strongly water-wet behaviour at high pressure conditions.

To summarise the literature, goniometry and micromodel contact angle measurements of CO₂ and other gases, with water or brine, on various minerals representative of reservoir rocks were reported in literature at conditions applicable to CO₂ storage. Contact angles were found to be generally invariant with temperature, affected by pH, and change with time and repeated exposure. The wettability results were scattered and sometimes contradictory for relationships with pressure and brine salinity. The measurements were conducted under different conditions, making it more difficult to make a direct comparison. More quantitative and systematic methods of reporting findings were required. This was innately challenging as the rock substrates used were heterogeneous, further complicating attempts to generalise the trends observed. Effects of adding other gases such as N₂, H₂, O₂, Ar, SO₂, NO_x and CO, to the CO₂-brine-mineral system have yet to be studied. The substrate preparation methods for the different minerals were important to develop consistent protocols, with reproducible results across research groups.

4 Experimental Methodology

This chapter outlines the approach taken in the interfacial properties (IFP) measurements. First, the IFP apparatus is described, followed by the design, construction and commissioning process. The experimental procedures when operating the IFP apparatus for interfacial tension (IFT) and contact angle (CA) measurements are then presented. The materials used for the experiments and validation of the measurements, are followed by the final section on data analysis.

4.1 Equipment Description

The interfacial property (IFP) apparatus used to carry out pendant-drop interfacial tension (IFT), tilting plate, and volumetric expansion and contraction contact angle (CA) measurements for drops and bubbles is shown in Figures 4.1 and 4.2. The main high-pressure (up to 50 MPa) high-temperature (up to 473 K) titanium view cell (C1) was closed at both ends by sapphire windows with stainless steel threaded cap assemblies, sealed with Viton O-rings and PEEK back-up films. The axially opposed windows allow for illumination of the drop or bubble with a diffuse LED light source, and a CCD camera was used to capture the image. The view cell, light source and camera were secured on an automated tilting base, with rotational flexibility of $\pm 90^\circ$ from baseline. The substrate holder (see Figure 4.3), with manually-operated magnetic-coupled rotation and translation, allowed for contact angle measurements at high pressures. The maximum substrate dimensions were 11.6 mm x 10.6 mm x 7.0 mm. The IFT was determined from images of a pendant-drop by means of axisymmetric drop-shape analysis (ADSA). The contact angle was determined from images of a drop or bubble formed on the substrate, by numerical extrapolation of the profile at the contact point, using a circular-fit fitting function.

High-pressure Quizix syringe pumps (P1 and P2), and CMD 500B dual controller drivers linked directly to the PC, were used for pressure control and injection of experimental fluids. A circulating chiller-heater allowed for temperature control of these pumps. Fluid was injected into the view cell through capillary tubing of 1.6 mm OD x 0.3 mm ID. The view cell had two inlet ports, one for liquid (N1) and another for gas (N2) injection; one outlet port at the bottom of the vessel for drainage; and off-centred ports for the magnetic substrate adjuster rod traversing through the vessel. The vessel was protected from hazardous overpressure by a rupture-disk safety device (V8), rated for 65 MPa. The mixing of the view cell contents was accomplished with a magnetic stirrer. A flow-through pressure transducer (DJ Instruments, model DF2) was located in the tubing external to the view cell for pressure measurement, with standard uncertainty of 35 kPa. All fluid mixture-wetted components exposed to high pressure and temperature were made of titanium grades 2, 3, 4, and 5.

The temperature of the vessel was maintained by an externally-insulated five-piece aluminium jacket fitted with four electric cartridge heaters, and a temperature sensor operating with a proportional-integral-differential temperature controller. A calibrated platinum resistance thermometer (PRT, Pt100) was inserted into the wall of the view cell for temperature measurement, with standard uncertainty of 0.025 K. The voltages from the pressure sensor and resistances of the PRT were logged, and converted into vessel temperatures and pressures in the Agilent 34972A Data Acquisition (DAQ) Unit, and displayed in real-time via the Keysight VEE programme panel.

A manually operated diaphragm vacuum pump (P3) allowed the empty system to be evacuated. This was also used for degassing liquid feeds to prevent any build-up of gas bubbles in the vessel. To reduce the vibrations for good stable data collection, a foam mat between the base and the table was used as a shock absorber. The pressure vessel and high pressure pumps were enclosed in an aluminium frame with polycarbonate windows for safety protection. The liquid waste stream was

collected in the drain bottle, with the gas waste stream separated off and vented via the vent line to the atmosphere outside the laboratory building. An inert gas purge was installed to dilute any flammable waste. An emergency stop valve was installed for the flammable-gas cylinder feed, to enable an emergency supply cut-off accessible from outside the laboratory.

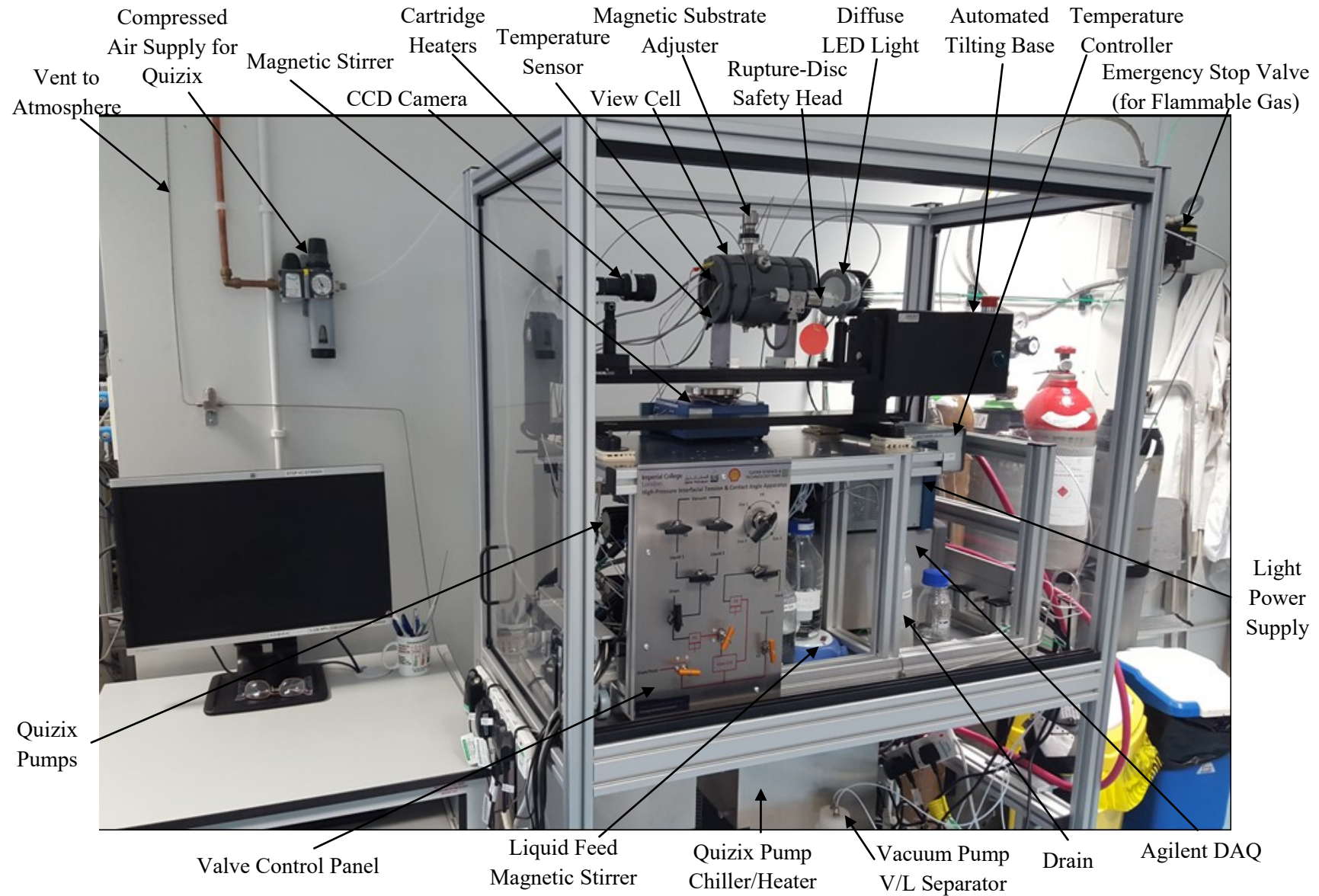


Figure 4.1 Interfacial properties apparatus set-up, with the frame front polycarbonate panels removed.

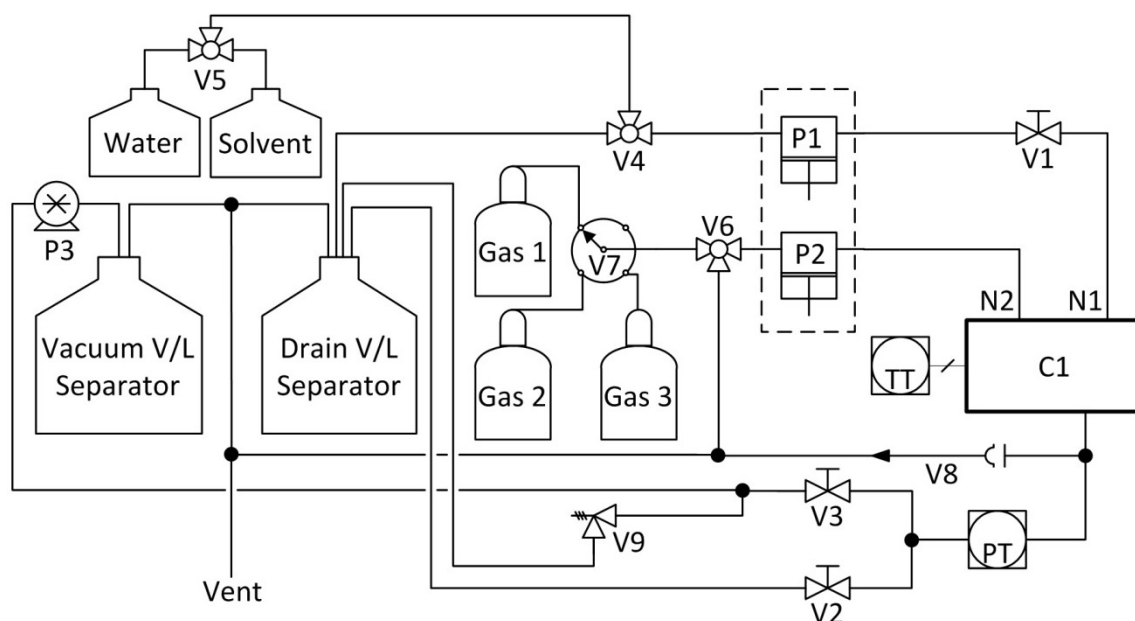


Figure 4.2 Interfacial properties apparatus, where the gas cylinder provides pressurised gas to the view cell. C1: optical cell with stirrer; P1, P2: high-pressure Quizix pumps; P3: vacuum pump; TT: platinum resistance thermometer (Pt100); PT: flow-through pressure transducer; N1, N2: injection ports; V1, V2, V3: high-pressure valves; V4, V5, V6: three-way valves; V7: four-way switch; V8: rupture-disc safety head; V9: relief valve.

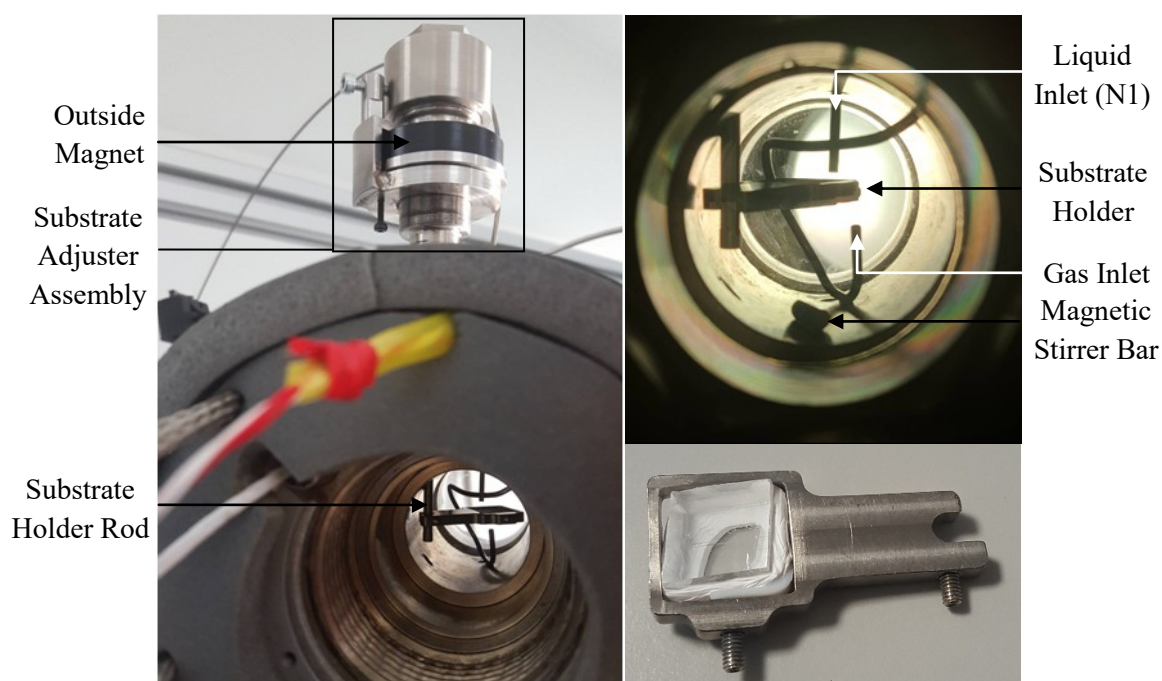


Figure 4.3 *Left.* Magnetic substrate adjuster assembly after installation into the view cell. *Top right.* Substrate holder inside the view cell, showing the inlet port positions. *Bottom right.* Substrate holder with a calcite substrate sample moulded to fit with PTFE tape.

4.2 Equipment Design, Construction and Commissioning

4.2.1 Material of Construction

The interfacial properties apparatus was designed for experiments involving brine systems in the presence of CO₂, N₂, Ar and H₂, from ambient temperature up to 473.15 K and at pressures up to 50 MPa. Titanium Grade 4 was chosen for this purpose, as it has high tensile strength to withstand high pressures, and corrosion resistance to seawater, sour and oxidising acidic media [229]. A thin invisible surface oxide film of mainly TiO₂, was formed when contacted with trace oxygen or moisture. This helps to protect the metal from corrosive environments even at high temperatures. The low thermal expansion coefficient of titanium provided enhanced interface compatibility with the sapphire window, minimising warpage and fatigue effects of temperature cycling over experimental runs. Interference with the magnetic stirrer was minimised as titanium was essentially nonmagnetic.

The highest strength commercially available grade of nominally-pure titanium was Titanium Grade 4. This was used in the manufacture of the vessel and substrate holder. The substrate adjuster rod was made of Titanium Grade 3. The locking grub screws were made of Titanium Grade 2.

Table 4.1 Key design properties of Titanium Grade 4 [229].

Property	Value	Condition
Temperature Limit	427 °C	Continuous Service
Melting Point, Approx.	1660 °C	-
σ_u , Ultimate Tensile Strength	365 MPa	At 204 °C
	552 MPa	At room temperature
σ_y , Yield Strength, 0.2% offset	255 MPa	At 204 °C
	483 MPa	At room temperature
Charpy V-notch impact	13 - 27 J	At 25 °C
Coefficient of Thermal Expansion	$9.2 \times 10^{-6} \text{ } ^\circ\text{C}^{-1}$	0 - 315 °C
Density	4510 kg/m ³	-
Thermal Conductivity	$17.0 \text{ Wm}^{-1}\text{K}^{-1}$	-

4.2.2 Pressure Vessel

4.2.2.1 View Cell

The engineering drawing and details of the view cell design can be found in Section 8.3 of the Appendix. The High Pressure Safety Code [230] empirical criteria were used in the high pressure duty assessment of the axis-symmetric, thick-walled pressure vessel design. Vessels with a diameter ratio, $K = OD/ID$, greater than 1.2, were classified as thick-walled. For the pressure duty assessment, the construction material was ductile, with ultimate tensile strength $\sigma_u < 10$ kbar, tensile yield strength $\sigma_y < 0.85 \cdot \sigma_u$, and a Charpy V-notch impact value of not less than 27 J, over the whole range of operating conditions. From Table 3.1, Titanium Grade 4 has an ultimate tensile strength of 365 MPa and yield strength in tension of 255 MPa at 204 °C, which was representative of the maximum working temperature of 200 °C. The Charpy V-notch impact upper limit was 27 J, satisfying the minimum requirement.

Under creep-free and fatigue-free conditions, a monobloc vessel made from a single piece of material apart from the end closures and fittings, free from cross-bores and welding was used for the pressure vessel design. The following empirical constraints were applied to ensure that the vessel behaves in an

elastic manner even during pressure test and would not deform permanently, provided that the vessel was strain-free prior to pressure application. In these equations, p_w was the working pressure.

$$\text{Yield pressure of the vessel} \quad p_y = \frac{\sigma_{y,204^\circ\text{C}}}{2} \left(\frac{K^2 - 1}{K^2} \right) \quad (4.1)$$

$$\text{Ultimate bursting pressure of the vessel} \quad p_b = 2\sigma_{u,204^\circ\text{C}} \left(\frac{K - 1}{K + 1} \right) \quad (4.2)$$

$$\text{Maximum allowable working pressure (MAWP)} \quad p_{\max} = \min\{0.67p_y, 0.25p_b\} \quad (4.3)$$

for $OD < 15$ cm

$$\text{Hydraulic test pressure} \quad p_{\text{test}} = 1.5p_w \quad (4.4)$$

Table 4.2 Pressure vessel design and corresponding high pressure duty assessment.

Design Parameter	Value	Assessment Parameter	Value (MPa)
Nominal outer diameter, OD	81.6 mm	Working pressure, p_w	50.0
Internal diameter, ID	33.0 mm	Hydraulic test pressure	75.0
Wall thickness	24.3 mm	MAWP, p_{\max}	71.4
K	2.47	Yield pressure, p_y	106.6
Reduction in area	16 %	Ultimate bursting pressure, p_b	309.4

The titanium bar had an outer diameter of 81.6 mm, after polishing off about 1.0 mm. The design parameters and resulting pressure duty assessment are summarised in Table 4.2. The K value of 2.47 was about double that of the 'thick-walled' guideline of 1.2. The assessment suggests that the chosen design dimensions have a maximum allowable working pressure of 71.4 MPa, and was satisfactory for use at the working pressure of 50.0 MPa.

Cross-bore holes were drilled in the vessel for the fluid inlet-outlet ports and the substrate adjuster rod fittings. These holes, drilled through the main bore of the cylinder, will create a stress concentration and result in a very small amount of permanent deformation. For vessels with $K > 2.5$, made of ductile material and operated within the conditions specified, the MAWP does not need to be reduced if the cross-bore diameter was less than half of the main bore. The K value of the chosen design was just below 2.5. However, the maximum cross-bore hole diameter was 6.35 mm, which was less than 20 % of the main-bore diameter of 33 mm. So it was reasonable to neglect MAWP decreases due to cross-bores.

4.2.2.2 End Closure

The end closure of the pressure vessel consisted of the sapphire window, sealing o-ring, PEEK back-up film and stainless steel threaded cap. For service up to MAWP of 71.4 MPa, the minimum thickness of an unclamped sapphire window of 33 mm unsupported diameter, was 18 mm. This was based on a safety factor of 4, and a 276 MPa apparent elastic limit of sapphire provided by the manufacturer, Crystran. With an additional margin of 24 %, the chosen window thickness was 22 mm. The windows were lightly chamfered at 45° to prevent stress concentration at sharp edges. The groove dimensions for the windows were 40.14 mm in diameter, and 22.5 mm in depth.

From BS-4518, an O-ring of nominal diameter 39.6 mm and cross-sectional diameter of 2.4 mm was chosen for sealing the Ø 40 mm window. Groove dimensions for static diametrical sealing were selected. The material Viton 75 or 90 was selected. Due to temperature and pressure cycling in the

experiments, as well as absorption of CO₂ in the O-rings, the phenomenon of explosive decompression damage to the O-rings was expected, and thus the O-rings were intended to be replaced after each experimental run. An annular 0.1 mm film of PEEK was positioned between the end cap and the sapphire window, to act as a back-up ring and protect the window when the vessel was under pressure.

Stainless steel was chosen for the cap material to prevent galling with the titanium vessel body. The minimum length of engaged end cap thread, L , required to withstand internal pressures up to MAWP, was calculated from the High Pressure Safety Code [230]:

$$p_{\max} = \frac{d_{\text{thread}} L}{2d_o^2} \left(\frac{2}{3} \sigma_y \right) \quad (4.5)$$

The mean diameter of the cap thread, d_{thread} , was 50.4 mm. With a nominal O-ring diameter, d_o , of 39.6 mm, the minimum thread length was 14.2 mm. The chosen diameter of the cap was 52.0 mm, with a pitch of 3.0 mm, and thread length of 23.0 mm.

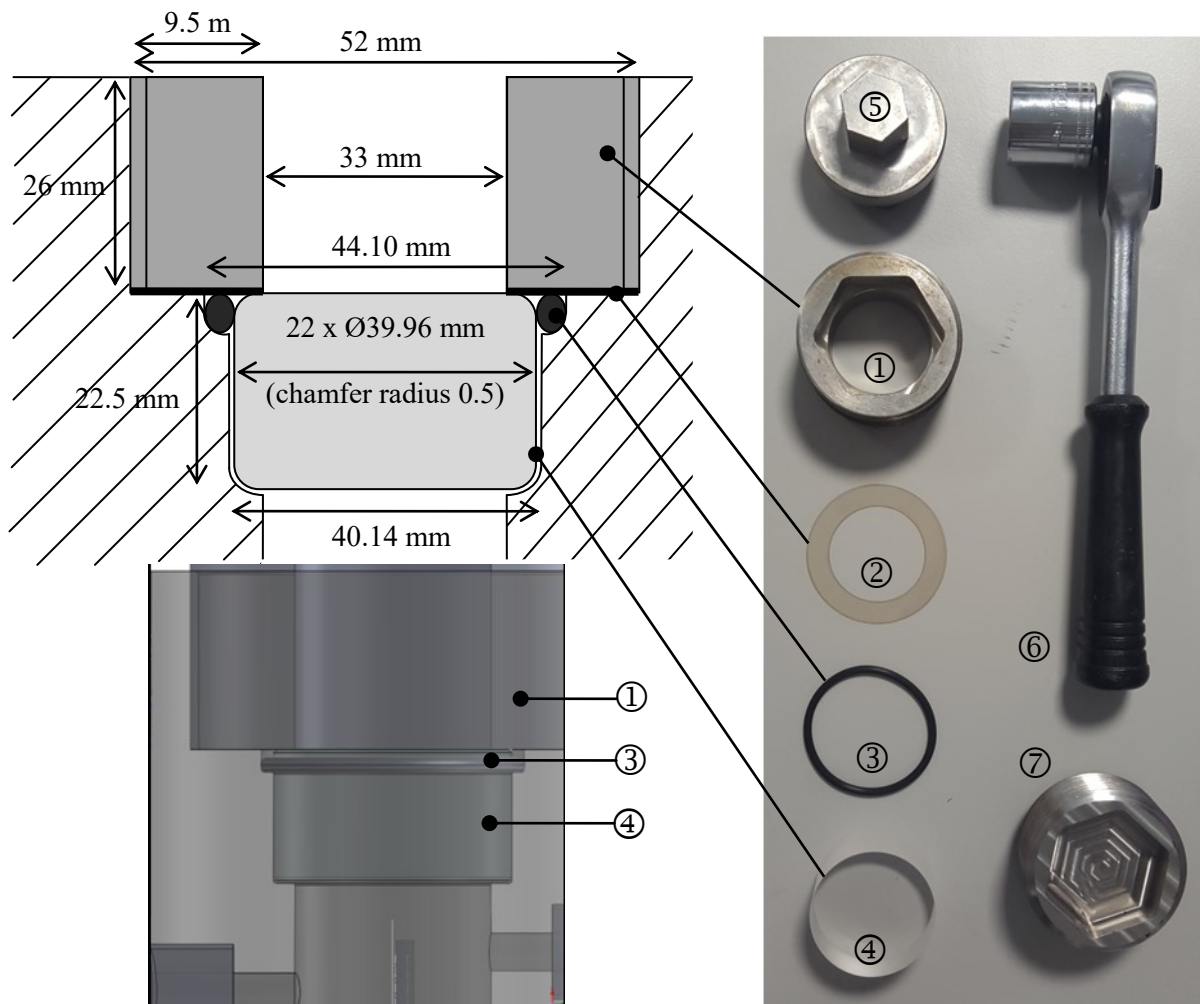


Figure 4.4 *Top left.* Dimensions of the end closure components. *Bottom left.* SolidWorks assembly of the end closure in the vessel. *Right.* Manufactured end closure components and installation tools: ① stainless steel cap, ② PEEK film, ③ Viton O-ring, ④ sapphire window, ⑤ cap installation tool, ⑥ ratchet wrench socket, ⑦ stainless steel blank cap.

4.2.2.3 Pressure Test

The Pressure Test Certificate can be found in Section 8.5 of the Appendix. The vessel assembly was pressure tested at room temperature prior to use, to ensure that the vessel conforms to the requirements under sound engineering practice. As the hydraulic test pressure of 115 MPa was above the maximum limit of the sapphire windows, stainless steel banks were used instead. The vessel was filled with water, and pressurised using a hand pump filled with paraffin oil. The vessel was first proven to be leak-free by pressurising to 11.5 MPa for 15 minutes. Then, the pressure test was conducted at 115 MPa for 30 minutes.

4.2.3 Substrate Adjuster

The engineering drawing and details of the substrate adjuster can be found in Section 8.4 of the Appendix. The design considerations for the substrate adjuster included space limitation within the vessel, sufficient surface area for drops to be formed and spread, accessible for changing substrates, minimum clearance between pressure fittings, stable as the vessel tilts on the tilting base, rotatable to facilitate cleaning, and translatable to reach the capillary tubing. These concerns were addressed by the final substrate adjuster design, which can rotate and move the substrate holder vertically within the view cell. The substrate adjuster contained two rings of ISO bonded NdFeB magnets, one inside the high pressure housing connected to a rod, and one outside the high pressure housing. The magnets were coupled, so when the outer ring was moved, for translation or rotation, the inner ring will follow. The substrate holder inside the view cell was locked with a M2 Hex grub screw on to a rod fixed to the inner ring. Therefore, movement of the inner ring magnet would allow control of substrate holder movement. The ease of access for changing substrates was aided by a set of installation tools, shown in Figure 3.6. For purposes of interfacial tension experiments and the pressure test, plugs were used to block the substrate adjuster ports.

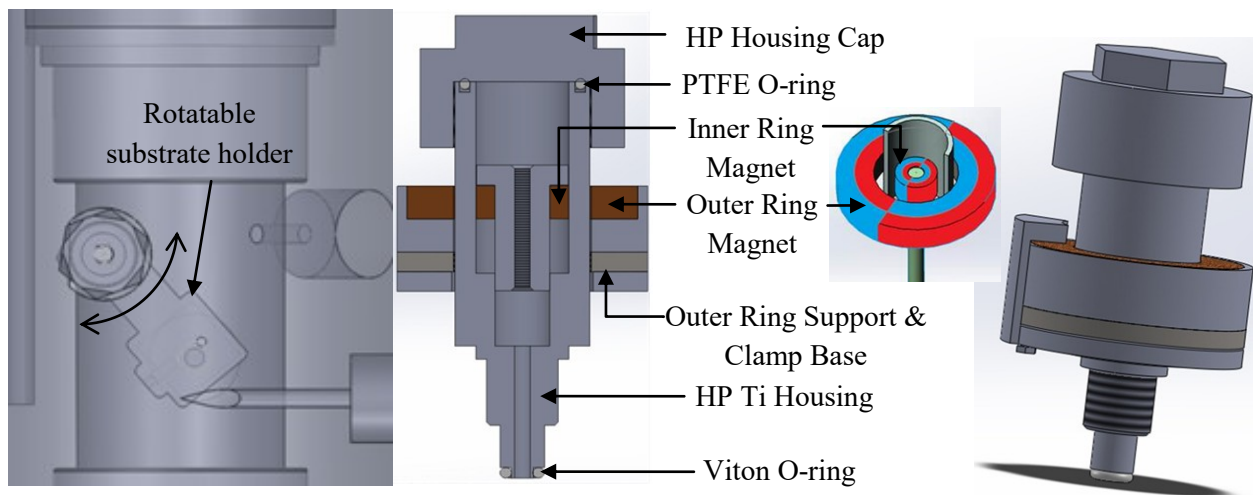


Figure 4.5 *Left.* Bird's-eye view of substrate holder positioning inside the view cell. *Centre.* Cross-section of the substrate adjuster, showing the magnetic coupling. *Right.* SolidWorks model of the substrate adjuster assembly.



Figure 4.6 Substrate adjuster kit: ① Substrate installation tool, ② extended M2 Allen Key, ③ substrate holder installation tool, ④ substrate holder, ⑤ substrate adjuster port plug.

4.2.4 Temperature regulation

The view cell was enclosed in a five-piece close-fitting aluminium-alloy heater shell, with borosilicate windows, insulated on the outside by a jacket of silicone sponge. Four cartridge heaters and an additional Pt100 temperature sensor were accommodated in axial holes bored in the heater shell, and used in conjunction with a proportional-integral-differential (PID) process controller to regulate the temperature. The temperature limit was set at 478 K to protect the vessel. The controller parameters were set by auto-tuning.

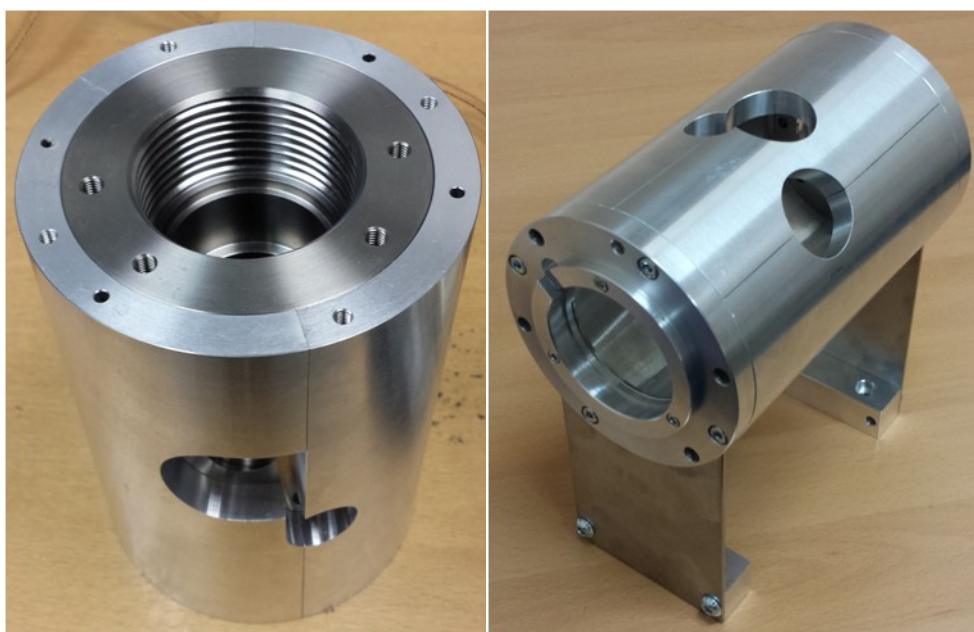


Figure 4.7 *Left.* Heater shell enclosing the view cell. *Right.* Heater shell assembled on to the saddle supports.

4.2.5 Commissioning

The vessel and all pressure fittings were pressurised to 17 MPa with helium, which was the outlet pressure limit of the regulator from the pressurised cylinder, and leak tested with an electronic helium leak detector. The high pressure fittings and vessel assembly downstream of the Quizix pumps were tested to 35 MPa with helium, and 50 MPa with water. A bulls eye level was used to ensure that the tilting base was flat. A standardised spherical and cylindrical calibration device was used to calibrate the length scale of the imaging programme, for a fixed focus and distance between the camera and the capillary tubing. The calibration tool has a diameter of (4.000 ± 0.001) mm. The uncertainty in image resolution was ± 0.5 pixels, which corresponded to an uncertainty in length of ± 0.008 mm. For a typical drop or bubble with diameter of 4 mm, the length scale uncertainty was about 0.2 %.

4.3 Experimental Systems and Conditions

4.3.1 Interfacial Tension

The interfacial tension measurements were carried out for binary systems, involving water and a gas, nitrogen, argon or hydrogen; and ternary systems, involving water and a mixture of carbon dioxide with nitrogen, argon or hydrogen. The conditions studied for the various systems are listed in Table 4.3.

Table 4.3 Interfacial tension systems studied at temperatures T and pressures p in this work.

System	Liquid	Gas	T/K	p/MPa
1	H ₂ O	N ₂	298, 323, 373, 448	2, 5, 10, 20, 30, 40
2	H ₂ O	N ₂ , CO ₂		
3	H ₂ O	Ar	298, 323, 373, 448, 473	2, 5, 10, 15, 20, 25, 30, 40, 50
4	H ₂ O	Ar, CO ₂		
5	H ₂ O	H ₂	298, 323, 373, 448	0.5, 1, 1.5, 2, 3.5, 5, 7.5, 10, 15, 20, 25, 30, 40, 45
6	H ₂ O	H ₂ , CO ₂	298, 323, 373, 448	0.5, 1, 2, 5, 10, 15, 20, 25, 30, 40, 45

4.3.2 Contact Angle

Contact angles of (CO₂ + brine) and (CO₂ + N₂ + brine) systems on calcite surfaces were measured at 333 K and 7 pressures, from (2 to 50) MPa, for a 1 mol·kg⁻¹ NaHCO₃ brine solution, using the dynamic tilting plate method on bubbles. For comparison, the tilting plate measurements were repeated at the same conditions for brine drops on calcite surfaces surrounded by pure CO₂. The conditions studied for the various systems are listed in Table 4.4.

Table 4.4 Contact angle systems studied at temperatures T and pressures p in this work, for a 1 mol·kg⁻¹ NaHCO₃ brine solution, using the tilting plate (TP) method.

System	Brine	Gas	Solid	T/K	p/MPa	Method
1	NaHCO ₃	CO ₂	Calcite	333	2, 5, 10, 20, 30, 40, 50	Bubble, TP
2	NaHCO ₃	CO ₂	Calcite			Drop, TP
3	NaHCO ₃	N ₂ , CO ₂	Calcite			Bubble, TP

4.4 Materials.

The sources and purities of the chemical used are detailed in Table 4.5. The purity and composition of the pure gas or gas mixtures were determined by the gas supplier, BOC. Pure deionised and degassed water (electrical resistivity > 18 MΩ·cm) was used. The sodium bicarbonate salt was purchased from Sigma Aldrich, with mass fraction purity of ≥ 0.995. The salt was dried in the oven at 373 K prior to use. The solution was prepared gravimetrically with relative uncertainties in mass below 0.01 %. The salt purity uncertainty, of about 0.5 %, was greater than the mass measurement uncertainty. The brine solution was vacuum degassed for 20 minutes before use. The Iceland Spar originates from Nuevo Leon, Mexico. The optical calcite has three sets of cleavages, parallel planes of weakness, which facilitate the cleaving of the mineral into smaller samples with naturally smooth surfaces. The samples with suitable smoothness and dimensions were selected for the experiments.

Table 4.5 Description of chemical samples, where x denotes mole fraction of a single substance or a mixture of defined composition and ρ_e denotes electrical resistivity.

Chemical name	Source	Purity	Additional purification
Carbon dioxide	BOC	$x \geq 0.99995$	None
Nitrogen	BOC	$x \geq 0.99998$	None
$[y \text{ CO}_2 + (1 - y) \text{ N}_2]$ $y = (0.5120 \pm 0.0050)$	BOC	$x \geq 0.99995$	None
Argon	BOC	$x \geq 0.99998$	None
$[y \text{ CO}_2 + (1 - y) \text{ Ar}]$ $y = (0.4973 \pm 0.0050)$	BOC	$x \geq 0.99995$	None
Hydrogen	BOC	$x \geq 0.99990$	None
$[y \text{ CO}_2 + (1 - y) \text{ H}_2]$ $y = (0.300 \pm 0.015)$	BOC	$x \geq 0.99990$	None
Water	Millipore Direct-Q UV3 apparatus	$\rho_e \geq 18 \text{ M}\Omega\cdot\text{cm}$ at $T = 298 \text{ K}$	Vacuum degassed
Sodium bicarbonate	Sigma Aldrich	$x \geq 0.995$	Dried in oven at 373 K
Optical calcite	Mexico	Iceland Spar	Clean with DI water, dry at 408 K for 1.5 hours

4.5 Experimental Procedure

4.5.1 Interfacial Tension

Prior to starting a set of experiments, the seals were replaced, and the wetted-components were cleaned by flushing, first with hexane, isopropanol, then water; followed by heating to 423 K, then cooled to room temperature; leak-tested with helium; and lastly evacuated. The view cell was first heated to the set experimental temperature. Pure degassed water was injected to form an aqueous phase in the bottom of the view cell. Pressurised non-aqueous components were slowly injected into the view cell, up to the set experimental pressure. The cell contents were stirred for at least 10 minutes to reach phase equilibrium. Through the top inlet port capillary tubing, a water pendant drop was formed. After creating a new drop, a few minutes was required to establish diffusive equilibrium between the drop and the bulk non-aqueous phase. The drop image was captured under back illumination with a video camera for 500 seconds, and analysed with commercial software (Advanced DROPimage, Ramé-Hart Instrument Co.). The axisymmetric drop shape analysis (ADSA) performed was based on the integration of the Young-Laplace equation. Two drops were discarded prior to creating a new drop for analysis, with $0.2 < \beta < 0.4$, and this was repeated for at least 3 measured drops. The pressure was then increased to the next set-point, and the measurement process repeated.

4.5.2 Contact Angle

The system was cleaned by flushing with hexane, isopropanol, and then water; followed by heating to 423 K, and then cooled to room temperature. The edges of a cleaved calcite sample were wrapped in PTFE tape, whilst keeping clear of the measured surface, to form a tight-fitting mould. The sample was locked in the substrate holder with a grub screw. The view cell window was opened and the substrate holder was locked onto the substrate holder rod. The camera was tilted about 1° to 3° towards the substrate surface, down for drops and up for bubbles. The sample was illuminated and checked to be flat against the imaging system baseline. The window was closed and the system was leak-tested with helium. The calcite was cleaned by flushing with deionised water, dried at 408 K for

1.5 hours, and then cooled to room temperature. The system was flushed with degassed brine. The view cell was then heated to 333 K.

For bubble measurements, sufficient brine was injected to cover the sample, and pressurised non-aqueous components slowly injected to reach the set experimental pressure. The view cell contents were stirred to reach phase equilibrium. A bubble was created from the bottom inlet port. The substrate holder was adjusted to catch the bubble, and moved up away from the capillary tubing after the bubble separated from the capillary tube. The back illuminated image was captured with a video camera for 90 seconds, from 0 ° to 90 ° tilt. The images were analysed every 0.2 seconds in the commercial software (Advanced DROPimage, Ramé-Hart Instrument Co.), by numerical extrapolation of the profile at the contact point using a circular-fit fitting function, as described in the Profile Fitting Methods of Section 2.2. After a measurement, the tilting base was returned to 0 °, and the substrate holder rotated to remove the bubble. A new bubble was formed and the measurement was repeated for at least 3 times. The pressure was increased up to the next set-point, and the measurement process repeated.

For drop measurements, brine was injected to form an aqueous layer at the bottom of the cell, and pressurised non-aqueous components slowly injected to reach the set experimental pressure. The contents were stirred to reach phase equilibrium. A drop was created from the top inlet port, and the substrate holder was adjusted to catch the drop. The substrate holder was then moved away from the capillary tubing for measurement, from 0 ° to 90 ° tilt. After a measurement, the drop was washed off the surface by dipping into the pool of brine. A new drop was formed and measured, and repeated for at least 3 drops. The pressure was then increased up to the next set-point, and the measurement process repeated.

4.6 Validation

4.6.1 Interfacial Tension

The pendant-drop method was validated by measurement of the surface tension of water at room temperature, shown in Table 4.6. This was in close agreement with the value obtained from the IAPWS recommended correlation by means of the REFPROP 9.1 software [188, 190, 231].

Table 4.6 Water surface tension measurements as compared to IAPWS recommended correlation values, and the experimental systems for which the validation applies.

T/K	Measured Surface Tension/ $mN \cdot m^{-1}$	Reference Surface Tension/ $mN \cdot m^{-1}$	Applicable Systems
298.44	71.9 ± 0.1	71.93 ± 0.05	$N_2 + H_2O$, $N_2 + CO_2 + H_2O$
298.48	72.0 ± 0.1	71.92 ± 0.05	$Ar + H_2O$, $Ar + CO_2 + H_2O$
298.07	72.1 ± 0.1	71.99 ± 0.05	$H_2 + H_2O$, $H_2 + CO_2 + H_2O$

4.6.2 Contact Angle

The IFP rig has been validated for static and dynamic contact angle measurements via comparison with 28 sources of PTFE-water-air results reported in literature [50, 232], as shown in Figure 4.8. The PTFE sample was cleaned with detergent and rinsed with distilled water. The static contact angle was measured to be 109 ± 3 °, by the sessile drop method, agreeing with literature results. A reasonable measurement error would be within ± 5 °. The tilting plate method was used to measure the advancing and receding angles. The maximum angle was measured to be 124 ± 3 °, agreeing with literature results. The minimum angle, 20.0 °, was significantly lower than those reported by Law and Zhao

[50], 91.9 °, Wu [232], 106 °, Sperati [232], 92 °, and Brewis [232], 90 °. The tilt angle which produced this result was 87 °.

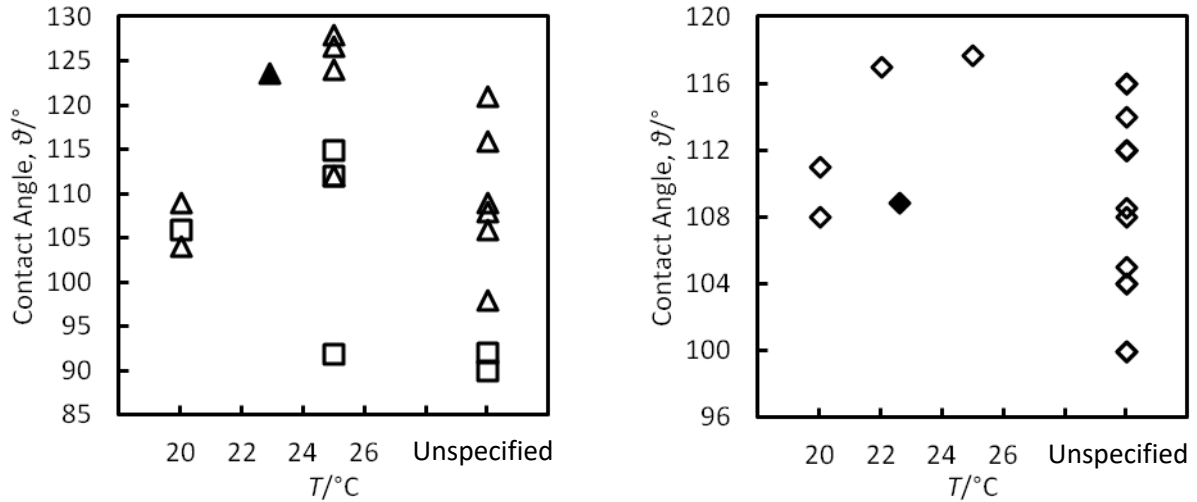


Figure 4.8 *Left.* PTFE-air dynamic contact angles from literature [50, 232]: advancing angles, \triangle , and receding angles, \square ; compared to the maximum angle, \blacktriangle , measured in this work by the tilting plate method. *Right.* PTFE-air static contact angles from literature [232], \diamond ; compared to the static contact angle measured in this work by the sessile drop method, \blacklozenge .

As suggested by Law and Zhao [50], the receding contact line may never reach mechanical equilibrium in the tilting base method. A comparison of the expansion-contraction method with the tilting base method reveals that the advancing angles measured agree, whereas the receding angles can be significantly different [66]. It was also observed here that as the trail edge drop shape changed, sometimes the trail edge contact point could not be located. Therefore, the tilting base method was not suitable for measuring the receding angle for drops.

4.7 Data Analysis

4.7.1 Drop Image Analysis

The Ramé-Hart DropImage Advanced software was selected for the digital image analysis. The theory behind the axisymmetric drop shape analysis method for pendant drops has been outlined in Section 2.2. For numerical solution algorithms and equations specific to the DropImage Advanced software, these are detailed in papers published by Hansen et al. [233, 234]. The Kutta-Merson's numerical integration algorithm with automatic step length adjustment was used in solving eq. 2.25 to 2.28, to calculate the possible theoretical profiles, from a viable range of β values between -0.55 and 10^{20} . The maximum relative error in the numerical integration was 10^{-4} . The imaged profiles were measured by cubic interpolation. The parameters, b and β , were correlated by curves that were fitted with linear polynomials by the method of least squares.

For pendant drops that are sufficiently long:

$$\beta = -0.12836 + 0.7577\sigma - 1.7713\sigma^2 + 0.5426\sigma^3 \quad (4.6)$$

where $\sigma = d_e/d_s$, d_e is the maximum diameter of the drop and d_s is the diameter of the drop at a distance of d_e from the drop apex.

With the same data, a function for $d_e/2b$ is found:

$$d_e/2b = 0.9987 - 0.1971\beta - 0.0734\beta^2 - 0.34708\beta^3 \quad (4.7)$$

For sessile drops, or pendant drops that are too short to measure d_s , b and β are replaced by the drop height H , and a transformed shape parameter B , respectively. This is described by the following relations:

$$\gamma = \Delta\rho g H^2 / B \quad (4.8)$$

$$R = d_e / 2 \quad (4.9)$$

$$\xi = H / R \quad (4.10)$$

$$B = \beta (H / b)^2 = f(\xi) \quad (4.11)$$

$$H / b = g(\xi) \quad (4.12)$$

$$\beta = f(\xi) / g(\xi)^2 \quad (4.13)$$

Polynomial functions of $f(\xi)$ and $g(\xi)$ are then used to calculate b and β from measurement of H and R .

The detection of the drop profile involved an edge-tracing filter routine, with increased subpixel accuracy than global thresholding and maximum gradient techniques. The programme used a local threshold and interpolation algorithm, where the coordinates of the drop profile were located by linear interpolation to a specific fraction, between the local maximum and minimum light intensity. The value of this fraction had significant influence on the final result, and comparing against known surface tensions would indicate the optimal light intensity value. Once a point was found, the next point was limited to the nearest point on the next line. At the bottom of the drop, the search direction was altered from horizontal to vertical. Drop profiles normally consist of 700 to 1000 points, requiring 2 to 3 seconds to complete the calculation. The same filter routine was used for contour detection in interfacial tension and contact angle measurements.

The contact angle measurement was independent of magnification, but depends on the aspect ratio. The Ramé-Hart DropImage Advanced software evaluated the contact angle by two different image analysis methods. The first was a numerical curve fitting with extrapolation at the contact point, where only a part of the drop or bubble was used. Various curve fitting methods were available, as described in the Profile Fitting Methods of Section 2.2. The circular fit was usually the most reliable. Both sides of the drop or bubble were measured independently. This method was suitable for the expansion-contraction method, where the drop profile was disturbed by the needle. The second method was the Young-Laplace method, where the theoretical profile was used to fit to the drop or bubble profile. Only an average of the angles on both sides was calculated, as the theoretical profile was always symmetrical. It was required that the whole drop to be visible. The first method, with circular fitting, was selected for these tilting base contact angle measurements.

4.7.2 Interfacial Tension

The interfacial tension measured changed with time, and the most suitable time frame for analysis was when diffusive equilibrium between the drop and the surrounding fluid interface had been established, as described by Georgiadis et al. [142]. The diffusion coefficient and solubility of N_2 [235], Ar [236], and H_2 [236] in water were considered in these calculations. Data analysis commenced at $t = 200$ s, continuing until the end of the experimental run at $t = 500$ s.

The interfacial tension was evaluated from the relation

$$\gamma = \Delta\rho g b^2 / \beta \quad (2.39)$$

where $\Delta\rho$ is the density difference between the two fluid phases, g is the gravitational acceleration, b is the radius of curvature at the apex of the drop, and β is a dimensionless shape parameter. R_0 and β are determined in the imaging software. The density difference between the aqueous and non-aqueous phases was calculated from

$$\Delta\rho = \rho_A - \rho_N \quad (4.14)$$

where ρ_A is the aqueous phase density, and ρ_N is the non-aqueous phase density. The presence of water in the non-aqueous phase was neglected as the composition was small at the temperature and pressures investigated. The non-aqueous components studied in this work generally have low solubility in water. However, the approximation of using pure component bulk phase densities instead of equilibrium phase densities of the mixture can introduce unnecessary errors in the calculated IFT, especially at conditions near to a barotropic transition [106]. Therefore, the presence of non-aqueous components in the aqueous phase was accounted for in the density calculations.

The non-aqueous phase was described by the Peng-Robinson (PR) equation of state. The aqueous phase was described by an extended form of the Henry's law combined with the non-random two-liquid (NRTL) [237] activity-coefficient model, where the parameters for the different gases are summarised in Table 4.8. This combined PR-NRTL model was used to find the equilibrium phase compositions of the mixture, via isochoric flash calculations from Whitson and Michelsen [238]. For the binary systems, the NRTL interaction parameters of N_2 , Ar and H_2 were set to zero. The densities of the non-aqueous phase were treated as if it was a pure component, and calculated from the EoS listed in Table 4.7. For ternary systems involving CO_2 , the CO_2 - H_2O NRTL interaction parameter was obtained from Hou et al. [239], whereas those involving N_2 , Ar and H_2 were set to zero. The initial phase compositions were required as inputs, and were estimated from the amount of fluids injected into the view cell. The non-aqueous phase density was calculated from the GERG-2008 mixture model, and the EoS of the pure components listed in Table 4.7, as implemented in REFPROP 9.1 software [240].

The equilibrium composition of the aqueous phase and the partial molar volumes of the components, V_i , were used to calculate the molar volume of the mixture, V_{mix} :

$$V_{\text{mix}} = \sum_{i=1}^N V_i x_i \quad (4.15)$$

where N is the number of components. The density of the aqueous phase was the inverse of the mixture molar volume. The partial molar volume of H_2 solutes in water at was taken as the 298.15 K value for all experimental conditions from Moore et al., 1982 [241]. It was assumed that the dissolved concentration is low and has limited uncertainty in the calculated aqueous phase density. The necessary parameters of the density calculation procedure for all mixtures are listed in Tables 4.7 and 4.8. The calculation procedure is summarised in Figure 4.9.

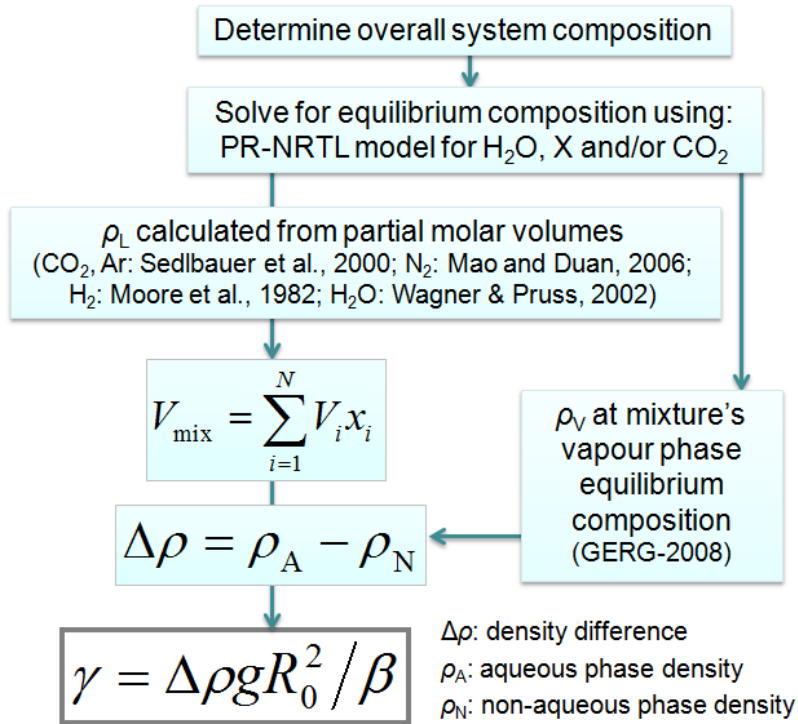


Figure 4.9 Density difference calculation procedure, where X = N₂, Ar, or H₂.

Table 4.7 Thermodynamic properties of the pure components for the PR EoS: critical temperature T_c , critical pressure p_c and acentric factor ω of the pure components studied in this work [190]. Equations of state (EoS) and partial molar volume models used in the calculation of the phase densities.

Component	T_c/K	p_c/MPa	ω	EoS	Partial Molar Volume
N ₂	126.20	3.3900	0.03900	Span et al., 2000 [242]	Mao and Duan [243]
Ar	150.86	4.898	-0.004	Tegeler et al., 1999 [244]	Sedlbauer et al. [245]
H ₂	33.145	1.2964	-0.219	Leachman et al., 2009 [246]	Moore et al. 1982 [241]
CO ₂	304.13	7.3773	0.22394	Span & Wagner, 1996 [247]	Sedlbauer et al. [245]
H ₂ O	647.10	22.064	0.34430	Wagner & Pruss, 2002 [248]	Wagner & Pruss, 2002 [248]

Table 4.8 Binary interaction parameters k_{ij} and Henry's constants H_{ij} for use in the PR-NRTL model, where $p_{\text{H}_2\text{O}}^{\text{sat}}$ is the vapour pressure of pure water at temperature T , a and b are PR EoS parameters.

System	Parameter Correlations	Ref.
	$k_{ij} = 0.33810 - 0.46426 \left(\frac{T_0}{T} \right) \quad (4.16)$	
CO ₂ -H ₂ O	$\ln(H_{ij} / \text{MPa}) = -6.1384 + 42.842 \left(\frac{T_0}{T} \right) - 44.358 \left(\frac{T_0}{T} \right)^2 + 12.786 \left(\frac{T_0}{T} \right)^3 \quad (4.17)$ $T_0 = 298.15 \text{ K}$	[239]
	$k_{ij} = -2.1008 + 5.82466 \times 10^3 T + 3.7711 \times 10^6 T^2 \quad (4.18)$	[249]
N ₂ -H ₂ O	$\ln(H_{ij} / \text{MPa}) = -\frac{9.67578}{T_r} + \frac{4.72162}{T_r} (1-T_r)^{0.355} \quad (4.19)$	[250]
	$+ \frac{11.70585}{T_r^{0.41}} \exp(1-T_r) + \ln(p_{\text{H}_2\text{O}}^{\text{sat}} / \text{MPa})$ $T_r = T / (647.096 \text{ K}) \quad (4.20)$	
	$k_{ij} = 0.03 \text{ K} / T \quad (251)$	[251]
Ar-H ₂ O	$\ln(H_{ij} / \text{MPa}) = -\frac{8.40954}{T_r} + \frac{4.29587}{T_r} (1-T_r)^{0.355} \quad (4.21)$	[250]
	$+ \frac{10.52779}{T_r^{0.41}} \exp(1-T_r) + \ln(p_{\text{H}_2\text{O}}^{\text{sat}} / \text{MPa})$	
	$k_{ij} = \frac{830.8 \left(\frac{T_0}{T} \right)^{-1.166} - \left(\frac{\sqrt{a_i(T)}}{b_i} - \frac{\sqrt{a_j(T)}}{b_j} \right)^2}{2 \frac{\sqrt{a_i(T) \cdot a_j(T)}}{b_i \cdot b_j}} \quad (4.22)$	[252]
H ₂ -H ₂ O	$\ln(H_{ij} / \text{MPa}) = -\frac{4.73284}{T_r} + \frac{6.08954}{T_r} (1-T_r)^{0.355} \quad (4.23)$	[250]
	$+ \frac{6.06066}{T_r^{0.41}} \exp(1-T_r) + \ln(p_{\text{H}_2\text{O}}^{\text{sat}} / \text{MPa})$	
CO ₂ -N ₂	$k_{ij} = -0.097 \quad (253)$	[253]
CO ₂ -Ar	$k_{ij} = -0.031 \quad (253)$	[253]
	$k_{ij} = \frac{265.9 \left(\frac{T_0}{T} \right)^{0.009} - \left(\frac{\sqrt{a_i(T)}}{b_i} - \frac{\sqrt{a_j(T)}}{b_j} \right)^2}{2 \frac{\sqrt{a_i(T) \cdot a_j(T)}}{b_i \cdot b_j}} \quad (4.24)$	[252]

5 Results - Interfacial Tension

The interfacial tension measurements of the binary systems ($\text{N}_2 + \text{H}_2\text{O}$), ($\text{Ar} + \text{H}_2\text{O}$), and ($\text{H}_2 + \text{H}_2\text{O}$), and ternary systems ($\text{CO}_2 + \text{N}_2 + \text{H}_2\text{O}$), ($\text{CO}_2 + \text{Ar} + \text{H}_2\text{O}$) and ($\text{CO}_2 + \text{H}_2 + \text{H}_2\text{O}$), are reported at pressures of (0.5 to 50.0) MPa, and temperatures of (298.15 to 473.15) K in the following sections of this chapter.

The standard relative uncertainties $u_r(\gamma)$ of the experimental data were estimated from the relation:

$$u_r(\gamma)^2 = \left[\frac{1}{\gamma} \left(\frac{\partial \gamma}{\partial T} \right)_p u(T) \right]^2 + \left[\frac{1}{\gamma} \left(\frac{\partial \gamma}{\partial p} \right)_T u(p) \right]^2 + \left[\frac{u(\Delta \rho)}{\Delta \rho} \right]^2 + \left[\frac{\sigma(\gamma)}{\gamma} \right]^2 \quad (5.1)$$

The expanded uncertainties at 95 % confidence are 0.05 K for temperature; 0.07 MPa for pressure; $0.019 \cdot \gamma$ for interfacial tension in the ($\text{N}_2 + \text{H}_2\text{O}$) system; $0.016 \cdot \gamma$ for interfacial tension in the ($\text{Ar} + \text{H}_2\text{O}$) system; $0.017 \cdot \gamma$ for interfacial tension in the ($\text{H}_2 + \text{H}_2\text{O}$) system; $0.032 \cdot \gamma$ for interfacial tension in the ($\text{CO}_2 + \text{N}_2 + \text{H}_2\text{O}$) system; $0.018 \cdot \gamma$ for interfacial tension in the ($\text{CO}_2 + \text{Ar} + \text{H}_2\text{O}$) system; and $0.017 \cdot \gamma$ for interfacial tension in the ($\text{CO}_2 + \text{H}_2 + \text{H}_2\text{O}$) system.

5.1 Binary Systems

For ease of comparing with literature values, empirical correlations are developed for the binary systems studied, optimised with the Eureka Modelling Engine [254, 255].

$$\gamma / (\text{mN} \cdot \text{m}^{-1}) = a_1 \left(\frac{p}{\text{MPa}} \right)^2 + a_2 \left(\frac{T}{\text{K}} \right)^2 + a_3 \left(\frac{p}{\text{MPa}} \right) + a_4 \left(\frac{p}{\text{MPa}} \right) + a_5 \left(\frac{T}{\text{K}} \right) \left(\frac{p}{\text{MPa}} \right) + a_6 \quad (5.2)$$

For the ($\text{N}_2 + \text{H}_2\text{O}$) system, this model is valid at $298.15 \leq T/\text{K} \leq 448.15$ K and $p \leq 40$ MPa, and the six parameters are listed in Table 5.1. The absolute average deviation is $0.42 \text{ mN} \cdot \text{m}^{-1}$ for the 84 measured data points; as shown in Figure 5.1, all points are fitted within their uncertainties. The literature results of Wiegand and Franck [256], Tian et al. [180], Yan et al. [181], Massoudi and King [146], and Slowinski *et al.* [143] are generally predicted by eq. (5.2) to within $3.0 \text{ mN} \cdot \text{m}^{-1}$.

For the ($\text{Ar} + \text{H}_2\text{O}$) system, this model is valid at $298.15 \leq T/\text{K} \leq 473.15$ K and $p \leq 50$ MPa, and the six parameters are listed in Table 5.1. The absolute average deviation is $0.29 \text{ mN} \cdot \text{m}^{-1}$ for the 135 measured data points; as shown in Figure 5.3, all points are fitted within their uncertainties. The literature results of Wiegand and Franck [256], and Massoudi and King [146] are generally predicted by eq. (5.2) to within $3.0 \text{ mN} \cdot \text{m}^{-1}$.

For the ($\text{H}_2 + \text{H}_2\text{O}$) system, this model is valid at $298.15 \leq T/\text{K} \leq 448.15$ K and $p \leq 45$ MPa, and the six parameters are listed in Table 5.1. The absolute average deviation is $0.17 \text{ mN} \cdot \text{m}^{-1}$ for the 129 measured data points; as shown in Figure 5.5, all points are fitted within their uncertainties. The literature results of Massoudi and King [146], and Slowinski *et al.* [143] are generally predicted by eq. (5.2) to within $2.1 \text{ mN} \cdot \text{m}^{-1}$.

Table 5.1 Fitting parameters of the empirical model (5.2) for the interfacial tension measurements.

System	a_1	a_2	a_3	a_4	a_5	a_6	σ	$10^2 \Delta_{AAD}$
N ₂ -H ₂ O	4.316×10^{-3}	-2.482×10^{-4}	0	-0.8826	1.322×10^{-3}	93.71	0.079	0.41
Ar-H ₂ O	3.234×10^{-3}	-2.500×10^{-4}	0	-0.8536	1.259×10^{-3}	94.02	0.063	0.56
H ₂ -H ₂ O	0	-2.619×10^{-4}	-0.02830	-0.2601	5.431×10^{-4}	96.28	0.055	0.29

5.1.1 (N₂ + H₂O) System

Four isotherms at temperatures between (298 and 448) K have been measured in the (N₂ + H₂O) system over a range of pressures from (2 to 40) MPa. The results are given in Table 5.2 and Figure 5.1. The relative standard deviation $\sigma(\gamma)/\gamma$ of the IFT data at each state point was evaluated from three to five repeated measurements and the average was found to be 0.2 %; in all cases it was < 0.7 %. The standard relative uncertainties $u_r(\gamma)$ were then calculated from eq. (5.1). Reliable measurements of the liquid and vapour phase densities under the conditions of interest are not available. To estimate the uncertainty $u(\Delta\rho)$ of the density difference, the calculated values of $\Delta\rho$, obtained with the PR-NRTL model and the mixture model in the REFPROP 9.1 database incorporating the equations of state of the pure components [188, 240, 242, 257], were compared with the density difference between the pure substances at the same temperature and pressure. The maximum difference in the density differences is 0.7 %, and the average absolute deviation is 0.2 %. Overall, the relative uncertainty of interfacial tension of all state points is 0.9 %, and the expanded relative uncertainty at 95 % confidence is 1.9 %.

Table 5.2 Interfacial tension γ for (N₂ + H₂O) at temperatures T and pressures p , with calculated density difference $\Delta\rho$.^a

p/MPa	T/K	$\gamma/\text{mN}\cdot\text{m}^{-1}$	$\Delta\rho/\text{kg}\cdot\text{m}^{-3}$	T/K	$\gamma/\text{mN}\cdot\text{m}^{-1}$	$\Delta\rho/\text{kg}\cdot\text{m}^{-3}$
2	298.24	71.1	974.1	373.25	58.2	941.6
5	298.19	69.3	943.0	373.23	57.2	916.5
10	298.15	66.9	888.6	373.15	55.6	875.1
20	298.25	63.2	792.2	373.15	53.3	799.8
30	298.17	60.8	712.8	373.13	51.2	738.2
40	298.20	59.2	651.8	373.13	50.4	685.6
2	323.22	67.1	967.9	448.02	43.3	877.7
5	323.22	65.7	938.6	447.98	42.8	858.3
10	323.21	63.5	888.1	448.05	41.9	826.2
20	323.21	60.4	800.8	448.02	40.5	766.7
30	323.13	58.2	728.9	448.03	39.5	715.8
40	323.13	56.5	670.4	448.00	38.9	671.2

^a Expanded uncertainties at 95 % confidence are $U(T) = 0.05$ K, $U(p) = 70$ kPa, and $U(\gamma) = 0.019\gamma$.

The interfacial tensions of the (N₂ + H₂O) system are observed to decrease with increasing pressure and temperature. The interfacial tension data are compared with the measurements of Wiegand and Franck [179], Tian et al. [258], Yan et al. [259], Massoudi and King [146], and Slowinski *et al.* [143] under overlapping p - T conditions, and the agreement is within $3.0 \text{ mN}\cdot\text{m}^{-1}$.

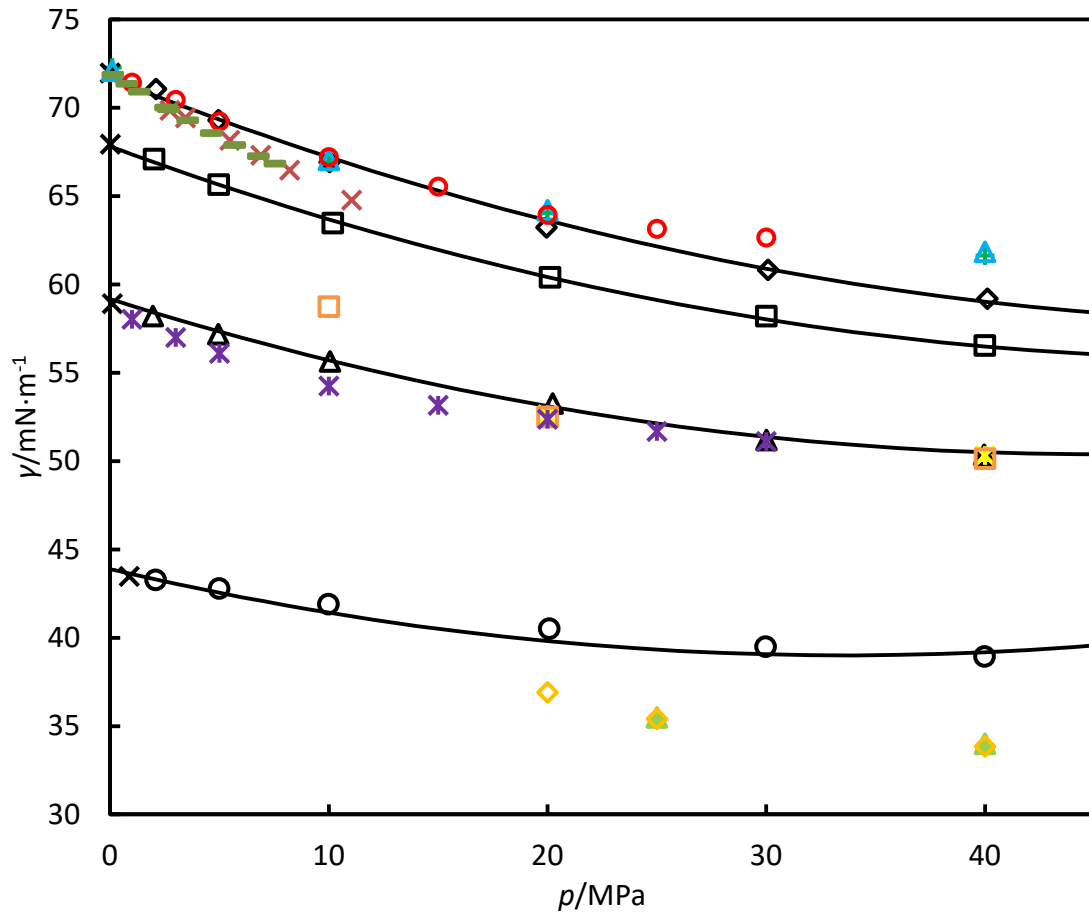


Figure 5.1 Interfacial tensions γ at various pressures p for the $(\text{N}_2 + \text{H}_2\text{O})$ system, along four isotherms: \diamond , 298 K; \square , 323 K; \triangle , 373 K; \circ , 448 K; —, Eq. (5.2). Interfacial tension measurements within the conditions studied in the present work, from Wiegand and Franck [260] at $+$, 298 K, $*$, 373 K, and \blacktriangle , 473 K; Tian et al. [258] at \triangle , 298 K, \square , 373 K, and \diamond , 473 K; Yan et al. [259] at \circ , 298 K and $*$, 373 K; Massoudi and King [146] at $-$, 298 K; and Slowinski *et al.* [143] at \times , 298 K. Surface tension of pure water, \times , as implemented in REFPROP 9.1 [188, 240].

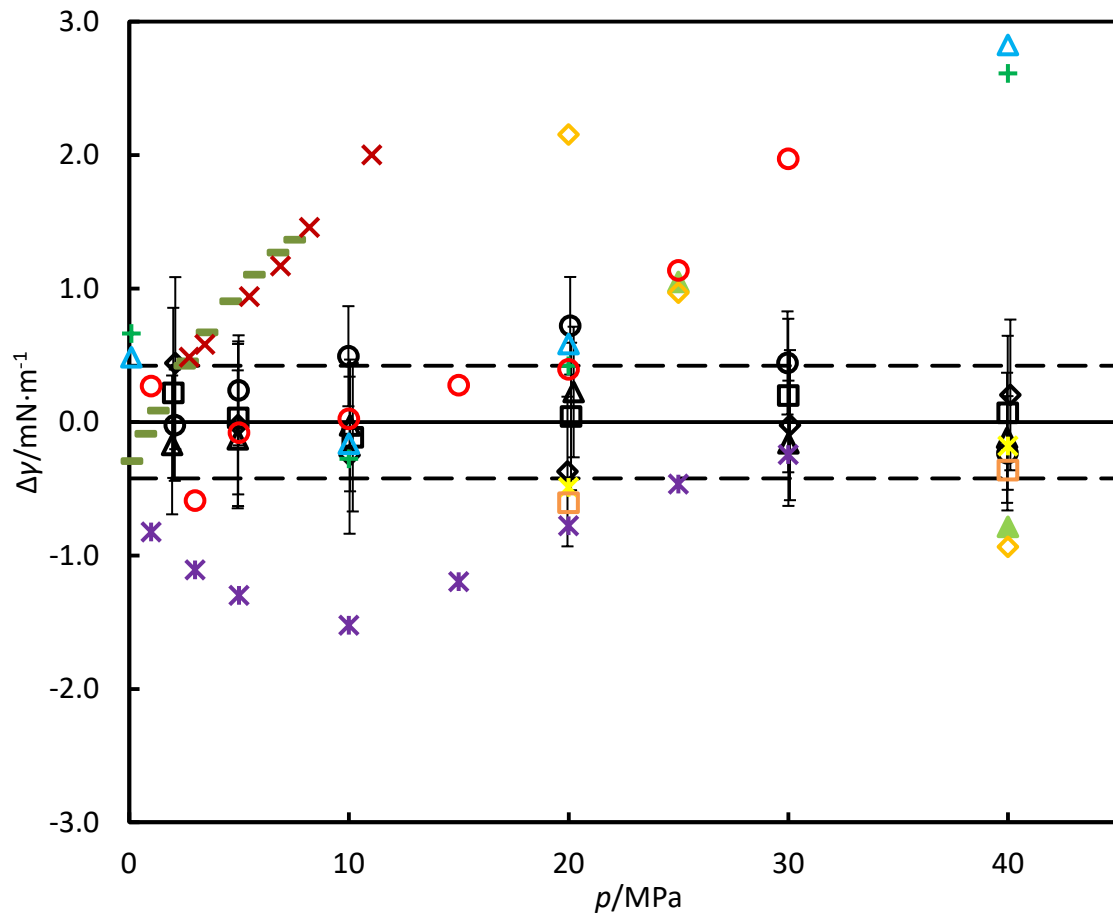


Figure 5.2 Difference in interfacial tension measurements of the ($\text{N}_2 + \text{H}_2\text{O}$) system from Eq. (5.2) at four isotherms: \diamond , 298 K; \square , 323 K; \triangle , 373 K; and \circ , 448 K. Deviations of the fitting equation from literature data: Wiegand and Franck [260] at $+$, 298 K, $*$, 373 K, and \blacktriangle , 473 K; Tian et al. [258] at \triangle , 298 K, \square , 373 K, and \diamond , 473 K; Yan et al. [259] at \circ , 298 K and $*$, 373 K; Massoudi and King [146] at $-$, 298 K; and Slowinski *et al.* [143] at \times , 298 K. Error bars show the expanded uncertainty of the measured data. Dashed lines show the absolute average deviation of the model.

5.1.2 (Ar + H₂O) System

Five isotherms at temperatures between (298 and 473) K were measured in the (Ar + H₂O) system over a range of pressures from (2 to 50) MPa. The results are given in Table 5.3 and Figure 5.3. The relative standard deviation $\sigma(\gamma)/\gamma$ of the IFT data at each state point was evaluated from three repeated measurements and the average was found to be 0.2 %; in all cases it was < 0.5 %. The standard relative uncertainties $u_r(\gamma)$ of the interfacial tensions were estimated from eq. (5.1). Reliable measurements of the liquid and vapour phase densities under the conditions of interest are not available. As a measure of the possible uncertainty of $\Delta\rho$, the density difference calculated with the PR-NRTL model and the mixture model in the REFPROP 9.1 database incorporating the equations of state of the pure components [188, 240, 244, 257], were compared with the density difference between the pure substances at the same temperature and pressure. The maximum absolute difference of $\Delta\rho$ was found to be 0.9 %, and average absolute difference to be 0.3 %. Finally, the relative uncertainty of interfacial tension of all state points was estimated to be 0.8 %, so that the expanded relative uncertainty at 95 % confidence is 1.6 %.

Table 5.3 Interfacial tension γ for (Ar + H₂O) at temperatures T and pressures p , with calculated density difference $\Delta\rho$.^a

p/MPa	T/K	$\gamma/\text{mN}\cdot\text{m}^{-1}$	$\Delta\rho/\text{kg}\cdot\text{m}^{-3}$	p/MPa	T/K	$\gamma/\text{mN}\cdot\text{m}^{-1}$	$\Delta\rho/\text{kg}\cdot\text{m}^{-3}$
2	298.00	71.6	965.3	25	373.31	51.6	657.8
5	297.99	69.7	916.5	30	373.29	50.8	605.0
10	298.00	67.4	832.9	40	373.27	49.3	510.2
15	298.01	65.3	748.7	50	373.30	48.2	430.0
20	298.02	63.3	665.1	2	448.12	43.1	871.6
25	298.02	61.9	590.7	5	448.05	42.5	841.7
30	298.02	60.7	522.0	10	448.07	41.3	792.4
40	298.02	58.6	405.9	15	448.11	40.3	744.4
51	298.04	57.0	316.7	20	448.08	39.5	698.1
2	323.14	67.1	958.8	25	448.07	38.8	653.9
5	323.16	65.7	914.2	30	448.02	38.3	612.3
10	323.17	63.2	839.1	40	448.04	37.3	534.4
15	323.17	61.1	764.4	50	448.06	36.6	464.7
20	323.19	59.4	692.5	2	473.70	37.3	843.8
25	323.17	57.9	624.6	5	473.69	36.5	815.9
30	323.15	56.5	561.2	10	473.72	35.6	770.2
40	323.17	54.5	457.0	15	473.72	34.8	725.4
50	323.11	53.3	366.9	20	473.74	34.1	682.9
2	373.25	58.5	933.3	25	473.76	33.7	642.7
5	373.25	57.2	896.3	30	473.77	33.1	602.8
10	373.28	55.5	833.6	40	472.90	32.9	531.0
15	373.27	53.9	772.4	45	472.78	32.8	500.1
20	373.29	52.7	714.0				

^a Expanded uncertainties at 95 % confidence are $U(T) = 0.05$ K, $U(p) = 70$ kPa, and $U(\gamma) = 0.016\gamma$.

As expected, the interfacial tensions of the (Ar + H₂O) system are observed to decrease with increasing pressure and temperature. When the interfacial tension data are compared with those of

Wiegand and Franck [256], and Massoudi and King [146] at overlapping p - T conditions, the agreement is found to be within about $2.0 \text{ mN}\cdot\text{m}^{-1}$.

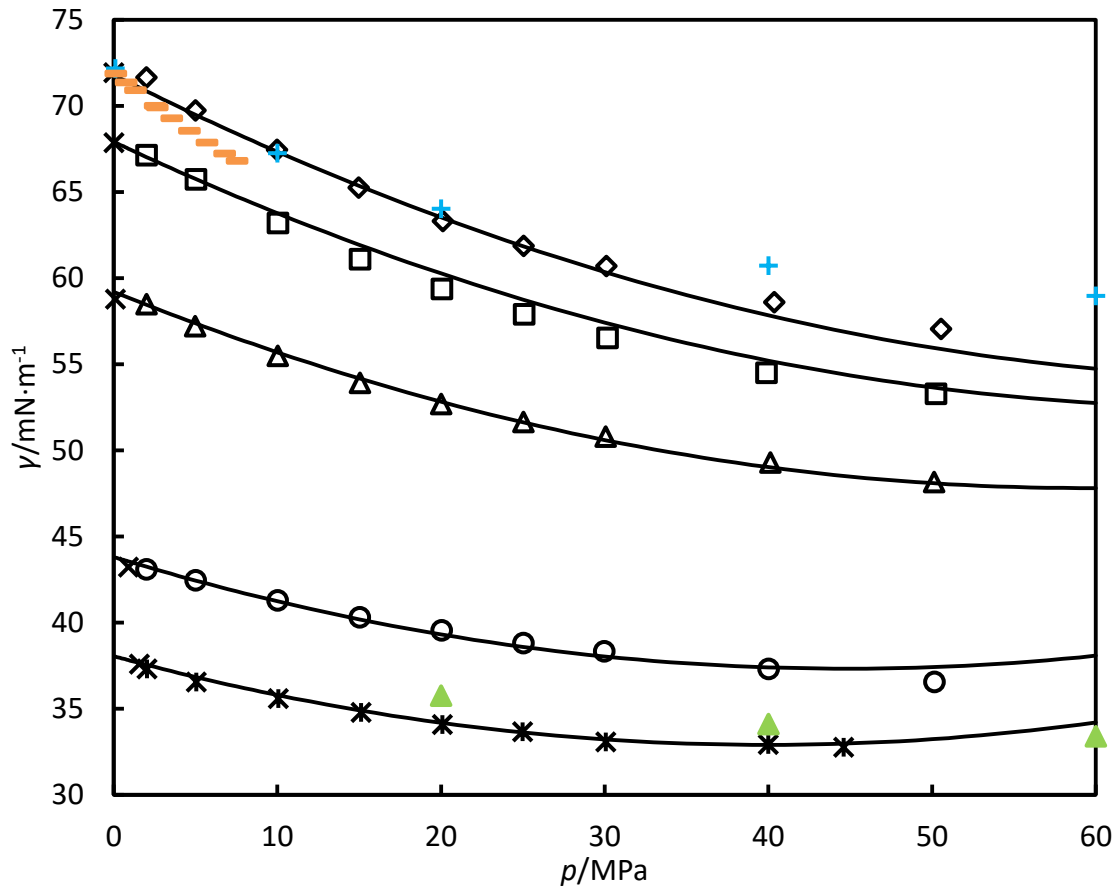


Figure 5.3 Interfacial tensions γ at various pressures p for the (Ar + H₂O) system, along five isotherms: \diamond , 298 K; \square , 323 K; \triangle , 373 K; \circ , 448 K; $*$, 473 K; —, Eq. (5.2). Interfacial tension measurements within the conditions studied in the present work, from Wiegand and Franck [260] at $+$, 298 K, and \blacktriangle , 473 K; and Massoudi and King [146] at $-$, 298 K. Surface tension of pure water, \times , as implemented in REFPROP 9.1 [188, 240].

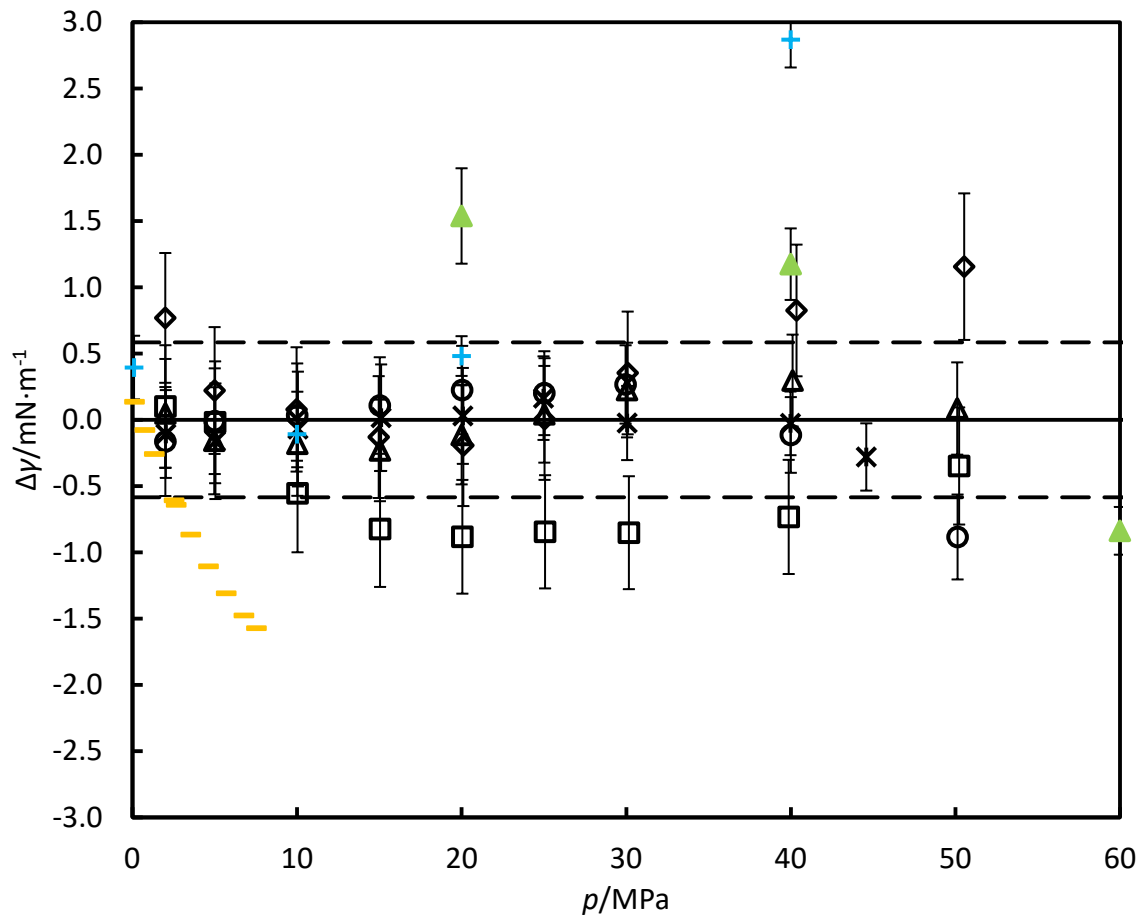


Figure 5.4 Difference in interfacial tension measurements of the (Ar + H₂O) system from Eq. (5.2) at five isotherms: \diamond , 298 K; \square , 323 K; \triangle , 373 K; \circ , 448 K; and $*$, 473 K. Deviations of the fitting equation from literature data: Wiegand and Franck [260] at $+$, 298 K, and \blacktriangle , 473 K; and Massoudi and King [146] at $-$, 298 K. Error bars show the expanded uncertainty of the measured data. Dashed lines show the absolute average deviation of the model.

5.1.3 (H₂ + H₂O) System

Four isotherms at temperatures between (298 and 448) K have been measured in the (H₂ + H₂O) system over a range of pressures from (0.5 to 45) MPa. The results are given in Table 5.4 and Figure 5.5. The relative standard deviation $\sigma(\gamma)/\gamma$ of the IFT data at each state point was evaluated from three repeated measurements and the average was found to be 0.3 %; in all cases it was < 0.9 %. The standard relative uncertainties $u_r(\gamma)$ were then calculated from eq. (5.1). Reliable measurements of the liquid and vapour phase densities under the conditions of interest are not available. To estimate the uncertainty $u(\Delta\rho)$ of the density difference, the calculated values of $\Delta\rho$, obtained with the PR-NRTL model and the mixture model in the REFPROP 9.1 database incorporating the equations of state of the pure components [188, 240, 246, 257], were compared with the density difference between the pure substances at the same temperature and pressure. The maximum difference in the density differences is 1.4 %, and the average absolute deviation is 0.4 %. Overall, the relative uncertainty of interfacial tension of all state points is 0.8 %, and the expanded relative uncertainty at 95 % confidence is 1.7 %.

Table 5.4 Interfacial tension γ for (H₂ + H₂O) at temperatures T and pressures p , with calculated density difference $\Delta\rho$.^a

p/MPa	T/K	$\gamma/\text{mN}\cdot\text{m}^{-1}$	$\Delta\rho/\text{kg}\cdot\text{m}^{-3}$	p/MPa	T/K	$\gamma/\text{mN}\cdot\text{m}^{-1}$	$\Delta\rho/\text{kg}\cdot\text{m}^{-3}$
0.5	298.03	72.3	996.8	30.1	323.02	66.5	978.4
1.0	298.03	72.9	996.5	40.1	323.00	65.8	976.4
2.0	298.04	73.0	996.1	0.5	372.74	59.8	958.5
3.5	298.05	72.8	995.4	1.0	372.77	59.7	958.3
5.0	298.04	72.6	994.7	2.0	372.78	59.7	958.0
7.5	298.04	72.2	993.6	5.0	372.87	59.5	957.1
10.1	298.04	71.9	992.6	10.0	372.81	59.3	955.9
15.0	298.06	71.3	990.7	15.0	372.73	59.0	954.7
20.1	298.06	70.8	989.0	20.1	372.85	58.7	953.6
25.0	298.04	70.3	987.5	25.2	372.77	58.5	952.7
30.1	298.06	69.8	986.2	29.8	372.77	58.1	951.9
39.9	298.09	69.1	983.9	40.1	372.78	57.6	950.5
45.2	298.05	68.7	983.0	1.5	448.04	44.0	891.9
0.5	323.02	68.9	987.8	2.0	448.02	44.1	891.9
1.0	322.90	69.3	987.7	5.0	448.24	43.8	891.5
2.0	322.98	69.3	987.2	10.0	448.29	43.7	891.2
3.5	323.00	69.1	986.6	15.0	448.28	43.4	891.0
5.0	322.99	68.9	986.0	20.0	448.33	43.3	890.8
10.0	323.00	68.3	984.2	25.0	448.31	43.2	890.7
15.0	323.00	67.8	982.5	30.1	448.31	42.9	890.6
20.0	323.01	67.2	981.0	40.1	448.35	43.2	890.4
25.0	323.01	66.8	979.7				

^a Expanded uncertainties at 95 % confidence are $U(T) = 0.05$ K, $U(p) = 70$ kPa, and $U(\gamma) = 0.017\gamma$.

The interfacial tensions of the (H₂ + H₂O) system has an unexpectedly interesting behaviour, increasing initially with pressure at low pressures from the surface tension value of water, creating a small hump, followed by the expected fairly linear decrease with increasing pressure. This initial increase is observed clearly at 298 K and 323 K, but not at the two higher temperatures, where IFT

varies less with pressure. In comparison to literature results, the 298 K data of Slowinski et al. [143] and Massoudi and King [146] were both lower than the values measured in this work. The initial hump was not observed by these authors, and a linear IFT-pressure relationship was found. The measurements from these works were found to be consistently lower, when compared to more recent measurements for other reported systems, such as the (H₂O + N₂) system [171] and (H₂O + Ar) system [216]. The interfacial tensions measured at 298 K in this work were compared with the data of Slowinski et al. [143] and Massoudi and King [146], and the agreement was within 2.1 mN·m⁻¹.

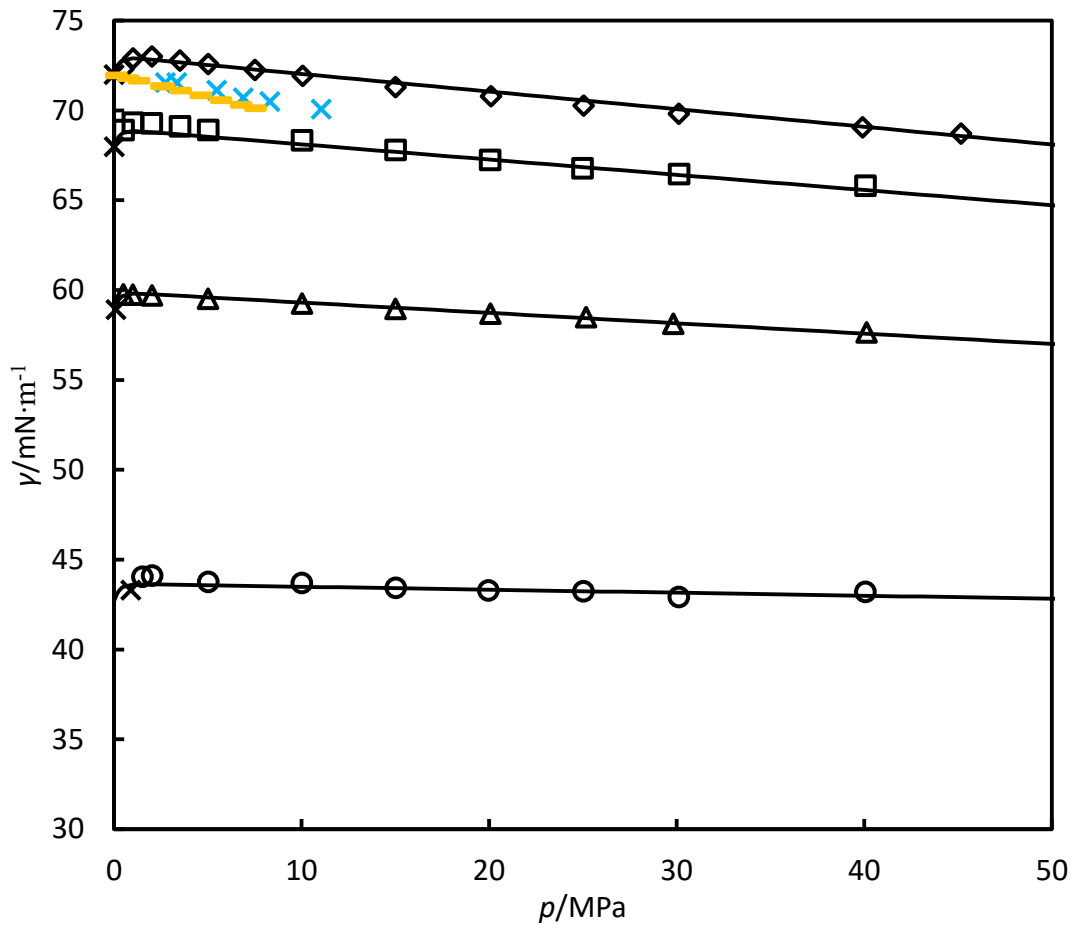


Figure 5.5 Interfacial tensions γ at various pressures p for the ($\text{H}_2 + \text{H}_2\text{O}$) system, along four isotherms: \diamond , 298 K; \square , 323 K; \triangle , 373 K; \circ , 448 K; —, Eq. (5.2). Interfacial tension measurements reported in literature at 298 K: —, Massoudi and King [146]; and \times , Slowinski *et al.* [143]. Surface tension of pure water, \times , as implemented in REFPROP 9.1 [188, 240].

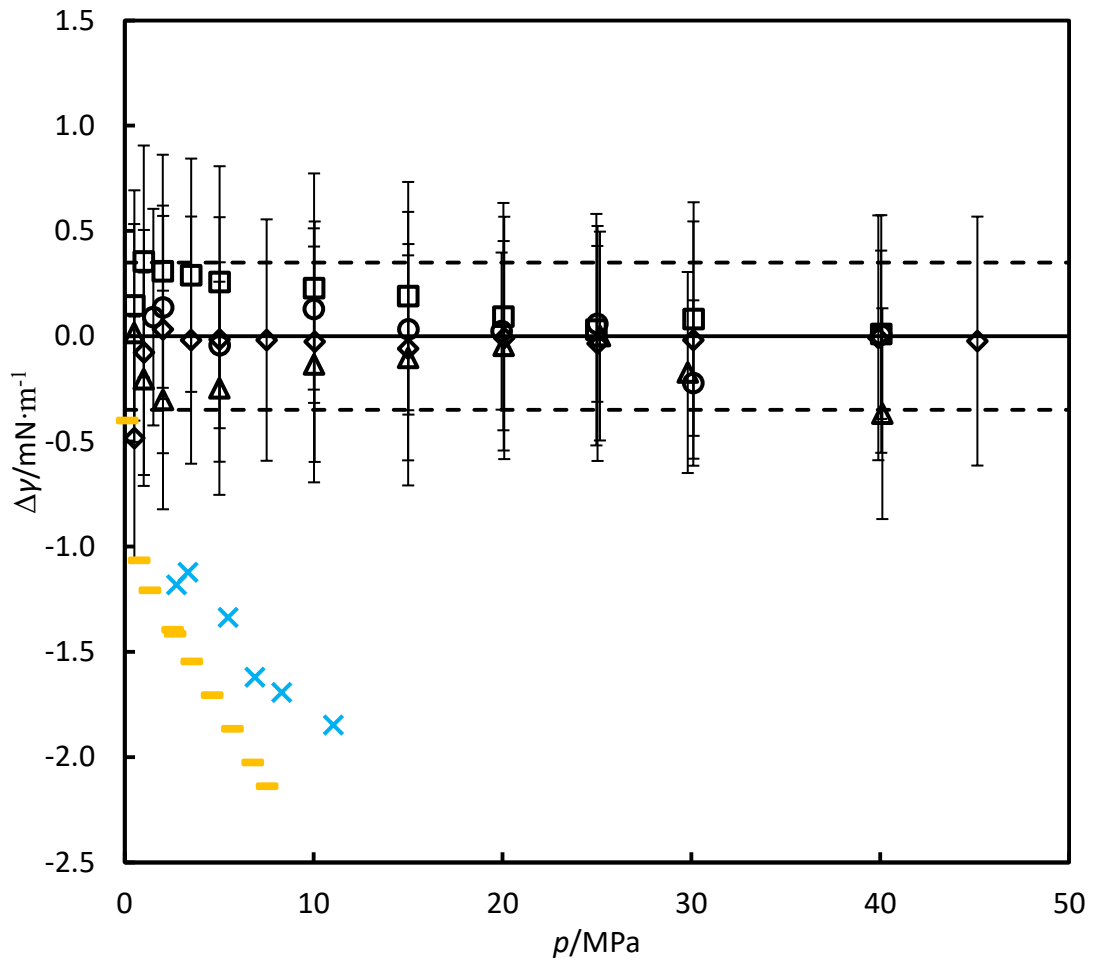


Figure 5.6 Difference in interfacial tension measurements of the ($\text{H}_2 + \text{H}_2\text{O}$) system from Eq. (5.2) at four isotherms: \diamond , 298 K; \square , 323 K; \triangle , 373 K; and \circ , 448 K. Deviations of the fitting equation from literature data at 298 K: $-$, Massoudi and King [146]; and \times , Slowinski *et al.* [143]. Error bars show the expanded uncertainty of the measured data. Dashed lines show the absolute average deviation of the model.

5.2 Ternary Systems

5.2.1 (CO₂ + N₂ + H₂O) System

In the (CO₂ + N₂ + H₂O) system, four isotherms were measured at temperatures between (298 and 448) K at pressures from (2 to 40) MPa. The results are given in Table 5.5. In Figure 5.7, the interfacial tension data are found to be similar to those of Yan et al., which relate to the gas phase mixture composition of [x CO₂ + (1 - x) N₂] with x = 0.5072, at two overlapping temperature conditions of (298 and 373) K. The relative standard deviation $\sigma(\gamma)/\gamma$ of the IFT data at each state point was evaluated from three repeated measurements; the average was 0.3 %, and in all cases it was < 1.3 %. The overall relative uncertainty $u_r(\gamma)$ was calculated from eq. (5.1). The coexisting phase compositions and density difference depend upon the overall system composition. The water level in the cell, and the known composition of the feed gas, were used to determine the standard relative uncertainty of the density difference, which was estimated to be 1 %. The relative standard uncertainty of interfacial tension at all state points is 1.6 %, and the expanded relative uncertainty at 95 % confidence is 3.2 %.

Table 5.5 Interfacial tensions γ at temperatures T and pressures p for the gas phase mixture composition of [x CO₂ + (1 - x) N₂], with x = 0.5120; x_i and y_i are the calculated liquid and vapour phase compositions respectively, where 1 = CO₂, 2 = H₂O, 3 = N₂.^a

p/Mpa	T/K	$\gamma/\text{mN}\cdot\text{m}^{-1}$	$\Delta\rho/\text{kg}\cdot\text{m}^{-3}$	x_1	x_2	x_3	y_1	y_2	y_3
2	298.18	64.0	969.0	0.0055	0.9943	0.0001	0.5103	0.0021	0.4876
5	298.17	55.9	921.8	0.0112	0.9885	0.0003	0.5099	0.0015	0.4886
10	298.17	46.6	824.1	0.0160	0.9835	0.0005	0.5092	0.0019	0.4889
20	298.16	39.6	634.4	0.0175	0.9815	0.0010	0.5072	0.0056	0.4872
30	298.17	38.3	479.2	0.0174	0.9812	0.0014	0.5044	0.0113	0.4843
40	298.15	37.7	399.0	0.0174	0.9810	0.0017	0.5014	0.0174	0.4812
2	323.12	63.0	963.9	0.0030	0.9969	0.0001	0.5075	0.0082	0.4844
5	323.11	56.2	919.7	0.0070	0.9928	0.0002	0.5088	0.0046	0.4866
10	323.12	46.4	839.0	0.0109	0.9887	0.0004	0.5084	0.0045	0.4870
20	323.10	40.4	678.1	0.0137	0.9855	0.0008	0.5064	0.0079	0.4856
30	323.10	39.1	537.2	0.0145	0.9844	0.0011	0.5037	0.0132	0.4830
40	323.10	38.1	452.0	0.0149	0.9837	0.0014	0.5010	0.0186	0.4804
2	373.25	55.2	937.0	0.0016	0.9983	0.0001	0.4813	0.0596	0.4590
5	373.25	50.1	901.4	0.0040	0.9959	0.0002	0.4965	0.0295	0.4740
10	373.25	45.9	840.1	0.0068	0.9928	0.0004	0.5002	0.0217	0.4781
20	373.23	40.6	716.1	0.0103	0.9890	0.0007	0.4996	0.0221	0.4782
30	373.25	37.7	605.6	0.0121	0.9869	0.0010	0.4973	0.0265	0.4763
40	373.22	35.8	523.5	0.0132	0.9855	0.0013	0.4937	0.0311	0.4752
2	448.03	43.1	879.7	0.0008	0.9991	0.0001	0.2743	0.4642	0.2615
5	448.02	40.6	849.0	0.0028	0.9969	0.0003	0.4041	0.2094	0.3864
10	448.02	37.7	802.2	0.0055	0.9939	0.0006	0.4438	0.1299	0.4262
20	447.98	33.0	711.4	0.0096	0.9892	0.0011	0.4603	0.0949	0.4447
30	448.02	30.2	631.5	0.0124	0.9859	0.0017	0.4630	0.0880	0.4490
40	448.03	28.1	560.0	0.0144	0.9835	0.0022	0.4631	0.0868	0.4501

^a Expanded uncertainties at 95 % confidence are $U(T) = 0.05$ K, $U(p) = 70$ kPa, and $U(\gamma) = 0.032\gamma$.

5.2.2 (CO₂ + Ar + H₂O) System

For the (CO₂ + Ar + H₂O) system, five isotherms were measured at temperatures between (298 and 473) K at pressures from (2 to 50) MPa. The results are given in Table 5.6 and Figure 5.8. The relative standard deviation $\sigma(\gamma)/\gamma$ of the IFT data at each state point was evaluated from three repeated measurements; the average was 0.5 %, and in all cases it was < 1.6 %. The standard relative uncertainties $u_r(\gamma)$ were calculated from eq. (5.1). The coexisting phase compositions and density difference depend upon the overall system composition. The water level in the cell, and the known composition of the feed gas, were used to determine the standard relative uncertainty of the density difference, which was estimated to be 1 %. The relative standard uncertainty of interfacial tension at all state points is 0.9 %, and the expanded relative uncertainty at 95 % confidence is 1.8 %.

Table 5.6 Interfacial tensions γ at temperatures T and pressures p for the gas phase mixture composition of $[x \text{ CO}_2 + (1 - x) \text{ Ar}]$, with $x = 0.4973$; x_i and y_i are the calculated liquid and vapour phase compositions respectively, where 1 = CO₂, 2 = H₂O, 3 = Ar. ^a

p/Mpa	T/K	$\gamma/\text{mN}\cdot\text{m}^{-1}$	$\Delta\rho/\text{kg}\cdot\text{m}^{-3}$	x_1	x_2	x_3	y_1	y_2	y_3
2	297.75	64.5	964.0	0.005	0.994	0.000	0.496	0.002	0.502
5	297.75	56.2	905.4	0.011	0.988	0.001	0.495	0.001	0.504
10	297.90	44.6	770.1	0.015	0.983	0.001	0.494	0.001	0.504
15	297.93	36.4	592.5	0.016	0.982	0.002	0.494	0.002	0.504
20	297.94	31.1	440.2	0.016	0.982	0.002	0.493	0.004	0.503
25	297.95	28.5	342.1	0.016	0.982	0.002	0.493	0.005	0.502
30	297.96	27.2	275.5	0.016	0.982	0.003	0.492	0.006	0.502
40	297.96	25.3	189.5	0.015	0.982	0.003	0.491	0.009	0.500
51	297.98	24.4	133.0	0.015	0.982	0.003	0.490	0.010	0.499
2	322.77	62.6	957.1	0.003	0.997	0.000	0.493	0.007	0.499
5	322.77	56.0	904.8	0.007	0.993	0.000	0.494	0.004	0.502
10	322.79	47.6	801.1	0.011	0.989	0.001	0.494	0.004	0.502
15	322.77	40.3	669.5	0.012	0.987	0.001	0.493	0.004	0.502
20	322.78	35.5	545.3	0.013	0.986	0.002	0.493	0.006	0.502
25	322.77	32.3	445.4	0.013	0.985	0.002	0.492	0.007	0.501
30	322.79	30.2	368.5	0.013	0.985	0.002	0.491	0.009	0.500
40	322.78	28.0	264.8	0.013	0.984	0.002	0.490	0.012	0.499
50	322.77	26.7	197.7	0.013	0.984	0.003	0.489	0.014	0.497
2	373.01	56.5	932.5	0.002	0.998	0.000	0.469	0.057	0.474
5	373.06	52.5	890.3	0.004	0.996	0.000	0.483	0.028	0.489
10	372.99	47.0	813.3	0.007	0.993	0.001	0.487	0.020	0.494
15	372.99	42.7	729.7	0.008	0.990	0.001	0.487	0.019	0.495
20	372.96	39.0	643.1	0.010	0.989	0.001	0.486	0.019	0.494
25	372.95	35.7	563.3	0.011	0.988	0.002	0.486	0.021	0.494
30	372.98	32.9	492.3	0.011	0.987	0.002	0.485	0.023	0.493
40	372.98	29.2	380.4	0.012	0.986	0.002	0.483	0.026	0.491
50	372.97	28.0	302.1	0.012	0.985	0.002	0.481	0.029	0.490
2	448.28	42.0	874.2	0.001	0.999	0.000	0.271	0.456	0.273
5	448.33	39.8	841.1	0.003	0.997	0.000	0.392	0.212	0.396
10	448.35	36.4	782.9	0.005	0.994	0.001	0.433	0.129	0.438
15	448.33	33.8	726.1	0.007	0.991	0.001	0.445	0.104	0.451
20	448.34	31.2	665.4	0.009	0.989	0.002	0.449	0.094	0.456
25	448.33	29.2	609.7	0.010	0.988	0.002	0.451	0.090	0.459

30	448.35	27.3	555.1	0.011	0.986	0.002	0.452	0.088	0.460
40	448.37	24.6	460.2	0.013	0.984	0.003	0.452	0.088	0.460
50	448.38	23.3	384.5	0.013	0.983	0.003	0.451	0.089	0.459
2	473.29	37.4	849.7	0.000	1.000	0.000	0.113	0.772	0.114
5	473.30	35.5	819.2	0.002	0.997	0.000	0.322	0.352	0.326
10	473.29	32.5	765.7	0.005	0.995	0.001	0.393	0.210	0.397
15	473.32	30.1	716.1	0.006	0.992	0.001	0.414	0.166	0.419
20	473.35	28.0	663.7	0.007	0.991	0.002	0.424	0.147	0.429
25	473.34	26.0	612.5	0.008	0.989	0.002	0.429	0.137	0.435
30	473.31	24.6	561.2	0.009	0.988	0.003	0.431	0.131	0.437

^a Expanded uncertainties at 95 % confidence are $U(T) = 0.05$ K, $U(p) = 70$ kPa, and $U(\gamma) = 0.018\gamma$.

5.2.3 (CO₂ + H₂ + H₂O) System

For the (CO₂ + H₂ + H₂O) system, four isotherms were measured at temperatures between (298 and 448) K at pressures from (0.5 to 45) MPa. The results are given in Table 5.7 and Figure 5.9. The relative standard deviation $\sigma(\gamma)/\gamma$ of the IFT data at each state point was evaluated from three repeated measurements; the average was 0.2 %, and in all cases it was < 0.5 %. The standard relative uncertainties $u_r(\gamma)$ were calculated from eq. (5.1). The coexisting phase compositions and density difference depend upon the overall system composition. The water level in the cell, and the known composition of the feed gas, were used to determine the standard relative uncertainty of the density difference, which was estimated to be 1 %. Finally, the overall standard relative uncertainty of interfacial tension of all state points was found to be 1.7 %.

Table 5.7 Interfacial tensions γ at temperatures T and pressures p for the gas phase mixture composition of $[x \text{ CO}_2 + (1 - x) \text{ H}_2]$, with $x = 0.300$; x_i and y_i are the calculated liquid and vapour phase compositions respectively, where 1 = CO₂, 2 = H₂O, 3 = H₂.^a

p/Mpa	T/K	$\gamma/\text{mN}\cdot\text{m}^{-1}$	$\Delta\rho/\text{kg}\cdot\text{m}^{-3}$	x_1	x_2	x_3	y_1	y_2	y_3
0.5	298.03	72.0	994.7	0.0009	0.9991	0.0000	0.2979	0.0066	0.6955
1.0	298.04	71.7	992.3	0.0017	0.9982	0.0001	0.2988	0.0034	0.6978
2.0	298.03	69.7	987.6	0.0033	0.9965	0.0002	0.2991	0.0019	0.6990
5.0	298.07	64.5	972.9	0.0072	0.9923	0.0005	0.2990	0.0010	0.7001
10.0	298.05	57.5	947.5	0.0118	0.9872	0.0010	0.2985	0.0007	0.7007
15.0	298.07	52.8	922.0	0.0148	0.9838	0.0014	0.2982	0.0007	0.7010
20.0	298.05	49.5	897.2	0.0167	0.9814	0.0019	0.2980	0.0008	0.7012
25.0	298.05	46.9	874.1	0.0180	0.9797	0.0023	0.2979	0.0009	0.7013
30.1	298.04	45.3	852.7	0.0188	0.9784	0.0027	0.2978	0.0010	0.7013
40.0	298.06	43.6	816.2	0.0199	0.9767	0.0035	0.2976	0.0011	0.7012
1.0	322.96	67.4	983.4	0.0010	0.9989	0.0001	0.2960	0.0130	0.6910
2.0	322.86	66.8	978.7	0.0020	0.9979	0.0002	0.2977	0.0069	0.6954
5.0	322.97	63.0	964.6	0.0044	0.9952	0.0004	0.2985	0.0034	0.6980
10.0	322.96	57.8	941.0	0.0075	0.9916	0.0009	0.2985	0.0024	0.6991
15.0	322.96	53.9	917.7	0.0097	0.9890	0.0013	0.2984	0.0021	0.6995
20.0	322.96	50.9	895.3	0.0113	0.9870	0.0017	0.2982	0.0021	0.6997
29.9	322.97	46.6	854.9	0.0134	0.9841	0.0025	0.2980	0.0022	0.6998
39.8	322.96	44.5	820.8	0.0146	0.9822	0.0032	0.2978	0.0024	0.6997
45.1	322.98	43.8	804.7	0.0151	0.9813	0.0036	0.2978	0.0025	0.6997

1.0	373.41	58.9	953.8	0.0005	0.9994	0.0001	0.2681	0.1062	0.6257
2.0	373.43	58.2	949.6	0.0010	0.9988	0.0002	0.2835	0.0549	0.6616
5.0	373.41	56.4	937.4	0.0024	0.9971	0.0005	0.2923	0.0249	0.6827
10.0	373.44	53.2	917.0	0.0044	0.9947	0.0009	0.2951	0.0151	0.6898
15.0	373.44	50.3	897.3	0.0059	0.9927	0.0014	0.2959	0.0120	0.6921
20.0	373.32	48.3	878.4	0.0072	0.9909	0.0019	0.2962	0.0105	0.6933
30.0	373.32	45.0	843.6	0.0092	0.9881	0.0027	0.2964	0.0094	0.6943
40.1	373.33	43.1	813.0	0.0106	0.9859	0.0035	0.2964	0.0089	0.6947
2.0	448.25	43.4	884.7	0.0005	0.9993	0.0002	0.1645	0.4515	0.3840
5.0	448.21	42.8	873.6	0.0017	0.9977	0.0006	0.2413	0.1954	0.5632
10.0	448.29	41.0	857.5	0.0034	0.9952	0.0014	0.2676	0.1080	0.6245
15.0	448.47	39.3	841.5	0.0049	0.9929	0.0022	0.2762	0.0789	0.6450
20.0	448.58	37.9	826.3	0.0062	0.9908	0.0029	0.2805	0.0642	0.6553
25.1	448.67	36.8	811.8	0.0074	0.9889	0.0036	0.2830	0.0553	0.6616
30.0	448.78	35.9	798.4	0.0084	0.9872	0.0043	0.2847	0.0496	0.6657
40.1	448.79	34.0	773.0	0.0102	0.9841	0.0057	0.2868	0.0419	0.6712
44.7	448.87	33.3	762.5	0.0109	0.9828	0.0063	0.2875	0.0396	0.6729

^a Expanded uncertainties at 95 % confidence are $U(T) = 0.05$ K, $U(p) = 70$ kPa, and $U(\gamma) = 0.017\gamma$.

5.3 Modelling

In this section, the ternary experimental data is first modelled with an empirical model, then with the SGT + SAFT-VR Mie analysis for systems involving CO₂, N₂ and Ar only. In the case of systems involving H₂, the SAFT modelling approach is complicated by the partial quantum behaviour, and is beyond the scope of this research. The parameterization procedure and parameters used are detailed, and the results are compared with models proposed in the literature.

5.3.1 Empirical Model

Theoretical approaches based on equations of state in combination with gradient theory, may be capable of describing ternary IFT data [216], and this is explored in Section 5.5.2. For the present purpose of observing trends and developing a computationally rapid empirical model for ternary systems, a simple relationship between the ternary system IFT and the constituent binary sub-system IFT is sought. Shah et al. [182] proposed a mole-fraction-weighted average for this purpose, and was applied to the (CO₂ + H₂S + H₂O) system with some success. This approach is used, and has been modified to include the presence of water in the vapour phase as follows:

$$\gamma_{X\text{-CO}_2\text{-H}_2\text{O}} = (y_X \cdot \gamma_{X\text{-H}_2\text{O}} + y_{\text{CO}_2} \cdot \gamma_{\text{CO}_2\text{-H}_2\text{O}}) / (y_X + y_{\text{CO}_2}). \quad (5.3)$$

The equilibrium vapour compositions were calculated using the PR-NRTL model, and the interfacial tensions of the binary systems were evaluated from Eq. (5.2) for the (N₂ + H₂O), (Ar + H₂O) and (H₂ + H₂O) systems, and from the SAFT-VR Mie + SGT model of Chow et al. [216] for the (CO₂ + H₂O) system, with validity from 298 < T/K < 448. The predictions are compared with the experimental data in Figure 5.7 for the (CO₂ + N₂ + H₂O) system, Figure 5.8 for the (CO₂ + Ar + H₂O) system, and Figure 5.9 for the (CO₂ + H₂ + H₂O) system. The empirical model predicts the ternary system IFT with average absolute deviation of 5.5 % for the (CO₂ + N₂ + H₂O) system, 21.2 % for the (CO₂ + Ar + H₂O) system, and 7.6 % for the (CO₂ + H₂ + H₂O) system. In general, the simple empirical model is satisfactory at the two higher temperatures, (373 and 448) K, but fails at the lower temperatures, (298 and 323) K, and high pressures.

Table 5.8 Average absolute relative deviations Δ_{AAD} between experimental interfacial tensions and values calculated from Eq. (5.3) for isotherms at temperatures T , and overall average absolute relative deviations $\Delta_{\text{AAD,overall}}$ for each system investigated.

System	$\Delta_{\text{AAD,overall}}/\%$	T/K	$\Delta_{\text{AAD}}/\%$
(CO ₂ + N ₂ + H ₂ O)	5.5	298	12.2
		323	6.8
		373	1.3
		448	1.8
(CO ₂ + Ar + H ₂ O)	21.2	298	43.7
		323	25.2
		373	10.3
		448	5.8
(CO ₂ + H ₂ + H ₂ O)	7.6	298	13.6
		323	9.7
		373	3.5
		448	2.2

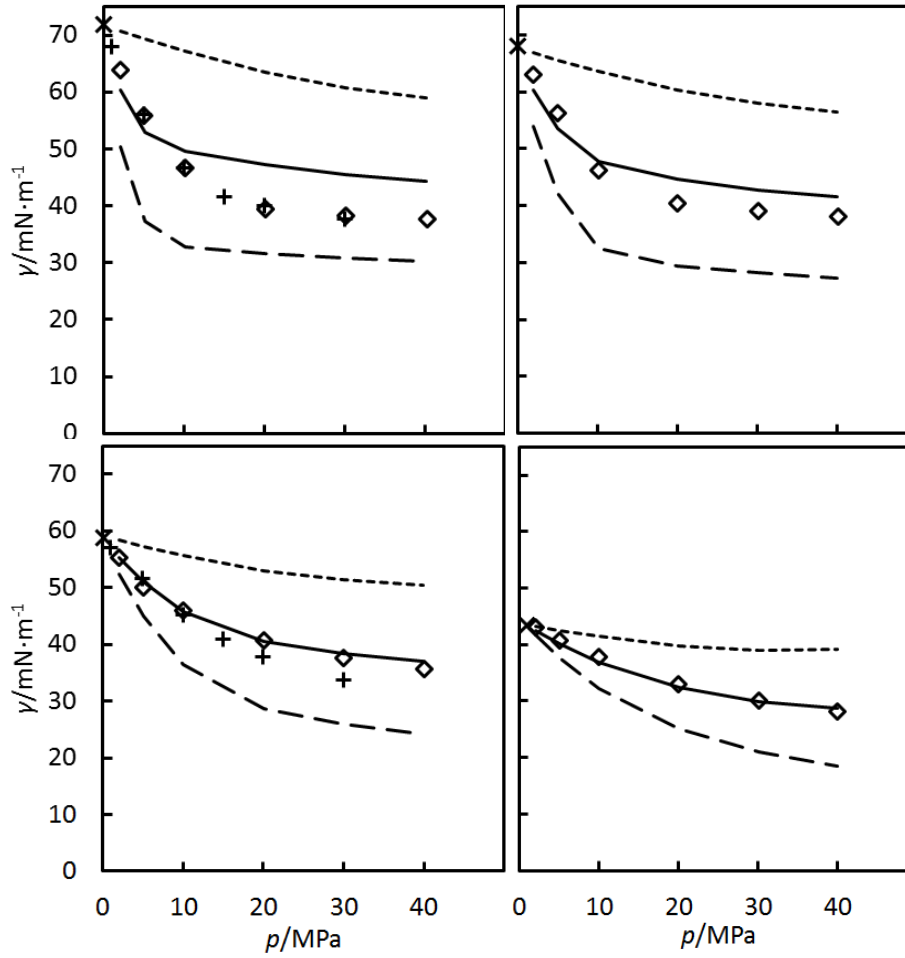


Figure 5.7 Interfacial tensions at various pressures for the gas phase mixture composition of $[x \text{ CO}_2 + (1 - x) \text{ N}_2]$: \diamond , measured values with $x = 0.5120$; $+$, values from Yan et al. [259] with $x = 0.5072$; $— —$, $(\text{CO}_2 + \text{H}_2\text{O})$ from the SAFT-VR Mie + SGT model of Chow et al. [216]; $----$, $(\text{N}_2 + \text{H}_2\text{O})$ from Eq. (5.2); $—$, $(\text{CO}_2 + \text{N}_2 + \text{H}_2\text{O})$ prediction from Eq. (5.3). From top left to right at 298 K and 323 K; bottom left to right at 373 K and 448 K.

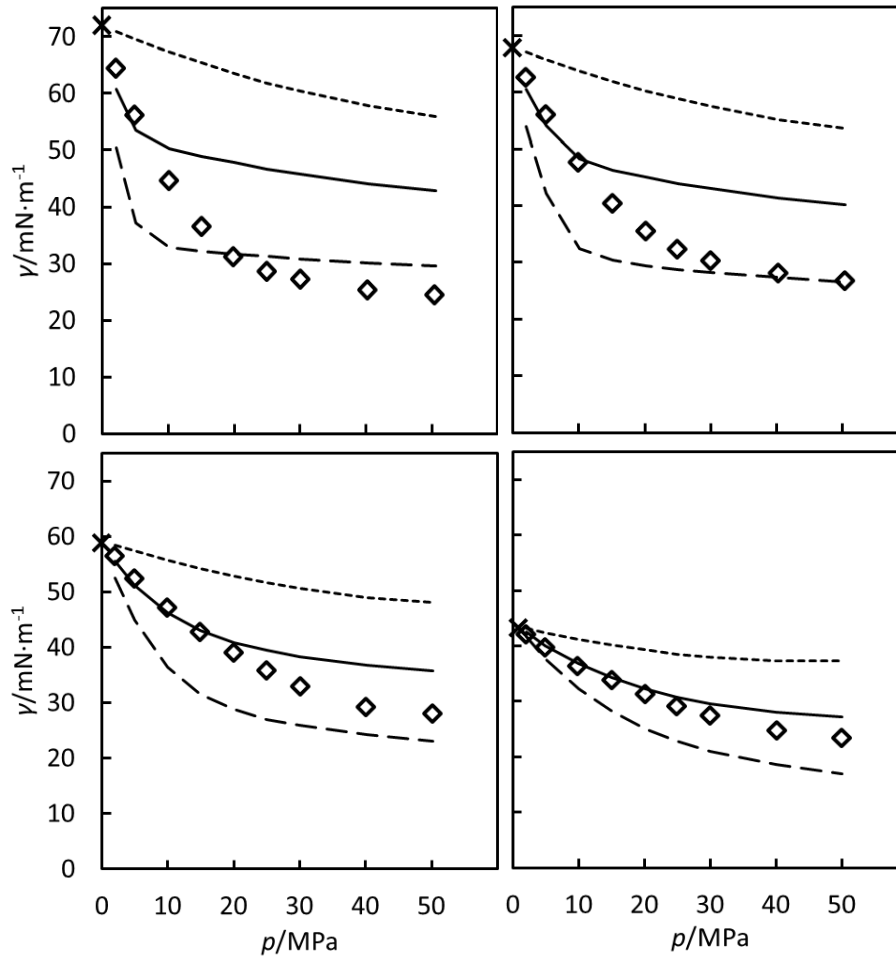


Figure 5.8 Interfacial tensions at various pressures for the gas phase mixture composition of $[x \text{ CO}_2 + (1 - x) \text{ Ar}]$: \diamond , measured values with $x = 0.4973$; — —, $(\text{CO}_2 + \text{H}_2\text{O})$ from the SAFT-VR Mie + SGT model of Chow et al. [216]; - - - -, $(\text{Ar} + \text{H}_2\text{O})$ from Eq. (5.2); — · — ·, $(\text{CO}_2 + \text{Ar} + \text{H}_2\text{O})$ prediction from Eq. (5.3). From top left to right at 298 K and 323 K; bottom left to right at 373 K and 448 K.

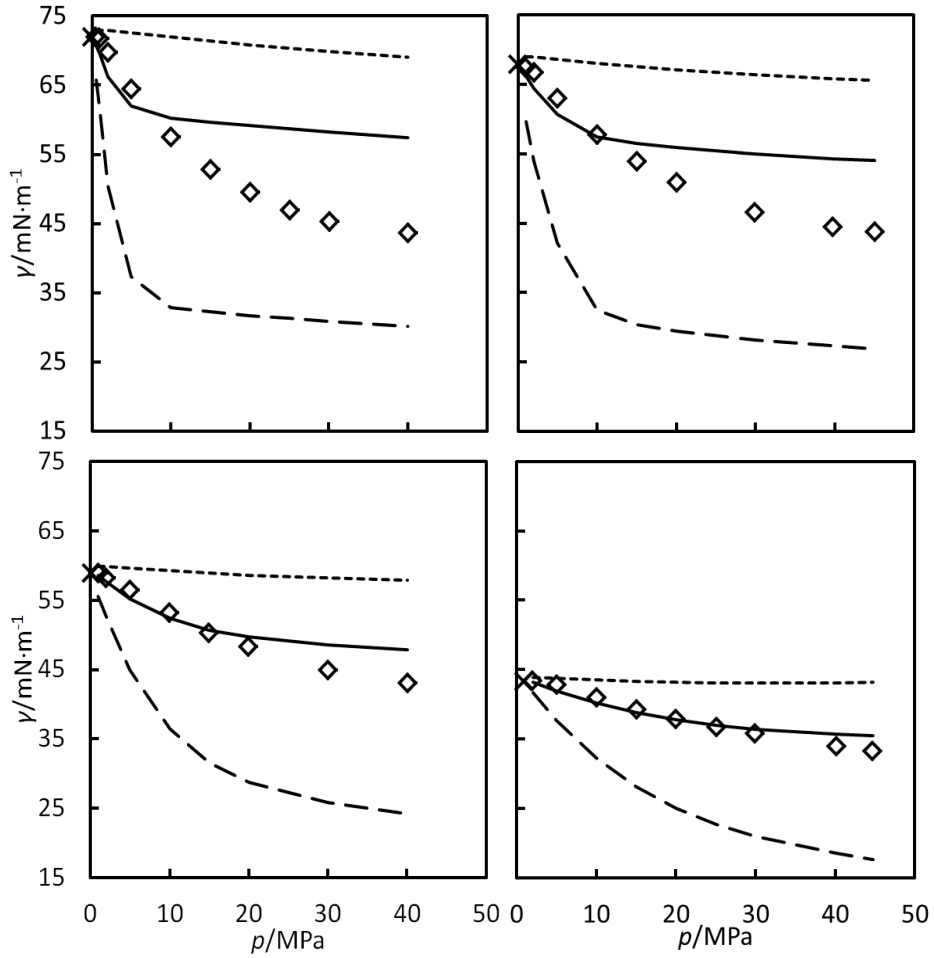


Figure 5.9 Interfacial tensions at various pressures for the gas phase mixture composition of $[x \text{ CO}_2 + (1 - x) \text{ H}_2]$: \diamond , measured values with $x = 0.300$; — —, $(\text{CO}_2 + \text{H}_2\text{O})$ from the SAFT-VR Mie + SGT model of Chow et al. [216]; - - - -, $(\text{H}_2 + \text{H}_2\text{O})$ from Eq. (5.2); — · — ·, $(\text{CO}_2 + \text{H}_2 + \text{H}_2\text{O})$ prediction from Eq. (5.3). From top left to right at 298 K and 323 K; bottom left to right at 373 K and 448 K.

5.3.2 Square Gradient Theory + SAFT

Theoretical approaches based on molecular equations of state, such as SAFT, in combination with DFT or GT has been shown to be capable of describing ternary system IFTs with relative success. In the case of systems involving H₂, the SAFT modelling approach is complicated by the partial quantum behaviour. Therefore, the following SGT + SAFT-VR Mie analysis is limited to the systems involving CO₂, N₂ and Ar. The parameterization procedure follows the standard approach where parameters of the pure components are obtained from pure-component experimental data, and binary interaction parameters are estimated from selected binary data. The SAFT-VR Mie model parameters for CO₂, N₂ and Ar are taken from Dufal *et al.* [261], and parameters for H₂O (with the generic Mie association kernel) are taken from Dufal *et al.* [130]. These model parameters are summarised in Table 5.9. All models employ a λ_r -6 potential, which is consistent with the theory of London [262].

The H₂O molecule is described as spherical with four association sites, two of type e and two of type H, where only unlike (e-H) bonding is allowed [130]. H₂O is the only self-associating molecule within the components analysed. Both Ar and N₂ are non-associating and are described only by the four Mie potential parameters and the number of segments in a molecular chain. CO₂ was described as a non-self-associating molecule. However, in order to describe the binary interaction between H₂O and CO₂, a solvation approach [263, 264] was taken. The interaction between H₂O and CO₂ is described by a single association site on the CO₂ molecule that interacts with two sites on H₂O. The single site on CO₂ represents the solvation of the electronegative oxygen atoms by the electropositive hydrogen atoms in H₂O. A binary interaction parameter, $k_{\text{CO}_2, \text{H}_2\text{O}}$, was also introduced. Both $k_{\text{CO}_2, \text{H}_2\text{O}}$ and the site-site association interaction between CO₂ and H₂O have been determined by matching to experimental mutual solubility data [239] for the CO₂-H₂O VLE between (298.15 and 448.15) K and (1.6 to 17.5) MPa, as described by Chow *et al.* [216].

Table 5.9 Pure-component parameters in SAFT-VR Mie, m is the number of segments of diameter σ making up a molecular chain of segments interacting through a Mie potential with repulsive exponent λ_r and attractive exponent λ_a and a well-depth of ε ; N_{types} is the number of site types and N_{sites} is the number of sites of each type, interacting with an association energy of ε_{HB} and a volume of K between sites of unlike type.

Comp.	m	σ [Å]	λ_r	λ_a	ε/k_B [K]	$N_{\text{types}} / N_{\text{sites}}$	$\varepsilon_{\text{HB}}/k_B$ [K]	K [Å ³]	Ref.
H ₂ O	1.0000	3.0555	35.823	6.00	418.00	2/2	1600.00	496.66	[130]
CO ₂	1.6939	3.0471	18.131	6.00	236.12	-	-	-	[261]
N ₂	1.4214	3.1760	9.875	6.00	72.44	-	-	-	[261]
Ar	1.0000	3.4038	12.085	6.00	117.84	-	-	-	[261]

The binary interaction parameters are given in Table 5.10. SAFT-VR Mie binary interaction parameters, k_{ij} , for the dispersive energy between H₂O, CO₂ and gaseous components have been estimated from data in [239]. The description of pressure effect on the solubility of N₂ in H₂O is challenging for SAFT type models. In the present work, a temperature-dependent binary interaction parameter, k_{ij} , was estimated using experimental solubility data of N₂ in H₂O at temperatures between (274.20 and 362.95) K [265]. $k_{\text{H}_2\text{O}, \text{Ar}}$ and $\Gamma_{\text{H}_2\text{O}, \text{Ar}}$ were estimated using data from [266], $k_{\text{CO}_2, \text{N}_2}$ and $\Gamma_{\text{CO}_2, \text{N}_2}$ were estimated using data from [267], and $k_{\text{CO}_2, \text{Ar}}$ and $\Gamma_{\text{CO}_2, \text{Ar}}$ were estimated using data from [268].

Table 5.10 Binary parameters used in SAFT-VR Mie between H₂O (component 1) and other components in the mixture. Here, k_{ij} are the binary parameters, N_{sites} are the number sites interacting with one site type on H₂O with an energy of ε_{HB} and a volume of K , and Γ_{ij} are the binary parameters.

Comp j	$k_{\text{H}_2\text{O},j}$	N_{sites}	$\varepsilon_{\text{HB}}/k_{\text{B}}$ [K]	K [Å ³]
CO ₂	0.01521	1	1376.9676	275.8941
Comp j	$k_{\text{H}_2\text{O},j}$	$k_{\text{CO}_2,j}$	$\Gamma_{\text{H}_2\text{O},j}$	$\Gamma_{\text{CO}_2,j}$
CO ₂	0.01521			
N ₂	$-0.8800 + 0.002110(T/\text{K})$	-0.3130		-0.4092
Ar	-0.0964	0.1625	-0.2340	0.2955

The influence parameters were expressed as linear functions of temperature following Eq. (5.4), with constants a_{ii}^1 and a_{ii}^0 listed in Table 5.11.

$$L_{ii} = a_{ii}^1 T + a_{ii}^0, \quad (5.4)$$

The pure-component influence parameters were determined from surface tension data at the experimental temperatures for each substance. The correlated surface tension obtained from NIST REFPROP 9.1 software [190, 231], at temperatures between (278.15 and 478.15) K, was used for water. For the light gasses, N₂ and Ar, they are supercritical for the conditions examined. The critical temperature of CO₂, 304.13 K, is close to the lower end of the temperature range. Extrapolation of the influence parameter from lower temperatures is unreliable, especially as an analytical EOS, such as SAFT-VR, cannot represent the free energy accurately in the critical and subcritical regions simultaneously. As a result, the influence parameters for the non-aqueous components were estimated from binary interfacial-tension data using the measured experimental data.

Table 5.11 SGT influence parameters a_1 and a_0 for the components studied in this work.

Component	a_{ii}^1 [J m ⁵ mol ⁻² K ⁻¹]	a_{ii}^0 [J m ⁵ mol ⁻²]
H ₂ O	$9.749 \cdot 10^{-24}$	$9.624 \cdot 10^{-21}$
CO ₂	$3.189 \cdot 10^{-23}$	$-9.473 \cdot 10^{-21}$
N ₂	$2.723 \cdot 10^{-23}$	$-8.078 \cdot 10^{-21}$
Ar	$5.640 \cdot 10^{-24}$	$-1.040 \cdot 10^{-21}$

5.3.2.1 Comparison with experimental results

The differences between experimental data and SAFT-SGT calculations are quantified by the average absolute relative deviations Δ_{AAD} :

$$\Delta_{\text{AAD}} = \frac{1}{N_p} \sum_{i=1}^{N_p} \left| \frac{\gamma_{i,\text{exp}} - \gamma_{i,\text{calc}}}{\gamma_{i,\text{exp}}} \right|, \quad (5.5)$$

where $\gamma_{i,\text{exp}}$ and $\gamma_{i,\text{calc}}$ are the experimental and calculated interfacial tensions at the i^{th} state point, respectively, and N_p is the number of points compared. The Δ_{AAD} values are listed as an overall value for the systems considered and also by isotherms in Table 5.12.

The experimental interfacial tensions for the (N₂ + H₂O) system are compared to the SAFT-SGT calculations in Figures 5.10 and 5.11. The experimental interfacial tensions for the (Ar + H₂O) system are compared to the SAFT-SGT calculations in Figures 5.12 and 5.13. In both systems, the

experimental observations are captured accurately by the theory, and the overall values of Δ_{AAD} are comparable with the relative uncertainty of the data. In most cases, the Δ_{AAD} were higher at the lower temperatures.

Table 5.12 Average absolute relative deviations Δ_{AAD} between experimental interfacial tensions and values calculated from the SAFT + SGT approach for isotherms at temperatures T , and overall average absolute relative deviations $\Delta_{\text{AAD,overall}}$ for each system investigated.

System	$\Delta_{\text{AAD,overall}}/\%$	T/K	$\Delta_{\text{AAD}}/\%$
(N ₂ + H ₂ O)	1.5	298	2.6
		323	2.1
		373	0.7
		448	0.5
(Ar + H ₂ O)	1.8	298	1.0
		323	1.3
		373	0.3
		448	0.4
		473	1.4
(CO ₂ + N ₂ + H ₂ O)	3.6	298	5.1
		323	5.1
		373	2.8
		448	1.5
(CO ₂ + Ar + H ₂ O)	7.9	298	19
		323	12
		373	5.4
		448	2.1
		473	0.6

Considering the ternary system data, the SAFT-VR Mie + SGT predictions were carried out at the experimental state points specified by T , p and y_2/y_3 , where y_2 and y_3 are the gas-phase mole fractions of the two non-aqueous components. The experimental data and modelling results for the two ternary systems are compared in Figures 5.14 and 5.15. For (CO₂ + N₂ + H₂O) system, the predictions are satisfactory at all temperatures investigated and the overall Δ_{AAD} is about double the experimental uncertainty. This is compared with the AAD of 1.8 % reported by Khosharay and Varaminian [215], using a linear-gradient model based on the CPA equation of state, with the experimental data of Yan et al. [259]. For the (CO₂ + Ar + H₂O) system, the agreement was satisfactory at higher temperatures, but differs significantly at the two lower temperatures. The cause for the discrepancies at low temperatures may be due to the proximity to the critical temperature of CO₂. The agreement of the theoretical model performs significantly better than the empirical combining rule in Eq. 5.3. Considering the limited fitting required in this predictive model, the modelling results are fairly satisfactory.

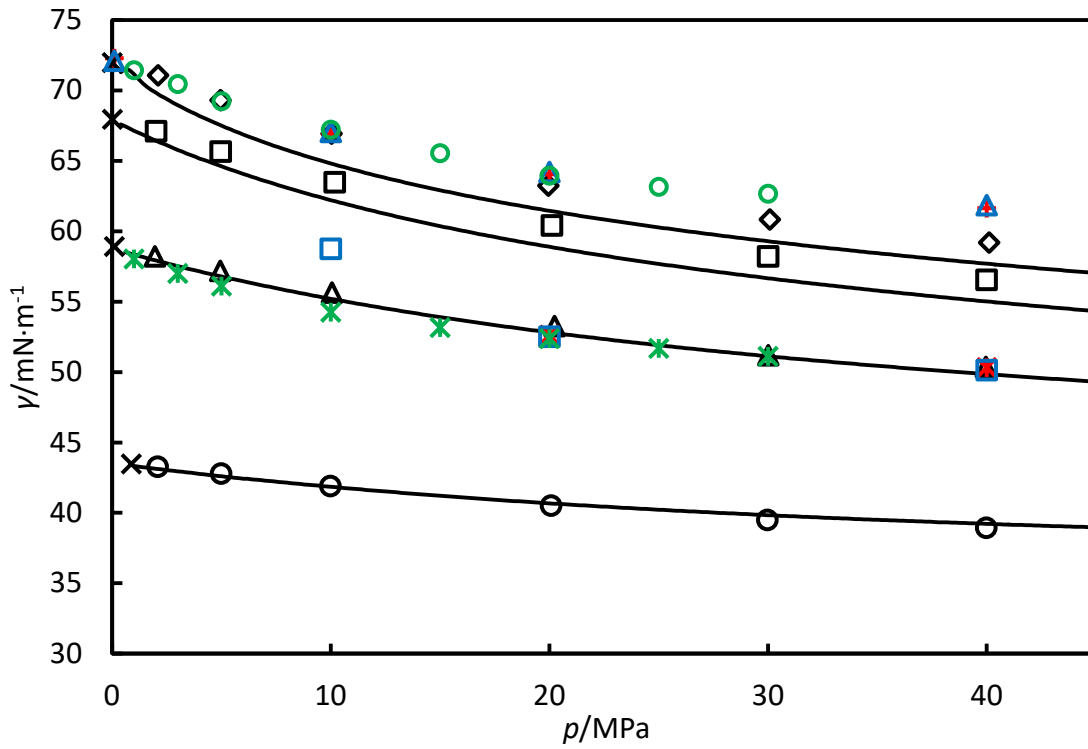


Figure 5.10 Interfacial tensions γ at pressures p for $(\text{N}_2 + \text{H}_2\text{O})$. Measured data: \diamond , 298 K; \square , 323 K; \triangle , 373 K; \circ , 448 K; —, SAFT + SGT calculations; \times , surface tensions for pure water [188, 190]. Literature data from Wiegand and Franck [179]: $+$, 298 K; $*$, 373 K. Literature data from Tian et al. [180]: \triangle , 298 K; \square , 373 K. Literature data from Yan et al. [181]: \circ , 298 K and $*$, 373 K.

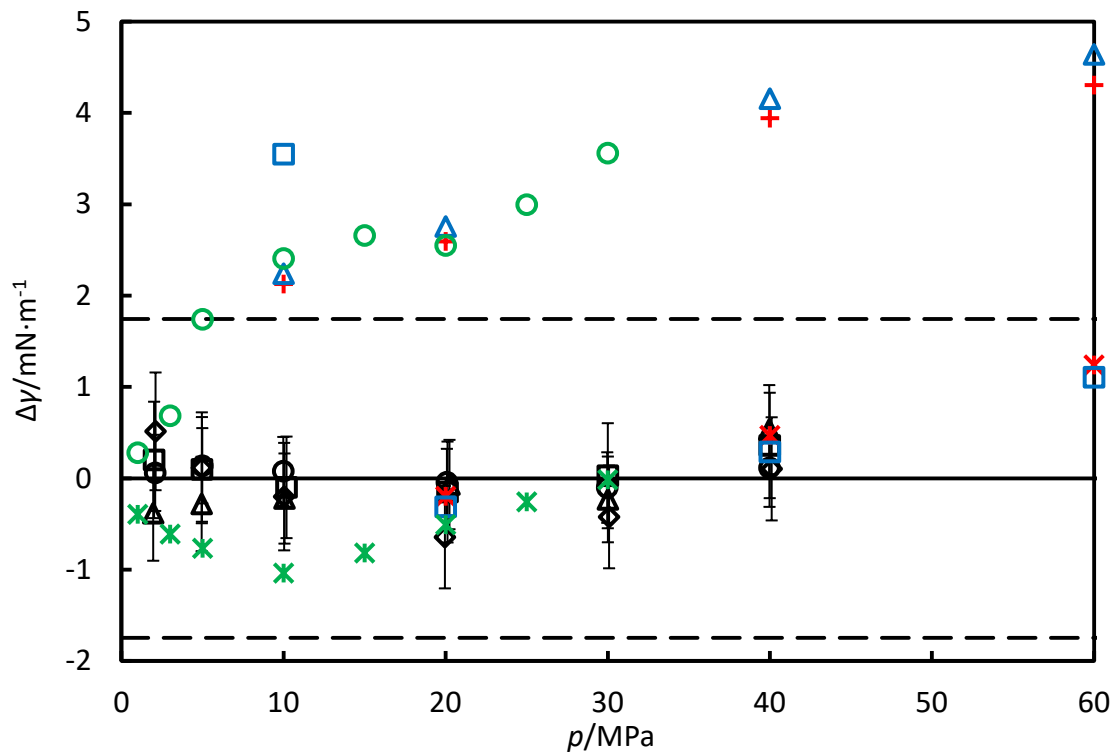


Figure 5.11 Difference $\Delta\gamma = (\gamma_{\text{exp}} - \gamma_{\text{calc}})$ between experimental interfacial tensions γ_{exp} of the ($\text{N}_2 + \text{H}_2\text{O}$) system and values γ_{calc} calculated using the SAFT + SGT approach. Experimental data: \blacklozenge , 298 K; \blacksquare , 323 K; \blacktriangle , 373 K; \bullet , 448 K. Literature data from Wiegand and Franck [179]: $\color{red}+$, 298 K; $\color{red}*$, 373 K. Literature data from Tian et al. [180]: $\color{blue}\triangle$, 298 K; $\color{blue}\square$, 373 K. Literature data from Yan et al. [181]: $\color{green}\circ$, 298 K and $\color{green}*$, 373 K. Dashed lines represent the average absolute deviation of the calculations from the experimental data.

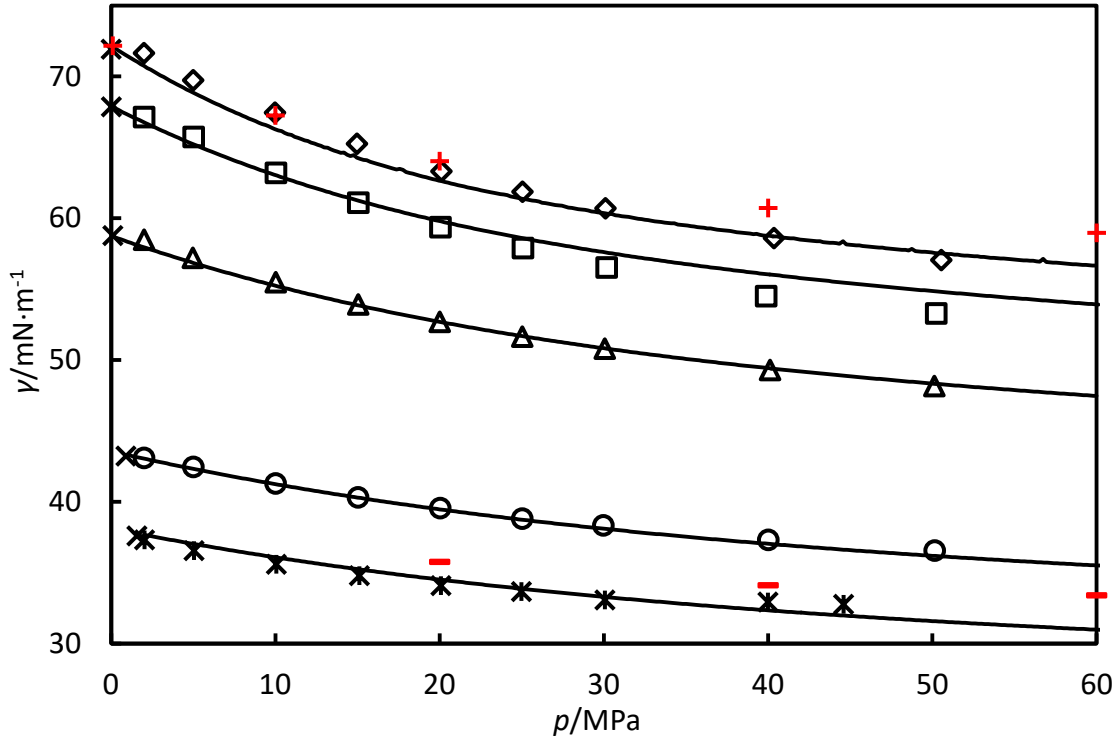


Figure 5.12 Interfacial tensions γ at pressures p for (Ar + H₂O). Experimental data: \diamond , 298 K; \square , 323 K; \triangle , 373 K; \circ , 448 K; $*$, 473 K; —, SAFT + SGT calculations; \times , surface tensions for pure water [188, 190]. Literature data from Wiegand and Franck [179]: $+$, 298 K; $-$, 373 K.

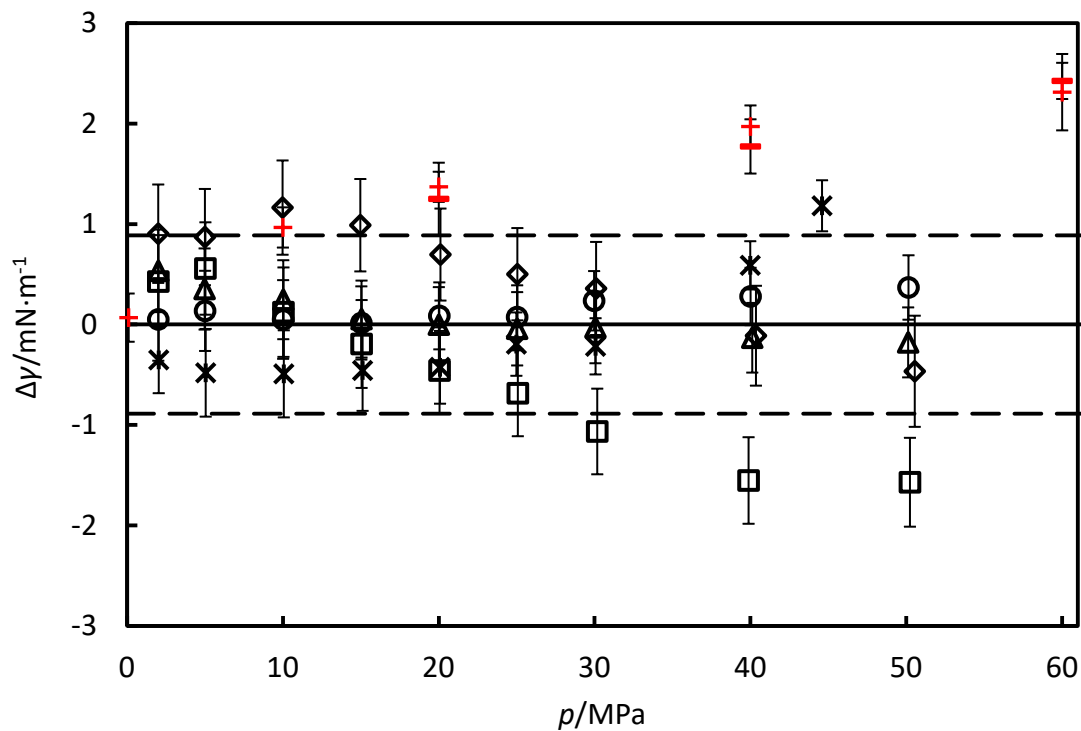


Figure 5.13 Difference $\Delta\gamma = (\gamma_{\text{exp}} - \gamma_{\text{calc}})$ between experimental interfacial tensions γ_{exp} of the (Ar + H₂O) system and values γ_{calc} calculated using the SAFT + SGT approach. Experimental data: \diamond , 298 K; \square , 323 K; \triangle , 373 K; \circ , 448 K; $*$, 473 K. Literature data from Wiegand and Franck [179]: $+$, 298 K; $-$, 373 K. Dashed lines represent the average absolute deviation of the calculations from the experimental data.

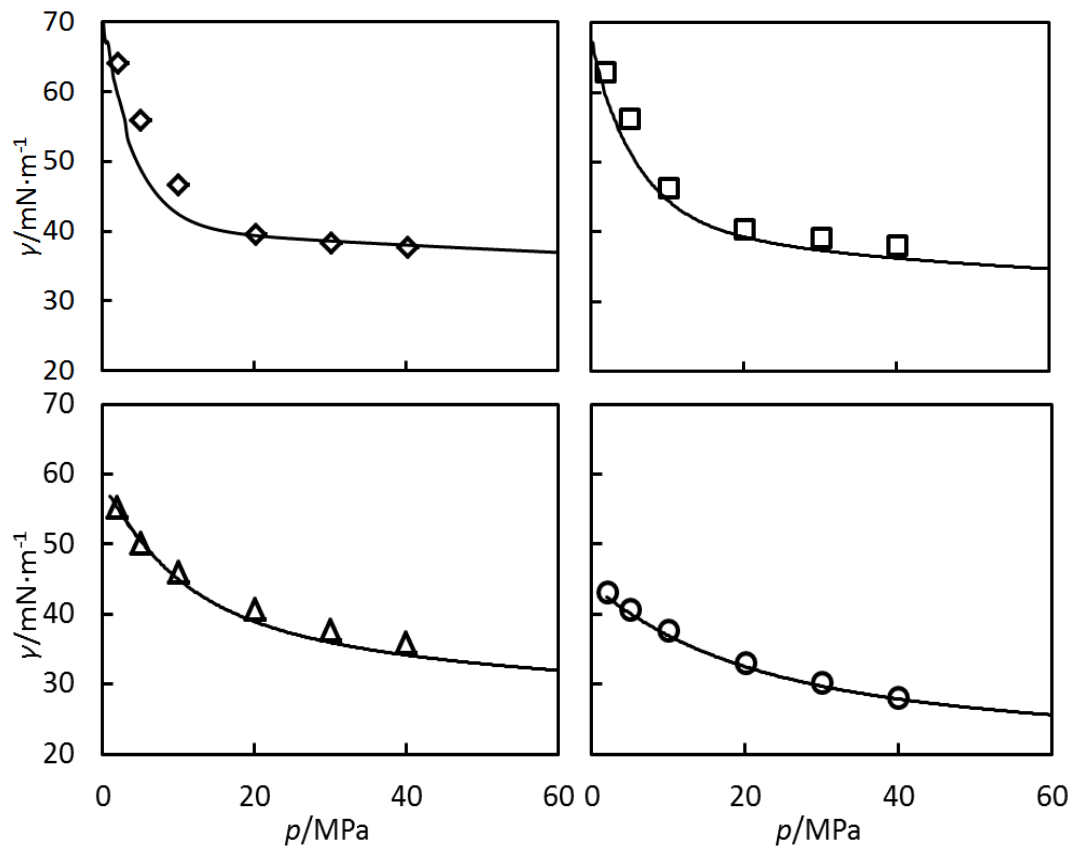


Figure 5.14 Interfacial tensions γ at pressures p for the $(\text{CO}_2 + \text{N}_2 + \text{H}_2\text{O})$ system. Experimental data: \diamond , 298 K; \square , 323 K; \triangle , 373 K; \circ , 448 K; —, SAFT + SGT calculations.

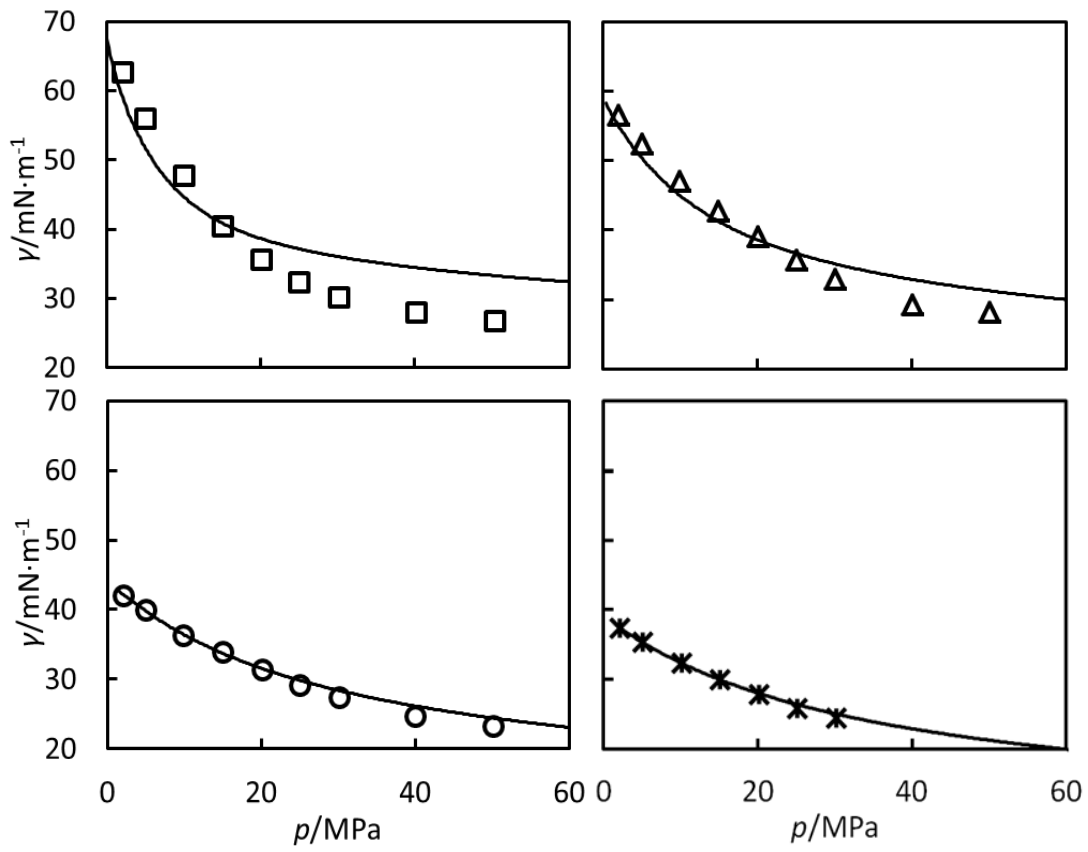


Figure 5.15 Interfacial tensions γ at pressures p for the $(\text{CO}_2 + \text{Ar} + \text{H}_2\text{O})$ system. Experimental data: \diamond , 298 K; \square , 323 K; \triangle , 373 K; \circ , 448 K; —, SAFT + SGT calculations.

6 Results - Contact Angle

This chapter reports the results of a feasibility study on the measurement of contact angles with the Interfacial Properties Rig. Contact angles of ($\text{CO}_2 + \text{brine}$) and ($\text{CO}_2 + \text{N}_2 + \text{brine}$) systems on calcite surfaces have been measured, at 333 K and 7 pressures, from (2 to 50) MPa, for a $1 \text{ mol}\cdot\text{kg}^{-1} \text{ NaHCO}_3$ brine solution, using the static and dynamic tilting base method on captive bubbles. The measurements were repeated at the same conditions for brine drops on calcite surfaces surrounded by CO_2 , for comparison of the two methods. The use of the NaHCO_3 brine solution was to slow down the dissolution of calcite in the acidic CO_2 -saturated brine.

6.1 Static Contact Angles

The static captive bubble images were captured at the start of each experimental condition, repeated for at least three times, and reproduced in Figure 6.1 for the ($\text{CO}_2 + \text{brine} + \text{calcite}$) system, and Figure 6.3 for the ($\text{CO}_2 + \text{N}_2 + \text{brine} + \text{calcite}$) system. The static sessile drop images were captured at the start of each experimental condition, repeated three times, and presented in Figure 6.2 for the ($\text{CO}_2 + \text{brine} + \text{calcite}$) system. The results are compared in Figure 6.4. For all of the methods, systems and conditions studied, calcite was found to be water-wet, with contact angles below 70° .

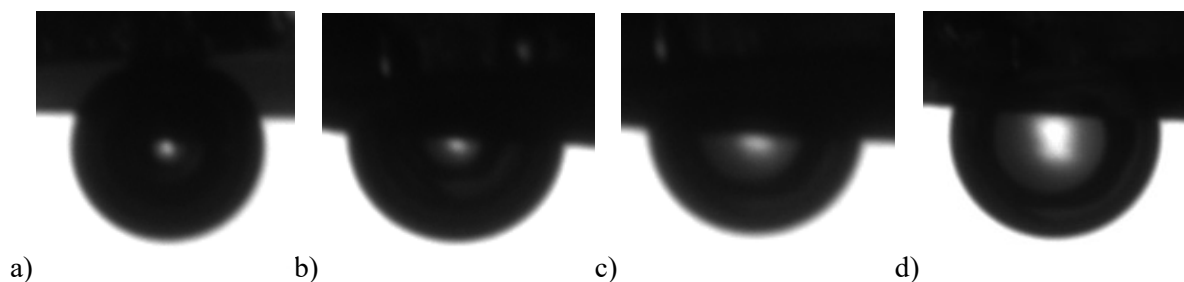


Figure 6.1 ($\text{CO}_2 + \text{brine} + \text{calcite}$) captive bubble at start of the experiment, at 333 K and a) 2 MPa b) 10 MPa c) 30 MPa d) 50 MPa

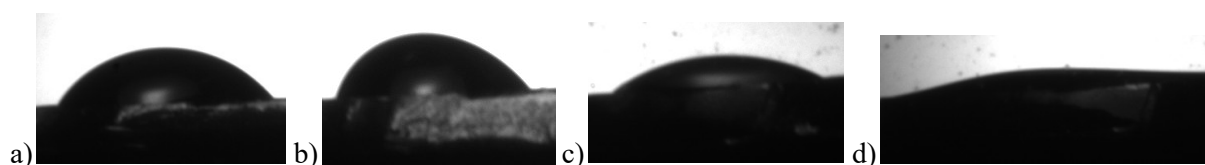


Figure 6.2 ($\text{CO}_2 + \text{brine} + \text{calcite}$) drop at start of the experiment, at 333 K and a) 2 MPa b) 10 MPa c) 30 MPa d) 50 MPa

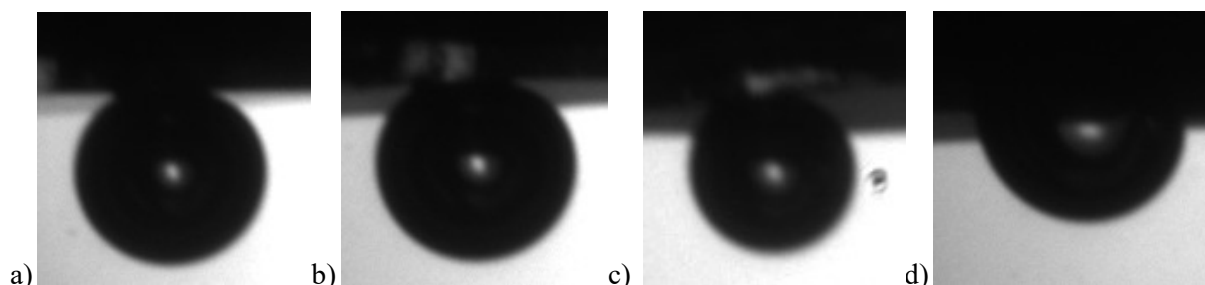


Figure 6.3 ($\text{CO}_2 + \text{N}_2 + \text{brine} + \text{calcite}$) captive bubble at start of the experiment, at 333 K and a) 2 MPa b) 10 MPa c) 30 MPa d) 50 MPa

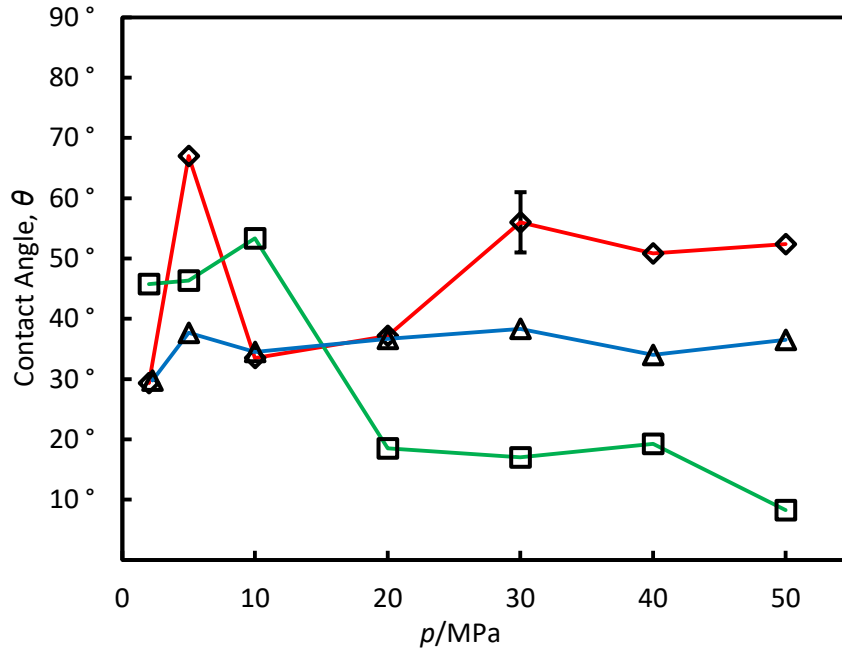


Figure 6.4 Static contact angles for the (CO₂ + brine + calcite) system measured with the ◇, captive bubble method, and □, sessile drop method; and the (CO₂ + N₂ + brine + calcite) system with the △, captive bubble method, at 333 K and pressures from (2 to 50) MPa. All contact angles are reported in the aqueous phase by manual reanalysis.

The captive bubble method of measuring the (CO₂ + brine + calcite) system yielded contact angles between 30 ° to 40 ° for pressures up to 20 MPa, with a possible anomaly at 5 MPa of 67 °. The high contact angle is possibly due to pinning of the bubble to surface heterogeneities, as discussed by Wang *et al.* [226]. The contact angles then increased within the range of 50 ° to 60 °, as pressure increased to 30 MPa and above. The change in behaviour was commonly attributed to the phase change near the critical pressure of CO₂. Neglecting the anomaly at 5 MPa, the (CO₂ + brine + calcite) system had similar contact angle values to the (CO₂ + N₂ + brine + calcite) system, for pressures below 20 MPa, measured with the captive bubble method. The addition of nitrogen to the system appears to have negligible effect on the contact angle when the pressure was less than 20 MPa. For pressures above 20 MPa, the contact angle for the (CO₂ + N₂ + brine + calcite) system remains fairly constant within the 30 ° to 40 ° range, differing from the CO₂-brine-calcite results. Farokhpour *et al.* [224, 225] found that calcite was strongly water-wet in the conditions studied, had no significant change in water-wettability with increasing pressure, except near critical pressure. They found that increasing the salt concentration had minor effects on CO₂ wettability.

The sessile drop method of measuring contact angles for the (CO₂ + brine + calcite) system produces results contradictory to the captive bubble method for the same system. The contact angles increase slightly with pressure, then above 10 MPa, decreases with increasing pressure. The recorded values between 10 ° to 20 ° agrees with the contact angle values reported by Farokhpour *et al.* [224, 225], measured using the captive bubble method, reported to be between 10 ° to 15 °, for a temperature of 309 K, over a comparable pressure range, in a 0.8 M NaCl brine solution. At 298 K, for pressures below CO₂ critical pressure, Espinoza and Santamarina [167] reported fairly constant contact angles of about 40 °, for a water droplet surrounded by CO₂ in water and NaCl brine, agreeing with our results. For pressures between critical to 10 MPa, the contact angle drops to about 30 °, differing from

our data here. As the measured results for the different methods on the same systems were inconclusive, it was not possible to say what the effect of adding nitrogen was on the contact angles.

The measured data was subject to large errors made in identifying the baseline, where a shadow of the substrate's further edge would cast a shadow on the closer edge to the camera in the images. This situation arises because the substrate has an irregular surface, slanted in certain parts from cleaving. This can be observed clearly in Figure 6.3a, where there appears to be two baselines, with different contact angles. In Figures 6.2 and 6.3, the images captured were not in focus and had imperfect horizontal substrate alignment. The software had problems identifying the baseline and edge of the bubble when the contours were blurred and less distinct. The data presented in Figure 6.4 was obtained by manual measurement, as the software calculated values were highly unreliable. For the sessile drop method, the measurements were further complicated by the residual drops and condensation on the windows, produced after pressure changes to the next measured state point.

6.2 Dynamic Contact Angles

The dynamic contact angle measurements carried out using the tilting plate method was unsuccessful. The baseline identification problem mentioned in Section 6.1 also applied to these measurements. The surface was not completely flat and had irregularities, so the bubble could move as the surface was tilted. The software could not find the bubble edge when the surface, bubble and background had insufficient contrast. For the drop measurements, the problem of the drop spreading outside of the imaged area as the plate was tilted also led to difficulties in the measurement.

6.3 Vertical Scanning Interferometry (VSI) Analysis

The calcite substrates used in the measurements were analysed with Vertical Scanning Interferometry (VSI), shown in Figure 6.5-6. The substrate surfaces made by cleaving had very uneven surfaces. A full scan of each substrate could not be taken due to the large variations. Therefore, several scans were taken of neighbouring sub-regions on each substrate. The surface of a reference freshly-cleaved substrate was analysed, and found to have significant surface irregularities.

In Figure 6.6, scans of various sub-regions of a substrate used for measurement are presented. This substrate has a central region where the surface presents significant damage. The cause for such damage is unclear. The pattern of the damaged surface does not correspond to typical pit patterns observed during the calcite dissolution process. Furthermore, the use of NaHCO_3 brine solution should have impeded such calcite dissolution. Farokhpoor *et al.* [224, 225], observed that the calcite surface became roughened after the experiments. The dissolution of CO_2 in water to form a weak carbonic acid could have caused the dissolution of parts of their calcite sample surface, creating surface heterogeneities. Their X-ray diffraction test showed that there were no mineralogy changes of the calcite surface after etching by dissolution in CO_2 saturated brine. However, such reactions could affect the physical characteristics of the sample, and hence the measured contact angles. Law and Zhao [50] cautions against making contact angle measurements on surfaces where dissolution occurs.

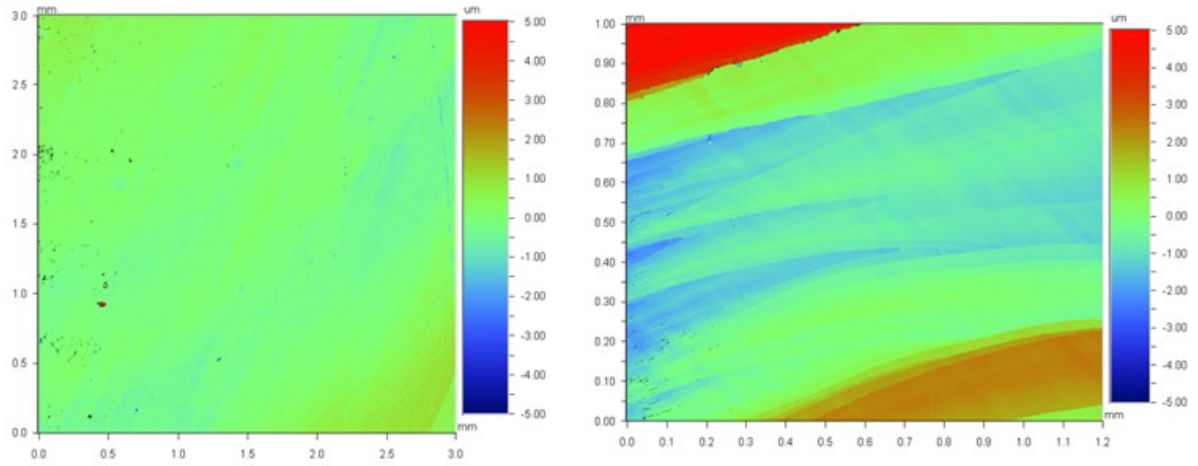


Figure 6.5 Vertical Scanning Interferometry (VSI) scans of two neighbouring sub-regions of the same reference substrate.

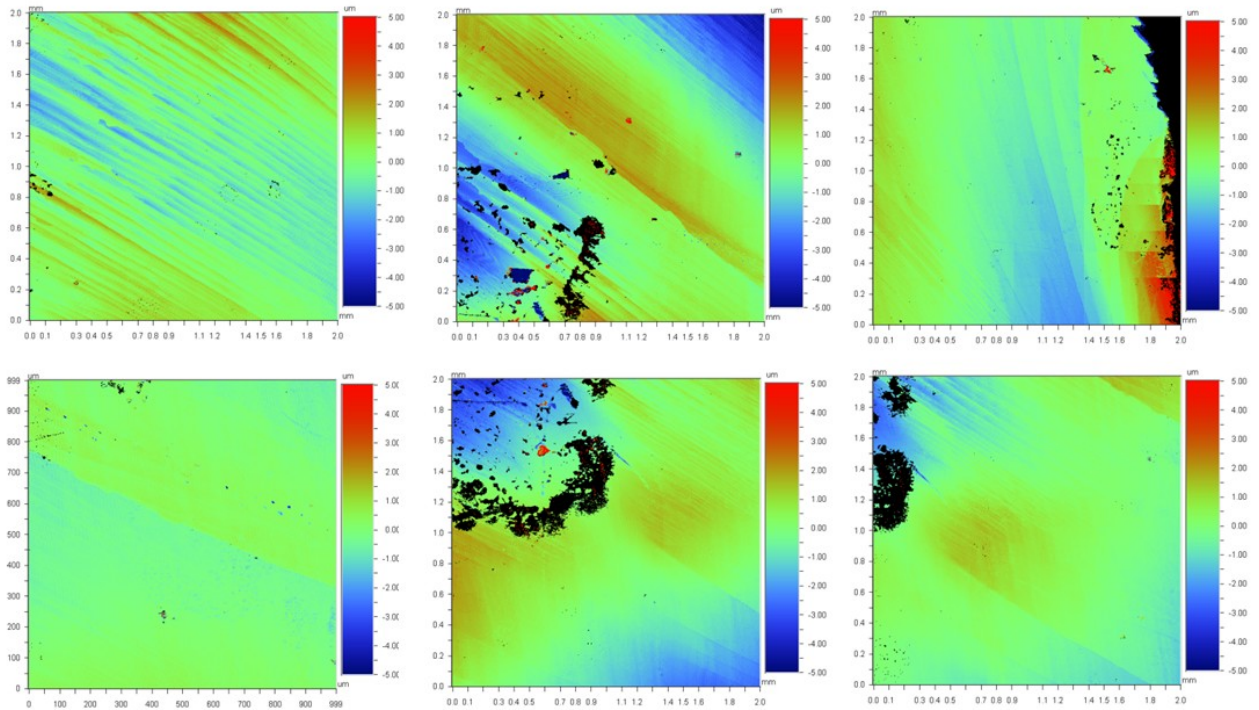


Figure 6.6 VSI scans of several neighbouring sub-regions on a substrate used for contact angle measurements of the (CO₂ + brine + calcite) system, at 333 K, from (2 to 50) MPa.

7 Conclusion

7.1 Effect of Gas Impurities

In Section 1.6, we introduced the effects of interfacial properties on the design and implementation of storage projects. One such parameter was the capillary entry pressure, which can be estimated by [17]:

$$p_{c,e} = \frac{2\gamma \cos \theta}{r}, \quad (1.1)$$

where $p_{c,e}$ is the capillary entry pressure, γ is the gas-brine interfacial tension, r is the effective pore throat radius, θ is the contact angle of the gas-brine-mineral surface.

From our measurements, we find that the addition of gas impurities, in particular, N_2 , Ar and H_2 , to the CO_2 storage stream, increases the interfacial tension of the system. The effect of adding N_2 gas to the CO_2 -brine-calcite system on contact angles was less clear, and for the purposes of this discussion, we will consider the overall effect on the calcite, which remains as water-wet for all conditions measured. Applying these findings on the capillary entry pressure, in eq. (1.1), qualitatively, we can understand that the increase in interfacial tension will cause a proportional increase in the capillary entry pressure. As calcite is found to be water-wet, with contact angles approximately between 10° to 60° , this sets a limit of $0.5 < \cos \theta < 1.0$, and the sign of the capillary entry pressure will remain the same.

In the case of injection, the CO_2 -rich stream needs to flow through the pores, so the CO_2 injection pressure is required to be greater than the surrounding formation brine pressure. The amount of overpressure required is estimated from the capillary entry pressure, using the effective pore radius of the reservoir:

$$p_{CO_2} - p_{brine} > p_{c,e}, \quad (1.2)$$

In the scenario when a gas impurity is added, the capillary entry pressure increases in response to interfacial tension changes. For a fixed formation brine pressure, this means that the lower limit for the injection pressure of the CO_2 -rich stream needs to be higher, when gas impurities are present. Higher injection pressures would lead to increased compression cost, additional safety risks of the process, and changes in the viscosity of the injected CO_2 stream, leading to altered flow patterns and behaviour. For caprock structural trapping to be effective, the overpressure must be less than the capillary entry pressure.

The SAFT + SGT IFT model created in this work can be added as a module to a reservoir simulator, such that for any composition of impurities present in the CO_2 stream, the IFT can be estimated. Improving the estimated IFT value means that the predictive performance of the reservoir simulator is also improved.

The contact angle is a measure of mineral wettability. Structural and capillary trapping are only effective if the rock formation is water-wet, when the cosine of the contact angle is non-negative. In the case of the calcite samples measured, representative of carbonate rock formations, we found that the mineral remains as water-wet for all conditions studied, including the addition of N_2 gas to the system. Therefore, structural and capillary trapping will remain effective for CO_2 streams with N_2 gas impurities, in carbonate rock formations.

7.2 Future Work

In terms of operability, the Interfacial Properties Rig can be improved upon in several ways. Firstly, for the image quality, a higher definition camera with faster frame rate can be used. The substrate installation procedure, and/or tools can be improved such that the substrate surface is ensured to be flat once fixed onto the substrate holder rod. Alternatively, the programme can be modified to allow tilted baselines, to match the surface imperfections which result from calcite cleaving. In order for the rig to be suitable for expansion and contraction contact angle measurements, a communication algorithm between the contact angle measurement programme, DropImage Advanced and the Quizix pumps needs to be constructed. A way of ensuring that the substrate holder rod does not become stuck in certain heights of the substrate manipulator needs to be found.

To overcome the difficulties of bubbles moving and slipping on slanted surfaces, the option of polishing the calcite surfaces can be tested. The surface roughness of the calcite can then be varied and investigated. This would be an interesting experiment, as the rough surfaces may be more representative of the carbonate reservoir rock formations than samples with perfectly smooth surfaces. However, the analysis of contact angles on rough surfaces will be more complex than those of smooth surfaces, and may be subject to even greater variations. The contact angle measurement and modelling of reactive systems such as CO₂ on calcite is an area that can be explored further.

In terms of IFT modelling with SGT + SAFT-VR Mie, the discrepancies at the low temperature conditions can be improved. In particular, data of the (CO₂ + Ar + H₂O) system are particularly poorly represented by the model at low temperatures and high pressures.

7.3 Summary

We reported interfacial tension measurements of the binary systems (N₂ + H₂O), (Ar + H₂O), and (H₂ + H₂O), and ternary systems (CO₂ + N₂ + H₂O), (CO₂ + Ar + H₂O) and (CO₂ + H₂ + H₂O), at pressures of (0.5 to 50.0) MPa, and temperatures of (298.15 to 473.15) K. The design of a custom-built Interfacial Properties Rig was detailed, capable of carrying out interfacial tension measurements by the pendant drop method, and contact angle measurements via static and dynamic methods. The interfacial tensions of all systems were found to decrease with increasing pressure. For ease of comparing with literature values, empirical correlations were developed for the binary systems. For the (N₂ + H₂O) system, the absolute average deviation is 0.42 mN·m⁻¹. For the (Ar + H₂O) system, the absolute average deviation is 0.29 mN·m⁻¹. For the (H₂ + H₂O) system, the absolute average deviation is 0.17 mN·m⁻¹.

Empirical predictions of the ternary systems, by means of empirical combining rules based on the coexisting phase compositions and the interfacial tensions of the binary sub-systems, were found to be somewhat inadequate at low temperatures. The use of SGT + SAFT-VR Mie to model interfacial tensions of the binary and ternary systems was reported, for systems involving CO₂, N₂ and Ar. The binary systems (N₂ + H₂O) and (Ar + H₂O), and ternary systems (CO₂ + N₂ + H₂O) and (CO₂ + Ar + H₂O), were modelled with average absolute relative deviations of 1.5 %, 1.8 %, 3.6 % and 7.9 % respectively.

A preliminary study of the feasibility to carry out contact angle studies with the Interfacial Properties Rig set-up was carried out. Contact angles of (CO₂ + brine) and (CO₂ + N₂ + brine) systems on calcite surfaces have been measured, at 333 K and 7 pressures, from (2 to 50) MPa, for a 1 mol·kg⁻¹ NaHCO₃ brine solution, using the static method on captive bubbles. The dynamic contact angle measurements were unsuccessful, and only the static contact angles are reported. The captive bubble and sessile drop methods used to measure the same CO₂-brine-calcite system produced contradictory trends. As the

measured results for the different methods on the same systems were inconclusive, it was not possible to determine what the effect of adding nitrogen was on the contact angles. Vertical Scanning Interferometry (VSI) analysis of the calcite substrate surfaces revealed significant surface irregularities of the samples produced via simple cleaving.

In the scenario when a gas impurity is added, the capillary entry pressure increases in response to interfacial tension changes. For a fixed formation brine pressure, this means that the lower limit for the injection pressure of the CO₂-rich stream needs to be higher, when gas impurities are present. For all of the methods, systems and conditions studied, calcite was found to be water-wet, with contact angles below 70 °. For structural and capillary trapping of CO₂ in water-wet carbonate rock formations, we conclude that it will remain effective for CO₂ streams with N₂ gas impurities.

8 References

- [1] Adoption of the Paris Agreement. Proposal by the President., in: Conference of the Parties Twenty-first session, Paris, 2015.
- [2] <http://climateactiontracker.org/news/253/Climate-pledges-will-bring-2.7C-of-warming-potential-for-more-action.html>, in: Climate pledges will bring 2.7°C of warming, potential for more action, Climate Action Tracker, 2015.
- [3] R.K. Pachauri, L.A. Meyer, Climate Change 2014: Synthesis Report, in, IPCC, 2014.
- [4] IEA, Energy Technology Perspectives in, Paris, France, 2015.
- [5] IEA, Energy Technology Perspectives, in, IEA, 2012.
- [6] Global Status CCS, in, Global CCS Institute, 2015.
- [7] <http://www.bgs.ac.uk/science/CO2/home.html>, in: CO₂ storage - Sleipner field beneath the North Sea, British Geological Survey, Natural Environment Research Council, 2016.
- [8] J. Serpa, J. Morbee, E. Tzimas, Technical and Economic Characteristics of a CO₂ Transmission Pipeline Infrastructure, in: JRC Scientific and Technical Reports, Institute for Energy, Joint Research Centre, European Commission, The Netherlands, 2011.
- [9] SaskPower, <http://saskpowerccs.com/ccs-projects/boundary-dam-carbon-capture-project/>, in: Boundary Dam Carbon Capture Project, SaskPower, 2016.
- [10] <http://www.energyglobal.com/downstream/the-environment/29062016/UK-sets-out-strategy-for-climate-action-3609/>, in, Energy Global, 2016.
- [11] H. Li, J.P. Jakobsen, Ø. Wilhelmsen, J. Yan, PVTxy properties of CO₂ mixtures relevant for CO₂ capture, transport and storage: Review of available experimental data and theoretical models, Applied Energy, 88 (2011) 3567-3579.
- [12] A. Georgiadis, G. Maitland, J.P.M. Trusler, A. Bismarck, Interfacial Tension Measurements of the (H₂O + CO₂) System at Elevated Pressures and Temperatures, J. Chem. Eng. Data 55 (2010) 4168–4175.
- [13] P. Olden, G. Pickup, M. Jin, E. Mackay, S. Hamilton, J. Somerville, A. Todd, Use of rock mechanics laboratory data in geomechanical modelling to increase confidence in CO₂ geological storage, International Journal of Greenhouse Gas Control, 11 (2012) 304-315.
- [14] B. Metz, O. Davidson, H. de Coninck, M.L.L. Meyer, Special Report on Carbon Dioxide Capture and Storage, in, IPCC, Cambridge, U.K, 2005.
- [15] S. Iglauer, M.S. Mathew, F. Bresme, Molecular dynamics computations of brine-CO₂ interfacial tensions and brine-CO₂-quartz contact angles and their effects on structural and residual trapping mechanisms in carbon geo-sequestration, Journal of Colloid and Interface Science, 386 (2012) 405-414.
- [16] W.R.I. (WRI), CCS Guidelines: Guidelines for Carbon Dioxide Capture, Transport, and Storage, (2008).
- [17] K. Thomas, D. Katz, M. Tek, Threshold pressure phenomena in porous media., SPE Journal, 8 (1968) 174-184.
- [18] CO₂ Trapping Mechanisms - Structural/Stratigraphic Trapping, in: http://www.co2captureproject.org/images/structural_storage1.jpg (Ed.), CO₂ Capture Project, 2016.
- [19] CO₂ Trapping Mechanisms - Residual Trapping, in: http://www.co2captureproject.org/images/residual_storage.jpg (Ed.), CO₂ Capture Project, 2016.
- [20] M. Akbarabadi, M. Piri, Relative permeability hysteresis and capillary trapping characteristics of supercritical CO₂/brine systems: An experimental study at reservoir conditions, Advances in Water Resources, 52 (2013) 190-206.
- [21] C.H. Pentland, R. El-Maghraby, A. Georgiadis, S. Iglauer, M.J. Blunt, Immiscible Displacements and Capillary Trapping in CO₂ Storage, Energy Procedia, 4 (2011) 4969-4976.

- [22] H.-J. Butt, K. Graf, M. Kappl, *Physics and Chemistry of Interfaces*, 2nd ed., Weinheim, 2006.
- [23] J.D. van der Waals, On the continuity of the gaseous and liquid states. English translation by J. S. Rowlinson, Dover Phoenix, Mineola, N.Y., USA (1988). in, University of Leiden, The Netherlands, 1873.
- [24] T. Young, An Essay on the Cohesion of Fluids., *Philosophical Transactions of the Royal Society of London*, 95 (1805) 65-87.
- [25] E.A. Guggenheim, *Thermodynamics* 4th ed., North Holland, Amsterdam, 1959.
- [26] R. Aveyard, D.A. Haydon, *An Introduction to the Principles of Surface Chemistry*, University Press, Cambridge, 1973.
- [27] W.A. Zisman, Relation of the Equilibrium Contact Angle to Liquid and Solid Constitution, in: F. Fowkes (Ed.) *Contact Angle, Wettability, and Adhesion*, *Advances in Chemistry.*, American Chemical Society, Washington, DC, 1964, pp. 1-51.
- [28] S. Iglauer, A. Paluszny, M.J. Blunt, Simultaneous oil recovery and residual gas storage: A pore-level analysis using in situ X-ray micro-tomography, *Fuel*, 103 (2013) 905-914.
- [29] Y. Yuan, T.R. Lee, *Contact Angle and Wetting Properties*, Springer, 2013.
- [30] H.B. Eral, D.J.C.M. 't Mannetje, J.M. Oh, Contact angle hysteresis: a review of fundamentals and applications, *Colloid and Polymer Science*, 291 (2012) 247-260.
- [31] J.G. Webster, H. Eren, *Measurement, Instrumentation, and Sensors Handbook: Spatial, Mechanical, Thermal, and Radiation Measurement.*, 2nd ed., CRC Press Boca Raton, Florida, 2014.
- [32] C. Garcia-Cordovilla, E. Louis, A. Pamies, The surface tension of liquid pure aluminium and aluminium-magnesium alloy, *J. Mater. Sci.*, 21 (1986) 2787-2792.
- [33] V. Schoettle, H.Y.J. Jennings, High-pressure high-temperature visual cell for interfacial tension measurement, *Rev. Sci. Instrum.*, 39 (1968) 386-388.
- [34] R. Simon, R.L. Schmidt, A system for determining fluid properties up 136 MPa and 473 K, *Fluid Phase Equilib.*, 10 (1983) 233-248.
- [35] F. Bashforth, J.C. Adams, An attempt to test the theories of capillary action by comparing the theoretical and measured forms of drops of fluid. With an explanation of the method of integration employed in constructing the tables which give the theoretical forms of such drops. , Cambridge, London, 1883.
- [36] S. Fordham, On the Calculation of Surface Tension from Measurements of Pendant Drops. , in: *Proceedings of the Royal Society of London. Series A, Mathematical and Physical Sciences.*, 1948, pp. 1-16.
- [37] O.S. Mills, Tables for use in the measurement of interfacial tensions between liquids with small density differences, *Br. J. Appl. Phys.*, 4 (1953) 247-252.
- [38] Y. Rotenberg, L. Boruvka, A.W. Neumann, Determination of Surface Tension and Contact Angle from the Shapes of Axisymmetric Fluid Interfaces, *J Colloid Interface Sci*, 93 (1983) 169-183.
- [39] P. Cheng, D. Li, L. Boruvka, Y. Rotenberg, A.W. Neumann, Automation of Axisymmetric Drop Shape Analysis for Measurements of Interfacial Tensions and Contact Angles, *Colloids and Surfaces*, 43 (1990) 151-167.
- [40] F.K. Skinner, Y. Rotenberg, A.W. Neumann, Contact angle measurements from the contact diameter of sessile drops by means of a modified axisymmetric drop shape analysis., *J Colloid Interface Sci*, 130 (1989) 25-34.
- [41] E. Moy, P. Cheng, Z. Policova, S. Treppo, D. Kwok, D.P. Mack, P.M. Sherman, A.W. Neumann, Measurement of contact angles from the maximum diameter of non-wetting drops by means of a modified axisymmetric drop shape analysis., *Colloids and Surfaces*, 58 (1991) 215-227.
- [42] O.I. del Río, A.W. Neumann, Axisymmetric Drop Shape Analysis: Computational Methods for the Measurement of Interfacial Properties from the Shape and Dimensions of Pendant and Sessile Drops., *J Colloid Interface Sci*, 196 (1997) 136-147.

- [43] A.W. Adamson, *Physical Chemistry of Surfaces*, 5th ed., John Wiley & Sons, New York, 1990.
- [44] L. Wilhelmy, Ueber die Abhängigkeit der Capillaritäts-Constanten des Alkohols von Substanz und Gestalt des benetzten festen Körpers. , *Annalen der Physik und Chemie*, 119 (1863) 117-217.
- [45] L. du Noüy, *J. Gen. Physiol.*, 1 (1919) 521.
- [46] J.F. Padday, Surface tension. II. The measurement of surface tension., in: E. Matijevic (Ed.) *Surface and Colloid Science*, John Wiley & Sons, New York, 1969.
- [47] A. Couper, Surface tension and its measurement, in: B.W. Rossiter, R.C. Baetzold (Eds.) *Physical Methods of Chemistry*, John Wiley & Sons, New York, 1993.
- [48] D.S. Ambwani, T.J. Fort, Pendant drop technique for measuring liquid boundary tensions, in: R.J. Good, R.R. Stromberg (Eds.) *Surface and Colloid Science*, Plenum Press, New York, 1979.
- [49] D.B. Thiessen, D.J. Chione, C.B. McCreary, W.B. Krantz, Robust digital image analysis of pendant drop shapes, *J Colloid Interface Sci*, 177 (1996) 658-665.
- [50] K.-Y. Law, H. Zhao, *Surface Wetting. Characterization, Contact Angle, and Fundamentals.*, Springer, 2016.
- [51] R.P. Woodward, <http://firsttenangstroms.com/pdfdocs/CAPaper.pdf>, in: Contact angle measurements using the drop shape method.
- [52] in: http://www.clspectrum.com/content/archive/2010/December/images/CLS_December_A11_Fig01.jpg (Ed.), 2010.
- [53] in: https://www.kruss.de/fileadmin/_processed_/csm_kruss_meth_captive_bubble_990bcfd061.png (Ed.), KRÜSS GmbH, 2016.
- [54] G.L. Mark, The determination of contact angles from measurements of the dimensions of small bubbles and drops. I. The spheroidal segment method for acute angles., *J Phys Chem*, 40 (1935) 159-167.
- [55] A.W. Neumann, R.J. Good, *Techniques of measuring contact angles. Surface and Colloid Science.*, Springer, 1979.
- [56] G.L. Mark, D.A. Lee, The determination of contact angles from measurements of the dimensions of small bubbles and drops II. The sessile drop method for obtuse angles., *J Phys Chem*, 40 (1935) 169-176.
- [57] A. Sklodowska, M. Wozniak, R. Matlakowska, The method of contact angle measurements and estimation of work of adhesion in bioleaching of metals. , *Biol Proc Online*, 1 (1999) 114-121.
- [58] V.A. Lubarda, K.A. Talke, Analysis of the equilibrium droplet shape based on an ellipsoidal droplet model., *Langmuir* 27 (2011) 10705-10713.
- [59] A. Kalantarian, R. David, A.W. Neumann, Methodology for high accuracy contact angle measurement., *Langmuir*, 25 (2009) 14146-14154.
- [60] O.I. del Río, D.Y. Kwok, R. Wu, J.M. Alvarez, A.W. Neumann, Contact angle measurements by axisymmetric drop shape analysis and an automated polynomial fit program., *Colloids and Surfaces A: Physicochemical and Engineering Aspects*, 143 (1998) 197-210.
- [61] A. Bateni, S.S. Susnar, A. Amirfazli, A.W. Neumann, A high-accuracy polynomial fitting approach to determine contact angles. , *Colloids and Surfaces A: Physicochemical and Engineering Aspects*, 219 (2003) 215-231.
- [62] A.F. Stalder, G. Kulik, D. Sage, L. Barbieri, P. Hoffmann, A snake-based approach to accurate determination of both contact points and contact angles., *Colloids and Surfaces A: Physicochemical and Engineering Aspects*, 286 (2006) 92-103.
- [63] http://www.face-kyowa.co.jp/english/en_science/en_theory/en_what_contact_angle/, in: What is Contact Angle?, Kyowa Interface Science Co. Ltd, 2016.
- [64] <http://www.ramehart.com/>, in: Technical Information, Ramé-Hart Instrument Co., 2015.

- [65] G. Macdougall, C. Ockrent, Surface energy relations in liquid/solid systems. 1. The adhesion of liquids to solids and a new method of determining the surface tension of liquids., *Proc R Soc Lond A*, 180 (1942) 151-173.
- [66] E. Pierce, F.J. Carmona, A. Amirfazli, Understanding of sliding and contact angle results in tilted plate experiments, *Colloids and Surfaces A: Physicochemical and Engineering Aspects*, 323 (2008) 73-82.
- [67] B. Krasovitski, A. Marmur, Drops down the hill. Theoretical study of limiting contact angles and the hysteresis range on a tilted plate., *Langmuir*, 21 (2005) 3881-3885.
- [68] D.B. Macleod, Relation Between Surface Tension and Density,, *Trans. Faraday Soc.*, 19 (1923).
- [69] H.T. Davis, *Statistical mechanics of phases, interfaces, and thin films*, Wiley-VCH, New York, 1996.
- [70] R. Evans, Density Functionals in the Theory of Nonuniform Fluids, in: D. Henderson (Ed.) *Fundamentals of Inhomogeneous Fluids*, Marcel Dekker, New York, 1992, pp. 85-177.
- [71] J.D. van der Waals, Thermodynamische theorie der capillariteit in de onderstelling van continue dichtheidsverandering, in: *Verhandelingen der Koninklijke Akademie van Wetenschappen te Amsterdam*, University of Leiden, 1893.
- [72] F.I. Llovel, A. Galindo, F.J. Blas, G. Jackson, Classical density functional theory for the prediction of the surface tension and interfacial properties of fluids mixtures of chain molecules based on the statistical associating fluid theory for potentials of variable range, *Journal of Chemical Physics*, 133 (2010).
- [73] H. Kahl, S. Enders, Calculation of surface properties of pure fluids using density gradient theory and SAFT-EOS, *Fluid Phase Equilibria*, 172 (2000) 27-42.
- [74] D.-Y. Peng, D.B. Robinson, A New Two-Constant Equation of State, *Ind. Eng. Chem. Fundam.*, 15 (1976) 59-64.
- [75] A. Gil-Villegas, A. Galindo, P.J. Whitehead, S.J. Mills, G. Jackson, A.N. Burgess, Statistical associating fluid theory for chain molecules with attractive potentials of variable range, *Journal of Chemical Physics*, 106 (1997) 4168.
- [76] R. Evans, The nature of the liquid-vapour interface and other topics in the statistical mechanics of non-uniform, classical fluids, *Advances in Physics*, 28 (1979) 143-200.
- [77] F. Llovel, A. Galindo, F.J. Blas, G. Jackson, Classical density functional theory for the prediction of the surface tension and interfacial properties of fluids mixtures of chain molecules based on the statistical associating fluid theory for potentials of variable range, *The Journal of chemical physics*, 133 (2010) 024704.
- [78] A. Georgiadis, F. Llovel, A. Bismarck, F.J. Blas, A. Galindo, G.C. Maitland, J.P.M. Trusler, G. Jackson, Interfacial tension measurements and modelling of (carbon dioxide+n-alkane) and (carbon dioxide+water) binary mixtures at elevated pressures and temperatures, *The Journal of Supercritical Fluids*, 55 (2010) 743-754.
- [79] S. Toxvaerd, Hydrostatic equilibrium in fluid interfaces, *The Journal of chemical physics*, 64 (1976) 2863-2867.
- [80] S. Toxvaerd, Statistical mechanical and quasithermodynamic calculations of surface densities and surface tension, *Molecular Physics*, 26 (1973) 91-99.
- [81] S. Toxvaerd, Perturbation theory for nonuniform systems - surface tension, *The Journal of chemical physics*, 55 (1971) 3116-3120.
- [82] M.J.D. Powell, *A Hybrid Method for Nonlinear Equations*, Numerical Methods for Nonlinear Equations Gordon and Breach, London, 1970.
- [83] A. Gil-Villegas, A. Galindo, P.J. Whitehead, S.J. Mills, G. Jackson, A.N. Burgess, Statistical associating fluid theory for chain molecules with attractive potentials of variable range, *The Journal of chemical physics*, 106 (1997) 4168-4186.

- [84] A. Galindo, L.A. Davies, A. Gil-Villegas, G. Jackson, The thermodynamics of mixtures and the corresponding mixing rules in the SAFT-VR approach for potentials of variable range, *Molecular Physics*, 93 (1998) 241-252.
- [85] J.W. Cahn, J.E. Hilliard, Free energy of a nonuniform system. I. Interfacial free energy, *Journal of Chemical Physics*, 28 (1958) 258.
- [86] A. Mejía, H. Segura, J. Wisniak, I. Polishuk, Correlation and prediction of interface tension for fluid mixtures: An approach based on cubic equations of state with the wong-sandler mixing rule, *Journal of Phase Equilibria & Diffusion*, 26 (2005) 215-224.
- [87] A. Mejía, H. Segura, L.F. Vega, J. Wisniak, Simultaneous prediction of interfacial tension and phase equilibria in binary mixtures, *Fluid Phase Equilibria*, 227 (2005) 225-238.
- [88] M.L. Michelsen, J.M. Mollerup, *Thermodynamic models: fundamentals & computational aspects*, Second Ed ed., Tie-Line Publications, Holte, Denmark, 2007.
- [89] B.S. Carey, L.E. Scriven, H.T. Davis, Semiempirical theory of surface tension of binary systems, *AIChE Journal*, 26 (1980) 705-711.
- [90] B.S. Carey, *The gradient theory of fluid interfaces*, in, University of Minnesota, 1979.
- [91] B.S. Carey, L.E. Scriven, H.T. Davis, Semiempirical theory of surface tensions of pure normal alkanes and alcohols, *AIChE Journal*, 24 (1978) 1076-1080.
- [92] P.M.W. Cornelisse, *The square gradient theory applied - simultaneous modelling of interfacial tension and phase behaviour*, in, Delft University of Technology, 1997.
- [93] P.M.W. Cornelisse, C.J. Peters, J. de Swaan Arons, Application of the Peng-Robinson equation of state to calculate interfacial tensions and profiles at vapour-liquid interfaces, *Fluid Phase Equilib.*, 82 (1993) 119-129.
- [94] P.M.W. Cornelisse, C.J. Peters, J. de Swaan Arons, Simultaneous prediction of phase equilibria, interfacial tension and concentration profiles, *Molecular Physics*, 80 (1993) 941-955.
- [95] B.S. Carey, *The gradient theory of fluid interfaces*, in, University of Minneapolis, 1979, pp. 461.
- [96] C. Miqueu, B. Mendiboure, A. Graciaa, J. Lachaise, Modeling of the surface tension of multicomponent mixtures with the gradient theory of fluid interfaces, *Industrial & Engineering Chemistry Research*, 44 (2005) 3321-3329.
- [97] M. Sahimi, H. Davis, L. Scriven, Thermodynamic modeling of phase and tension behavior of CO₂/hydrocarbon systems, *Society of Petroleum Engineers Journal*, 25 (1985) 235-254.
- [98] E. Schäfer, F. Horbach, S. Enders, Modeling of liquid-liquid interfacial properties of binary and ternary mixtures, *Journal of Chemical & Engineering Data*, 59 (2014) 3003-3016.
- [99] P.M. Larsen, B. Maribo-Mogensen, G.M. Kontogeorgis, A collocation method for surface tension calculations with the density gradient theory, *Fluid Phase Equilibria*, 408 (2016) 170-179.
- [100] X. Liang, M.L. Michelsen, G.M. Kontogeorgis, Pitfalls of using the geometric-mean combining rule in the density gradient theory, *Fluid Phase Equilibria*, 415 (2016) 75-83.
- [101] X. Liang, M.L. Michelsen, G.M. Kontogeorgis, A density gradient theory based method for surface tension calculations, *Fluid Phase Equilibria*, 428 (2016) 153-163.
- [102] A. Mejía, H. Segura, J. Wisniak, I. Polishuk, Association and molecular chain length effects on interfacial behavior, *Physics and Chemistry of Liquids*, 44 (2006) 45-59.
- [103] S. Enders, H. Kahl, Interfacial properties of water + alcohol mixtures, *Fluid Phase Equilibria*, 263 (2008) 160-167.
- [104] P.M.W. Cornelisse, M. Wijtkamp, C.J. Peters, J. de Swaan Arons, Interfacial tensions of fluid mixtures with polar and associating components, *Fluid Phase Equilibria*, 150-151 (1998) 633-640.
- [105] T. Zeiner, P. Schrader, S. Enders, D. Browarzik, Phase- and interfacial behavior of hyperbranched polymer solutions, *Fluid Phase Equilibria*, 302 (2011) 321-330.

- [106] C. Cumicheo, M. Cartes, H. Segura, E.A. Müller, A. Mejía, High-pressure densities and interfacial tensions of binary systems containing carbon dioxide+n-alkanes: (n-dodecane, n-tridecane, n-tetradecane), *Fluid Phase Equilibria*, 380 (2014) 82-92.
- [107] O.G. Niño Amézquita, S. Enders, P.T. Jaeger, R. Eggers, Interfacial properties of mixtures containing supercritical gases, *Journal of Supercritical Fluids*, 55 (2010) 724-734.
- [108] G. Niño-Amézquita, D. van Putten, S. Enders, Phase equilibrium and interfacial properties of water+CO₂ mixtures, *Fluid Phase Equilibria*, 332 (2012) 40-47.
- [109] S. Khosharay, M. Abolala, F. Varaminian, Modeling the surface tension and surface properties of (CO₂ + H₂O) and (H₂S + H₂O) with gradient theory in combination with sPC – SAFT EOS and a new proposed influence parameter, *Journal of Molecular Liquids*, 198 (2014) 292-298.
- [110] Y.-X. Zuo, E.H. Stenby, A linear gradient theory model for calculating interfacial tensions of mixtures, *Journal of Colloid and Interface Science*, 182 (1996) 126-132.
- [111] G.J. Gloor, G. Jackson, F.J. Blas, E.M. del Rio, E. de Miguel, An accurate density functional theory for the vapor-liquid interface of associating chain molecules based on the statistical associating fluid theory for potentials of variable range, *Journal of Chemical Physics*, 121 (2004) 12740-12759.
- [112] G.J. Gloor, G. Jackson, F.J. Blas, E.M. del Rio, E. de Miguel, Prediction of the vapor-liquid interfacial tension of nonassociating and associating fluids with the SAFT-VR density functional theory, *J Phys Chem C*, 111 (2007) 15513-15522.
- [113] D.-Y. Peng, D.B. Robinson, The characterization of the heptanes and heavier fractions for the GPA Peng-Robinson programs, in, *Gas Processors Association, GPA*, 1978.
- [114] G. Soave, Equilibrium constants from a modified Redlich-Kwong equation of state, *Chem. Eng. Sci.*, 27 (1972) 1197-1203.
- [115] G.M. Kontogeorgis, G.K. Folas, *Thermodynamic models for industrial applications - from classical and advanced mixing rules to association theories*, Wiley, New York, 2010.
- [116] E.A. Müller, K.E. Gubbins, Molecular-based equations of state for associating fluids: A review of soft and related approaches, *Industrial & Engineering Chemistry Research*, 40 (2001) 2193-2211.
- [117] I.G. Economou, Statistical associating fluid theory: a successful model for the calculation of thermodynamic and phase equilibrium properties of complex fluid mixtures, *Industrial & Engineering Chemistry Research*, 41 (2002) 953-962.
- [118] P. Paricaud, A. Galindo, G. Jackson, Recent advances in the use of the SAFT approach in describing electrolytes, interfaces, liquid crystals and polymers, *Fluid Phase Equilibria*, 194-197 (2002) 87-96.
- [119] S.P. Tan, H. Adidharma, M. Radosz, Recent advances and applications of statistical associating fluid theory, *Industrial & Engineering Chemistry Research*, 47 (2008) 8063-8082.
- [120] L.A. Davies, A. Gil-Villegas, G. Jackson, An analytical equation of state for chain molecules formed from Yukawa segments, *The Journal of chemical physics*, 111 (1999) 8659-8665.
- [121] L.A. Davies, A. Gil-Villegas, G. Jackson, Describing the properties of chains of segments interacting via soft-core potentials of variable range with the SAFT-VR approach, *International Journal of Thermophysics*, 19 (1998) 675-686.
- [122] T. Lafitte, D. Bessieres, M.M. Piñeiro, J.L. Daridon, Simultaneous estimation of phase behavior and second-derivative properties using the statistical associating fluid theory with variable range approach., *The Journal of chemical physics*, 124 (2006) 024509.
- [123] T. Lafitte, A. Apostolakou, C. Avendaño, A. Galindo, C.S. Adjiman, E.A. Müller, G. Jackson, Accurate statistical associating fluid theory for chain molecules formed from Mie segments., *Journal of chemical physics*, 139 (2013) 154504.
- [124] L. Lee, L. *Molecular Thermodynamics of Nonideal Fluids*, Butterworths, Boston, 1988.
- [125] J.A.A. Barker, D. Henderson, Perturbation theory and equation of state for fluids: The square - well potential, *Journal of Chemical Physics*, 47 (1967) 2856-2861.

- [126] J.A.A. Barker, D. Henderson, Perturbation theory and equation of state for fluids. II. A successful theory of liquids, *Journal of Chemical Physics*, 47 (1967) 2856-2861.
- [127] T. Boublík, Hard-sphere equation of state, *Journal of Chemical Physics*, 53 (1970) 471.
- [128] G.a. Mansoori, Equilibrium Thermodynamic Properties of the Mixture of Hard Spheres, *Journal of Chemical Physics*, 54 (1971) 1523.
- [129] B.-j. Zhang, Calculating thermodynamic properties from perturbation theory, *Fluid Phase Equilibria*, 154 (1999) 1-10.
- [130] L.T. Dufal S., Haslam A. J., Galindo A., Clark G. N. I., Vega C., Jackson G., The A in SAFT : Developing the contribution of association to the free energy within a Wertheim TPT1 treatment of generic Mie fluids, *Molecular Physics*, 113 (2015) 948-984.
- [131] L.T. Dufal S., Haslam A. J., Galindo A., Clark G. N. I., Vega C., Jackson G., The A in SAFT: developing the contribution of association to the free energy within a Wertheim TPT1 treatment of generic Mie fluids, *Mol. Phys.*, (accepted) (2015).
- [132] M.S. Wertheim, Fluids with highly directional attractive forces. I. Statistical thermodynamics, *Journal of Statistical Physics*, 35 (1984) 19-34.
- [133] M.S. Wertheim, Fluids with highly directional attractive forces. II. Thermodynamic perturbation theory and integral equations, *Journal of Statistical Physics*, 35 (1984) 35-47.
- [134] M.S. Wertheim, Fluids with highly directional attractive forces. III. Multiple attraction sites, *Journal of Statistical Physics*, 42 (1986) 459-476.
- [135] M.S. Wertheim, Fluids with highly directional attractive forces. IV. Equilibrium polymerization, *Journal of Statistical Physics*, 42 (1986) 477-492.
- [136] G. Mie, Zur kinetischen Theorie der einatomigen Körper, *Annalen der Physik*, 316 (1903) 657-697.
- [137] G. Jackson, W.G. Chapman, K.E. Gubbins, Phase-equilibria of associating fluids - spherical molecules with multiple bonding sites, *Molecular Physics*, 65 (1988) 1-31.
- [138] T. Boublík, Background correlation functions in the hard sphere systems, *Molecular Physics*, 59 (1986) 775-793.
- [139] A. Gil-villegas, G. Jackson, The thermodynamics of mixtures and the corresponding mixing rules in the SAFT-VR approach for potentials of variable range, *Molecular Physics*, 93 (1998) 241-252.
- [140] G.H. Hudson, J.C. McCoubrey, Intermolecular forces between unlike molecules. A more complete form of the combining rules, *Transactions of the Faraday Society*, 56 (1960) 761.
- [141] A.J. Haslam, A. Galindo, G. Jackson, Prediction of binary intermolecular potential parameters for use in modelling fluid mixtures, *Fluid Phase Equilibria*, 266 (2008) 105-128.
- [142] A. Georgiadis, G. Maitland, J.P.M. Trusler, A. Bismarck, Interfacial Tension Measurements of the (H₂O + CO₂) System at Elevated Pressures and Temperatures, *Journal of Chemical & Engineering Data*, 55 (2010) 4168-4175.
- [143] E.J.J. Slowinski, E.E. Gates, C.E. Waring, The Effect of Pressure on the Surface Tensions of Liquids, *J. Phys. Chem.*, 61 (1957) 808-810.
- [144] G.J. Heuer, Interfacial tension of water against hydrocarbon and other gases and adsorption of methane on solids at reservoir temperatures and pressures., in, University of Texas, 1957.
- [145] E.W. Hough, B.B.J. Wood, M.J. Rzasas, Adsorption at Water-Helium, -Methane and -Nitrogen Interfaces at Pressures to 15,000 p.s.i.a., *J. Phys. Chem.*, 56 (1952) 996-999.
- [146] R. Massoudi, A.D.J. King, Effect of Pressure on the Surface Tension of Water. Adsorption of Low Molecular Weight Gases on Water at 25°, *J. Phys. Chem.*, 78 (1974) 2262-2266.
- [147] R. Massoudi, A.D.J. King, Effect of Pressure on the Surface Tension of Aqueous Solutions. Adsorption of Hydrocarbon Gases, Carbon Dioxide, and Nitrous Oxide on Aqueous Solutions of Sodium Chloride and Tetra-n-butylammonium Bromide at 25°, *J. Phys. Chem.*, 79 (1975) 1670-1675.

- [148] C. Jho, D. Nealon, S. Shogbola, A.D.J. King, Effect of Pressure on the Surface Tension of Water: Adsorption of Hydrocarbon Gases and Carbon Dioxide on Water at Temperatures between 0 and 50°C, *Journal of Colloid and Interface Science*, 65 (1978) 141-154.
- [149] B.-S. Chun, G.T. Wilkinson, Interfacial Tension in High-Pressure Carbon Dioxide Mixtures, *Ind. Eng. Chem. Res.*, 34 (1995) 4371-4377.
- [150] A. Wesch, N. Dahmen, K. Ebert, J. Schön, Grenzflächenspannungen, Tropfengrößen und Kontaktwinkel im Zweiphasensystem H₂O/CO₂ bei Temperaturen von 298 bis 333 K und Drücken bis 30 MPa., *Chemie Ingenieur Technik*, 69 (1997) 942–946.
- [151] P.T. Jaeger, Grenzflächen und Stofftransport in verfahrenstechnischen Prozessen am Beispiel der Hochdruck-Gegenstromfraktionierung mit überkritischem Kohlendioxid, Shaker Verlag, Aachen, 1998.
- [152] S.R.P. da Rocha, K.P. Johnston, Molecular Structure of the Water–Supercritical CO₂ Interface, *J Phys Chem B*, 105 (2001) 12092-12104.
- [153] A. Hebach, A. Oberhof, N. Dahmen, A. Kogel, H. Ederer, E. Dinjus, Interfacial tension at elevated pressures - measurements and correlations in the water plus carbon dioxide system, *J Chem Eng Data*, 47 (2002) 1540-1546.
- [154] F. Tewes, F. Boury, Thermodynamic and Dynamic Interfacial Properties of Binary Carbon Dioxide-Water Systems, *J. Phys. Chem. B*, 108 (2004) 2405-2412.
- [155] J.-Y. Park, J.S. Lim, C.H. Yoon, C.H. Lee, K.P. Park, Effect of a Fluorinated Sodium Bis(2-ethylhexyl) Sulfosuccinate (Aerosol-OT, AOT) Analogue Surfactant on the Interfacial Tension of CO₂ + Water and CO₂ + Ni-Plating Solution in Near- and Supercritical CO₂, *Journal of Chemical & Engineering Data*, 50 (2005) 299-308.
- [156] C.-Y. Sun, G.-J. Chen, Measurement of Interfacial Tension for the CO₂ Injected Crude Oil + Reservoir Water System, *J. Chem. Eng. Data*, 50 (2005) 936-938.
- [157] D. Yang, P. Tontiwachwuthikul, Y. Gu, Interfacial Interactions between Reservoir Brine and CO₂ at High Pressures and Elevated Temperatures, *Energy & Fuels*, 19 (2005) 216-223.
- [158] J.L. Dickson, G. Gupta, T.S. Horozov, B.P. Binks, K.P. Johnston, Wetting phenomena at the CO₂/water/glass interface., *Langmuir*, 22 (2006) 2161-2170.
- [159] T. Akutsu, Y. Yamaji, H. Yamaguchi, M. Watanabe, R.L. Smith, H. Inomata, Interfacial tension between water and high pressure CO₂ in the presence of hydrocarbon surfactants, *Fluid Phase Equilibria*, 257 (2007) 163-168.
- [160] P. Chiquet, J.-L. Daridon, D. Broseta, S. Thibeau, CO₂/water interfacial tensions under pressure and temperature conditions of CO₂ geological storage, *Energy Conversion and Management*, 48 (2007) 736-744.
- [161] Y. Sutjiadi-Sia, P. Jaeger, R. Eggers, Interfacial phenomena of aqueous systems in dense carbon dioxide, *The Journal of Supercritical Fluids*, 46 (2008) 272-279.
- [162] C. Chalbaud, M. Robin, J.M. Lombard, F. Martin, P. Egermann, H. Bertin, Interfacial tension measurements and wettability evaluation for geological CO₂ storage, *Advances in Water Resources*, 32 (2009) 98-109.
- [163] C. Chalbaud, M. Robin, J.M. Lombard, H. Bertin, P. Egermann, Brine/CO₂ Interfacial Properties and Effects on CO₂ Storage in Deep Saline Aquifers, *Oil & Gas Science and Technology*, 65 (2010) 541-555.
- [164] S. Bachu, D.B. Bennion, Interfacial Tension between CO₂, Freshwater, and Brine in the Range of Pressure from (2 to 27) MPa, Temperature from (20 to 125) °C, and Water Salinity from (0 to 334 000) mg·L⁻¹, *Journal of Chemical & Engineering Data*, 54 (2009) 765–775.
- [165] S. Bachu, D. Brant Bennion, Dependence of CO₂-brine interfacial tension on aquifer pressure, temperature and water salinity, *Energy Procedia*, 1 (2009) 3157-3164.

- [166] C.A. Aggelopoulos, M. Robin, E. Perfetti, O. Vizika, CO₂/CaCl₂ solution interfacial tensions under CO₂ geological storage conditions: Influence of cation valence on interfacial tension, *Advances in Water Resources*, 33 (2010) 691-697.
- [167] D.N. Espinoza, J.C. Santamarina, Water-CO₂-mineral systems: Interfacial tension, contact angle, and diffusion—Implications to CO₂geological storage, *Water Resources Research*, 46 (2010).
- [168] P.K. Bikkina, Contact angle measurements of CO₂–water–quartz/calcite systems in the perspective of carbon sequestration, *International Journal of Greenhouse Gas Control*, 5 (2011) 1259-1271.
- [169] X. Li, E. Boek, G.C. Maitland, J.P.M. Trusler, Interfacial Tension of (Brines + CO₂): (0.864 NaCl + 0.136 KCl) at Temperatures between (298 and 448) K, Pressures between (2 and 50) MPa, and Total Molalities of (1 to 5) mol·kg⁻¹, *Journal of Chemical & Engineering Data*, 57 (2012) 1078-1088.
- [170] X. Li, E.S. Boek, G.C. Maitland, J.P.M. Trusler, Interfacial Tension of (Brines + CO₂): CaCl₂(aq), MgCl₂(aq), and Na₂SO₄(aq) at Temperatures between (343 and 423) K, Pressures between (2 and 50) MPa, and Molalities of (0.5 to 5) mol·kg⁻¹, *Journal of Chemical & Engineering Data*, 57 (2012) 1369-1375.
- [171] Y.T.F. Chow, G.C. Maitland, J.P.M. Trusler, Interfacial tensions of the (CO₂ + N₂ + H₂O) system at temperatures of (298 to 448)K and pressures up to 40MPa, *The Journal of Chemical Thermodynamics*, 93 (2016) 392-403.
- [172] L.M.C. Pereira, A. Chapoy, R. Burgass, M.B. Oliveira, J.A.P. Coutinho, B. Tohidi, Study of the impact of high temperatures and pressures on the equilibrium densities and interfacial tension of the carbon dioxide/water system, *J Chem Thermodynamics*, 93 (2016) 404-415.
- [173] M.B. King, A. Mubarak, J.D. Kim, T.R. Bott, The Mutual Solubilities of Water with Supercritical and Liquid Carbon Dioxide, *The Journal of Supercritical Fluids*, 5 (1992) 296-302.
- [174] A. Hebach, A. Oberhof, N. Dahmen, Density of Water + Carbon Dioxide at Elevated Pressures: Measurements and Correlation, *Journal of Chemical & Engineering Data*, 49 (2004) 950-953.
- [175] Y.T.F. Chow, G. Maitland, J.P.M. Trusler, Interfacial tensions of (CO₂ + N₂ + H₂O) system at temperatures of (298 to 448) K and pressures up to 40 MPa, *Journal of Chemical Thermodynamics*, (submitted) (2015).
- [176] B.-Y. Cai, J.-T. Yang, T.-M. Guo, Interfacial Tension of Hydrocarbon + Water/Brine Systems under High Pressure, *Journal of Chemical & Engineering Data*, 41 (1996) 493-496.
- [177] C. Duchateau, D. Broseta, A simple method for determining brine-gas interfacial tensions, *Advances in Water Resources*, 42 (2012) 30-36.
- [178] W.L. Masterton, J. Bianchi, E.J.J. Slowinski, Surface Tension And Adsorption In Gas-Liquid Systems At Moderate Pressures, *J. Phys. Chem.*, 67 (1963) 615-618.
- [179] G. Wiegand, E.U. Franck, Interfacial tension between water and non-polar fluids up to 473 K and 2800 bar, *Berichte der Bunsen-Gesellschaft für Physikalische Chemie*, 98 (1994) 809–817.
- [180] Y.-L. Tian, Y.-F. Xiao, H.-X. Zhu, D. Xi-Jing, R. Xiao-Wen, Z. Feng-Cai, Interfacial Tensions between Water and Non-polar Fluids at High Pressures and High Temperatures, *Acta Phys.-Chim. Sin*, 13 (1997) 89-95.
- [181] W. Yan, G.-Y. Zhao, G.-J. Chen, T.-M. Guo, Interfacial Tension of (Methane + Nitrogen) + Water and (Carbon Dioxide + Nitrogen) + Water Systems, *J. Chem. Eng. Data*, 46 (2001) 1544-1548.
- [182] V. Shah, D. Broseta, G. Mouronval, F. Montel, Water/acid gas interfacial tensions and their impact on acid gas geological storage, *International Journal of Greenhouse Gas Control*, 2 (2008) 594-604.
- [183] E.W. Hough, M.J. Rzas, B.B.J. Wood, Interfacial Tensions at Reservoir Pressures and Temperatures; Apparatus and the Water-Methane System, *Petroleum Transactions, AIME*, 192 (1951) 57-60.

- [184] H.Y.J. Jennings, G.H. Newman, The Effect of Temperature and Pressure on the Interfacial Tension of Water Against Methane-Normal Decane Mixtures, *SPE Journal*, 251 (1971).
- [185] W. Sachs, V. Meyn, Pressure and temperature dependence of the surface tension in the system natural gas/water principles of investigation and the first precise experimental data for pure methane/water at 25°C up to 46.8 MPa, *Colloids and Surfaces A: Physicochemical and Engineering Aspects*, 94 (1995) 291-301.
- [186] Q.-Y. Ren, G.-J. Chen, W. Yan, T.-M. Guo, Interfacial Tension of (CO₂ + CH₄) + Water from 298 K to 373 K and Pressures up to 30 MPa, *J. Chem. Eng. Data*, 45 (2000) 610-612.
- [187] C.-Y. Sun, G.-J. Chen, L.-Y. Yang, Interfacial Tension of Methane + Water with Surfactant near the Hydrate Formation Conditions, *J. Chem. Eng. Data*, 49 (2004) 1023-1025.
- [188] W. Wagner, A. Pruss, The IAPWS Formulation 1995 for the Thermodynamic Properties of Ordinary Water Substance for General and Scientific Use, *Journal of Physical and Chemical Reference Data*, 31 (2002) 387-535.
- [189] C. Tegeler, R. Span, W. Wagner, A new equation of state for argon covering the fluid region for temperatures from the melting line to 700 K at pressures up to 1000 MPa, *Journal of Physical and Chemical Reference Data*, 28 (1999) 779-850.
- [190] E.W. Lemmon, M.L. Huber, M.O. McLinden, NIST standard reference database 23: Reference fluid thermodynamic and transport properties - REFPROP, Version 9.1, in, National Institute of Standards and Technology Gaithersburg, 2013.
- [191] V. Shah, D. Broseta, G. Mouronval, F. Montel, Water/acid gas interfacial tensions and their impact on acid gas geological storage, *Int. J. Greenh. Gas Control*, 2 (2008) 594-604.
- [192] P.M.W. Cornelisse, C.J. Peters, J. De Swaan Arons, Simultaneous prediction of phase equilibria, interfacial tension and concentration profiles, *Mol. Phys.*, 80 (1993) 941-955.
- [193] W. Yan, G.-Y. Zhao, G.-J. Chen, T.-M. Guo, Interfacial Tension of (Methane + Nitrogen) + Water and (Carbon Dioxide + Nitrogen) + Water Systems, *J. Chem. Eng. Data*, 46 (2001) 1544-1548.
- [194] V. Shah, D. Broseta, Predicting interfacial tension between water and nonpolar fluids from a cahn-type theory, *Langmuir*, 23 (2007) 12598-12605.
- [195] A. Georgiadis, F. Llovel, A. Bismarck, F.J. Blas, A. Galindo, G.C. Maitland, J.P.M. Trusler, G. Jackson, Interfacial tension measurements and modelling of (carbon dioxide+n-alkane) and (carbon dioxide+water) binary mixtures at elevated pressures and temperatures, *J. Super. Crit. Fluids*, 55 (2010) 743-754.
- [196] T. Lafitte, D. Bessieres, M.M. Piñeiro, J.L. Daridon, Simultaneous estimation of phase behavior and second-derivative properties using the statistical associating fluid theory with variable range approach, *J. Chem. Phys.*, 124 (2006) 024509.
- [197] T. Lafitte, B. Mendiboure, M.M. Piñeiro, D. Bessières, C. Miqueu, Interfacial properties of water/CO₂: A comprehensive description through a gradient theory-SAFT-VR mie approach, *Journal of Physical Chemistry B*, 114 (2010) 11110-11116.
- [198] L.C. Nielsen, I.C. Bourg, G. Sposito, Predicting CO₂-water interfacial tension under pressure and temperature conditions of geologic CO₂ storage, in: *Geochimica et Cosmochimica Acta*, Elsevier Ltd, 2012, pp. 28-38.
- [199] J. Gross, J. Vrabec, An equation-of-state contribution for polar components: dipolar molecules, *AIChE Journal*, 52 (2006) 1194-1204.
- [200] G.M. Kontogeorgis, E.C. Voutsas, I.V. Yakoumis, D.P. Tassios, An equation of state for associating fluids, *Industrial & Engineering Chemistry Research*, 35 (1996) 4310-4318.
- [201] S. Khosharay, F. Varaminian, Modeling interfacial tension of (CH₄+N₂)+H₂O and (N₂+CO₂)+H₂O systems using linear gradient theory, *Korean Journal of Chemical Engineering*, 30 (2013) 724-732.

- [202] N. Von Solms, M.L. Michelsen, G.M. Kontogeorgis, N.V. Solms, Computational and physical performance of a modified PC-SAFT equation of state for highly asymmetric and associating mixtures, *Industrial & engineering chemistry research*, 42 (2003) 1098-1105.
- [203] V. Papaioannou, T. Lafitte, C. Avendaño, C.S. Adjiman, G. Jackson, E.a. Müller, A. Galindo, Group contribution methodology based on the statistical associating fluid theory for heteronuclear molecules formed from Mie segments., *Journal of chemical physics*, 140 (2014) 054107.
- [204] E.A. Müller, A. Mejía, Resolving discrepancies in the measurements of the interfacial tension for the CO₂ + H₂O mixture by computer simulation, *Journal of Physical Chemistry Letters*, 5 (2014) 1267-1271.
- [205] S.H. Huang, M. Radosz, Equation of state for small, large, polydisperse and associating molecules, *Industrial and Engineering Chemistry Research*, 29 (1990) 2284-2294.
- [206] S. Khosharay, F. Varaminian, Experimental and modeling investigation on surface tension and surface properties of (CH₄ + H₂O), (C₂H₆ + H₂O), (CO₂ + H₂O) and (C₃H₈ + H₂O) from 284.15 K to 312.15 K and pressures up to 60 bar, *International Journal of Refrigeration*, 47 (2014) 26-35.
- [207] G. Soave, Equilibrium constants from a modified Redlich-Kwong equation of state, *Chem. Eng. Sci.*, 27 (1972) 1197-1203.
- [208] S. Khosharay, Linear gradient theory for modeling investigation on the surface tension of (CH₄+H₂O), (N₂+H₂O) and (CH₄+N₂)+H₂O systems, *Journal of Natural Gas Science and Engineering*, 23 (2015) 474-480.
- [209] D.-Y. Peng, D.B. Robinson, A new two-constant equation of state, *Ind. Eng. Chem. Fundam.*, 15 (1976) 59-64.
- [210] F. Llovel, N. Mac Dowell, F.J. Blas, A. Galindo, G. Jackson, Application of the SAFT-VR density functional theory to the prediction of the interfacial properties of mixtures of relevance to reservoir engineering, *Fluid Phase Equilibria*, 336 (2012) 137-150.
- [211] C. Miqueu, B. Mendiboure, C. Graciaa, J. Lachaise, Modelling of the surface tension of binary and ternary mixtures with the gradient theory of fluid interfaces, *Fluid Phase Equilibria*, 218 (2004) 189-203.
- [212] C. Miqueu, B. Mendiboure, A. Graciaa, J. Lachaise, Petroleum mixtures: An efficient predictive method for surface tension estimations at reservoir conditions, *Fuel*, 87 (2008) 612-621.
- [213] E.A. Müller, A. Mejía, Interfacial properties of selected binary mixtures containing n-alkanes, *Fluid Phase Equilibria*, 282 (2009) 68-81.
- [214] T. Lafitte, B. Mendiboure, M.M. Piñeiro, D. Bessières, C. Miqueu, Interfacial Properties of Water/CO₂: A Comprehensive Description through a Gradient Theory-SAFT-VR Mie Approach, *The Journal of Physical Chemistry B*, 114 (2010) 11110–11116.
- [215] S. Khosharay, F. Varaminian, Modeling interfacial tension of (CH₄+N₂)+H₂O and (N₂+CO₂)+H₂O systems using linear gradient theory, *Korean Journal of Chemical Engineering*, 30 (2013) 724-732.
- [216] Y.T.F. Chow, D.K. Eriksen, A. Galindo, A.J. Haslam, G. Jackson, G.C. Maitland, J.P.M. Trusler, Interfacial tensions of systems comprising water, carbon dioxide and diluent gases at high pressures: Experimental measurements and modelling with SAFT-VR Mie and square-gradient theory, *Fluid Phase Equilibria*, 407 (2016) 159-176.
- [217] P. Jaeger, A. Pietsch, Characterization of reservoir systems at elevated pressure, *Journal of Petroleum Science and Engineering*, 64 (2009) 20-24.
- [218] D. Broseta, N. Tonnet, V. Shah, Are rocks still water-wet in the presence of dense CO₂ or H₂S?, *Geofluids*, 12 (2012) 280-294.
- [219] Y. Kim, J. Wan, T.J. Kneafsey, T.K. Tokunaga, Dewetting of silica surfaces upon reactions with supercritical CO₂ and brine: pore-scale studies in micromodels, *Environmental Science & Technology*, 46 (2012) 4228-4235.

- [220] S. Saraji, L. Goual, M. Piri, Wettability in CO₂/Brine/Quartz Systems: An Experimental Study at Reservoir Conditions, in: SPE Annual Technical Conference and Exhibition, Society of Petroleum Engineers, San Antonio, Texas, USA, 2012.
- [221] N. Siemons, H. Bruining, H. Castelijn, K.H. Wolf, Pressure dependence of the contact angle in a CO₂-H₂O-coal system, *Journal of Colloid and Interface Science*, 297 (2006) 755-761.
- [222] R. Sakurovs, S. Lavrencic, Contact angles in CO₂-water-coal systems at elevated pressures, *International Journal of Coal Geology*, 87 (2011) 26-32.
- [223] N. Shojai Kaveh, K.H. Wolf, S.N. Ashrafizadeh, E.S.J. Rudolph, Effect of coal petrology and pressure on wetting properties of wet coal for CO₂ and flue gas storage, *International Journal of Greenhouse Gas Control*, 11 (2012) 91-101.
- [224] R. Farokhpoor, B.J.A. Bjørkvik, E. Lindeberg, O. Torsæter, Wettability behaviour of CO₂ at storage conditions, *International Journal of Greenhouse Gas Control*, 12 (2013) 18-25.
- [225] R. Farokhpoor, B.J.A. Bjørkvik, E. Lindeberg, O. Torsæter, CO₂ Wettability Behavior During CO₂ Sequestration in Saline Aquifer -An Experimental Study on Minerals Representing Sandstone and Carbonate, *Energy Procedia*, 37 (2013) 5339-5351.
- [226] S. Wang, Z. Tao, S.M. Persily, A.F. Clarens, CO₂ Adhesion on Hydrated Mineral Surfaces, *Environ Sci Technol*, 47 (2013) 11858-11865.
- [227] S. Iglauer, A. Salamah, M. Sarmadivaleh, K. Liu, C. Phan, Contamination of silica surfaces: Impact on water-CO₂-quartz and glass contact angle measurements, *International Journal of Greenhouse Gas Control*, 22 (2014) 325-328.
- [228] P.K. Bikkina, Reply to the comments on "Contact angle measurements of CO₂-water-quartz/calcite systems in the perspective of carbon sequestration", *International Journal of Greenhouse Gas Control*, 7 (2012) 263-264.
- [229] Titanium Alloy Guide, in: RMI Titanium Company, 2000.
- [230] H.P.T. Association, High Pressure Safety Code, London (c/o Dr G. Saville, Department of Chemical Engineering, Imperial College, SW7 BY) : The Association, 1977., 1988.
- [231] International Association for the Properties of Water and Steam, Release on the surface tension of ordinary water substance, *Physical Chemistry of Aqueous Systems*, in: 12th International Conference on the Properties of Water and Steam, Orlando, Florida, 1994, pp. A139-A142.
- [232] Surface Energy Data for PTFE: Polytetrafluoroethylene, in, Diversified Enterprises, 2009.
- [233] F.K. Hansen, G. Rødsrud, Surface tension by pendant drop : I. A fast standard instrument using computer image analysis., *J Colloid Interface Sci*, 141 (1991) 1-9.
- [234] F.K. Hansen, Surface Tension by Image Analysis: Fast and Automatic Measurements of Pendant and Sessile Drops and Bubbles. , *J Colloid Interface Sci*, 160 (1993) 209-217.
- [235] R.T. Ferrell, D.M. Himmelblau, Diffusion coefficients of nitrogen and oxygen in water, *Journal of Chemical & Engineering Data*, 12 (1967) 111-115.
- [236] D.L. Wise, G. Houghton, The diffusion coefficients of ten slightly soluble gases in water at 10-60°C, *Chem. Eng. Sci.*, 21 (1966) 999-1010.
- [237] H. Renon, J.M. Prausnitz, Local compositions in thermodynamic excess functions for liquid mixtures, *AIChE J.* , (1968) 135-144.
- [238] C.H. Whitson, M.L. Michelsen, The negative flash, *Fluid Phase Equilibr.*, 53 (1989) 51-71.
- [239] S.-X. Hou, G.C. Maitland, J.P.M. Trusler, Measurement and modeling of the phase behavior of the (carbon dioxide+water) mixture at temperatures from 298.15K to 448.15K, *Journal of Supercritical Fluids*, 73 (2013) 87-96.
- [240] E.W. Lemmon, M.L. Huber, M.O. McLinden, NIST Standard Reference Database 23: Reference Fluid Thermodynamic and Transport Properties-REFPROP, Version 9.1, in, National Institute of Standards and Technology, Standard Reference Data Program, Gaithersburg, 2013.

- [241] J.C. Moore, R. Battino, T.R. Rettich, Y.P. Handa, E. Wilhelm, Partial Molar Volumes of "Gases" at Infinite Dilution in Water at 29815 K, *J. Chem. Eng. Data* 27 (1982) 22-24.
- [242] R. Span, E.W. Lemmon, R.T. Jacobsen, W. Wagner, A. Yokozeki, A Reference Equation of State for the Thermodynamic Properties of Nitrogen for Temperatures from 63.151 to 1000 K and Pressures to 2200 MPa, *Journal of Physical and Chemical Reference Data*, 29 (2000) 1361-1433.
- [243] S. Mao, Z. Duan, A thermodynamic model for calculating nitrogen solubility, gas phase composition and density of the N_2 - H_2O - $NaCl$ system, *Fluid Phase Equilibria*, 248 (2006) 103-114.
- [244] C. Tegeler, R. Span, W. Wagner, A New Equation of State for Argon Covering the Fluid Region for Temperatures from the Melting Line to 700 K at Pressures up to 1000 MPa, *J. Phys. Chem. Ref. Data*, 28 (1999) 779-850.
- [245] J. Sedlbauer, J.P. O'Connell, R.H. Wood, A new equation of state for correlation and prediction of standard molal thermodynamic properties of aqueous species at high temperatures and pressures, *Chemical Geology*, 163 (2000) 43-63.
- [246] J.W. Leachman, R.T. Jacobsen, S.G. Penoncello, E.W. Lemmon, Fundamental Equations of State for Parahydrogen, Normal Hydrogen, and Orthohydrogen, *J. Phys. Chem. Ref. Data*, 38 (2009) 721-748.
- [247] R. Span, W. Wagner, A New Equation of State for Carbon Dioxide Covering the Fluid Region from the Triple-Point Temperature to 1100 K at Pressures up to 800 MPa, *J. Phys. Chem. Ref. Data*, 25 (1996) 1509-1596.
- [248] W. Wagner, A. Pruss, The IAPWS Formulation 1995 for the Thermodynamic Properties of Ordinary Water Substance for General and Scientific Use, *J. Phys. Chem. Ref. Data*, 31 (2002) 387-535.
- [249] A.M. Abudour, S.A. Mohammad, K.A.M. Gasem, Modeling high-pressure phase equilibria of coalbed gases/water mixtures with the Peng–Robinson equation of state, *Fluid Phase Equilib.*, 319 (2012) 77-89.
- [250] R. Fernández-Prini, J.L. Alvarez, A.H. Harvey, Henry's Constants and Vapor–Liquid Distribution Constants for Gaseous Solutes in H_2O and D_2O at High Temperatures, *J. Phys. Chem. Ref. Data* 32 (2003) 903.
- [251] M.J. Lazzaroni, D. Bush, C.A. Eckert, R. Gläser, High-pressure vapor–liquid equilibria of argon+carbon dioxide+2-propanol, *J. Supercrit. Fluids*, 37 (2006) 135-141.
- [252] R. Privat, J.-N. Jaubert, Predicting the Phase Equilibria of Carbon Dioxide Containing Mixtures Involved in CCS Processes Using the PPR78 Model, (2014).
- [253] M. Mantovani, P. Chiesa, G. Valenti, M. Gatti, S. Consonni, Supercritical pressure–density–temperature measurements on CO_2 - N_2 , CO_2 - O_2 and CO_2 -Ar binary mixtures, *Journal of Supercritical Fluids*, 61 (2012) 34-43.
- [254] M. Schmidt, H. Lipson, Eureka [Software], in, www.nutonian.com, 2014.
- [255] M. Schmidt, H. Lipson, Distilling Free-Form Natural Laws from Experimental Data, *Science*, 324 (2009) 81-85.
- [256] G. Wiegand, E.U. Franck, Interfacial tension between water and non-polar fluids up to 473 K and 2800 bar, *Ber. Bunsenges. Phys. Chem.*, 98 (1994) 809–817.
- [257] O. Kunz, W. Wagner, The GERG-2008 Wide-Range Equation of State for Natural Gases and Other Mixtures: An Expansion of GERG-2004, *Journal of Chemical & Engineering Data*, 57 (2012) 3032–3091.
- [258] Y.-L. Tian, Y.-F. Xiao, H.-X. Zhu, D. Xi-Jing, R. Xiao-Wen, Z. Feng-Cai, Interfacial Tensions between Water and Non-polar Fluids at High Pressures and High Temperatures, *Acta Physico-Chimica Sinica*, 13 (1997) 89-95.

- [259] W. Yan, G.-Y. Zhao, G.-J. Chen, T.-M. Guo, Interfacial Tension of (Methane + Nitrogen) + Water and (Carbon Dioxide + Nitrogen) + Water Systems, *Journal of Chemical & Engineering Data*, 46 (2001) 1544-1548.
- [260] G. Wiegand, E.U. Franck, Interfacial tension between water and non-polar fluids up to 473 K and 2800 bar, *Berichte der Bunsengesellschaft für physikalische Chemie*, 98 (1994) 809–817.
- [261] S. Dufal, T. Lafitte, A. Galindo, G. Jackson, A.J. Haslam, Developing intermolecular-potential models for use with the SAFT-VR Mie Equation of State, *AIChE Journal*, 61 (2015) 2891-2912.
- [262] R. Eisenschitz, F. London, über das Verhältnis der van der Waalsschen Kräfte zu den homöopolaren Bindungskräften, *Zeitschrift für Physik*, 60 (1930) 491-527.
- [263] G.M. Kontogeorgis, G.K. Folas, N. Muro-Suñé, F. Roca Leon, M.L. Michelsen, Solvation phenomena in association theories with applications to oil & gas and chemical industries, *Oil and Gas Science and Technology*, 63 (2008) 305-319.
- [264] L. Avaullee, C.S. Adjiman, F. Calado, P. Duchet-Suchaux, J. Fuentes, A. Galindo, G. Jackson, T. Lafitte, C.C. Pantelides, V. Papaioannou, In preparation, (2015).
- [265] A. Chapoy, A.H. Mohammadi, B. Tohidi, D. Richon, Gas solubility measurement and modeling for the nitrogen + water system from 274.18 K to 363.02 K, *Journal of Chemical & Engineering Data*, 49 (2004) 1110-1115.
- [266] R. Crovetto, Solubilities of inert gases and methane in H₂O and in D₂O in the temperature range of 300 to 600 K, *Journal of Chemical Physics*, 76 (1982) 1077.
- [267] G.H. Zenner, L.I. Dana, Liquid-vapor equilibrium compositions of carbon dioxide-oxygen-nitrogen mixtures, *Chemical Engineering Progress Symposium Series*, 44 (1963) 36-41.
- [268] C. Coquelet, A. Valtz, F. Dieu, D. Richon, P. Arpentinier, F. Lockwood, Isothermal *P*, *x*, *y* data for the argon+carbon dioxide system at six temperatures from 233.32 to 299.21 K and pressures up to 14 MPa, *Fluid Phase Equilibria*, 273 (2008) 38-43.

9 Appendix

9.1 Piping and Instrumentation Diagram (P&ID)

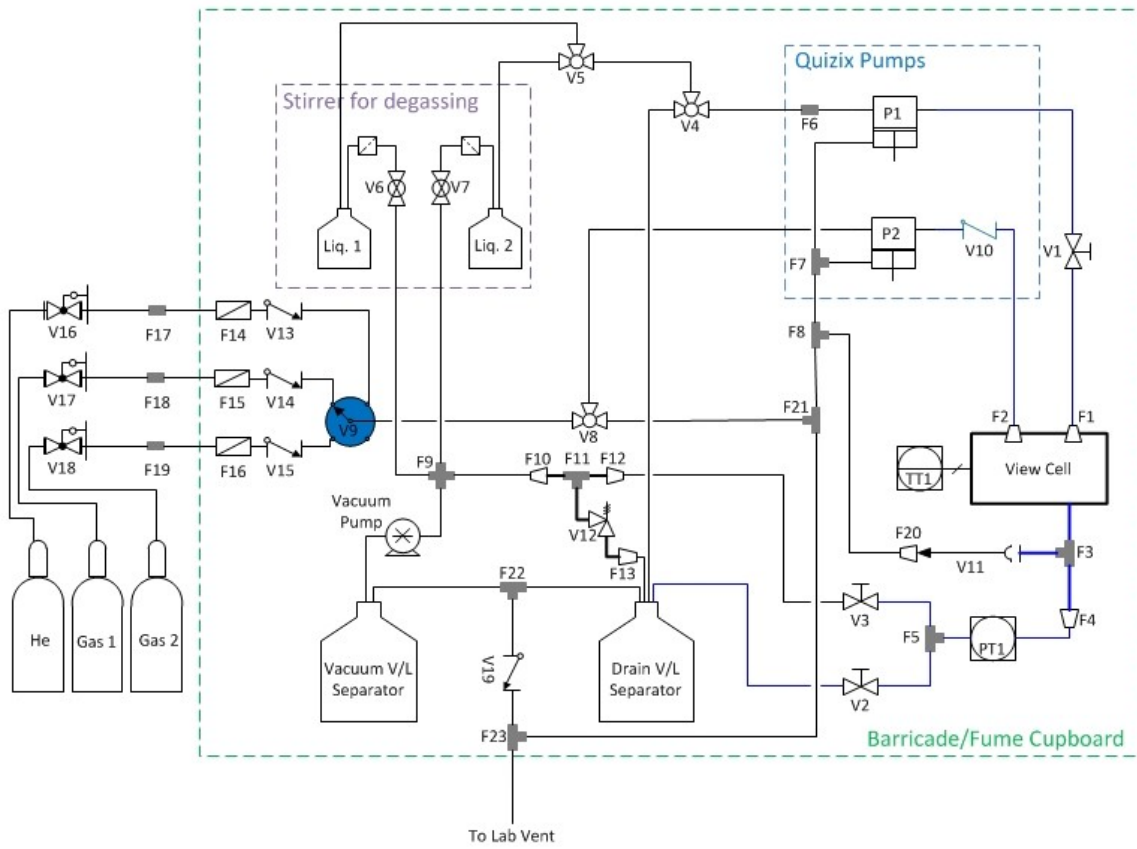


Figure 9.1 Piping and Instrumentation Diagram (P&ID) of the IFP Apparatus

9.2 List of IFP Apparatus Components

Table 9.1 Equipment specification

Temp. range	Pres. Range	Footprint (L x H x W)			Weight	Max. Power Consumption
		Workstation	Small Frame	Large Frame		
0-200 °C	0.1-50 MPa	0.7x0.9x0.8 m	0.6x0.46x1 m	1.3x1.9x1.2 m	280 kg	2800 watts

Table 9.2 Major components of the apparatus

Ref No.	Components	Manufacturer	Material	Model	T, P Limits
-	View Cell	Imperial College	Titanium Gr4	Custom	473 K 50 MPa
-	Windows	Crystran	Sapphire	40 mm Ø x 22 mm thick	473 K 50 MPa
F1 F2 F4	Reducers 1/4HP-1/16LHP	Sitec	Titanium Gr5	625.2321-Ti5	100 MPa
V11	Safety Head	Body	Titanium Gr5	720.5032-2-Ti5	100 MPa
		Burst Disc		Sitec	728.0650-Ti
V1 V2 V3	Type 2 LHP Valve	Sitec	Titanium Gr5	610.3220-Ti5	100 MPa
F5	Tee 1/16 LHP	Sitec	Titanium Gr5	620.1323-Ti5	100 MPa
F3	Tee 1/4	Sitec	Titanium Gr5	720.1433-Ti5	200 MPa
V10	Type 6 Check Valve	Sitec	Titanium Gr5	620.4426-Ti5	200 MPa
P1 P2	Quizix Pumps	Strata Technology Ltd	HC276	CP153 Q5210-HC	283-338 K 68 MPa
-	Chiller	Huber/ Radleys	Air-cooled	HB 2008.0020.99	253-473 K
			Silicon Oil	HB 6162	
V9	5-Way Ball Valve	Swagelok	Stainless steel	SS-43ZFS2-049	338 K 17 MPa
V4 V5 V8	3-Way Ball Valve	Swagelok	Stainless steel	SS-41GXS2	420 K 17 MPa
V12	Low-Pressure Proportional Relief Valve	Swagelok	Stainless steel	SS-RL3S4	408K @ 1.55 MPa
V13 V14 V15 V19	Check Valve	Swagelok	Stainless steel	SS-CHS2-1/3	41.3 MPa @ 310 K
F9	Union Cross	Swagelok	Stainless steel	SS-200-4	-
F7 F8 F11 F21 F22 F23	Union Tee	Swagelok	Stainless steel	SS-200-3	-
F6	Union	Swagelok	Stainless steel	SS-200-6	-
F17 F18 F19	Bulkhead Union	Swagelok	Stainless steel	SS-200-61	-
F14 F15 F16	0.5 µm Filter	Swagelok	Stainless steel	SS-2TF-05	41.3 MPa @ 310 K
F10 F12 F13	Reducer 1/4-1/8	Swagelok	Stainless steel	SS-400-6-2	-
F20	Reducer 3/8-1/8	Swagelok	Stainless steel	SS-200-1-6RS	-
V6 V7	Ball Valve	Ham-Let	Stainless steel	H800SSSL1/8	20.7 MPa

					422 K
-	Rod Lip Seal	Parker/Ceetac	Fiberglass Filled PTFE	M203 FBC 0200 00300 036 SVM	144-575 K
-	1/16" Tubing	Thames Restek	Titanium Gr2	1.6 mm OD x 0.3 mm ID	88 MPa @ 298 K; 53 MPa @ 477 K
-	¼" Tubing	Hi-Pro	Titanium Gr2	6.35 mm OD x 2.5 mm ID	78 MPa @ 298 K; 50 MPa @ 477 K
-	¼" Tubing	FTI Ltd.	Stainless steel	-	59 MPa
-	1/8" Tubing	FTI Ltd.	Stainless steel	-	59 MPa
-	1/8" Tubing	Polyflon	PTFE	-	298 K 2.8 MPa
PT1	Pressure Transducer	DJ Instruments	Titanium	DF2-TI-04-500 BAR	100 MPa 233-333 K
TT1	Temperature Sensor	Sensing Devices Ltd	-	4.76 mm x 75 mm	473 K

Table 9.3 Major additional components

Name	Ref. No.	Quantity	Manufacturer
Monochrome CCD Camera	p/n 100-12-F4	1	Ramé-Hart Instrument Co.
LED Light Assembly	LMH020-1250-35G9- 00000TW	1	CREE
LED Light Heat Sink	LMH020-HS00-0000- 0000001	1	CREE
LED Light Power Supply	615-1666	1	B&K
Calibration Tool	p/n 100-27-31-U Custom plates	1	Ramé-Hart Instrument Co./ Imperial College
Bullseye Level	LVL01	1	Thorlabs Ltd.
Optical Stand Assembly	Miscellaneous	3	Thorlabs Ltd.
Automated Tilting Base	p/n 100-25-A	1	Ramé-Hart Instrument Co.
Magnetic Stirrer	STI2273	1	Scientific Laboratory Supplies
Magnetic Stirrer Bar	Z329126-10EA	10	Sigma Aldrich
Aluminium Heating Jacket	Custom	1	Imperial College
Insulating Windows	56 mm Ø x 4 mm thick Borosilicate	2	UQG Ltd.
Temp. PID Controller	2216e Custom enclosure	1	Eurotherm/ Imperial College
Cartridge Heaters	E5A45-E12	4	Watlow Ltd.
Data Acquisition Unit (DAQ)	34972A, 34901A	1	Agilent/RS Components
Vacuum Pump	VACU732202	1	VWR International Ltd
Substrate Holder Assembly	Titanium Gr4 body/ Titanium Gr2 screws/	1	Imperial College/ Fastenright Ltd.

	PTFE O-ring/ Viton O-ring/ Magnet		
Substrate Holder Rod	Titanium Gr3 (0.2 Ra)	2	West Midland Grinding
Rod Plugs	Stainless Steel body/ Titanium Gr4 insert	2	Imperial College
Substrate Installation Tool	Aluminium	1	Imperial College
Extended M2 Allen Key	Aluminium	1	Imperial College
Substrate Holder Installation Tool	Aluminium	1	Imperial College
CPU Tower	N/A	1	HP
Power Sockets	N/A	13 (3 extension cables)	N/A
Barricade Frame	Custom	2	Phoenix Mecano/ Imperial College
Frame Castors	611-4414	4	RS Components
Workstation	Custom	1	W E Marson & Co Ltd
Fume Cupboard	N/A	1	N/A

Table 9.4 Spares and service kit

Name	Description	Ref. No.	Quantity	Manufacturer
Window Removal Tool	Stainless Steel	17 mm HEX drive	1	Imperial College
Window Blanks	Stainless Steel	40 mm Ø x 22 mm thick	2	Imperial College
Window O-rings	Viton BS-4518 0396-24	BS129V75, BS129V90	100 each	Polymax
Window Back-up Films	Sapphire & insulating windows	PEEK 0.1 mm	10 per pair	Imperial College/ Goodfellow Cambridge Ltd
Windows	Sapphire	40 mm Ø x 22 mm thick	1	Crystran
Insulating Windows	Borosilicate	56 mm Ø x 4 mm thick	1	UQG Ltd.
Rod Seal	O-ring	4.1 mm ID X 1.6 mm DS, V75	16 each	Polymax
	Back-up ring	PEEK		
Brine Filter	10 µm pore size	A-446	20	Kinesis Ltd.
Sitec Check Valve	Ceramic Ball	791.38.0014-8	3	Sitec
Liquid Feed Cap	-	-	2	Kinesis Ltd.
Liquid Feed Cap Sleeves & Plugs	-	Miscellaneous	5	Kinesis Ltd.
Safety Rupture Disc	Titanium Gr5	65 MPa	2	Sitec
1/16" Tubing	Titanium Gr2	1.6 mm OD x 0.3 mm ID	4 m	Thames Restek
1/16" Sleeves	Titanium Gr5	620.0220-Ti5	8	Sitec
Type 2 LHP Valve	Titanium Gr2	610.3220-Ti5	2	Sitec
Quizix Pump Speedbite Fittings	1/8" and 1/16" sleeves	SSL10 HC276 SP20 HC276	5 each	Autoclave Engineer/Hydrasun
Quizix Pump Tool Kit	Safety disc, piston extraction, spanner		1	Strata Technology Ltd.

Table 9.5 Consumables of the apparatus

Name	Description	Purpose	Quantity	Supplier
Helium & Regulator	-	Leak test	1	BOC
Dip-Tube Carbon Dioxide & Regulator	111304-F	Measurement	1	BOC
Nitrogen & Regulator	-	Measurement	1	BOC
Argon & Regulator	-	Measurement	1	BOC
Hydrogen & Regulator	-	Measurement	1	BOC
Hexane	-	Cleaning	1 L	Sigma Aldrich
Acetone	-	Cleaning	1 L	Sigma Aldrich
Deionised water	-	Measurement	-	-
Salts	-	Measurement	500 g	Sigma Aldrich
Rock samples	11.6 mm x 10.6 mm x 7.0 mm	Measurement	-	-
Compressed air	4-6 bar	Quizix Pump	-	-
Silicon Oil	HB 6162	Refrigerant for chiller/heater	10 L	Radleys
1 L glassware	-	Collect effluent/ cleaning fluids	5	-

9.3 View Cell Design

Table 9.6 O-ring and groove dimensions for static diametrical sealing

O-ring reference no.	0396-24	Groove width	3.3 (O-ring)
Nominal internal diameter	39.6 ± 0.30 mm	Total diametrical clearance, G_{max}	$0.10 < G < 0.14$ mm
Cross-sectional diameter	2.4 ± 0.08 mm	Window diameter, d_1	39.96 ± 0.01 mm
Outer diameter	44.4 mm	d_2 , max.	40.14 mm
Radial depth	2.07 mm	Lead in chamfer	0.7
Groove diameter	44.10 mm	Max. radius	0.2

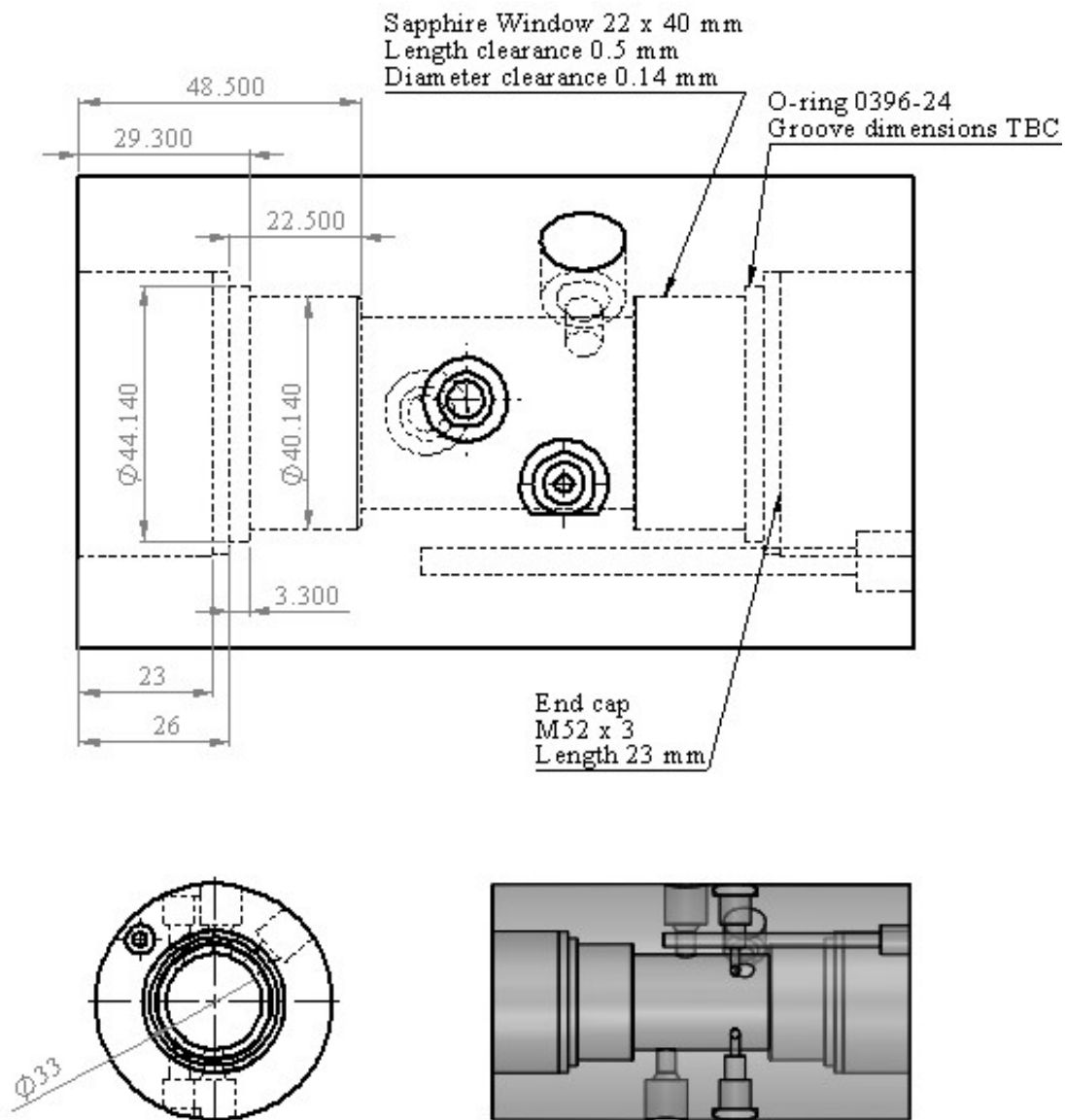


Figure 9.2 Engineering drawing of the view cell vessel

9.4 Substrate Adjuster

The design of the substrate adjuster consisted of two coupled-magnets that controls the up-down movement and rotation of the rod connecting the substrate holder (see Figure 8.3). The dimensions of the high pressure housing was constrained by the dimensions of the magnets that could be supplied by Magnet Sales & Service Ltd, and the available space around the view cell inlet port. The design parameters and dimensions of the high pressure housing of the adjuster are given in Table 8.7. The housing is made of titanium grade 12 (see Figure 8.4); containing the inner ring, the smaller magnet, and the rod (see Figure 8.3c) in the inside; and an outer ring with the larger magnet on the outside. The outer ring was supported on a stainless steel plate and locked with a clamp mechanism. The high pressure titanium housing was closed at the top with a titanium cap. The bottom part fits into the high pressure port of the view cell. The seal used was a face seal with a Viton O-ring (4.1 mm ID x 1.6 mm CS) and a PEEK backup ring.

Table 9.7 Design parameters of the high pressure housing for the substrate adjuster assembly

Parameter	Value
Inner diameter, ID	14.3 mm
Outer diameter, OD	20.3 mm
Wall thickness	3 mm
Diameter ratio, $K=OD/ID$	1.42
Working pressure, p_w	30 MPa
Yield pressure, p_y	76.5 MPa
Burst pressure, p_b	124.61 MPa
MAWP, p_{max}	31.15 MPa
Test pressure, p_{test}	46.7 MPa
Total Length	108.8 mm

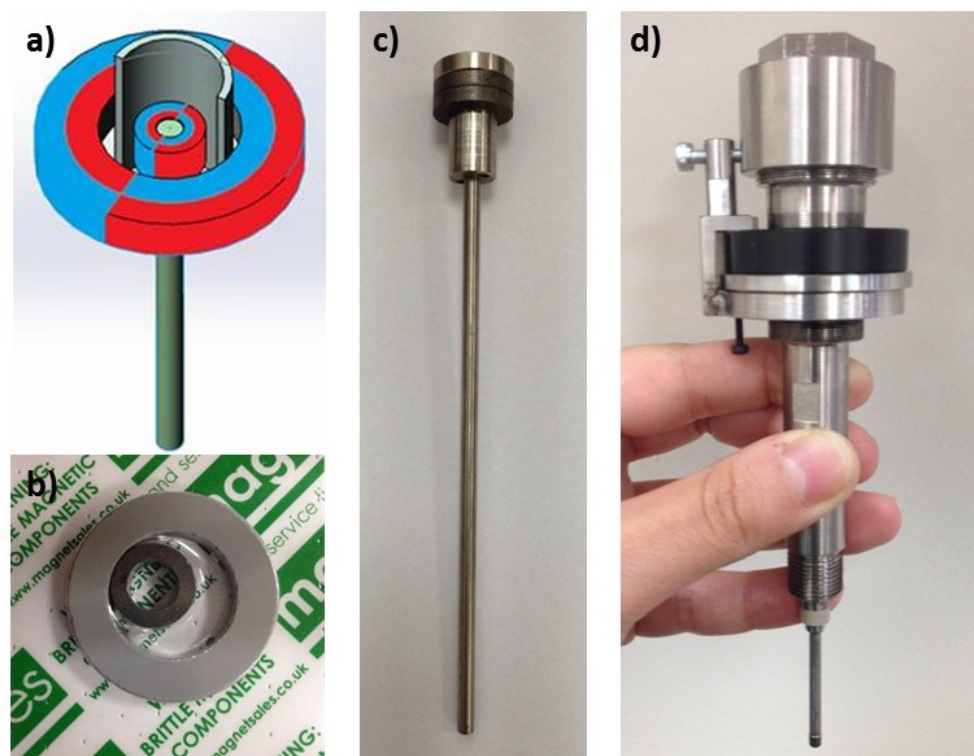


Figure 9.3 a) Magnet assembly drawing (Magnet Sales & Service Ltd). b) Iso Bonded NdFeB rings as supplied. c) Rod with the inner ring and magnets. d) Magnetic substrate adjuster assembly.

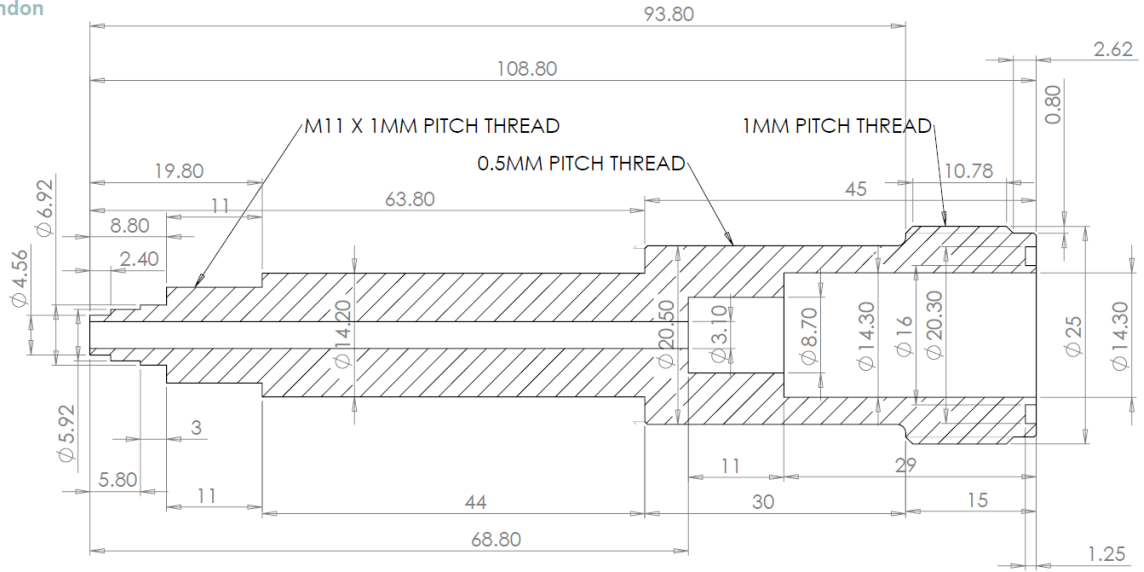


Figure 9.4 Engineering drawing of the substrate adjuster assembly

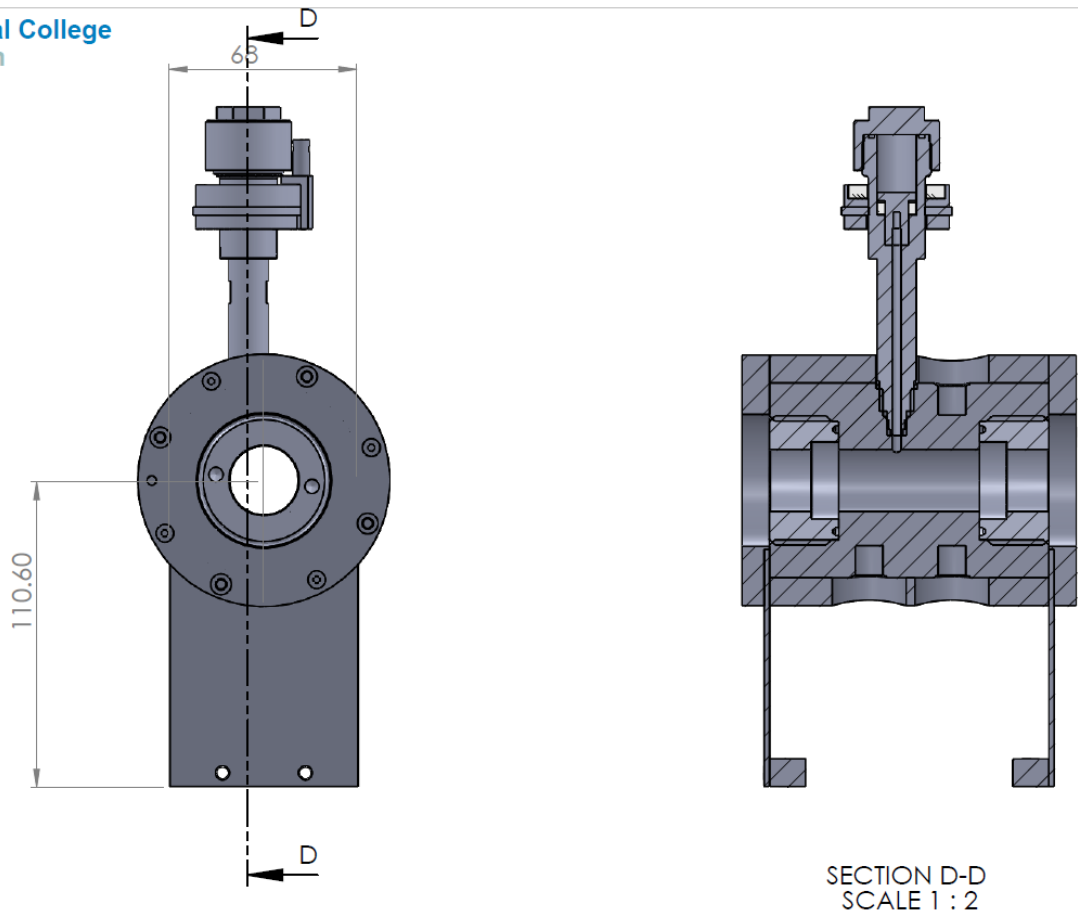


Figure 9.5 Assembly of the view cell with the magnetic manipulator.

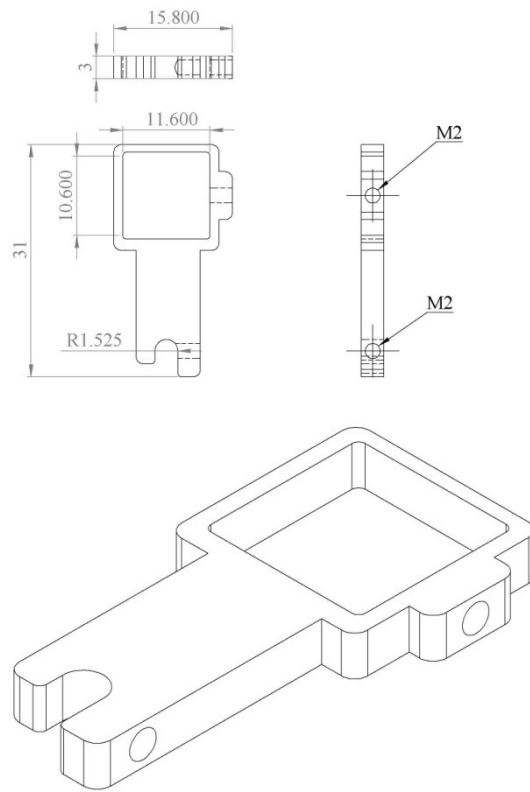




Figure 9.6 Engineering drawing of the substrate holder

9.5 Pressure Test Certificate

Pressure Test Certificate

Vessel	Description: Material: Titanium Grade 4 Overall external dimensions: H = 144.0 mm; D = 81.6 mm Inner dimensions: H = 48.0 mm; D = 33.0 mm	
	Manufacturer: Chemical Engineering Workshop, Imperial College London Year of construction: 2014	
Specifications		
Operating Pressure OP Min./Max. (bar)	0	500
Operating Temperature OT Min./Max. (°C)	0	200
Capacity V (litre)	0.0411	
Test Pressure PT (bar)	1150	
Specific Tests		
	Pressure (bar)	Duration at test pressure (min)
Leak Test Medium: water	115	15
Proof Pressure Test Medium: water	1150	30
Remarks	See '7th March 2014 - Vessel Pressure Test Log'	
<u>Test Result:</u>		
The vessel conforms to the requirements under sound engineering practice.		
		
Tested by: Florence Chow	Witnessed by: J. P. Martin Trusler	
Date: 7 March 2014		